UNIVERSITY OF LEEDS

Temporal Dynamics of the Mixed Magnetic Phase of B2-Ordered FeRh

Jamie Robert Massey

University of Leeds

School of Physics and Astronomy

Submitted in accordance with the requirements for the degree of

Doctor of Philosophy

September, 2019

For Alan and Diane
and the loving memory of Emma Louise Scott.

Intellectual Property Statement

The candidate confirms that the work submitted is his own and that appropriate credit has been given where reference has been made to the work of others.

This copy has been supplied on the understanding that it is copyright material and that no quotation from the thesis may be published without proper acknowledgement.

The right of Jamie Robert Massey to be identified as Author of this work has been asserted by him in accordance with the Copyright, Designs and Patents Act 1988.

Work from the following jointly authored publication was presented in this work:

J. R. Massey*, K. Matsumoto*, M. Strungaru*, R. C. Temple, T. Higo, K. Kondou, R. F. L. Evans, G. Burnell, R. W. Chantrell, Y. Otani, and C. H. Marrows. *Phase Boundary Exchange Coupling in the Mixed Magnetic Phase Regime of a Pd-doped FeRh Epilayer.* arXiv preprint arXiv:1807.01615, in preperation for submission to Physical Review Materials. * these authors contributed equally to this work.

Work from this publication is included in chapters 5 and 6. Some figures have been taken from this jointly authored work.

Work attributed to the candidate: The author here is responsible for: the conception of the experimental idea, the design, growth and characterisation of the sample, the performance and analysis of the magnetic resonance experiments on the Pd-doped FeRh layer and writing the manuscript.

Work attributed to others: K. Matsumoto was responsible for setting up the measurement apparatus in RIKEN and preliminary magnetic resonance measurements on Py and Pd-doped FeRh. M. Strungaru is responsible for the performance and analysis of the computer simulations. R. C. Temple assisted in the sample design. T. Higo is responsible for the measurement of the sample thickness. R. F. L. Evans is responsible for the software used to perform the simulations. K. Kondou, R. W. Chantrell, Y. Otani, and C. H. Marrows helped to supervise the project. J. R. Massey and C. H. Marrows wrote the manuscript, with all authors contributing to the final version.

R. C. Temple, T. P. Almeida, **J. R. Massey**, K. Fallon, R. Lamb, S. A. Morley, F. Maccherozzi, S. S. Dhesi, D. McGrouther, S. McVitie, T. A. Moore, and C. H. Marrows. *Antiferromagnetic-ferromagnetic phase domain development in nanopatterned FeRh islands.* Physical Review Materials **2**, 104406, 2018.

Work from this publication is not explicitly presented in this thesis, but a figure from this paper is used in chapter 7 to help demonstrate a point and aid the interpretation of that experiment. This figure is reused with permission from the relevant publishing house.

Work attributed to the candidate: Preliminary growth and characterization of the FeRh/NiAl bilayer system and assistance with the beamtime experiment.

Work attributed to others: R. C. Temple was responsible for the growth and characterization of the films presented in that work as well as the data/image analysis. R. C. Temple, T. P. Almeida, K. Fallon, R. Lamb,

S. A. Morley, F. Maccherozzi, S. S. Dhesi and T. A. Moore were involved in the data aquisition for the PEEM images. T. P. Almeida, K. Fallon, R. Lamb, D. McGrouther and S. McVitie are responsible for the tranmission electron microscopy images seen in this publication. T. A. Moore, and C. H. Marrows. D. McGrouther, S. McVitie, T. A. Moore, and C. H. Marrows supervised the project. R. C. Temple and C. H. Marrows wrote the manuscript, whilst all authors were involved in discussions regarding the work and commented on the manuscript.

Acknowledgements

I'd like to begin this section by thanking my supervisor, Prof. Chris Marrows, for a number of things. Firstly, for the opportunity to come to Leeds do my PhD in such a fantastic group and for the countless opportunities to talk about my work around the world. As well as for all the invaluable encouragement and patience shown towards me during my PhD. I would also like to thank my supervisor at Diamond, Dr. Paul Steadman, for making me feel welcome down south and for all your help on the beamtime experiments.

I'd also like to thank the other academics within the group, with special mentions to Gavin, Brian and Mannan, for their fruitful discussions around the coffee table every morning. I would also like to extend my thanks to the Condensed Matter group in Leeds as a whole, for being a supportive and fun place to do a PhD. Most notably I would like to thank Rowan for his help and friendship during the course of our time together at Leeds. I would also like to thank Ben, Ris, Kowsar, George, Josh, Matt, Phillipa, Sophie and Joe for making Leeds a very enjoyable place to do a PhD.

I would also like to thank Kenta, Jorge and everyone at RIKEN for making me feel welcome during my time there. It was a truly unforgettable experience and I would like to thank everyone involved in making it so.

No acknowledgements list would be complete without Louise, Simon, Shaun, Ross, Liam, Matt and Tally for their friendship over the years. As well as the team at CrossFit Leeds, whom I thank for giving me somewhere to go of an evening to unconsciously work on the problems of my PhD. To Dan, Joe, Steve, Jay, Kostas, Paul, and Philly I extend my most sincere thanks for making my time in Leeds so enjoyable.

I would also like to thank Chloë, whom I thank for your perserverance and patience with me over the last few years. I hope to be able to repay the favour in the years to come.

Finally, I would like to thank my family, whose unwavering love and support have allowed me to chase this dream of mine and to whom I cannot find the words to truely express my gratitude for all your help over the years.

Abstract

B2-ordered FeRh undergoes a first-order metamagnetic transition from an antiferromagnet (AF) to a ferromagnet (FM) upon heating. Thin films of B2-ordered FeRh are grown using DC magnetron sputtering and characterized for their behaviour at GHz frequencies and their dynamic behaviour over hour timescales.

Ferromagnetic resonance investigations reveal a change in the spectroscopic splitting factor, g, through the range of the transition probed here. By introducing a model that describes the development of the two magnetic phases through the transition, this change in g is shown to be consistent with the development of an exchange coupling across the magnetic phase boundary that induces a non-zero magnetic moment in the AF phase as the result of a thickness dependent phase transition in the AF layer. The influence of such a phase transition is also seen in the extracted value of the Gilbert damping parameter in this experiment.

Spin-wave resonance measurements are then performed to try and conclusively measure the exchange coupling between the two magnetic states in FeRh. Measuring the exchange stiffness through the transition reveals that the AF phase has a non-zero exchange energy that varies through the measurement range probed here. The behaviour of the exchange stiffness in the AF layer is attributed to a combination of both the onset of the exchange coupling and the presence of evanescent spin-waves, both of which are consequences of the thickness dependent phase transition in the AF layer.

It was then shown that the structure of both magnetic phases could be measured directly with X-Ray Magnetic Dichroism using both linearly and circularly polarized light. The objects measured in these experiments are then characterized for their dynamic properties using X-Ray Photon Correlation Spectroscopy. These studies reveal reveal that the dynamic behaviour of the system is dependent on the type of magnetic dichroism used to probe it. This study also shows it is possible use x-ray magnetic linear dichroism to directly measure the structural and dynamic behaviour of AF materials.

Contents

Abbreviations

AF	Antiferromagnetic	RASOR	Reflectivity and Advanced Scattering from Ordered Regimes
AFMR	Antiferromagnetic Resonance	RF	Radio Frequency
BCC	Body Centred Cubic	RKKY	Ruderman-Kittel-Kasuya-Yosida
CCD	Charged Coupled Device	RMSAXS	Resonant Magnetic Small Angle X-Ray Scattering
CER	Compressed Exponential Relaxation	RMXS	Resonant Magnetic X-Ray Scattering
DC	Direct Current	SAXS	Small Angle X-Ray Scattering
ESW	Evanescent Spin-Wave	SER	Stretched Exponential Relaxation
FM	Ferromagnetic	SQUID	Superconducting Quantum Interference Device
FMR	Ferromagnetic Resonance	SWR	Spin-Wave Resonance
GSG	Ground-Signal-Ground	TDPT	Thickness Dependent Phase Transition
LLG	Landau-Lifschitz-Gilbert	VNA	Vector Network Analyser
MCA	Magnetocrystalline Anisotropy	VSM	Vibrating Sample Magnetometer
ME	Magnetoelastic	XAS	X-Ray Absorption Spectroscopy
MMP	Mixed Magnetic Phase	XMCD	X-Ray Magnetic Circular Dichroism
MPB	Magnetic Phase Boundary	XMLD	X-Ray Magnetic Linear Dichroism
PEEM	Photoemission Electron Microscopy	XNLD	X-Ray Natural Linear Dichroism
PM	Paramagnetic	XPCS	X-Ray Photon Correlated Spectroscopy
PNR	Polarized Neutron Reflectometry	XRD	X-Ray Diffraction
PSSW	Perpendicular Standing Spin-Wave	XRR	X-Ray Reflectivity

Chapter 1

Introduction

1.1 Spintronics

Conventional electronics refers to the transfer of information by the manipulation of electrical charge [1, 2]. However, as the rich and vibrant research field of condensed matter physics continues to blossom, a new path for the data transfer has emerged in the form of spintronics [1, 2]. Spintronics is the transfer of information via the manipulation of both charge and spin currents and takes place in magnetic materials [1, 2]. Research into spintronic devices requires understanding of new and exciting science in a wide range of material systems, with a view to their application in industrial settings.

As the circuitry based on conventional electronics nears its theoretical capacity, spintronic devices can provide the increase in data capacity and performance required to revolutionize the capabilities of information technology [2]. Devices developed from research into spintronics have already provided replacements for hardware based on conventional electronics in computer hard disk drives [1]. The components involved in computer hardware perform a number of different tasks and any new technologies must also be versatile if they are to replace the existing structures [2]. Devices using spintronics must be capable of performing a variety of different tasks which range from being able to operate in the GHz frequency regime to storing information for long periods [2]. As such, a wide variety of different materials and device architectures are used to try and realise these different possibilities [1, 2].

One material that has seen a surge of interest for applications in spintronic device architectures is the B2-ordered FeRh alloy [3–7], which is a material that undergoes a first-order metamagnetic transition from being in an antiferromagnetic (AF) to a ferromagnetic (FM) state at the technologically relevant temperature of ≈ 380 K [8, 9]. This magnetic transition is accompanied by changes in volume [10–12] and resistivity [9, 13] and is also sensitive a range of various stimuli [4, 5, 11, 14–29]. The combination of all of these different aspects of the metamagnetic transition in FeRh make it an ideal candidate for use in spintronic devices [3–7].

As this is a first-order phase transition there exists a region within the transition in which both magnetic phases are expected to be present which is known as the mixed magnetic phase (MMP) [7, 12, 27, 30–37]. Not much is known about the properties of the material in this region of the transition and a greater understanding is required as it may provide a greater functionality to spintronic devices based on FeRh.

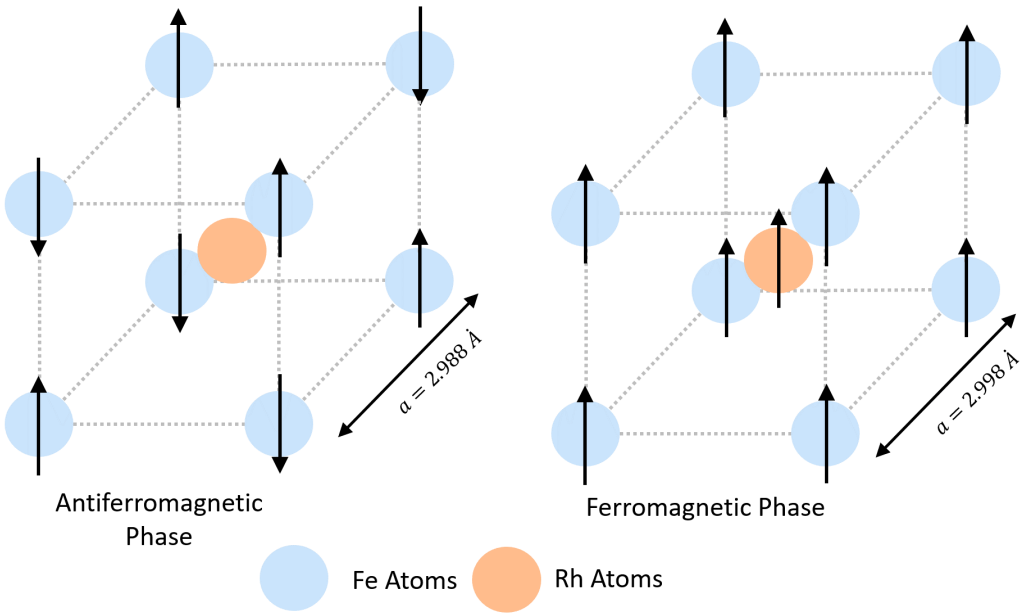

Figure 1.1: The unit cell of the two magnetic phases present in B2-ordered FeRh with their spin structure indicated by the arrows.

1.2 General Overview of FeRh

The metamagnetic transition in B2-ordered FeRh was first discovered by Fallot and Hocart, who demonstrated that the system underwent a first-order phase transition from a non-magnetic state to that of a FM state upon heating in 1939 [8]. When the heating continues, the FM state of FeRh undergoes a second-order phase transition to a paramagnetic (PM) state at Curie temperatures around 650 K [9]. On cooling from the PM state, the FM state is recovered at the Curie temperature [8, 9]. However, the transition to a non-magnetic state is seen to be hysteretic in temperature with a difference of around 10 K between states of the same magnetization for the different temperature sweep directions [8, 9]. The non-magnetic state was later found to be that of the G-type antiferromagnet (AF) using neutron diffraction, where the spins in the AF phase are aligned along the (111) crystal plane [38, 39]. These studies also revealed that each Fe atom had a magnetic moment $\approx 3\ \mu_B$ in either magnetic phase, but that the Rh atom gained a magnetic moment of $\approx 1\ \mu_B$ in the FM phase compared to magnetic moment of $0\ \mu_B$ it possesses in the AF phase [38, 39]. FeRh has a CsCl or

B2 structure which comprises of two interlinked simple cubic structures, one for each elemental species, that form a body centred cubic structure [8]. In this configuration, the central atom is of a different atomic species to the remainder of the atoms in the unit cell, which has a lattice constant of ≈ 2.99 Å for B2-ordered FeRh [8]. A diagram of the structure of the unit cell and the spin configuration for the two magnetic phases is shown in Fig. 1.1.

The change in the magnetic state of the system across the transition has also been found to be accompanied by changes in the resistivity [9, 13] and volume, with the FM phase having a 1% larger volume than the AF whilst the B2 order is retained [10–12]. The change in resistivity was later attributed to a release of electrons in a manner similar to that of a Mott insulator-metal transition, implying a change in the electronic band structure of the system [13]. As consistent with the first-order phase transition, a large change in entropy is also observed alongside the magnetic transition [14, 40]. This change in entropy leads to a large magnetocaloric response in the system [21, 41–43]. Example traces through the transition that show the changes of the magnetization, resistivity, entropy and volume are included in Fig. 1.2. As changes in the resistivity and crystal structure accompany the magnetic transition, the first-order phase transition in FeRh can be thought of as a coupled magnetostructural phase transition.

One of the most fascinating properties of this phase transition is that the transition temperature can be manipulated using a wide variety of internal and external stimuli [4, 5, 11, 14–29]. Firstly, it was shown that the inclusion of chemical dopants within the film can change the transition temperature by Kouvel [14]. This work also showed that the direction in which the transition temperature changed was dependent on the identity of the dopant, with Pd doping pushing the transition temperature down and Ir doping increasing the transition temperature [14]. This was investigated further by Barua *et al.*, who collated the transition temperatures of FeRh doped with various elements and showed that the direction in which the transition temperature changes is dependent on the number of electrons in the valence band of the dopant material [15]. The application of strain is also seen to affect the transition temperature, as this acts to stabilize one magnetic phase over the other depending on the type of strain [4, 5, 11, 16–19]. The metamagnetic transition in FeRh alloys is seen in a small composition range centred around 50:50 at % [20], as such it follows that the transition temperature is also sensitive to the alloy composition [20–22], with Fe rich materials have a lower transition

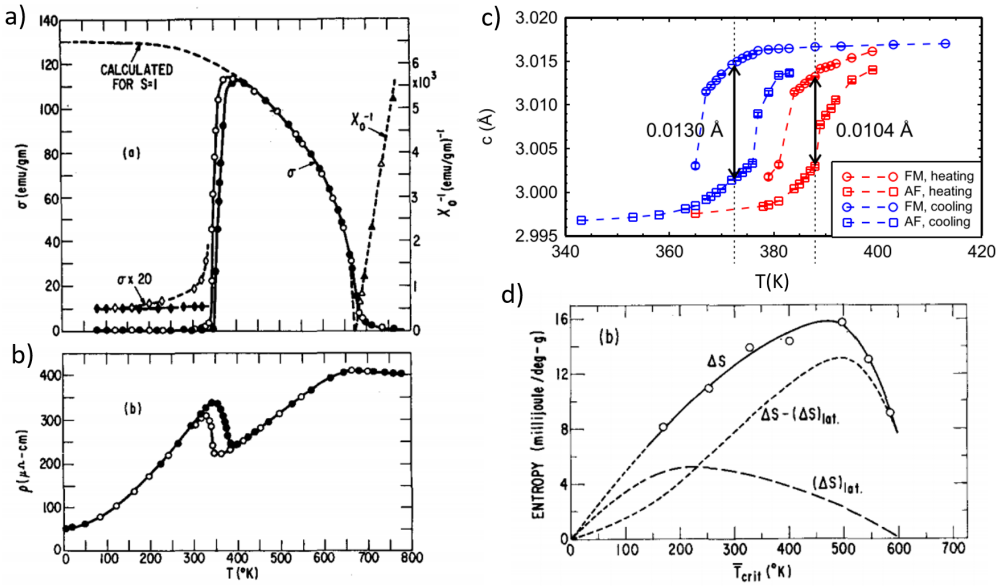

Figure 1.2: Examples of the different properties of the metamagnetic transition in FeRh. Panel (a) shows the magnetization as a function of temperature upon warming (black circles) and cooling (white circles). Panel (b) shows the change in resistivity against temperature for the same sample with the points taken on the different transition branches shown in the same way. The figures in panel (a) and (b) are taken from Ref. [9]. Panel (c) shows the value of the out of plane lattice constant, c, as a function of temperature taken from Ref. [12]. Panel (d) shows the difference in entropy across the transition as a function of the transition temperature for a variety of samples, each with different transition temperatures, taken from Ref. [14]. The dashed lines here show the predicted value of the change in entropy due to contributions from the lattice and the difference between the measured and expected value [14]. It is clear here that contributions from the lattice alone fail to account for the behaviour seen in FeRh.

temperature than their Rh rich counterparts [22]. The application of external magnetic field has also been seen to lower the transition temperature by ≈ -8 K T^{-1} by Maat *et al.* [23]. The transition in FeRh is also seen to be sensitive to finite size effects [18, 19, 24–27]. It has also been seen to be possible to alter the magnetic state of FeRh via the injection of spin polarized currents from a Co electrode [28, 29].

The work of Maat *et al.* also suggests that the nucleation dynamics of the two mag-

netic phases is different between temperature sweep directions, with the FM domains nucleating around centres of local symmetry breaking on heating and the AF domains nucleating homogeneously through the film when cooling [23]. This asymmetry is also seen in investigations into the development of the lattice constant through the phase transition, which reveal that the FM phase is retained through much larger portions of the transition than the AF phase when heating [12]. This is attributed to the supercooling of the FM domains, whilst the equivalent superheating process is not seen for AF domains when heating, implying that the FM state is metastable [12]. This asymmetry in the stability of the two magnetic states is responsible for the temperature hysteresis of the transition. As the behaviour of the transition is different between the two temperature sweep directions, they are, from this point forward, treated as separate entities and are referred to as the heating and cooling branches of the transition respectively.

1.2.1 Origin of the Metamagnetic Transition

From an energetics perspective, the metamagnetic transition in B2-ordered FeRh can be explained by comparing the Helmholtz Free energies, F, of the two magnetic states. The Helmholtz free energy of a system in the absence of external field is given by [44]:

$$F = U - TS, \tag{1.1}$$

where U is the internal energy of the state and encompasses the contributions to the energy from the electrons, the lattice and the magnons for the purposes of this discussion, T is the temperature and S is the entropy of the state. It is known that the FM state of FeRh has a higher entropy than the AF state [14, 21, 40–43] and that the two states have different internal energies [45–48], with the AF state being stable at lower temperatures. As the temperature increases, F will decrease in the FM state at a faster rate than that of the AF state and the transition will occur at temperatures where the Helmholtz free energy of the FM state becomes lower than that of the AF state. The temperature where the energy of the two states is equal is taken to be the transition temperature. The addition of a magnetic field term into this equation will also act to reduce the energy of the FM phase, leading to the reduction in the transition temperature seen in the experiments [23].

Though the energetics of the phase transition are straightforward, the identity of the physical mechanism responsible for the transition remains an open question for this

material. There are three quantities that vary across the transition: the resistivity, the magnetic state and the volume, each of which could be responsible for the transition. There have been a number of theories put forward to explain the origin of the transition, such as exchange inversion as the lattice expands upon heating [49], changes in the electronic band structure [50], both of which have been dismissed on entropy grounds as being too small to account for the measured values [14, 45]. It was found that only by taking a holistic approach to the nature of the transition and considering contributions from the lattice, the electrons and the magnons to the change in entropy, can the behaviour of the transition be adequately explained [45]. This finding implies that the magnetostructural phase transition in FeRh comes as a collective entity and that changes in the various properties across the transition are coupled to each other and cannot be separated [45]. This theory was later confirmed by Gu and Antropov who calculated the expected change in entropy across the phase transition and found that contributions from all three of these physical changes are required to explain the entropy change in the transition [47].

The theory that the transition is not driven exclusively by changes to one property through the transition was expanded upon by Sandratskii and Mavropolous, who devised a hypothesis for the physical mechanism behind the transition [48]. In this work it is theorized that the Rh atom has its 3d shell hybridized to the two Fe sublattices in AF FeRh, and if there is an asymmetry in the alignment of magnetic moments on the two Fe sublattices then a magnetic moment develops on the Rh atom [48]. The emergence of the moment on the Rh atom then changes the magnon density of states at the Fermi energy to favour the presence of the FM state [48]. This, in turn, increases the asymmetry in the alignment of the magnetic moments of the two Fe sublattices, increasing the Rh moment and therefore the asymmetry in the magnon density of states at the Fermi energy. The emergence of the Rh moment begins a positive feedback loop which continues until the material has fully undergone the transition from an AF to an FM state [48].

Interest in ascertaining the origin of the driving force behind the transition was reinvigorated with the advent of picosecond laser pulses [51–53]. Measuring the system at this temporal resolution provided access to the timescales over which the response of the system to heating could be measured, with the idea being that it may be able to separate the responses of the different changing quantities as the transition progressed

[51–53]. Thiele *et al.* presented work that concluded that changes in the electronic structure were responsible for the transition [51], whilst a similar study performed by Ju *et al.* suggested that this is not the case and that the driving forces behind the transition cannot be separated [52]. Stroboscopic X-Ray Magnetic Circular Dichroism (XMCD) measurements were performed by Radu *et al.* that provide picosecond resolution to the evolution of the magnetic moments of the two atomic species in response to being heated by a laser pulse [53]. These measurements suggest that the ratio of the magnetic moments of the two atomic species develop simultaneously through the measurement time upon heating with a laser pulse [53]. These results implies that changes in the physical properties of the material across the transition are linked together and are intimately entangled to the behaviour of the Rh moment as consistent with the predictions of the positive feedback loop predicted by Sandratskii and Mavropolous [48].

1.2.2 FeRh for use in Spintronic Applications

As the metamagnetic transition in FeRh is close to room temperature and is accompanied by changes in a plethora of measurable quantities, it has seen a surge in interest for use in a range of potential magnetic storage device architectures [3–7]. Each of these possible architectures makes use of different facets of the transition to demonstrate how FeRh could be utilized in future device structures. The large change in magnetization has been used to reduce the writing field in a FePt/FeRh bilayer for use in heat assisted magnetic recording [3]. The magnetic state of the system has been directly manipulated using voltage by changing the strain coming from a piezoelectric substrate [4, 5]. More recently, the AF phase of FeRh has been shown to demonstrate distinct resistance states when the system is cooled from the FM phase in the presence of an externally applied magnetic field with the field oriented in different directions within the film plane [54]. This has been utilized by Moriyama *et al.* to show that the AF phase of FeRh demonstrates read-write capabilities required of spintronic devices and could be a candidate for use in AF memory devices [6]. Le Gräet *et al.* has also made clever use the thickness dependent dopant gradients to create a transition temperature gradient across the film thickness [7]. By creating this transition temperature gradient, it is possible to then define a boundary between the two magnetic phases that can be moved up and down the film as a solid object, changing the resistance and

magnetization of the system in a controllable way [7].

In order to achieve the necessary information density to improve the current state of the art, spintronic devices must be operable on the nm length scale [1, 2]. As such, the effect of reducing the system size in FeRh has seen increased interest of late [18, 19, 24–27]. The first of these investigations came in the form of studying nanoparticles, which are seen to grow in FeRh when the film thickness is below a certain threshold, and exhibit core-shell AF/FM properties due to different transition temperatures between the bulk and the surface [24]. By taking the dimensions of FeRh wires down to the μm scale, it has been shown to be possible to see the switching of individual regions of material [25, 26]. The resistance in this case shows jagged features, as opposed to the smooth transition measured in bulk films, which is attributed to the switching of individual regions of material where the size of the object is now confined by the system geometry [25, 26]. Interestingly, these jagged features are prominent when heating. On cooling, however, the transition is seen to take place within one or two steps, which is consistent with the observation of supercooled FM material seen by de Vries *et al.* [12, 25, 26]. The effect of confining the system size by growing ultrathin films has also been studied by Barton *et al.* who show that the thinner the film thickness, the more prominent the effect of the substrate strain is on the properties of the material [19]. This work suggests that a strained region at the interface has different properties to that of the rest of the film and that an exchange coupling between the strained and unstrained layer might affect the properties of the devices [18, 19]. The most recent work that focusses on finite size effects in FeRh is that of Temple *et al.* who performed XMCD-Photoelectron emission microscopy (PEEM) on nanopatterned islands of FeRh [27]. This work shows that the process used to create these structures destroys the B2-order in parts of the film, which changes its properties [27]. These effects become more prominent as the size of the system decreases [27].

Le Gräet *et al.*'s work brings us on to the concept of the magnetic phase boundary (MPB), which here is defined as the region between the AF and FM phases. Between the transition extremes, there exists temperatures where both magnetic phases are present [7, 12, 27, 30–37]. Most of the spintronic devices that exist based on FeRh use either the completely AF or FM phase of FeRh or the transition between the two and miss out the MMP entirely [3–6]. However, as shown by the experiments that focus on the confinement of the system size in wires [25, 26], extending these devices

to encompass the MMP opens the system up to a larger number of distinct resistance states. Therefore, FeRh in the MMP could provide an increased data density and may lead to a breakthrough in the ability to store large amounts of data effectively and efficiently.

1.3 The Mixed Magnetic Phase of B2-Ordered FeRh

The issue that comes with using FeRh's MMP is that it is not well studied and its properties are poorly understood. One possible use of spintronic devices are for high frequency data processing which require operations at GHz frequencies to improve on the current state of the art [2]. In order to ascertain if the MMP of FeRh is suitable for use in these types of devices, its response to GHz excitations should be studied. Previous studies of this nature suggest and then dispute the presence of an exchange coupling present between the two magnetic phases in the MMP [55, 56]. The exchange coupling between the two phases is henceforth discussed as the interphase exchange coupling. The conflicting information makes it difficult to ascertain whether the exchange coupling is present, but the understanding of this phenomena is essential for the design of FeRh based spintronic devices in both the AF and the MMP regimes.

Another issue facing the understanding of the MMP is that the development of AF domains through the transition is very poorly studied. This is mainly attributed to the difficulty in imaging the AF phase using conventional magnetic imaging techniques due to its lack of a net magnetic moment. There is one study that has used X-Ray Magnetic Linear Dichroism (XMLD)-PEEM to measure the size of the AF domains in the nominally fully AF phase, but which has a low point density through the remainder of the transition [35]. More information is needed on the development of the AF phase in the MMP in order to be able to understand its properties and make use of it in spintronic devices.

Another possible use for spintronic devices is for long term magnetic storage [1, 2]. If the MMP of FeRh is to be used to access these higher data density regions, it may be useful to know whether these magnetic states are stable over long timescales. However, again, little is known about the dynamic behaviour of the MMP through the transition as there are few studies on it [57, 58]. In order to ascertain the suitability of the MMP for this purpose, its long term stability and therefore its dynamic behaviour must be studied.

The remainder of this literature review will be split into sections concerning each of these aforementioned points, the magnetic resonance experiments and the interphase exchange coupling, the development of the magnetic domain structure through the transition and the dynamic behaviour of the MMP.

1.3.1 GHz Frequency Behaviour Measured Using Ferromagnetic Resonance

Exchange coupling at an AF/FM interface is known to lead to exchange bias in these systems [59–62]. However, there exists no conclusive study that demonstrates the presence of exchange bias between the two magnetic phases in FeRh. This could be because of the domain structure in FeRh means that no bias is seen across the sample in the MMP, or that the energy difference between the two magnetic phases is comparable to the temperature fluctuations where the transition exists [46, 47] and any exchange bias is taken out of the system quicker than it can be measured using magnetometry techniques. Despite the lack of evidence for exchange bias in this system, the exchange coupling at the interface between the two magnetic phases is said to play an important role in the properties of devices based on the AF phase of FeRh [6]. FM material is found at the surface with the substrate in the AF phase, which means it is difficult to isolate the fully AF phase in thin film FeRh and the potential for exchange coupling is still present in that region of the transition [37].

There have been studies based on Ferromagnetic Resonance (FMR) in FeRh that allude to the presence of an interphase exchange coupling without providing a solid foundation for this claim [55], that have since been contradicted [56]. All studies, of which there are three, show a change in temperature dependent behaviour of the system between the MMP and the fully FM state due to the emergence of an anisotropy field that emerges when entering the MMP [55, 56, 63]. The three existing studies provide two explanations as to the origin of this extra anisotropy energy: exchange coupling between the two phases [55] and magnetoelastic effects due to strain at the interface between the two magnetic phases [56]. The other study fails to provide an explanation for the behaviour instead attributing it to general phase coexistence [63].

Of the two studies that present an argument for the origin of the anisotropy field, only one provides a quantitative estimate of the expected field [56]. This field is said to be due to strain between the film and the substrate and fails to fully account for

the size of the anisotropy field seen in the MMP [56]. The work where the origin of the anisotropy field is attributed to exchange coupling between the two magnetic phases fails to provide a rigorous argument for this claim [55]. The origin of the emergent anisotropy field in the MMP remains an open question, as neither of the current explanations adequately explain the observed behaviour. But what is clear, is that any spintronic devices that intend to operate using the MMP of FeRh in this GHz frequency regime require a greater understanding of this emergent anisotropy field in the MMP.

The Gilbert damping in the fully FM regime has been measured to be $\alpha = (1.3 \pm 0.8) \times 10^{-3}$ [55] which is very low compared to other metallic ferromagnets, such as Py, where $\alpha \approx 10 \times 10^{-3}$ [64]. The development of the damping through the transition was reported by Kumar *et al.* and is seen to increase across the entire temperature range encompassed by the transition [56]. The reason for this increase across the entire transition is unknown at this current time [56].

There are also other magnetic resonance techniques such as spin-wave resonance (SWR), which can be used to measure the exchange stiffness of a material [64–71] and antiferromagnetic resonance, (AFMR) which provides an insight into the properties of the AF regions [68, 72]. There are currently no studies that present results using either of these techniques on the FeRh system.

1.3.2 Characterization of the Domain Structure of Both Magnetic Phases Through the Transition

As this is a first-order phase transition, the coexistence of both FM and AF domains through the transition is expected. As such, the development of the magnetic domains has been well characterized using a plethora of different imaging techniques, including high resolution x-ray diffraction (XRD) [12, 30], Lorentz transmission electron microscopy [31], XMCD-PEEM on sheet films [32–34] and more recently, in nano-patterned islands [27], XMLD-PEEM [35], electron holography [36] and with polarized neutron reflectivity (PNR) [7, 37].

In general, these studies show a coexistence of the two magnetic phases between the two extreme magnetic states of the transition [7, 12, 27, 30–37]. The FM domains are seen to nucleate as flux closed structures around 200 nm in diameter [27, 31]. As the transition progresses, more of these domains are seen to nucleate and those that

already exist increase in size [27, 31]. This process continues until the arrangement is such that neighbouring domains coalesce into larger domains [27, 31–35]. Eventually, when all of the material is in the FM state, the domain structure is seen to take a striped orientation in the absence of external magnetic fields [27, 31–35]. When cooling, the disintegration of the larger FM domains into smaller ones when moving into the MMP appears to be homogenous through the surface of the film when imaged with XMCD-PEEM, whereas the nucleation centres are concentrated around defects and centre of local symmetry breaking when heating [27, 32–34].

In order to get a complete understanding of the domain development through the magnetic phase transition, a technique that is sensitive to the magnetic structure within the bulk of the material is required. There have been few studies that present such investigations, which all suggest that the development of the magnetic domains through the transition is not confined to the surface [7, 36, 37]. PNR measurements reveal a section of residual FM material at the surface with the substrate well into the nominally AF phase, which is attributed to substrate strain [37]. As the metamagnetic transition in FeRh is defect driven [23, 30], this may be expected as the surface breaks the symmetry. Further to this, the development of the magnetic domains through the transition has been imaged through a vertical cross-section of a FeRh thin film using electron holography [36]. This work shows the transition temperature is lower at the surface than in the bulk of the material, meaning that the FM domains nucleate at the either surface and proceed into the bulk as the transition progresses [36].

Combining these observations with those of the surface sensitive measurements leads to some interesting interpretations of the development of the domain configuration through the transition. The 2D techniques suggest that the nucleation of FM domains begins with flux closed structures, which grow in size and number through the transition until the entire surface is covered in FM material. However, it is seen from XMCD-PEEM measurements that the completion of the surface state is seen well before the entire sample is FM as measured from the magnetization [32]. This is then consistent with the depth dependent profile of the transition, in that the material at either surface is the first to become FM and these FM domains then permeate into the bulk of the material [36]. For regions of the transition where the surface is covered but the transition is not complete, this implies that the domain configuration can be modelled as a FM/AF/FM trilayer configuration. The magnetic profile at the top surface of the

material is seen to be intact for temperatures where the transition is more than 80% complete, as defined by the magnetization, implying that the trilayer model applies through this temperature range [32].

All of the measurements listed in this section are taken using techniques reliant on the presence of a magnetic moment [7, 12, 27, 30–34, 36, 37]. This means that the development and properties of the FM phase is well documented, whilst the same properties of the AF material remain poorly studied. There is one study published in the literature that uses XMLD-PEEM to focus on the AF domain development, which is produced by Baldasseroni *et al.* [35]. Here, the measurements of the AF domain size are presented alongside length scales extracted from XMCD-PEEM measurements for the same temperature and appear to hold steady at 300 nm in the nominally fully AF regime. As the AF domain size is consistent when moving through the transition it suggests that the AF domains do not coalesce like their FM counterparts and that their size is limited by the defect density on the film surface [35]. The development of the AF domains throughout the transition is poorly understood and a better understanding of this region is required in order to fully understand the material. Investigations into this area may also lead to structural information about the MPB, which is also poorly studied.

A technique that may be of use in the measurement of the AF phase is that of Resonant Magnetic Small Angle X-Ray Scattering (RMSAXS) which has been shown to be capable of measuring the size of objects using XMCD [73–75]. RMSAXS combines Resonant Magnetic X-Ray Scattering (RXMS), which is used to probe dichroism phenomena [76, 77], with Small Angle X-Ray Scattering (SAXS), which is used to probe the length scale of objects between 1 and several 100 nms in size [73–75, 78, 79]. By combining the two it is therefore theoretically possible to observe scattering from large magnetic objects. This was first achieved by Fischer *et al.* [73] who measured the RMSAXS from a FeGd layer at the Gd L_3 edge and demonstrated magnetic peaks in the SAXS profile consistent with other measurements made of the size of the Gd rich regions. This work also predicted and measured an increase in signal for FM materials when using XMCD at an absorption edge sensitive to the presence of magnetism [73]. Kortright *et al.* also used XMCD to demonstrate that this technique can be used to distinguish between charge and magnetic contributions to the scattering by applying a magnetic field and comparing the development of the peaks through a field sweep [74].

RMSAXS has since become a useful tool for measuring the structure of FM materials [75, 79]. As yet, the validity of the technique to measure objects using XMLD is unclear and could provide a method for measuring the magnetic structure of AF materials.

1.3.3 Dynamic Behaviour of Magnetic Systems Studied Using X-Ray Photon Correlation Spectroscopy

Ascertaining the long term stability of the FeRh's MMP is key to identifying its suitability for use in magnetic storage devices. As the energy difference between magnetic states is comparable to the size of thermal fluctuations in the transition region [46, 47], it might be that the magnetic state in the MMP will change without external perturbation and give the system dynamic properties. Such behaviour has been measured previously in FeRh using magnetometry techniques by Loving [58]. In the Loving work, the relaxation was fitted to an Avrami model, which models the nucleation and development of domains in a system [58]. In this case, as the measurement technique is only sensitive to FM domains in this system, the relaxation behaviour is attributed to the nucleation and growth of FM domains [58]. It was then possible to fit the behaviour to an Arrhenius equation to extract the temperature independent activation energy, E_A, of this nucleation process to be $E_A/k_B = 13000 \pm 4000$ K for FeRh grown on MgO [58]. Recent advances in synchrotron technology mean it is now possible to measure the dynamic behaviour of magnetic systems using techniques such as X-Ray Photon Correlation Spectroscopy (XPCS) [80–87]. Such behaviours have not been studied in FeRh using XPCS and a greater understanding of their dynamic behaviour would be of great use in designing of spintronic devices based on FeRh.

Magnetic frustration is expected in the boundary between the two magnetic phases in B2-ordered FeRh as the two exchange interactions cannot be fully resolved [18]. The presence of the frustration would lead to a spin-glass-like state as seen previously in the grain boundaries of ball-milled FeRh [57]. However, in this experiment it is unclear as to whether the disorder induced by the fabrication method, as is seen from the Temple *et al.* study [27], contributes to the generation of the spin-glass state as there is no evidence of such a state in pristine B2-ordered thin films presented in the literature. The spin glass state has been seen using PNR in films that have been irradiated with ions resulting in damage to the structure [88], which supports the theory that the spin-glass state is a consequence of the removal of B2 order. The presence of a magnetic

glass phase has also been seen in this system, when cooling through to low temperatures with a large external magnetic field applied through the cooling process [89]. In the hypothetical environment in which these potential storage devices will be held, the presence of an externally applied magnetic field is not necessarily guaranteed so it is pertinent to address the relaxation behaviour in the absence of external perturbations.

XPCS has been used to measure the dynamic properties in a wide range of magnetic systems including Artificial Spin-Ice systems [82, 83], metallic glass materials [84, 85] and even AF materials [86, 87, 90]. The dynamic behaviour of the AF materials has been measured using scattering from charge density waves [86], directly from AF materials using coherent linearly polarized light of a single polarization [87, 90] and even in an artificial AF system found in the Artificial Spin Ice geometry [83]. It is unclear as to whether XMLD can be used to directly measure the dynamic behaviour in magnetic systems and could again, open the door for the direct measurements of dynamic behaviour in AF materials.

The XPCS studies based on the dynamic properties of AF materials concentrate on the dynamic behaviour of magnetic domain walls [83, 86, 87]. These are seen to exhibit jammed dynamic behaviour [83, 86, 87], which is where the competing exchange interactions over long distances mean it is difficult to relieve the frustration across the entire sample [87]. For the dynamic behaviour of AF systems, these long range exchange interactions will be that of the Ruderman-Kittel-Kasuya-Yosida interaction [87], however, for systems in which regions of FM material are expected, the dipolar interaction between magnetic moments of two nearby domains may also affect the properties of the domain wall.

In order to identify the dynamic properties of both magnetic phases, investigations using both XMLD and XMCD should be performed throughout the transition using XPCS. This will add greater depth to the discussion regarding the suitability of the MMP of FeRh for use in spintronic applications.

1.4 Thesis Overview

From the above review of the literature it is clear that the knowledge of the properties of the MMP of B2-ordered FeRh could be improved. For the purposes of this thesis the deficiencies in the knowledge of the MMP are the presence of an exchange coupling between the two magnetic phases, where the current literature is contradictory and

fails to explain the behaviour adequately, the characterization of the two magnetic phases relative to one another throughout the transition, as little is known about the development of the AF phase and finally, the dynamic behaviour of the MMP in terms of the release of the magnetic frustration expected at the interface between the two magnetic phases. The work in this thesis will be split into 3 distinct investigations, where each of these aforementioned points will be addressed in turn.

Firstly, the presence of the interfacial exchange coupling will be investigated using a combination of FMR, the results of which are presented in chapter 5, and SWR investigations, the results of which are presented in chapter 6. Together these measurements show that there is indeed an interphase exchange coupling that develops with AF layer thickness in a manner consistent with a thickness dependent phase transition in the AF layer.

The study of the development of the two magnetic phases through the transition was performed using RMSAXS utilising both XMCD and XMLD to access the two magnetic phases and is shown in chapter 7. These measurements show that it is possible to measure both magnetic phases using a combination of XMLD and XMCD, however it was not possible to measure the AF phase through the entirety of the transition. The regions of the transition where the AF phase can be probed yield scattering from length scales of ≈ 150 nm.

The scattering objects identified in the RMSAXS experiment are then probed for their dynamic properties using XPCS in chapter 8. These investigations demonstrate that the dynamic behaviour of AF materials can be measured directly using XMLD and provide further insight into the dynamic behaviour of magnetic systems. The two types of magnetic dichroism are seen to have different sensitivities to the various relaxation processes present in FeRh.

In order to add context to these experiments, the results chapters are preceded by a review of some concepts fundamental to the understanding of the FeRh system and the interpretation of the experimental data, which is seen in chapter 2. A chapter detailing the theoretical basis for x-ray scattering from magnetic systems is included in chapter 3, to help aid understanding of these experiments. A full list of the experimental methods and technical specifications used in this work is included in chapter 4.

The thesis will culminate in a series of concluding remarks and an outline of possible directions for future work regarding these experiments in chapter 9.

Chapter 2

Fundamental Concepts

This chapter will provide some introductory theory of magnetism that is relevant to understanding of the investigations presented in this thesis and the understanding of the FeRh system itself. As the FeRh system presents both ferromagnetic (FM) and antiferromagnetic (AF) phases, the definition of these terms with regards to their exchange energy will be presented. The evolution of the two magnetic phases is understood in terms of magnetic domains, which are also discussed here in terms of the demagnetizing field. Exchange coupling across the magnetic phase boundary (MPB) is considered in chapters 5 and 6, the theory pertaining to this investigation is also discussed here. The concept of magnetic frustration and relaxation, which is investigated in chapter 8, is addressed alongside possible sources of such behaviour that may be present in the FeRh system. Finally, the nature of phase transition according to their order is discussed.

2.1 Exchange

The Pauli Exclusion Principle states that no two electrons can exist in the same quantum state, which is determined by a set of quantum numbers for each electron [91]. For the purposes of this discussion there are two relevant quantum numbers, that of the orbital angular momentum, m_l and that of the spin angular momentum m_s and the Pauli Exclusion Principle means that two electrons that possess the same value for one of these quantum numbers must have different values of the other [91, 92].

As electrons are indistinguishable from one another, a two electron system, in which electrons are seen at positions $\mathbf{r}_1$ and $\mathbf{r}_2$, should yield the same electron density regardless of the relative orientation of the two electrons [93]. Therefore, the total wavefunction of the system $\Psi(\mathbf{r}_1, \mathbf{r}_2)$ should obey [93],

$$|\Psi(\mathbf{r}_1, \mathbf{r}_2)|^2 = |\Psi(\mathbf{r}_2, \mathbf{r}_1)|^2. \tag{2.1}$$

The total wavefunction of the two electron system is made up of the contributions from the spatial part of the wavefunction Φ and the spin wavefunction, χ, such that $\Psi(\mathbf{r}_1, \mathbf{r}_2) = \Phi(\mathbf{r}_1, \mathbf{r}_2)\chi(\mathbf{r}_1, \mathbf{r}_2)$. In order to obey the Pauli Exclusion Principle, the wavefunction must be asymmetric under spatial inversion of the two electrons and therefore $\Psi(\mathbf{r}_1, \mathbf{r}_2) = -\Psi(\mathbf{r}_2, \mathbf{r}_1)$ [93]. There are two possible ways to achieve this: The spatial part of the wavefunction could be asymmetric under spatial inversion, whilst the spin is symmetric, or *vice versa*. When the spin wavefunction is symmetric, there are three possible solutions to this equation and these are known as the triplet states,

where the total spin of the wavefunction can be $S_z = 0, \pm 1$, when the spin wavefunction is asymmetric, there is one possible solution to this equation which is known as the singlet state where $S_z = 0$ [93].

For the triplet states, the asymmetric spatial wavefunction means that the electrons will never occupy by the same physical space [93]. This is not the case for the singlet state with the symmetric spatial wavefunction and the electrons in this scenario can occupy the same physical space. Due to Coulomb repulsion, the distance between the two electrons will help to determine its energy and the triplet and singlet states may have different energies. It is possible to directly evaluate the energy associated with each of these configurations considering the Hamiltonian for the Coulomb interaction, $\mathcal{H}(\mathbf{r}_1, \mathbf{r}_2)$ via [93],

$$E_{\mathrm{T,\,S}} = \int \Phi^*_{\mathrm{A,\,S}}(\mathbf{r}_1, \mathbf{r}_2)\mathcal{H}(\mathbf{r}_1, \mathbf{r}_2)\Phi_{\mathrm{A,\,S}}(\mathbf{r}_1, \mathbf{r}_2)d\mathbf{r}_1 d\mathbf{r}_2, \tag{2.2}$$

where $E_{\mathrm{T,\,S}}$ is the energy of the triplet and singlet state, respectively, $\Phi_{\mathrm{A}}(\mathbf{r}_1, \mathbf{r}_2)$ is antisymmetric spatial wavefunction, $\Phi_{\mathrm{S}}(\mathbf{r}_1, \mathbf{r}_2)$ is the symmetric spatial wavefunction and Φ^* represents the complex conjugate of the quantity.

It is possible to define the exchange integral, J, to be half of the difference in energy between the two states which takes the form [93],

$$J = \frac{E_{\mathrm{T}} - E_{\mathrm{S}}}{2} = \int \psi^*_1(\mathbf{r}_2)\psi^*_2(\mathbf{r}_1)\mathcal{H}(\mathbf{r}_1, \mathbf{r}_2)\psi_1(\mathbf{r}_1)\psi_2(\mathbf{r}_2)d\mathbf{r}_1 d\mathbf{r}_2, \tag{2.3}$$

where, $\psi_{\mathrm{i}}(\mathbf{r}_j)$ is the spatial wavefunction of electron i at position j. For two electrons, which whose spin properties are governed by the dimensionless operator $\hat{\mathbf{S}}$, the energy due to the exchange interaction the between the two can be expressed in the following Hamiltonian,

$$\mathcal{H} = -2J\hat{\mathbf{S}}_1 \cdot \hat{\mathbf{S}}_2. \tag{2.4}$$

It follows then that for systems in which $J > 0$ the triplet spin state is favoured and for systems in which $J < 0$ the singlet state is favoured.

Electrons can exist with one of two spin polarizations [93]. When a magnetic field $\mu_0\mathbf{H}$ is applied and as the energy of the electron with magnetic moment μ follows $E \propto -\mu \cdot \mathbf{H}$, electrons with one spin polarization will have a lower energy compared to the other. Therefore, it is possible to think of the two spin polarizations as two separate entities which can be collected into groups or bands [94]. The number of electrons that exhibit each spin projection is determined by the number of available states with energies lower than the Fermi energy.

When a magnetic field is applied, the energy of these two bands will move in opposite directions and will create an asymmetry in the number of occupied electron states at the Fermi energy. This asymmetry in the number of states occupied by electrons of the different spin polarizations means that a net magnetic moment has been induced in the system. Materials where it is possible to induce a magnetic moment in this manner, that do not exhibit a magnetic moment in the absence of externally applied magnetic fields, are known as paramagnets [94]. However, there are materials in which this asymmetry in the occupied number of electrons between the two different spin projections is an inherent property of the material. In order for this to be the case, the energy difference between the two spin configurations and the asymmetry in the number of state for the two spin projections must exceed a certain threshold defined by the Stoner Criterion [94],

$$Ug(E_{\mathrm{F}}) > 1, \tag{2.5}$$

where U is a measure of the exchange energy and $g(E_{\mathrm{F}})$ is the density of states at the Fermi energy, E_{F} [94]. Materials that satisfy this condition are known as Ferromagnets and each adjacent pair of electrons has $J > 0$. Systems in which every pair of electrons must satisfy $J < 0$ has the spin of each electron aligned antiparallel to that of its neighbour. If the exchange coupling between adjacent spins is strong enough, then it is not possible to induce an asymmetry in the density of states at the Fermi energy due to the application of magnetic fields. Therefore, these materials are neither paramagnetic nor ferromagnetic and are known instead as antiferromagnets [94]. In ferromagnetic (FM) materials, all of the magnetic moments are aligned along a given direction, this is known as the direction of the magnetization. In antiferromagnetic (AF) materials, all of the spin magnetic moments are aligned antiparallel to its neighbour, however, this must be along a given direction. The direction about which these spins are aligned is known as the spin-axis of the AF material, which is described by the Néel vector, **L**.

2.2 Spin-Orbit Coupling

For an atom with an electron orbiting around the nucleus there are two frames of reference that can be considered, that in which the electron is at rest and the one in which the nucleus is it rest. When considering the system from the rest frame of the electron, the charged nucleus rotates around the electron and produces a current

[95]. This current then brings with it a magnetic field, $\mathbf{H}_{\mathrm{SO}}$, that can interact with the magnetic moment, $\mathbf{m}$, of the electron. The energy associated with the interaction between the field and the electrons magnetic moment is given by the Hamiltonian [95],

$$\mathcal{H}_{\mathrm{SO}} = -\frac{1}{2}\mathbf{m} \cdot \mathbf{B}_{\mathrm{SO}}. \tag{2.6}$$

The field due to the motion of the nucleus is determined by its velocity $\mathbf{v}$ and its distance from the electron $\mathbf{r}$ such that $\mathbf{B}_{\mathrm{SO}} = k\mathbf{r} \times \mathbf{v}$ where k is a constant. It is possible to rewrite this field in terms of the angular momentum as $\mathbf{L} \propto \mathbf{r} \times \mathbf{v}$. Therefore, as the magnetic moment of the electron is proportional to its spin $\mathbf{S}$, the Hamiltonian can be rewritten such that [95],

$$\mathcal{H}_{\mathrm{SO}} = \lambda \mathbf{S} \cdot \mathbf{L}, \tag{2.7}$$

where λ is a constant. As this interaction is between the spin and angular momentum parts of the electron wavefunction, it is known as the spin-orbit interaction. It follows from this Hamiltonian that for a given value of L, as there are two possible orientations of the spin angular momentum of the electron, there are two possible energy states of this system. Therefore, spin-orbit coupling splits the energy levels of the two spin projections within an orbital.

Spin-orbit coupling can also affect a materials g-factor [96, 97], g, which describes the ability of the magnetic moment to couple to an externally applied magnetic field [68, 95]. The magnetic moment operator can be rewritten in terms of the orbital and spin angular momentum operators such that,

$$\hat{\mu} = \mu_{\mathrm{B}}(g_{\mathrm{L}}\hat{\mathbf{L}} + g_{\mathrm{S}}\hat{\mathbf{S}}), \tag{2.8}$$

where $g_{\mathrm{L,S}}$ are g-factors for the orbital and spin angular momentum quantum numbers respectively. However, these two quantum numbers are not necessarily applicable for a large number of electrons and it is more appropriate to use the total angular momentum quantum number $\mathbf{J} = \mathbf{L} + \mathbf{S}$ [95]. Inputting this into equation 2.8 leads to [95],

$$\hat{\mu} = \mu_{\mathrm{B}} g \hat{\mathbf{J}}. \tag{2.9}$$

By multiplying both sides of these two equations by $\hat{\mathbf{J}}$ and equating them leads to the expression

$$g\hat{\mathbf{J}}^2 = g_{\mathrm{L}}\hat{\mathbf{L}} \cdot \hat{\mathbf{J}} + g_{\mathrm{S}}\hat{\mathbf{S}} \cdot \hat{\mathbf{J}}, \tag{2.10}$$

from which an expression for g can be derived as,

$$g = \frac{3}{2} + \frac{S(S+1) - L(L+1)}{2J(J+1)}, \tag{2.11}$$

where the values of $g_{\mathrm{L}} = 1$ and $g_{\mathrm{S}} \approx 2$, as is the case for electrons, is assumed [95]. Therefore, the ability of the magnetic moment to couple to the field can be changed depending on the value of L and S.

2.3 Magnetic Fields Within a Ferromagnetic Material

Within a material with a magnetization, the total magnetic induction $\mathbf{B}$ is given by [98],

$$\mathbf{B} = \mu_0(\mathbf{H} + \mathbf{M}), \tag{2.12}$$

where $\mathbf{H}$ is the magnetic field and $\mathbf{M}$ is the magnetization of the material. The magnetization and the magnetic field are linked and so it is possible to rewrite this equation as [98]:

$$\mathbf{B} = \mu_0(1 + \chi)\mathbf{H}, \tag{2.13}$$

where $\chi = \mathbf{M}/\mathbf{H}$ is the magnetic susceptibility of the material. For FM materials, $\chi \gg 0$, for PM materials $\chi > 0$ and χ for AF materials increases approaching the Neél temperature [98].

At the surface of the magnetic material $\mathbf{M}$ suddenly becomes 0, and Maxwell's equation that states $\nabla \cdot \mathbf{B} = 0$ means that there is a divergence of $\mathbf{M}$ at the surface such that [99]

$$\nabla \cdot \mathbf{M} = -\nabla \cdot \mathbf{H}. \tag{2.14}$$

This non-zero divergence of $\mathbf{M}$ then implies the presence of magnetic charge at the materials surface that act as a source of a magnetic field both inside and outside the magnetic material. Within the material, this field is aligned in the opposite direction to that of $\mathbf{M}$ and is known as the demagnetizing field $\mathbf{H}_{\mathrm{Demag}}$ [99]. The demagnetizing field exists only within the material and may vary through the material depending on its shape. Outside the material, there is a magnetic field known as the stray field $\mathbf{H}_{\mathrm{Stray}}$. The energy associated with this field across the whole sample associated with the demagnetizing field is given by,

$$E_{\mathrm{Demag}} = -\frac{\mu_0}{2} \int \mathbf{M} \cdot \mathbf{H}_{\mathrm{Demag}} dV. \tag{2.15}$$

Therefore, by creating domains whose magnetization is oppositely aligned, it is possible to reduce the magnetization over the volume and minimize the energy due to the demagnetizing field, which is given by $\mathbf{H}_{\text{Demag}} = -\mathcal{N}_{\text{Demag}}\mathbf{M}$, where $\mathcal{N}_{\text{Demag}}$ is the demagnetizing tensor [68, 99].

2.4 Anisotropy

Anisotropic materials have different properties depending on which direction they are studied in. In magnetic materials, this asymmetry means that the magnetization will align preferentially along a given different direction, which is known as the easy axis [100]. This behaviour can also apply to crystal plane, but this duscission will take place with reference to a preferred axis. There is then an energy cost of trying to rotate the magnetization away from this axis. There are different types of anisotropy that fall into one of two categories, which are shape anisotropy, due to the attempts of the system to reduce the demagnetizing field and magnetocrystalline anisotropy (MCA), due to crystal structure [100]. Anisotropy energies are often expressed in terms of their anisotropy energy density K.

For shape anisotropy, the attempts to minimize the demagnetizing field will lead to a favoured direction of the magnetization of the particle. This means that energy must be introduced into the system in order to rotate the magnetic moment of the domain, where

$$K_{\text{Shape}} = \frac{1}{2}\mu_0 \mathcal{N}_{\text{Demag}} M_{\text{S}}^2. \tag{2.16}$$

For MCA there are two main types each with subcategories. These are the uniaxial anisotropy and cubic anisotropy, each of which will be discussed in turn. In systems that exhibit uniaxial MCA, there is a single preferential direction known as the easy axis. Rotating the magnetization to the axis perpendicular to this easy axis requires the most energy and this axis is known as the hard axis. The energy required to rotate the magnetization away from the easy axis is going to depend on the strength of the MCA, K, and the angle between the magnetization and the easy axis, θ. As such, the energy per unit volume associated with the MCA is given by [100],

$$E = K_{\text{MCA}} \sin^2(\theta) + \mathcal{O}(\sin(\theta)) \tag{2.17}$$

where $\mathcal{O}(\sin(\theta))$ is used here to indicate the presence of corrections to this energy that use higher even powers of $\sin(\theta)$, which are not discussed in this work.

MCA encompasses many different sources of anisotropy which are discussed through this work, one of which is that of magnetoelastic (ME) effects which is brought about due to strain at the interface [56, 100]. These effects are born of the coupling between the crystal structure and the magnetization. In some materials the length of the system depends on the orientation of the magnetization [100]. This means that changing the orientation of the magnetization must also change the physical structure of the system, which brings with it an anisotropy. This anisotropy links the magnetic properties of the material with strain in the system and is known as ME coupling [100]. In FeRh it is known that strain can be used to stabilize different magnetic states and as such any ME effects play a profound role in the FeRh system [18, 19, 37, 56]. The anisotropy energy that comes from ME effects is given by [56],

$$K_{\mathrm{ME}} = -\frac{3\lambda E \epsilon_{\mathrm{x}}}{2}, \tag{2.18}$$

where λ is the linear saturation magnetostriction, which is a measure of the change of size of the system when it is magnetized, E is the Youngs Modulus of the material and ϵ_{x} is the strain in the x direction.

The other source of MCA that is considered in this thesis is that which is brought about due to exchange coupling at the interface between an AF and FM layer [61]. The mechanism behind this is discussed in more detail in section 2.6. But as this is a surface effect its strength will be determined by size of the film in which the MCA has an effect, which in this case is the AF layer. The contribution to the MCA is given by,

$$K_{\mathrm{EC}} = -\frac{J_{\mathrm{EC}}}{2t_{\mathrm{FM}}}\sqrt{1-\left(\frac{J_{\mathrm{EC}}}{2K_{\mathrm{AF}}t_{\mathrm{AF}}}\right)^2}, \tag{2.19}$$

where J_{EC} is the strength of the exchange coupling across the interface, t_{FM} is the thickness of the FM layer, K_{AF} is the MCA constant of the AF layer and t_{AF} is the thickness of the AF layer.

There is also cubic anisotropy, which is present in systems that exhibit cubic structures and the energy is given by,

$$E = K_1(\alpha_{\mathrm{x}}^2\alpha_{\mathrm{y}}^2 + \alpha_{\mathrm{y}}^2\alpha_{\mathrm{z}}^2 + \alpha_{\mathrm{x}}^2\alpha_{\mathrm{z}}^2), \tag{2.20}$$

where α_{i} is the cosine of the angle between a cube edge and the magnetization. FeRh has been shown to exhibit a weak uniaxial anisotropy when the magnetization is oriented

within the film plane and quite a substantial uniaxial anisotropy when the magnetization is oriented out of plane [55]. In cubic crystal systems such as FeRh it may be energetically favourable to destroy the cubic symmetry and deform the system as opposed to rotating the magnetization to the hard axis of the material [100]. As FeRh exhibits a uniaxial MCA, this case is believed to be true here.

When considering only the coherent rotation of a magnetic system that can be described by a single macrospin, the energy of the system can be described by the Stoner-Wolfarth model [100]. Considering a system with uniaxial anisotropy in which the magnetic field, H_{Ext}, is applied at an angle θ to the easy axis of the system whilst the magnetization lies at an angle β to the easy axis, the total energy density of the system can be described by,

$$E = K_{\mathrm{Eff}} \sin(\beta)^2 - \mu_0 H_{\mathrm{Ext}} M_{\mathrm{S}} \cos(\theta - \beta)\,. \tag{2.21}$$

The anisotropy constant in this case is an effective anisotropy that can be made up a combination of each of the different types of anisotropy seen here such that,

$$K_{\mathrm{Eff}} = K_{\mathrm{Shape}} + K_{\mathrm{ME}} + K_{\mathrm{EC}}. \tag{2.22}$$

All concepts discussed here are applicable to both FM and AF materials. For the FM materials the energy comes in rotating the direction of the magnetization. For the AF materials the energy cost comes with rotating the spin-axis of the AF material.

2.5 Magnetic Domains and Domain Walls

Within magnetic materials the orientation of the magnetization vector is not always constant. At the edges of the material, the magnetic configuration will be shaped by its attempts to minimize the demagnetizing field and the energy across the materials volume according to equation 2.15. In order to do this there may be adjacent regions of magnetic material whose magnetization vector points in different directions. These regions of material with their magnetization vector pointing in different directions are known as domains [100]. The region between two domains is then known as the domain wall [100]. For AF materials there is a preferential direction along which the spin-axis lies, which may be different depending on the orientation of the crystal at each given point. There also may be magnetic defects in the system which requires a reorientation

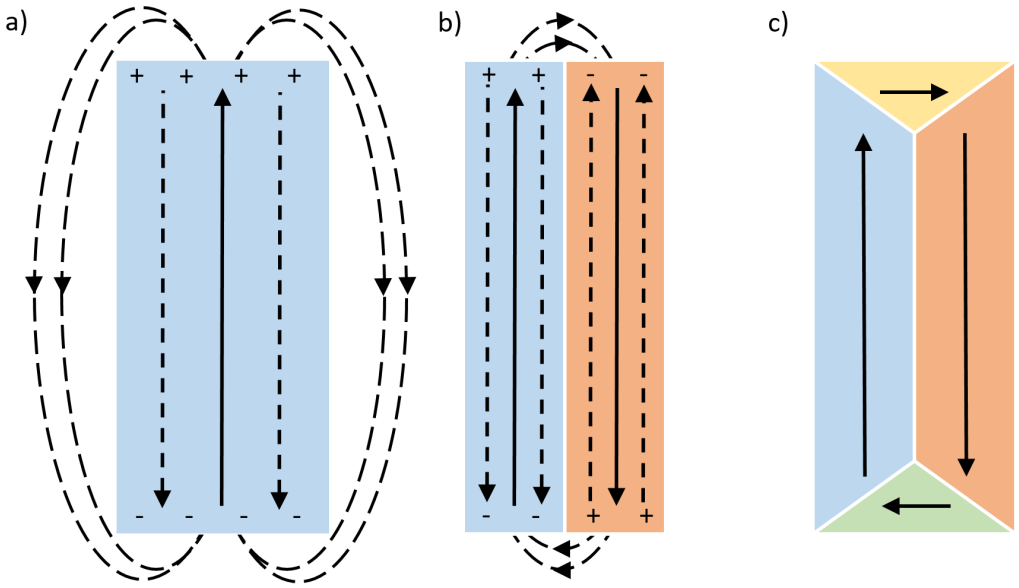

Figure 2.1: Process of minimizing the energy due to the demagnetizing field by the creation of magnetic domains. Panel (a) is a single domain and has a large demagnetizing field as shown by the dashed lines. The dashed lines outside the sample show the stray field. Panel (b) shows a domain configuration where there are two oppositely magnetized domains, which have reduced both the demagnetizing and stray fields but have not removed them completely. Panel (c) shows a configuration in which the demagnetizing field has been minimized. All solid arrows here show the direction of the magnetization within each coloured domain and the $+, -$ are used to indicate the presence of magnetic charge.

of the spins around it to minimize the demagnetizing energy. Both of these phenomena mean that AF domains are possible and are defined by the direction of their spin-axis.

An example of creation of domains to minimize the demagnetization energy is shown in Fig. 2.1. In which a uniformly magnetized region is shown in panel (a). The demagnetizing field, which is shown by the dashed lines in the sample, for this situation is large. The presence of magnetic charge on the surface of the material, shown by $+, -$ means that stray field is also present outside the material. However, it is possible to reduce both of these fields by breaking the sample into oppositely magnetized domains such as those seen in panel (b). By adopting the domain configuration seen in panel

(c), it is possible to minimize both the demagnetizing field within the sample and the stray field by creating flux closed structure within the material.

If one is to think microscopically about the spins in the domain wall region, the magnetization vector must rotate between the orientations of the two domains. There are two types of domain wall, which are determined by the direction through which the spins rotate within the wall itself. Domains in which the magnetization vectors are oriented π radians to their neighbour are often separated by Bloch domain walls, where the magnetization rotates in the direction perpendicular to the direction in through which the magnetization changes [100]. Domain walls in which the spins rotate within the same plane through which the magnetization is rotated are known as Néel walls and are common for orientations in which the magnetization vector is rotated by $\pi/2$ radians [100].

For Bloch walls the magnetization must travel through an angle π. This takes place over the N spins present in the wall, meaning that the difference in angle between adjacent spins is π/N. In Bloch walls the spins are rotated through planes of atoms and it is possible to discuss the energy involved in the rotation in terms of a surface energy. The energy required per unit area to rotate the magnetization through π/N according to equation 2.4 is [100],

$$\sigma_{\mathrm{BW}} = \frac{JS^2\pi^2}{Na^2} \tag{2.23}$$

where J is the exchange constant, S is the spin per atom and a is the lattice constant of the material. The ability of the spin to rotate is dependent on its ability to overcome other sources of energy that may align the spin in a given direction, such as the anisotropy energy. The consideration of the anisotropy energy adds a surface energy term into equation 2.24 such that [100],

$$\sigma_{\mathrm{BW}} = \frac{JS^2\pi^2}{Na^2} + \frac{NKa}{2}. \tag{2.24}$$

Minimizing this equation with respect to N leads to the size of the Bloch wall as [100],

$$\delta = Na = S\pi\sqrt{\frac{2J}{Ka}}. \tag{2.25}$$

This is the size of the domain wall for two FM domains. The same relation is seen to apply for two adjacently orientated AF domains [101].

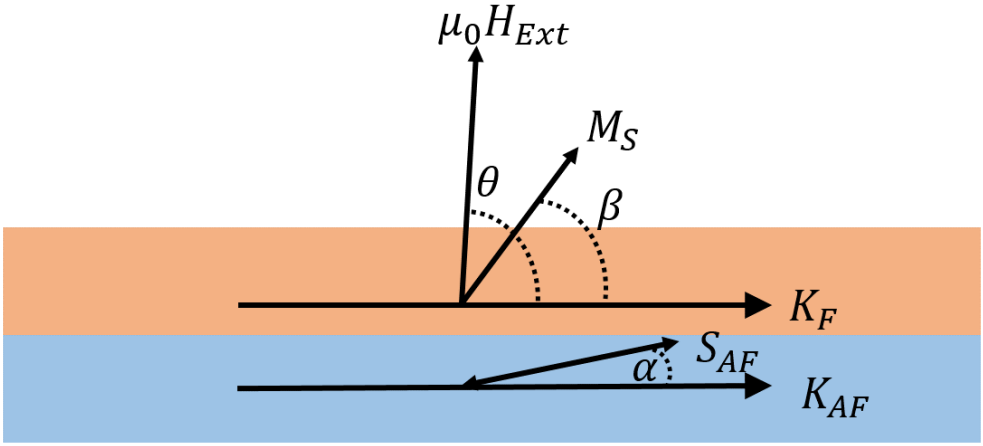

Figure 2.2: Set up of an exchange coupled FM/ AF bilayer. The FM layer is shown in red and the AF layer in blue. The easy axis of the anisotropy for both layers are shown by K_{FM} and K_{AF} respectively. The direction of the easy axis is the same for both materials. The external magnetic field $\mu_0 H_{\mathrm{Ext}}$ is oriented at angle θ to the easy axis direction. The magnetization of the FM layer, M_{S}, is oriented at angle β to the easy axis, whilst direction of the spin-axis of the AF material, S_{AF}, can be found at angle α to the easy axis.

2.6 Interfacial Anisotropy Energy Due To Exchange Coupling

When AF materials are in direct contact with a FM material, it is possible that the exchange coupling across the interface can affect the behaviour of both layers. In practice, this exchange coupling manifests itself as an extra anisotropy energy by creating an energy barrier that favours the alignment of the spins at the interface in a given direction [61]. This anisotropy energy means that there is a difference in energy required to rotate the magnetization into and out of the axis favoured by the exchange coupling. It is possible to directly evaluate the size of this energy difference by looking at the behaviour of the energy density of the AF/FM bilayer system [61].

An example schematic of the orientation and quantities mentioned in this section are shown in Fig. 2.2. Here, both layers share an easy axis for their uniaxial ansitropy

which is shown by $\mathbf{K}_{\mathrm{FM}}$ and $\mathbf{K}_{\mathrm{AF}}$ for the FM and AF layers respectively. Both layers are assumed to rotate as a single spin or spin-axis and that the interface between them is atomically smooth [61]. In practice, the direction of the FM layer is changed by applying an external magnetic field, $\mu_0\mathbf{H}_{\mathrm{Ext}}$, and changing the direction of the field relative to an axis of the film in question. The magnetic field is applied at an angle θ to the easy axes of the two layers. The magnetization of the FM layer $\mathbf{M}_{\mathrm{S}}$ is situated at an angle of β whilst the spin-axis of the AF layer, $\mathbf{S}_{\mathrm{AF}}$ is rotated through angle α. The exchange coupling across the surface has strength J_{EC} and is dependent on the angle between the spin-axis of the AF layer and the magnetization of the FM layer. For the purposes of this discussion $J_{\mathrm{EC}} = JS_{\mathrm{AF}}S_{\mathrm{FM}}/a^2$, where J is the exchange interaction between the FM and AF spins at the interface and S_{i} is the spin in the ith layer [61, 102]. In this model, the FM layer is of thickness t_{FM} and AF layer has a thickness of t_{AF}.

Firstly, considering the situation where the AF is rigid and $\alpha = 0$ for $\theta = 0$ it is possible to write the energy per unit area of the system, E, as [61]:

$$E = -\mu_0 H_{\mathrm{Ext}} t_{\mathrm{FM}} M_{\mathrm{S}} \cos(-\beta) + K_{\mathrm{FM}} t_{\mathrm{FM}} \sin^2(\beta) - J_{\mathrm{EC}} \cos(\beta)\,. \tag{2.26}$$

Minimizing this equation with respect to β leads to two solutions for $\beta = 0, \pi$, which give the field required to switch the magnetization direction both into (1) and out (2) of the direction favoured by the exchange coupling. This leads to expressions for the field required to switch the direction of the magnetization H_{C} between these two directions as,

$$\mu_0 H_{\mathrm{C}}^{1,2} = \frac{2K_{\mathrm{F}}t_{\mathrm{F}} \pm J_{\mathrm{EC}}}{M_{\mathrm{F}}t_{\mathrm{F}}}. \tag{2.27}$$

By adding one to the other and halving the result, it is possible to find the asymmetry in the field required to switch the magnetization between the different directions as $\mu_0 H_{\mathrm{EC}}$ via,

$$\mu_0 H_{\mathrm{EC}} = \frac{-J_{\mathrm{EC}}}{M_{\mathrm{F}}t_{\mathrm{F}}}. \tag{2.28}$$

As this is the difference in field required to switch the magnetization between the two different directions, it is taken that this is an anisotropy field.

However, it may not always be the case that $\alpha = 0$ or $\theta = 0$ and its contribution must also be considered. In this case the E of the system can be written as [61]:

$$E = -\mu_0 H_{\mathrm{Ext}} M_{\mathrm{S}} t_{\mathrm{FM}} \cos(\theta - \beta) + K_{\mathrm{FM}} t_{\mathrm{FM}} \sin^2(\beta) + K_{\mathrm{AF}} t_{\mathrm{AF}} \sin^2(\alpha) - J_{\mathrm{EC}} \cos(\beta - \alpha)\,, \tag{2.29}$$

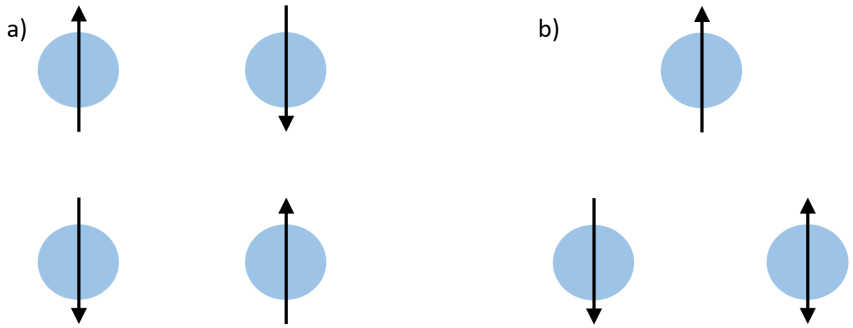

Figure 2.3: Examples of frustrated systems for AF exchange interactions. The square lattice seen in panel (a) has all of the exchange interactions satisfied between all points if the exchange interaction are AF. Panel (b) shows a triangular system in which the AF interactions cannot be satisfied at all points and the system is then frustrated.

Minimizing the energy with respect to angles α, β and assuming that the anisotropy of the FM is negligible leads an equation for the dependence of the anisotropy field due to exchange coupling $\mu_0 H_{\mathrm{EC}}$ on both t_{AF} and t_{FM} [61],

$$\mu_0 H_{\mathrm{EC}} = \mu_0 H_{\mathrm{EC}}^{\mathrm{Max}} \sqrt{1 - \left(\frac{J_{\mathrm{EC}}}{2K_{\mathrm{AF}} t_{\mathrm{AF}}}\right)^2}, \tag{2.30}$$

where the maximum anisotropy field due to the exchange coupling in the system, $\mu_0 H_{\mathrm{EC}}$ is the same as the form given by equation 2.28. This shows the field expected for the form of the ansiotropy presented in equation 2.19. This solution is only valid in the situation where $\theta = \beta = 0$ and it is not possible to get analytical expressions for other cases [61].

2.7 Relaxation in Magnetic Systems

For certain orientations of spins and exchange interactions, it is not possible to satisfy all of the exchange interactions at a given point. Pictorial examples of two possible spin configurations are included in Fig. 2.3 to help demonstrate this phenomena. All of the exchange interactions between adjacent spins in this figure are taken to be AF with $J < 0$. All of the interactions on the square lattice seen in panel (a) can be satisfied and the system exists in the lowest possible energy state. However, the same cannot be said

for the triangular lattice seen in panel (b), where it is not possible to arrange the spins in a manner that satisfies all the exchange interactions. The ground state of the system cannot be reached in this case and a series of spin configurations with degenerate energies are instead present. This inability of the system to enter its lowest energy configuration is known as frustration [103]. If there are thermal fluctuations present in excess of the size of the energy barrier between degenerate states, it is possible for the system to move between these spin configurations with degenerate energies in an attempt to achieve a lower energy configuration. The process over moving through these spin configurations in an attempt to reach the state with the lowest energy is known as relaxation [103].

When cooling, there will be a temperature below which it is no longer possible for the thermal fluctuations to overcome the energy barrier between states with different spin configurations that have degenerate energies. This means that the system is then stuck or frozen into frustrated state. The inability of a system to change below a certain temperature is characteristic of glassy materials and magnetic materials that exhibit such behaviour are known as spin-glasses [103].

In FeRh it is known that the FM state is metastable above the transition temperature, and so as the difference in energy between the two magnetic phases is comparable to the temperatures at which the transition occurs, it is possible that AF material will undergo a transformation to the FM phase due to thermal fluctuations [12, 46, 47, 58]. The probability of a thermally activated transition occurring at a given temperature, T, is given by,

$$P \propto e^{-\frac{\Delta E}{k_{\mathrm{B}}T}}, \tag{2.31}$$

where ΔE is the difference in energy between the two states and k_{B} is the Boltzmann constant. Therefore, it may be expected that FeRh may exhibit magnetic relaxation in which the energy of the state is reduced by the spontaneous nucleation of an FM domain from an AF domain.

The inability of a system to resolve all of the exchange interactions present at a given point is not limited to spatial constraints. There may also be competing exchange interactions present in the system which cannot be resolved exactly. This case applies in FeRh where there are coexisting regions of FM and AF material. To help aid this point a demonstration of this frustrated system in FeRh is shown in Fig. 2.4. This figure shows the orientation of spins at the interface between the two magnetic phases

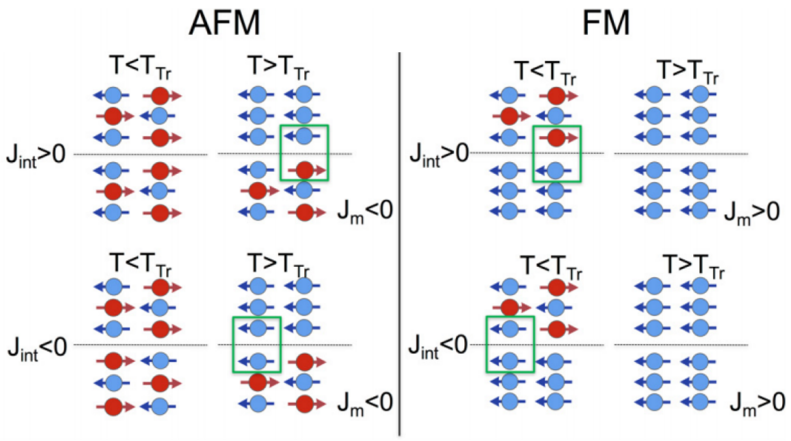

Figure 2.4: Example of a frustrated magnetic system at the boundary between the two magnetic states in B2 ordered FeRh. This figure takes there to be two adjacent layers of FeRh with an exchange coupling of strength J_{Int} present across the interface between the two. The bottom layer is taken to have a different transition temperature to that of the top layer and is either AF (left column) or FM (right column) above and below the transition temperature T_{Tr} of the top layer. The label at the top of each column here denotes the state of the bottom layer. The nature of the exchange energy in the bottom layer is shown by J_{M}. This figure shows the spin orientation at the boundary between the two both above and below T_{Tr} for different orientations of J_{Int}. The sites where the exchange interactions cannot be resolved fully and are therefore frustrated are shown by the green boxes. Image taken from Ref. [18].

and their development relative to the transition temperature T_{Tr} taken from Ref. [18]. In this figure it is taken that there are two layers of FeRh with different transition temperatures that are exchange coupled across the interface according to the interfacial exchange coupling J_{Int}. The bottom layer is taken to exhibit in either an AF state or an FM state throughout the temperature range, with the nature of the state shown by J_{M} [18]. Each of the different columns show the spin orientation above and below the transition temperature where the bottom layer is in an AF state (left column) and an FM state (right column) [18]. It can be seen that there are exchange interactions at the surface that cannot be satisfied for each of the different possible combinations of J_{Int} and J_{M}, which are highlighted by the green boxes. These unsatisfied exchange

interactions leads to frustration in the system at the interface between the two magnetic phases [18].

As it is not possible to reach the ground state configuration at the magnetic phase boundary (MPB), the spin structure in this region is expected to fluctuate between degenerate energy states in an attempt to enter the ground state. The fluctuations in the MPB may be due to competition between the direct exchange interactions or there could be longer range interactions that contribute to these proceedings such as the Ruderman-Kittel-Kasuya-Yosida (RKKY) interaction or the dipolar interaction between two FM domains. [87, 103], each of which shall be discussed in turn.

2.7.1 Ruderman-Kittel-Kasuya-Yosida Interaction

In metals, the valence electrons are delocalized from their host atom and form a gas like entity within the material, whilst the core shell electrons remain localized to the lattice site [94]. As the delocalized electrons approaches an electron localized at lattice point i, they are subject to an exchange field which perturbs the state of the electron. This interaction aligns the spins of the two electrons due to the paramagnetic susceptibility of the delocalized electron gas [94]. This delocalized electron can then travel around the material and interact with another electron, localized at lattice point, j, in the same way. The spin state of the delocalized electron then influences the spin state of the localized electron at point j on the lattice, due to the field created by the magnetic moment. This then means that the electron at lattice point i will then have an influence of the spin state of the electron localized at the lattice point j, which is mediated by the transfer of the delocalized electrons between the two points. The interaction of the spin states of two electrons in this way is known as RKKY coupling [94]. This exchange interaction adds a term into the Hamiltonian that is similar in nature to that presented in equation 2.4 but is now dependent on the distance between the points i and j, r_{ij} via,

$$\mathcal{H}(r_{\mathrm{ij}}) = -2J_{\mathrm{RKKY}}(r_{\mathrm{ij}})\hat{\mathbf{S}}_{\mathrm{i}} \cdot \hat{\mathbf{S}}_{\mathrm{j}}, \tag{2.32}$$

where,

$$J_{\mathrm{RKKY}}(r_{\mathrm{ij}}) \propto \frac{\cos(2k_{\mathrm{F}}r_{\mathrm{ij}})}{r_{\mathrm{ij}}^3}, \tag{2.33}$$

in which k_{F} is the Fermi wavevector [94]. The periodic nature of this quantity means that it can oscillate between being a positive and negative quantity, which means that it

can mediate both FM and AF exchange interactions between two electrons depending on the distance between them. The complicated nature of the domain structure in FeRh means that there may be competing RKKY interactions present between the domains that act on the spins in the domain wall which cannot be solved, leading to frustration.

2.7.2 Dipolar Interaction

The FM domains in FeRh each have a net magnetic moment. By its nature a magnetic moment is a magnetic dipole, where the field created by the moment forms closed loops that go from one end of the dipole to the other. When considering situations where the dipolar field associated with the magnetic moment of a given domain, μ_{i}, can interact with the magnetic moment of another domain μ_{j}, which are separated by a vector $\mathbf{r}_{\mathrm{ij}}$, the magnetostatic potential energy, E is given by,

$$E = \frac{\mu_0}{r_{\mathrm{ij}}^3}\left[\mu_{\mathrm{i}} \cdot \mu_{\mathrm{j}} - \frac{3}{r_{\mathrm{ij}}^2}(\mu_{\mathrm{i}} \cdot \mathbf{r}_{\mathrm{ij}})(\mu_{\mathrm{j}} \cdot \mathbf{r}_{\mathrm{ij}})\right]. \tag{2.34}$$

The dipolar interaction is anisotropic and arranging the magnetization to minimize the energy in a system with a large number of randomly orientated magnetic domains may not be possible, which will lead to frustration.

2.8 The Order of Phase Transitions

Phase transitions are characterized according to their order [104, 105]. The order of a phase transition refers to the order of the derivative of the free energy that first becomes discontinous [105]. For first-order phase transitions, such as the transition between the AF and FM state in FeRh, the first derivatiive of the free energy is discontinuous [105]. This means that there will be a discontinuity in the enthalpy at the transition temperature which will result in a latent heat in the system [105]. This latent heat leads to the coexitence of the two phases and such behaviour has been well studied in FeRh [7, 12, 27, 30–32, 34, 35]. Second-order phase transitions, such as the transition from a FM to a paramagnet at the Curie Temperature, has discontinuities in the second derivative of the free energy [105]. This means that there is no latent heat and no phase coexistence [105]. Approaching the transition point in second-order phase transition systems, the length of the correlations of the order parameter in the system diverge, as does the magnetic susceptibility [104, 106]. This behaviour is not expected in the systems with first order phase transitions.

Chapter 3

Characterization of Magnetic Materials Using X-Rays

X-rays are a powerful tool in the characterisation of materials. X-Rays experience scattering from both charge and magnetic objects within the systems in question and can therefore be used to characterize atomic and magnetic structures [76]. The magnetic signal can be enhanced using resonant absorption at given metal edge [76]. The experiments presented in this thesis utilize x-rays to characterize both the magnetic and atomic structure of B2-ordered FeRh thin films. The structural characterization is included throughout the thesis whilst chapters 7 and 8 will focus on the characterization of the magnetic structure and the dynamic behaviour of the magnetic regions, respectively. This chapter is included to provide a theoretical basis for the interpretation of the results of these experiments.

3.1 Non-Resonant X-Ray Scattering

Light waves traveling in a given direction can be described using its electric field, $\mathbf{E}$, which oscillates according to the energy and position of the light wave such that [76],

$$\mathbf{E} = E_0 \epsilon e^{-i(\omega t - \mathbf{k}\cdot\mathbf{r})}, \tag{3.1}$$

where E_0 is the field strength, ϵ is the polarization vector, ω is the angular frequency, t is the time, $\mathbf{k}$ is the wavevector of the light and $\mathbf{r}$ is the position vector. When an x-ray is incident (a) upon a single electron, the oscillating electric field of the x-ray causes the electron to oscillate in tandem. The subsequent motion of the electron is dipolar and produces an oscillatory electric field which causes the photon to be re-emitted. The emitted (b) electric field a distance R from the electron is given by [76],

$$\mathbf{E}_\mathrm{b}(R) = -\left(\frac{e^2}{4\pi\epsilon_0 m_\mathrm{e} c^2}\right)\frac{e^{ik_\mathrm{b}R}}{R}[\hat{\mathbf{k}}_\mathrm{a} \times \mathbf{E}(t)] \times \hat{\mathbf{k}}_\mathrm{b}, \tag{3.2}$$

where e is the magnitude of the electron charge, ϵ_0 is the permittivity of free space, m_e is the mass of the electron, c is the speed of light and $\hat{\mathbf{k}}$ denotes a unit vector. The quantity enclosed by the brackets is known as the classical electron radius or Thompson scattering length, $r_0 = 2.82 \times 10^{-15}$ m, and $\frac{e^{ikR}}{R}$ reflects the spherical wave nature of the emitted photon far from the source [76].

As light is made up of both oscillating electric and magnetic fields, it is necessary to consider the effect of the oscillating magnetic field may have on the electron. If the electron possesses a spin magnetic moment, $\mathbf{s}$, the torque from the oscillating magnetic

field causes the moment to precess in a cone about the principle axis of the field in a dipolar motion. The electric field radiated from the magnetic dipole for a spin vector, $\mathbf{s}$, is given by [76],

$$\mathbf{E}_\mathrm{b} = ir_0 \frac{\hbar\omega}{m_e c^2} \frac{e^{ik_\mathrm{b}R}}{R} [\mathbf{s} \times (\hat{\mathbf{k}}_\mathrm{a} \times \mathbf{E}(t))] \times \hat{\mathbf{k}}_\mathrm{b}. \tag{3.3}$$

It is clear from equations 3.2 and 3.3 that the magnitude of the magnetic scattering is lower than that of charge scattering by a factor of $\hbar\omega/m_e c^2$. Magnetic scattering causes the polarization of the light to be rotated whereas it is conserved for charge scattering due to the nature of the phase factor for each scattering type [76].

The polarization dependent scattering length for charge scattering is defined as [76],

$$f_\mathrm{C}(\epsilon_\mathrm{a}, \epsilon_\mathrm{b}) = r_0 \epsilon_\mathrm{a} \cdot \epsilon_\mathrm{b}, \tag{3.4}$$

whilst the same quantity for magnetic scattering is defined by [76],

$$f_\mathrm{M}(\epsilon_\mathrm{a}, \epsilon_\mathrm{b}) = -ir_0 \frac{\hbar\omega}{m_e c^2} \mathbf{s} \cdot (\hat{\mathbf{k}}_\mathrm{a} \times \epsilon_\mathrm{a}) \times (\hat{\mathbf{k}}_\mathrm{b} \times \epsilon_\mathrm{b}). \tag{3.5}$$

The total scattering length is then given by $f = f_\mathrm{C} + f_\mathrm{M}$ [74, 76]. The differential scattering cross-section for single electron scattering, which is the intensity scattered into a solid angle, Ω, is then defined as

$$\frac{d\sigma}{d\Omega} = |f(\epsilon_\mathrm{a}, \epsilon_\mathrm{b})|^2. \tag{3.6}$$

Extending the single electron approach to the configuration of electrons within an atom requires integrating the contribution from each of the electrons within the atom, which leads to the atomic form factor defined by [76],

$$F^0(\mathbf{Q}) = -\frac{1}{e} \int \rho(\mathbf{r}) e^{i\mathbf{Q}\cdot\mathbf{r}} d\mathbf{r}. \tag{3.7}$$

This equation shows the atomic form factor as a Fourier transform of the charge density, ρ. The scattering vector $\mathbf{Q}$ is defined as $\mathbf{Q} = \mathbf{k}_\mathrm{b} - \mathbf{k}_\mathrm{a}$, where $\mathbf{k}$ is the photon wavevector and is defined as $|k| = 2\pi/\lambda$, with λ being the wavelength of light. $\mathbf{Q}$ is introduced at this stage to reflect the now angle dependent nature of the scattering, as the differences in path length between x-rays scattered from opposite sides of the atom are on the order of the wavelength of light and may cause interference. Processes in which the energy of the photon is conserved and $|\mathbf{k}_\mathrm{a}| = |\mathbf{k}_b|$ are known as elastic processes, where $|\mathbf{Q}|$ can be given the functional form [76, 107],

$$|\mathbf{Q}| = \frac{4\pi}{\lambda} \sin\theta, \tag{3.8}$$

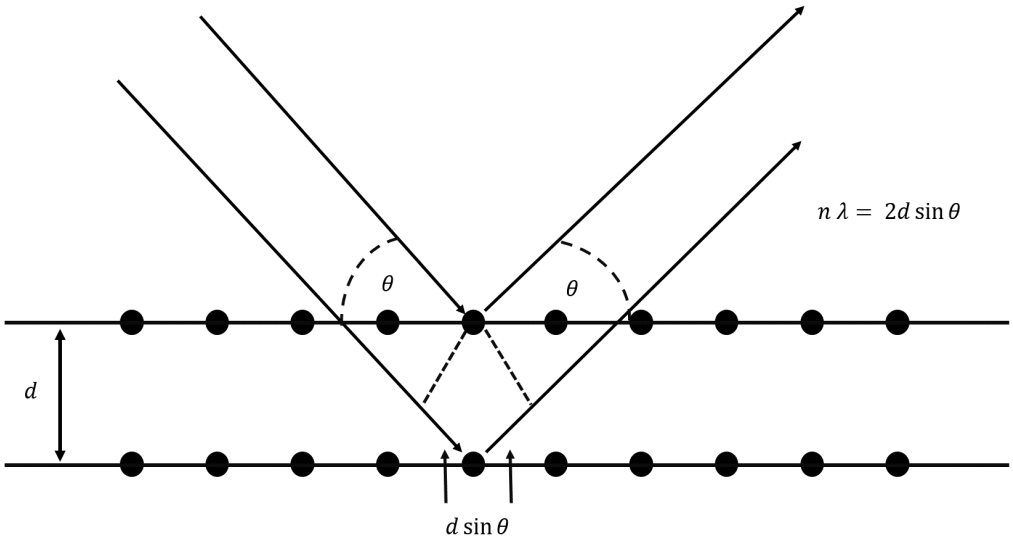

Figure 3.1: Demonstration of the path difference length in Bragg scattering. The circles represent atoms with the solid black lines being the diffraction planes a distance d apart. The incoming and outgoing x-rays are at an angle θ to the surface of the film. The path difference between the two light paths is $2d\sin\theta$ which is equal to an integer number of wavelengths $n\lambda$ for constructive interference.

where θ is the angle subtended between $\mathbf{k}_{\mathrm{a,b}}$ and $\mathbf{Q}$.

The atomic scattering length, f^{atom}, is then defined as the product of the atomic form factor and the scattering length of a single electron such that the differential cross-section becomes

$$\left(\frac{d\sigma}{d\Omega}\right)_{\mathrm{atom}} = |f^{\mathrm{atom}}|^2 = |f(\epsilon_{\mathrm{a}}, \epsilon_{\mathrm{b}})|^2 |F^0(\mathbf{Q})|^2. \tag{3.9}$$

Up to this point, the scattering from an electron and a collection of electrons within an atom has been described. Now, it is necessary to expand the discussion to scattering from a collection of atoms. As the crystal lattice is a regular arrangement of atoms for which the scattering theory is well established [76, 108–110], it is sensible to start the discussion there.

3.1.1 Bragg Scattering

Considering two atomic planes a distance d apart, the path difference between the incoming and outgoing x-rays at an angle θ to the plane of the crystal is $2d\sin\theta$. Constructive interference from successive planes occurs when the path difference is equal to an integer number, n, of wavelengths such that [108, 110],

$$n\lambda = 2d\sin\theta. \tag{3.10}$$

This is known as Braggs' law and a diagram that helps to visualize the path of the x-ray in the material is included in Fig. 3.1 [110].

Scattering from crystal lattices is often spoken of in terms of the unit cell [76, 108, 109]. The unit cell of the crystal lattice is the smallest object that retains the overall symmetry of the system and can be repeated in three dimensions to build the entire lattice structure [108]. The simplest examples of the unit cell are the simple cubic, face-centred cubic and body centred cubic (BCC) structures [108]. Each of these structures has different characteristic scattering profiles that allow for the identification of the unit cell type. The unit cell vectors, $\mathbf{R}_\mathrm{n}$, of the crystal lattice can be described in terms of lattice vectors $\mathbf{a}$,

$$\mathbf{R}_\mathrm{n} = n_1\mathbf{a}_1 + n_2\mathbf{a}_2 + n_3\mathbf{a}_3, \tag{3.11}$$

where n are integers [108]. The incoming x-rays are described by plane waves and will have the periodicity of a unit cell for a given number of wavevectors. The reciprocal lattice is the set of all wavevectors, $\mathbf{k}$, that gives plane waves the periodicity of the unit cell [108]. This means that the in order to be in phase, a plane-wave at a given set of points, $\mathbf{R}$, must follow $e^{i\mathbf{K}\cdot\mathbf{R}} = 1$. The corresponding reciprocal lattice can also be expressed as the sum of reciprocal lattice vectors $\mathbf{b}$ whereby

$$\mathbf{K}_n = h\mathbf{b}_1 + k\mathbf{b}_2 + l\mathbf{b}_3, \tag{3.12}$$

where h, k, l are the Miller indices. The reciprocal lattice vectors $\mathbf{b}$ are functions of two lattice vectors and it follows that $\mathbf{a}_\mathrm{i}\cdot\mathbf{b}_j = \delta_{ij}$. Therefore, in order for $e^{i\mathbf{K}\cdot\mathbf{R}} = 1$ to be satisfied $\mathbf{K}\cdot\mathbf{R} = 0$. This condition allows for the determination of the different primitive unit cell types as they each have characteristic lattice vectors and certain planes that have forbidden reflections [108].

When considering the scattering from a unit cell, each of the atoms within the cell contributes to the scattering and so the total scattering can be described by the

structure factor which is defined as,

$$S(\mathbf{Q}) = \Sigma_{\mathrm{j}} f_{\mathrm{j}} e^{-i\mathbf{Q}\cdot\mathbf{r}_{\mathrm{j}}}, \tag{3.13}$$

where j is the number of atoms in the unit cell and r_{j} is the position vector of atom j within the unit cell [108]. The intensity of scattered light then can be written as

$$I(\mathbf{Q}) = |S(\mathbf{Q})\Sigma_{\mathbf{k}} e^{i(\mathbf{Q}\cdot\mathbf{R})}|^2. \tag{3.14}$$

It follows here that certain unit cell arrangements have forbidden reflections as the structure factor is 0. For BCC systems the (001) reflection is forbidden. However, for binary alloys such as FeRh, where the system takes on the structure of two interlocked simple cubic lattices, one for each atomic species, the asymmetry in the form factors lifts this restriction and the (001) reflection can be used to characterize the superlattice nature of the system [109].

The extension of the non-trivial nature of the unit cell to equation 3.10 leads to the space between adjacent planes being rewritten in terms of the lattice constant a, such that:

$$d_{hkl} = \frac{a}{\sqrt{h^2 + k^2 + l^2}}. \tag{3.15}$$

This is the length scale measured in x-ray diffraction experiments. The $\mathbf{Q}$ can now be extended to encompass Braggs' law for the first order diffraction peak such that $Q = 2\pi/d$, where d here describes the length scale of the periodicity of the scattering sites and can come from both magnetic and non-magnetic sources [76].

3.2 Magnetic Dichroism Using Polarized X-Rays

Dichroism is a difference in the absorption of light in a material. This section describes the dichroism techniques that are used to measure both the ferromagnetic (FM) and antiferromagnetic (AF) contributions to the resonant magnetic scattering seen in chapters 7 and 8. These experiments utilize both X-Ray Magnetic Circular Dichroism (XMCD), which is sensitive only to FM materials and X-Ray Magnetic Linear Dichroism (XMLD), which is sensitive to both AF and FM materials [76, 77].

3.2.1 X-Ray Magnetic Circular Dichroism

Circularly polarized x-rays can be used to probe the magnetic properties of a sample using XMCD. For transition metal magnets, the most prominent XMCD can be found

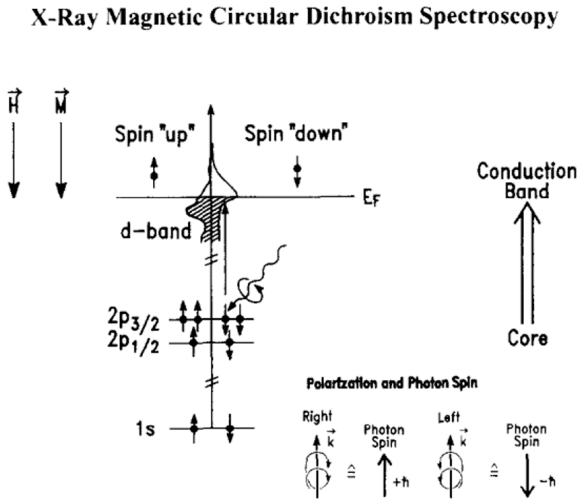

Figure 3.2: Schematic of the two-step process involved in XMCD. The first stage is signified by the incoming photon. The subsequent excitation to the $3d$ band is then sensitive to the number of available states in that band. These are dependent on the spin orientation of the initial state and so allow for probing of the magnetization. This dependence on the initial spin state describes the second phase of XMCD. Figure taken from Ref. [77].

in the L_3 and L_2 edges, which corresponds to transitions from the spin-orbit split $2p$ band to the $3d$ shell [76]. The L_3 edge refers to the transition from the $2p_{3/2}$ to the $3d$ shell, whereas the L_2 consists of transitions from the $2p_{1/2}$ to the $3d$ shell. This technique can be made to be element specific due to the different binding energies of the $2p$ electrons for different elements. An illustration of the physical processes involved is included in Fig. 3.2 [76, 77].

Firstly, the angular momentum of the incoming photons is transferred to the $2p$ electrons. The two helicities of light carry with them equal and opposite angular momentum of $L = \pm 1$ per photon, that is transferred entirely to the $2p$ electron upon absorption [76]. As the $2p$ electrons exhibit spin-orbit coupling, the incident angular momentum can be transferred to either the spin or orbital contributions to the angular momentum. Therefore, preferential excitations of specific spin states are possible but are dependent on the relative orientation of angular moment of the incoming photon and the direction of the magnetization [77]. This absorption of the angular momentum

by the $2p$ electrons is sufficient to liberate them from the $2p$ orbital, creating photoelectrons that can transfer into the $3d$ shell, should there be state available for them to do so [76, 77].

Here the magnetic properties of the material starts to become relevant. The next part of the process is known as the second stage of XMCD. The transition rate probability, T_{ab} from the initial state described by $|a\rangle$ to final state, $|b\rangle$, mediated by the interaction Hamiltonian, H_{I}, is given by Fermi's golden rule [76],

$$T_{\mathrm{ab}} \propto |\langle b| H_{\mathrm{I}} |a\rangle|^2. \tag{3.16}$$

This describes a first order transition process between the two states [76]. It therefore follows that the transition probability is dependent on the number of $|b\rangle$ states available. Inherently, magnetic materials have an asymmetry in the spin-polarized density of states at the Fermi energy. This asymmetry in the available states means that electrons in the $2p$ orbitals with one spin orientation will have a larger number of available states into which they can transition compared to the opposite spin orientation. This will therefore give one spin polarization a larger probability of absorption than the other. It is this difference in the absorption probability between the two spin orientations that makes the $3d$ band a detector for the spin angular momentum state of the excited photoelectrons.

The preferential excitation of light for electrons of one spin state compared to the other is the source of the signal for XMCD. It also means that it is possible to probe the magnetic moment of the system in question. The XMCD intensity follows [76],

$$I_{\mathrm{XMCD}} \propto \mathbf{m} \cdot \mathbf{L}_{\mathrm{Ph}}, \tag{3.17}$$

where $\mathbf{m}$ is the magnetic moment and $\mathbf{L}_{\mathrm{Ph}}$ is the angular momentum of the incoming photon. By taking a measurement in which the two quantities are aligned, I^+, and anti-aligned, I^-, and taking one from the other gives the difference intensity which is directly proportional to the atomic magnetic moment being measured [76],

$$\Delta I = \frac{I^+ - I^-}{I^+ + I^-}. \tag{3.18}$$

3.2.2 X-Ray Magnetic Linear Dichroism

XMLD can be used to measure anisotropy in electron orbital projection [76]. To achieve this, it uses what is known as the searchlight effect to identify which orbital projections are present [76]. The term searchlight comes from the fact that the polarization

dependent transition probability of an electron transitioning from a core to valence state is dependent on the shape of the valence state orbital. As orbitals are not always spherically symmetric, there are directions along which the projection of the orbital will be different to others. The overlap of the light and the orbital projection defines the probability of absorption, with light oriented in the same direction as the orbital experiencing a larger probability of being absorbed by the electron. Therefore, there will be different probabilities for the absorption of light of a given polarization for orbitals projected in different directions. This asymmetry allows for the identification of the direction in which the orbital is projected, with the polarization of the incoming light acting to illuminate the orbital projection direction, hence the term searchlight. By changing the direction of the linear polarization it is possible to compare the relative intensity of the orbitals in the two orientations and build up a picture of the anisotropy in orbital projection. As this is dependent on the shape of the orbital it does not exclusively require magnetism to be present and the general underlying technique is known as X-Ray Natural Linear Dichroism (XNLD). For spherically shaped orbitals the projection is the same in all directions and there is no XNLD.

Extending the technique to include magnetic materials requires a two-step model in a similar vein to the explanation of XMCD, so similar in fact that the first stage of both processes is the same. The differences between the two types of dichroism come in the second stage of the process, where for XMLD the transition probability is now dependent on the polarization of the orbital relative to the incoming x-ray polarization.

In systems with no spin-orbit coupling, the sum over all m_J orbital states for a given L is spherically symmetric and no XNLD is seen [76]. XMLD differs from XNLD in that the introduction of the spin-orbit coupling provides a preferential direction in which the orbitals will lie. This will increase the transition probability for light that is polarized along this preferential direction compared to the perpendicular direction. In FM materials, the two spin projections in the $3d$ band have a different energies at the Fermi level. The $2p$ orbitals in these materials also have their energy levels split via spin-orbit coupling. This spin-orbit coupling means that each of the orbitals corresponding to different m_J values present for each $2p$ orbitals ($m_J = \pm 3/2, \pm 1/2$ for $2p_{3/2}$ and $m_J = \pm 1/2$ for $2p_{1/2}$) each have a different energy and therefore require different excitation energies to transition to the $3d$ electron band. This means that there is an absorption peak at energies corresponding to each of the different m_J states that

can be seen in the XMLD spectra which allows for the identification of the orientation axis of the magnetic electrons [76]. Again, here the transition probability for each of the $2p$ orbitals has its probability defined by the number of states for the spin projection available in the $3d$ band. This means that a preferential transition probability for a given spin projection over the other will be present.

For AF materials there is no exchange splitting of the $3d$ shell energy bands. However, the spin-orbit coupling induces an anisotropy that causes the spins of the $3d$ electrons to align along a given direction. This again means there will be a preferential absorption probability for linear light polarized along this axis, compared to light polarized perpendicular to it. As there is still a spin-orbit splitting expected in the $2p$ orbitals, it is possible to identify the different orbitals due the difference in their binding energies. Though there may no longer be a preferential transition probability for a given spin projection in this scenario, the preferential orientation of the orbital direction means that the spherical symmetry is lifted and XMLD can be measured in AF materials [111]. The linear nature of the light means that it only possible to probe the axis along which these spins sit and not the direction of the spins themselves, which is the case for both AF and FM materials. Similar to XNLD and XMCD, taking the difference between two perpendicular orientations of the orbitals relative to the direction of linear polarization gives a difference in transition probability for each transition and allows for their identification [76, 77, 111].

3.2.3 Resonant Magnetic X-ray Scattering

The dichroism phenomena previously described all rely on the absorption of x-rays. In these processes a photon enters the system and releases and electron from its energy level, and is known as a photon in-electron out process. It is entirely possible however, that the excited photoelectron sits in the energy level to which it has transitioned and eventually decays back down to its original energy level. This process will release a photon of energy equal to the energy difference between energy levels. In this process a photon both enters and exits the system. In magnetic materials this process is known as Resonant Magnetic X-Ray Scattering (RMXS). An energy level schematic demonstrating the difference between the x-ray absorption and RMXS is shown in Fig. 3.3. RMXS occurs at a series of different binding energies, E_{n}, present in the atom [76].

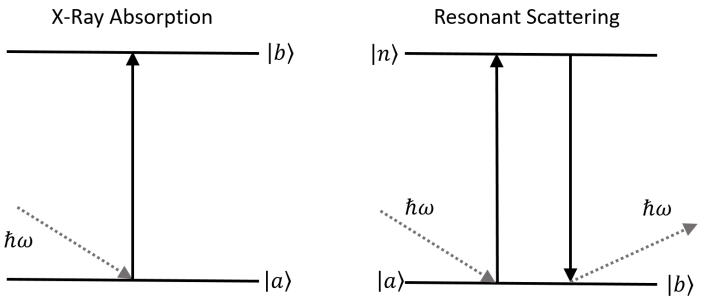

Figure 3.3: Energy level diagrams involved in the X-Ray absorption processes and resonant x-ray scattering. A photon enters the system in both cases and is absorbed by the photon causing a transition between the two energy levels. The X-ray absorption processes only concern the transition between $|a\rangle$ and $|b\rangle$. This process is then a photon in-electron out process. For resonant x-ray scattering the photoelectron decays back into its original state and releases energy as a photon, meaning it is a photon in-photon out process.

RMXS is known as a second order process as it requires the existence of an intermediate state $|n\rangle$ between the final and initial states [76]. This adds another term into the transition rate probability, seen in equation 3.16, such that it takes the form

$$T_{\mathrm{ab}} \propto \left| \langle b| H_{\mathrm{I}} |a\rangle + \sum_{n=1}^{\infty} \frac{\langle b| H_{\mathrm{I}} |n\rangle \langle n| H_{\mathrm{I}} |a\rangle}{E_{\mathrm{n}} - E_{\mathrm{a}}} \right|^2. \tag{3.19}$$

This excitation-deexcitation of the electron can be modeled as a harmonic oscillator. Doing so for the multielectron nature of the atom introduces a resonant factor into the scattering length, seen in equation 3.4 and 3.5, such that [76]

$$f_n(\omega) = F_n(\omega)(f_{\mathrm{C}} + f_{\mathrm{M}}), \tag{3.20}$$

with

$$F_n(\omega) = \frac{\omega^2}{(\omega^2 - \omega_n^2) + i\omega\Gamma_n}, \tag{3.21}$$

where n corresponds to the electron level and Γ_n is resonance linewidth related to the energy dissipation within the resonance. Defining $\Delta_n = \hbar\Gamma_n$ alongside the fact that $\Delta_n \ll E_n$ it is possible to rewrite equation 3.20 as a perturbation,

$$f(\mathbf{Q}, E) = f^0(\mathbf{Q}) + f'(E) + if''(E). \tag{3.22}$$

where $f_0 = Z$ the atomic number, $f'(E)$ is proportional to the magnetic scattering and $f''(E)$ is directly proportional to the x-ray absorption cross-section [76]. It is possible to calculate $f'(E)$ from $f''(E)$ using the Kramers-Kronig relation via [76],

$$f'(E) = \frac{2}{\pi} P \int_0^\infty \frac{\epsilon f''(\epsilon)}{E^2 - \epsilon^2} d\epsilon \tag{3.23}$$

where $P\int$ refers to the Cauchy principle integral value and ϵ is a dummy variable used for the integration. The dependence on $\mathbf{Q}$ for these core shell excitations is weak as their radius is much smaller than that of the incoming wavelength. Resonant absorption can enhance the magnetic scattering signal such that it is comparable to the charge scattering signal at an atomic absorption edge [76].

3.3 Small Angle X-Ray Scattering

Small Angle X-ray Scattering (SAXS) is a technique that is used to characterize objects between one and several hundreds of nm in size [78, 112]. As the name suggests, the large size of these objects means that the corresponding scattering pattern emerges in a narrow Q window close to 0. SAXS has been used to characterize particles in solution, polymers and even the size of magnetic domains in magnetic thin films [73–75, 78]. The work in this thesis combines RMXS with SAXS in a technique known as Resonant Magnetic Small Angle X-ray Scattering (RMSAXS) to investigate the size of the magnetic scatterers through both magnetic phases at various points through the transition, the results of which are presented in chapter 7.

As x-ray scattering from an atom is dependent on the objects' electron density it stands that the scattering length, f, is dependent on the shape and size of the scatterer in question. Therefore, the scattering length for atom j can be rewritten in terms of the scattering length density β, such that [112]:

$$f_j = \int \beta_j(\mathbf{R}) e^{i\mathbf{Q}\cdot\mathbf{R}} d^3\mathbf{r}. \tag{3.24}$$

It then follows by equation 3.6 that,

$$\left(\frac{d\sigma}{d\Omega}\right) \propto \left| \int \beta(\mathbf{r}) e^{i(\mathbf{Q}\cdot\mathbf{r})} dV \right|^2. \tag{3.25}$$

It follows then that for systems that exhibit two distinct phases, such as particles in a solution or a mixture of structural phases as is the case in B2-ordered FeRh, that

have a difference in the scattering length denisty, the intensity of the scattering can be described by the difference in scattering length density of the two phases $\Delta\beta$, such that the intensity then becomes [78, 112],

$$\left(\frac{d\sigma}{d\Omega}\right) \propto \left| \int \Delta\beta(\mathbf{r}) e^{i(\mathbf{Q}\cdot\mathbf{r})} dV \right|^2. \tag{3.26}$$

This is made possible via Babinet's principle as the average scattering length across the film is constant and can be subtracted which makes the difference the relevant quantity [78].

The derivation of the intensity of a SAXS profile included here will focus on the importance of structural correlations within the system, where the word correlation here refers to the distance between scatterers. The derivation of the intensity profiles in which there are no structural correlations assumes a dilute system which does not apply to the magnetic behaviour of B2-ordered FeRh and so is not included. Instead, the reader is invited to read the derivation in Ref. [112]

For the purposes of this derivation, $\Delta\beta$ is thought to contain positional correlations at a point $\mathbf{r}$ within the system depending of the position of the other scatterers at $\mathbf{r}_j$, and can be written as [112],

$$\Delta\beta(\mathbf{r}) = \hat{\beta}(\mathbf{r}) \otimes \sum_{j=1}^{N} \delta(\mathbf{r} - \mathbf{r}_j), \tag{3.27}$$

where $\hat{\beta}$ is the average difference in scattering length density through the film. When combining this with the intensity given by equation 3.26, it becomes

$$\left(\frac{d\sigma}{d\Omega}\right) \propto \left| F(\mathbf{Q}) \sum_{j=1}^{N} e^{i\mathbf{Q}\cdot\mathbf{r}_j} \right|^2, \tag{3.28}$$

Evaluating this integral leads to,

$$\left(\frac{d\sigma}{d\Omega}\right) \propto |F(\mathbf{Q})|^2 S(\mathbf{Q}), \tag{3.29}$$

where $S(\mathbf{Q})$ denotes the structure factor. This implies that the maximum intensity corresponding to a peak in the structure factor occurs when $\mathbf{Q} \cdot (\mathbf{r}_\mathrm{j} - \mathbf{r}_\mathrm{j'}) = 2\pi n$ where n is an integer, which is similar to the Bragg diffraction seen in section 3.1.1.

3.3.1 Resonant Magnetic Small Angle X-Ray Scattering

For RMXS, which is outlined in section 3.2.3, it is possible to relate f'' seen in equation 3.22, to the absorption coefficient $\mu(E)$ via the optical theorem, such that [73]

$$f''(E) = \frac{mcE}{4\pi e^2 h}\mu(E). \tag{3.30}$$

The magnetic absorption coefficient for the parallel/antiparallel alignment of the magnetic electrons relative to the photon propagation direction is given by:

$$\mu^{\pm}(E) = \mu_0(E) \pm \mu_{\text{mag}}(E), \tag{3.31}$$

where $\mu_0(E)$ is the contribution to absorption expected without resonant magnetic scattering and μ_{mag} is the magnetic contribution [73]. This then means that both f' and f'' acquire magnetic contributions depending on the polarization of the x-rays relative to the magnetization such that

$$f'^{\pm}(E) = f'(E) \pm f'_{\text{mag}}, \tag{3.32}$$

$$f''^{\pm}(E) = f''(E) \pm f''_{\text{mag}}, \tag{3.33}$$

This then leads to a difference in cross section between the two polarizations for a system containing a magnetic substance with f, f', f'' in a matrix that doesn't contribute to the scattering as [73]:

$$\left(\frac{d\sigma}{d\Omega}\right)^{+} - \left(\frac{d\sigma}{d\Omega}\right)^{-} \approx 4(f_0 + f')f'_{\text{mag}} + 4f''f''_{\text{mag}}. \tag{3.34}$$

This is taken to be the scattering intensity expected for the measurements taken using XMCD, which are presented in chapters 7 and 8.

3.4 X-Ray Photon Correlation Spectroscopy

X-ray Photon Correlation Spectroscopy (XPCS) is a powerful tool that has been used previously to measure various incarnations of dynamic behaviour in a plethora of magnetic systems [81–83, 85–87, 113]. It is used here to characterize the dynamic behaviour of the RMSAXS for both dichroism types in 8.

When coherent light is incident upon a sample that exhibits disorder, the scattering from these regions interacts either constructively or destructively depending on their

orientation. This gives rise to fine structure in the diffraction feature, which is known as a speckle pattern [114]. This speckle pattern requires the use of coherent light as the fine structure is averaged away for incoherent light. The size of the features within the speckle pattern are defined by λ/a, where λ is the wavelenth of the light and a is the coherent volume of the beam [115]. As the speckle pattern is a Fourier transform of the object that creates it, any changes in this object will result in a corresponding change in the speckle pattern in real time. The dynamical structure factor, $S(\mathbf{Q},\omega)$, is now defined to reflect the temporal dependence of the scattering as [81],

$$S(\mathbf{Q},\omega) = \frac{1}{2\pi}\int dt e^{-i\omega t}\langle\rho(\mathbf{Q},0)\rho(-\mathbf{Q},t)\rangle \tag{3.35}$$

with $\rho(-\mathbf{Q},t)$ being the Fourier transform of the electron density at time t and $\langle\rangle$ being a statistical average. This is used to compare the evolution of the system at time t with its original state. The frequency Fourier transform of this quantity is known as the intermediate scattering function (ISF) and for a number of scatterers, N, is [81]:

$$g_1(\mathbf{Q},t) = \frac{1}{N}\langle\rho(\mathbf{Q},0)\rho(-\mathbf{Q},t)\rangle. \tag{3.36}$$

The intensity of the scattering at a given time is expressed as [81]:

$$I(\mathbf{Q},t) = C\langle\rho(\mathbf{Q},t)\rho(-\mathbf{Q},t)\rangle, \tag{3.37}$$

where C is a constant [81]. If this quantity is completely dynamic then it is said to be homodyne i.e. of a single frequency, however, should there be a static reference signal then there is more than one frequency and it is described as being heterodyne [81]. The nature of this quantity affects the expected results and the model by which to fit the data in order to extract them.

In XPCS, the intensity correlation function, g_2, is measured and gives the temporal correlation between two images taken at arbitrary times. Tracking the progress of this quantity with time gives access to the development of the correlation of images in a series and therefore the systems dynamic behaviour. This can be written as the correlation between two arbitrary times t and $t+\tau$ as [81, 116]:

$$g_2(\mathbf{Q},t,t+\tau) = \frac{\langle I(\mathbf{Q},t)I(\mathbf{Q},t+\tau)\rangle}{\langle I(\mathbf{Q},t)\rangle^2} = 1 + A|F(\mathbf{Q},\tau)|^2, \tag{3.38}$$

where $F(\mathbf{Q},t) = g_1(\mathbf{Q},t)/g_1(\mathbf{Q},0)$. This is known as the Siegert relation [81, 117]. The analytical interpretation for homo- and heterodyne models for the g_2 function differs

in the sense that the heterodyne is modified to reflect the reference frequency whereas the homodyne model is not. The heterodyne model has extra terms that reflect this and takes the form [113, 117]:

$$g_2(\mathbf{Q}, t, t+\tau) = I_{\mathrm{R}}^2 + \langle I_{\mathrm{S}}(\tau)\rangle_t^2 [1+\beta|g_1(\mathbf{Q},\tau)|^2] + 2I_R\langle I_{\mathrm{S}}\rangle_t + 2I_{\mathrm{R}}\langle I_{\mathrm{S}}\rangle_t \beta Re[g_1(\mathbf{Q},\tau)], \quad (3.39)$$

where I_{R} is the intensity of the static reference signal and I_{S} is the sample signal intensity. It is evident here that if $I_{\mathrm{R}} = 0$ that the homodyne model is recovered.

Chapter 4

Experimental Methods

This chapter houses the methods and technical specifications for the experiments presented in the subsequent chapters. These fall into several categories: the first of which is the growth and fabrication of samples, which is followed by the general characterization for their structural and magnetic properties, the magnetic resonance techniques which encompasses both ferromagnetic and spin-wave resonance (FMR and SWR respectively) experiments, the soft x-ray methods for use in the Small Angle X-Ray Scattering (SAXS) and X-ray Photon Correlation Spectroscopy (XPCS) experiments and the computer simulations of atomistic spin dynamics. Each of these categories will be addressed in turn in this chapter.

4.1 Sample Fabrication Techniques

4.1.1 Direct Current Magnetron Sputtering

For the purposes of this thesis all samples were grown using direct current (DC) magnetron sputtering. These growths were performed in a Kurt. J. Lesker vacuum chamber at the University of Leeds. The vacuum is produced using a roughing pump to take the pressure in the growth chamber from atmospheric pressure into the mTorr regime. At this point a cryopump is employed to take the system to the $\sim 1 \times 10^{-7}$ Torr regime at room temperature. A liquid nitrogen trap is also used to remove any excess water that remains in the system. Base pressure at room temperature can reach the mid 10^{-8} Torr regime with the help of a turbo pump.

Growth of B2-ordered FeRh requires deposition onto a heated substrate. To this end a light is used to heat the substrate and the sample holder to the desired temperature from the rear. FeRh is grown at a substrate temperature of 600°C in this system [118] and the vacuum at these temperatures reaches $\sim 1 \times 10^{-7}$ Torr with the turbo pump operating.

Once the system is at base pressure and the substrate is at the desired deposition temperature, the actual deposition of the material is the next order of business. A schematic of a DC magnetron sputtering gun is shown in Fig. 4.1. Initially, Ar gas is pumped onto the target via an inlet in the shielding at a pressure of 5 mTorr. The target is held at a high negative voltage whilst the shielding is grounded. This causes electrons to accelerate away from the target and into the Ar gas, which in turn ionizes the Ar atoms creating a plasma. The newly generated Ar^+ ions are then accelerated

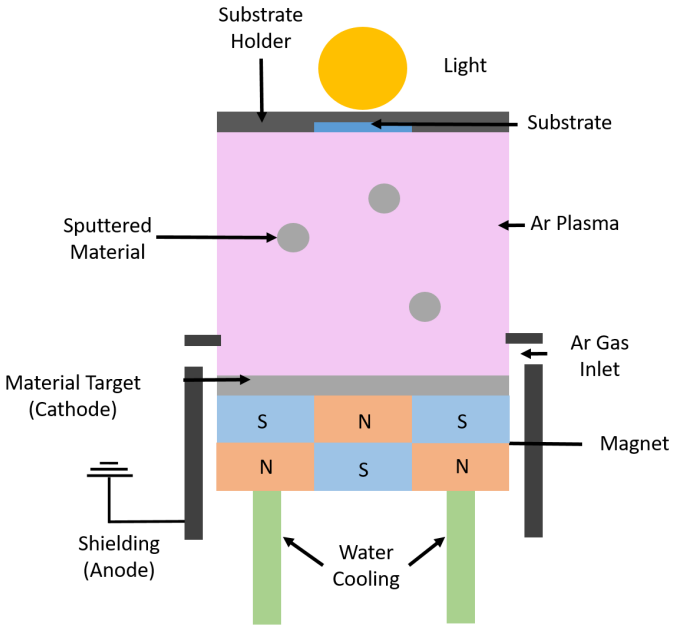

Figure 4.1: Schematic of a DC magnetron sputtering gun and heated substrate mount. The material is removed from the target via momentum transfer from the Ar ions, it then transfers towards the substrate where the thin film is formed.

back towards the target and remove material from the surface via momentum transfer. The material that is removed from the target is ionized and is travels towards the substrate, where they collect to form a thin film. Strong permanent magnets are placed underneath the target to trap the plasma near its surface via the Lorentz force, which increase the collision probability between the ions and the target.

4.1.2 HF Etch

For the experiments performed at soft x-ray facilities it is necessary to create x-ray transparent membranes of B2-ordered FeRh. Commercially available x-ray transparent membranes are made of Si_3N_4 which is amorphous and does not lend itself well to epitaxial growth of ordered material. For this reason, it is necessary to grow the FeRh on a substrate that promotes an ordered growth but can also be used to make x-ray transparent membranes afterwards.

To this end, R. Campion of the University of Nottingham kindly provided us with

a heterostructure of GaAs(substrate)/AlAs(25 nm)/GaAs(25 nm) which is used as the substrate in the growths described in chapters 7 and 8. This structure is used because the etching chemistry of the GaAs relative to AlAs is well known and can be used to remove the substrate from the film itself [119]. AlAs is more susceptible to etching than GaAs when exposed to hydrofluoric acid (HF), which means that the AlAs layer is destroyed before the surrounding GaAs layer [119]. The bottom substrate layer is removed from the rest of the stack leaving the GaAs(25 nm)/film structure. The FeRh layer is protected by the use a HF resistant wax, which is then removed after processing. The resultant film is then scooped up between two Cu grids with 500 μm $\times$ 500 μm windows, creating x-ray transparent membranes as required. N. Peters was kind enough to perform the HF etch of the samples presented in this thesis.

4.2 Sample Characterization Techniques

For the purposes of this thesis there are two main categories into which the sample characterization falls: that of the structural and the magnetic properties. Structural characterization of films are performed using X-ray Reflectivity (XRR) and X-ray Diffraction (XRD), with the magnetic properties being characterized by a Superconducting Quantum Interference Device Vibrating Sample Magnetometer (SQUID-VSM).

4.2.1 Structural Characterization

Characterizing a material for its structure has long been in the realm of the x-ray. The x-rays are incident on the film and depending on the angle of incidence, θ_{i}, two regimes can be probed that yield different properties of the material. Small grazing incidence angles ($\theta_{\mathrm{i}} < 10^{\circ}$) allow for the extraction of features with a large length scale such as the film thickness using XRR. Whereas the larger angles ($\theta_{\mathrm{i}} > 10^{\circ}$) correspond to smaller features such as the crystallographic or atomic scale structure parameterized by the lattice constant, a, and the extent to which it is chemically ordered, characterized by the B2 order parameter, S [109]. These smaller features of the sample are investigated using XRD.

All x-ray characterization measurements taken away from synchrotron facilities are performed using a Bruker-D8 advance system in the Bragg-Bretano geometry. This system uses Cu K_{α} light that is passed through a 4-bounce monochromator system before

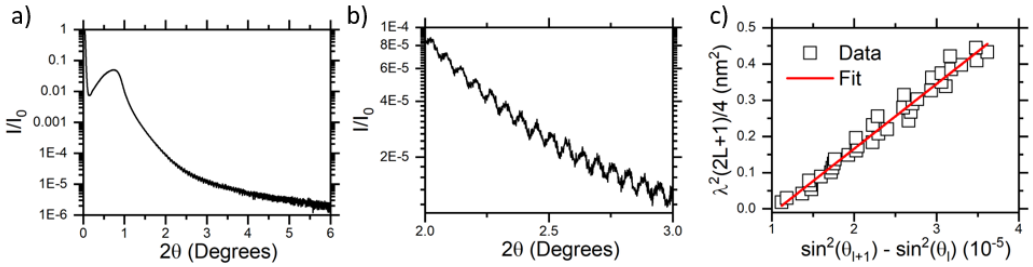

Figure 4.2: X-Ray Reflectivity examples. Panel a) shows an XRR scan of the Pd-doped FeRh sample used in the experiments presented in chapters 5 and 6 with panel b) demonstrating a close up of the Kiessig fringes. Panel c) shows the data and the plot used to extract the thickness of the films according to equation 4.2. This analysis is performed on the sample used in the FMR and SWR experiments the results of which are presented in chapters 5 & 6 respectively.

reaching the sample. This 4-bounce system is used to increase the monochromacity of the beam and improve the angular resolution. The angle θ is that which is subtended between the sample plane and the incident x-ray beam, with the detector always being rotated through 2θ. Performing the measurement in this way means that the scattering vector, $\mathbf{Q}$, is always normal to the film surface. Here, the sample is placed on the stage and held in place using a vacuum chuck. The source is kept at a constant angle with the sample and the detector being rotated through θ and 2θ respectively.

X-Ray Reflectivity

XRR is used to characterize the thickness of the film, t, using the method outlined by Kiessig [120]. To achieve this the reflection and transmission of the light from both the top surface of the structure and the bottom surface, where the film is in contact with the substrate, are considered. The critical angle θ_{C} is the angle at which the beam is totally externally reflected and after which reflections from the crystal planes can be seen. Once the x-ray light is inside the film, there is a fraction of the light that reflects from the bottom surface and approaches the top surface again where it can either be reflected or transmitted. By geometric means, the constructive interference condition for light at the top surface is then given by,

$$l\lambda = 2t\sqrt{\sin(\theta_{\mathrm{i}})^2 - \sin(\theta_{\mathrm{C}})^2}. \tag{4.1}$$

l here can be used to describe the number of times the light is totally internally reflected, which adds $2t$ to the path difference [120, 121]. These l integers are then assigned to the peaks in the system where the constructive interference condition is satisfied. By taking the difference in the square of the sine of the angle between adjacent peaks one can extract the thickness of the film via the equation [121]:

$$\sin(\theta_{l+1})^2 - \sin(\theta_l)^2 = \frac{\lambda^2(2l+1)}{4}\frac{1}{t^2}, \tag{4.2}$$

with t^{-2} begin taken as the gradient of the $\sin(\theta_{l+1})^2 - \sin(\theta_l)^2$ against $\lambda^2(2l+1)/4$ graph as shown in Fig. 4.2(c).

X-Ray Diffraction

Once the thickness of the film has been established, ascertaining the nature of the films structure is now the goal and to do that one continues to x-ray scan to $\theta_i > 10°$. This then leads to XRD, the theory for which is presented in section 3.1.1 where the object of interest here is the lattice parameter, a, given by equation 3.15.

B2 Order Parameter Calculation

B2-ordered systems are those in which there are two simple cubic lattices of different elements interlocked with each other to form a BCC-like structure such as that seen in Fig. 1.1. The unit cell of the B2-ordered system can be thought of as a simple cubic cage of atoms of one species with an atom from the other species placed in its centre. As alluded to in section 3.1.1, the asymmetry in form factors between the Rh and Fe now means that the (001) reflection is now longer forbidden for binary BCC alloys. So the presence of the (001) and (002) reflection confirms the presence of B2 order. The relative intensity of the Bragg peaks from the (001) and (002) reflections can be used to characterize the extent to which the material is ordered, denoted by the B2 order parameter, S [109].

The order parameter for a system with a fundamental reflection, f, which in this case corresponds to the (002) reflection and a superstructure reflection, s, which is the (001) reflection here is given by [109]:

$$S = \sqrt{\frac{I_s^E}{I_f^E}\frac{I_f^T}{I_s^T}}, \tag{4.3}$$

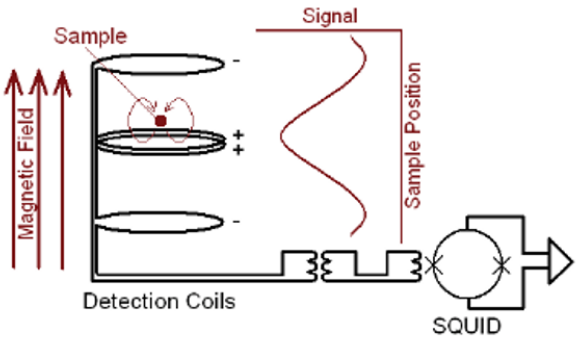

Figure 4.3: A schematic showing the measurement circuit diagram inside the Quantum Design SQUID-VSM. The stray field from the sample produces a signal in the coils through Faraday's law of induction. This signal then passes to the SQUID, which is inductively coupled to the measurement coils, and produces a measurable voltage which is used to calculate the magnetic moment of the sample. Image courtesy of Ref. [122].

where I is the intensity of the reflection, E is experimental measured value, taken to be the area under the peak, and T means that predicted from theory, which is given by [109],

$$I_{\mathrm{T}} \propto FF^{*}P\frac{1+\cos^{2}2\theta}{\sin 2\theta}, \tag{4.4}$$

with FF^{*} being the square of the total structure factor, P is the multiplicity of the diffraction plane and $(1+\cos^{2}2\theta)/\sin 2\theta$ is the Lorentz polarization factor that accounts for the unpolarized x-ray source [109]. Performing this calculation for FeRh yields the ratio $\sqrt{I_{\mathrm{s}}^{\mathrm{T}}/I_{\mathrm{f}}^{\mathrm{T}}} = 1.07$ which has been used to calculate S in FeRh using the method outlined by Warren [13, 109, 118]. The same value was adopted here for the calculations presented in this thesis.

4.2.2 Characterization of Magnetic Properties

The SQUID-VSM used in this thesis is a Quantum Design model capable of measuring the magnetic properties of the samples between 400 - 4 K in fields up to 7 T, and was used to characterize the magnetic properties of the samples. In order to achieve this, the samples are placed on a quartz paddle which is then attached to a carbon fibre rod and inserted into the sample chamber. The chamber is then pumped down from atmospheric pressures to the mTorr regime. The carbon fibre rod and the sample are

then forced to oscillate at a known frequency (14 Hz) between a series of coils. The stray field due to the magnetic moment in the sample causes the electrons within the coil to experience an electromotive force due to Faraday's law. This, in turn, causes an alternating current (AC) to flow within the coils, which can be used to calculate the magnetic moment. In this particular system a SQUID device is inductively coupled to the detection coils. A SQUID device consists of a ring of superconducting material, which has a Josephson junction on either side. There is a constant bias current passed across the loop and in the absence of magnetic field, this current is split equally between the two branches. However, when a magnetic field is present, the superconductor tries to cancel out the magnetic field by flowing a screening current around the loop. When the total current through one of the Josephson junctions exceeds the critical current, a voltage forms across the junction. The use of the SQUID here means that signals with a lower strength can be identified, increasing the sensitivity of the magnetometer so that it can measure signals down to $\approx 10^{-9}$ emu. This voltage across the Josephson junction is then picked up by a lock-in amplifier and the in phase component of the signal is then taken forward to calculate the magnetic moment. The system is calibrated against a sample of known magnetic moment before use.

4.3 Magnetic Resonance Techniques

This section describes techniques used for the FMR and SWR measurements presented in chapters 5 and 6, respectively. According to Larmor [68], the magnetization, $\mathbf{M}$, will precess around an externally applied magnetic field, $\mu_0\mathbf{H}_{\text{Ext}}$, subject to the following equation of motion,

$$\frac{d\mathbf{M}}{dt} = \gamma\mu_0(\mathbf{M} \times \mathbf{H}_{\text{Ext}}), \tag{4.5}$$

where t is the time, γ is the gyromagnetic ratio and μ_0 is the permeability of free space. Solving this equation of motion leads to the Larmor frequency, f_{L} as,

$$f_{\text{L}} = \frac{g\mu_0\mu_{\text{B}}}{h} H_{\text{Ext}}, \tag{4.6}$$

where g is the spectroscopic splitting factor, μ_{B} is the Bohr Magneton and h is Planck's constant [68].

The Larmor frequency corresponds to excitations in the radio frequency (RF) regime. If an external oscillating field is introduced into the system at the Larmor

frequency, the precession of the magnetization about the field is resonantly excited and the system acheives FMR [68]. In practice, this RF field is provided by an alternating current oscillating at RF that produces an oscillating Oersted field, $\mu_0 \mathbf{H}_{\mathrm{RF}}(t)$, within the plane of the film.

However, the externally applied magnetic field is not necessarily reflective of the field within the system and so there are extra factors to consider within this framework. As such an effective field $\mu_0 H_{\mathrm{Eff}}$, that accounts for a series of internal magnetic fields, replaces the $\mu_0 H_{\mathrm{Ext}}$ in equation 4.5 and takes the form [123],

$$\mathbf{H}_{\mathrm{Eff}} = \mathbf{H}_{\mathrm{Ext}} + \mathbf{H}_{\mathrm{RF}}(t) + \mathbf{H}_{\mathrm{K}} + \mathbf{H}_{\mathrm{Ex}} - \mathbf{H}_{\mathrm{Demag}}, \tag{4.7}$$

where $\mathbf{H}_{\mathrm{K}}$ is the magnetocrystalline anisotropy field, $\mathbf{H}_{\mathrm{Ex}}$ is the exchange field and $\mathbf{H}_{\mathrm{Demag}}$ is the demagnetization field. Here, the exchange field is considered separately to the other fields, as the exchange field gives rise to SWR whereas the other fields are responsible for FMR [123].

4.3.1 Ferromagnetic Resonance

The solution to equation 4.5 considering all but the exchange field in equation 4.7 for a thin film with the field is applied perpendicularly to the film plane gives the resonant frequency of the FMR mode, f, as [68],

$$f = \frac{g\mu_0\mu_{\mathrm{B}}}{h}\Big(H_{\mathrm{Ext}} - (M_{\mathrm{S}} - H_{\mathrm{K}})\Big), \tag{4.8}$$

where $\mu_0 M_{\mathrm{S}}$ is the saturation magnetization. $M_{\mathrm{S}} - H_{\mathrm{K}}$ is often refereed to as the effective magnetization M_{Eff} [68]. The reader is invited to read the full derivation in Ref. [68] if needed.

Intuitively, according to equation 4.5 the precession of the magnetization vector undergoes no energy loss and would continue forever without the need for any energy to be added into the system. To counteract this, Landau and Lifschitz put forward a new form of equation 4.5 which was then expanded upon by Gilbert to include a viscous damping term [124], at which point the equation became the known as the Landau-Lifschitz-Gilbert (LLG) equation. This viscous damping term takes the form of a torque that acts to align the magnetization and magnetic field vectors. The strength of this torque is characterized by the the Gilbert damping parameter, α. The LLG equation is given by [68, 124]

$$\frac{d\mathbf{M}}{dt} = \gamma(\mathbf{M} \times \mathbf{B}_{\mathrm{Eff}}) - \frac{\alpha}{M}\mathbf{M} \times \frac{d\mathbf{M}}{dt}. \tag{4.9}$$

The introduction of the Gilbert damping term here means that the magnetization will always align with the field vector after a certain time. FMR occurs when the energy injection from the RF field is equal and opposite to the energy loss through damping, as the two balance exactly and the magnetization precesses about the field with a fixed amplitude. Accounting for the Gilbert damping, the new form of the equation governing the excitation of the resonant frequency in 4.8 is [68],

$$f_0 = \frac{g\mu_0\mu_B}{h(1+\alpha^2)}\Big(H_{Ext} - (M_S - H_K)\Big). \tag{4.10}$$

4.3.2 Spin Pumping

For systems that have a FM in contact with a normal metal or antiferromagnetic (AF) material, a marked increase in damping is seen, which is attributed to a phenomena known as spin-pumping [125]. Spin-pumping is where the torque required to cause the precession of a moment about a magnetic field causes a spin-current to be emitted from it. The emission of this spin current then exerts a torque on the precessing moment causing it to align with the field faster and increasing the damping. The spin-current emitted from the FM layer then diffuses through the system and transfers angular momentum with it. In order to carry the angular momentum away from the FM layer there has to be an object into which the angular momentum can travel [125]. Such layers are known as spin-sink's and can be either a normal metal or an AF material. The spin current, $\mathbf{I}_S$, being removed from the FM to the spin-sink is given by [125],

$$\mathbf{I}_S = \frac{\hbar}{4\pi}\Big(A_R\mathbf{M}\times\frac{d\mathbf{M}}{dt} - A_I\frac{d\mathbf{M}}{dt}\Big), \tag{4.11}$$

where A_R and A_I are the interface parameters which take the form,

$$A_R = \frac{1}{2}\sum_j\Big[|r_j^{\uparrow} - r_j^{\downarrow}|^2 + |t_j^{\uparrow} - t_j^{\downarrow}|^2\Big], \tag{4.12}$$

$$A_I = \mathrm{Im}\sum_j\Big[r_j^{\uparrow}(r_j^{\downarrow})^* + t_j^{\uparrow}(t_j^{\downarrow})^*\Big], \tag{4.13}$$

where $r^{\uparrow\downarrow}$ is the coefficient of reflection at the FM-spin-sink interface for the up (down) spin electrons in the spin sink layer and $t^{\uparrow\downarrow}$ is the coefficient of transmission of the spin-up(down) electrons into the spin-sink layer from the FM. The summations here are over the number of FM-spin-sink interfaces, j [125]. It is then possible to write

$$A_R + iA_I = g^{\uparrow\downarrow} - t^{\uparrow\downarrow} \tag{4.14}$$

with $g^{\uparrow\downarrow}$ is the conductance matrix and $t^{\uparrow\downarrow}$ is the transmission matrix [125].

By conservation of angular momentum, the spin torque on the magnetization of the FM layer due to spin-pumping into the spin-sink layer leads to an additional term in the LLG equation [125]. This term then acts to renormalize the gyromagnetic ratio and the damping parameter such that [125],

$$\frac{\gamma_0}{\gamma} = 1 + \frac{g}{4\pi M_{\mathrm{T}}} \sum_{\mathrm{j}} A_{\mathrm{I}}, \tag{4.15}$$

$$\alpha = \frac{\gamma}{\gamma_0}\left[\alpha_0 + \frac{g}{4\pi M_{\mathrm{T}}} \sum_{\mathrm{j}} A_{\mathrm{R}}\right], \tag{4.16}$$

where the $_0$ subscript denotes the bulk value and M_{T} is the total magnetic moment of the FM layer [125]. Therefore, spin-pumping acts to increase the damping in the FM material.

For FM layers of thickness in excess of the spin-coherence length, which is defined as $\lambda_{\mathrm{SC}} = \pi/(k_{\uparrow} - k_{\downarrow})$, where $k_{\uparrow\downarrow}$ being the spin-up(down) Fermi wavevectors, the electrons scattered from one FM-spin-sink interface interfere incoherently at the other [125]. In this case, $t^{\uparrow\downarrow}$ vanishes and the mixing conductance is solely dependent on the reflection coefficients at each interface [125]. λ_{SC} is on the order of a few monolayers for transition metal magnets [125]. It has been seen that the $A_{\mathrm{I}} = \mathrm{Im}[g^{\uparrow\downarrow}]$ vanishes for both ballistic and diffusive contacts [125]. This means that no change in γ is expected but one would still expect the damping to increase, which can be described by an increase in α due to spin-pumping, α_{Pump}, via

$$\alpha = \alpha_0 + \frac{g_{\mathrm{L}}}{4\pi M_{\mathrm{T}}} \sum_{\mathrm{Interfaces}} A_{\mathrm{R}} = \alpha_0 + \alpha_{\mathrm{Pump}}. \tag{4.17}$$

4.3.3 Spin-Wave Resonance

The exchange field adds another torque in the same vein as the other fields seen in equation 4.7. In systems with magnetic discontinuities, the spins close to these sites will experience a different exchange field compared to those in the bulk of the material due to the different symmetries [123]. These discontinuities can present themselves at either surface of the film and add an extra anisotropy term that pins the spins [67, 68]. These pinned spins at either interface then act as nodes that define a standing wave upon excitation, whose length scale is defined by the film thickness [67, 68]. Inputting energy into the system via the oscillating RF field allows for the excitation of standing

spin-waves across the film thickness. Here, the twisting of adjacent spins gives access to the exchange stiffness A within the system. The energy of these spin-waves are subsequently defined by A and the film thickness, t. The new form of the resonant frequency of which depends on the number of antinodes across the film thickness or the mode number n, f_{n}, for the field applied perpendicularly to the film plane is given by [68],

$$f_{\mathrm{n}} = \frac{g\mu_0\mu_{\mathrm{B}}}{h(1+\alpha^2)}\Big(H_{\mathrm{Ext}} - (M_{\mathrm{S}} - H_{\mathrm{K}})\Big) + \frac{2Ag\mu_B}{hM_{\mathrm{S}}}\left(\frac{n\pi}{t}\right)^2, \tag{4.18}$$

where a is the lattice constant. The first term on the right hand side here is the frequency associated with FMR and the second is the extra energy associated with the excitation of the spin-wave. Please see Ref. [123] for a thorough derivation.

4.3.4 Experimental Set Up

A schematic of the apparatus used in both experiments is shown in Fig. 4.4. For these measurements the sample was placed face down on a Au Ground-Signal-Ground (GSG) geometry coplanar waveguide that had been patterned onto a thermally oxidised Si substrate. The sample is held in place using a polymer glue which is left to dry before use. The waveguide substrate is then attached to the heating plate in the centre of the magnet. The temperature of the heating plate was controlled using a voltage power supply. The temperatures available in this experiment ranged between 290 and 338 K and were limited by the application of the RF probes, which act as a heat sink. These probes were removed when heating past these temperatures to reset the sample. The applied magnetic field is measured using a Hall probe placed on the bottom magnet piece.

Measurements of the temperature were made by at a series of different voltages by placing a thermocouple as close to the sample as possible whilst the RF probes are in place. Difficulties in mounting the thermocouple to the waveguide substrate meant it was not possible to keep the thermocouple close to the sample during a measurement. Therefore, the temperature measurements were performed separately to any FMR/SWR measurement and the measured temperature was assigned to an output voltage on the heater. Where necessary, if measurements of the temperature were not taken for a given voltage, the temperature is interpolated from the existing measurements.

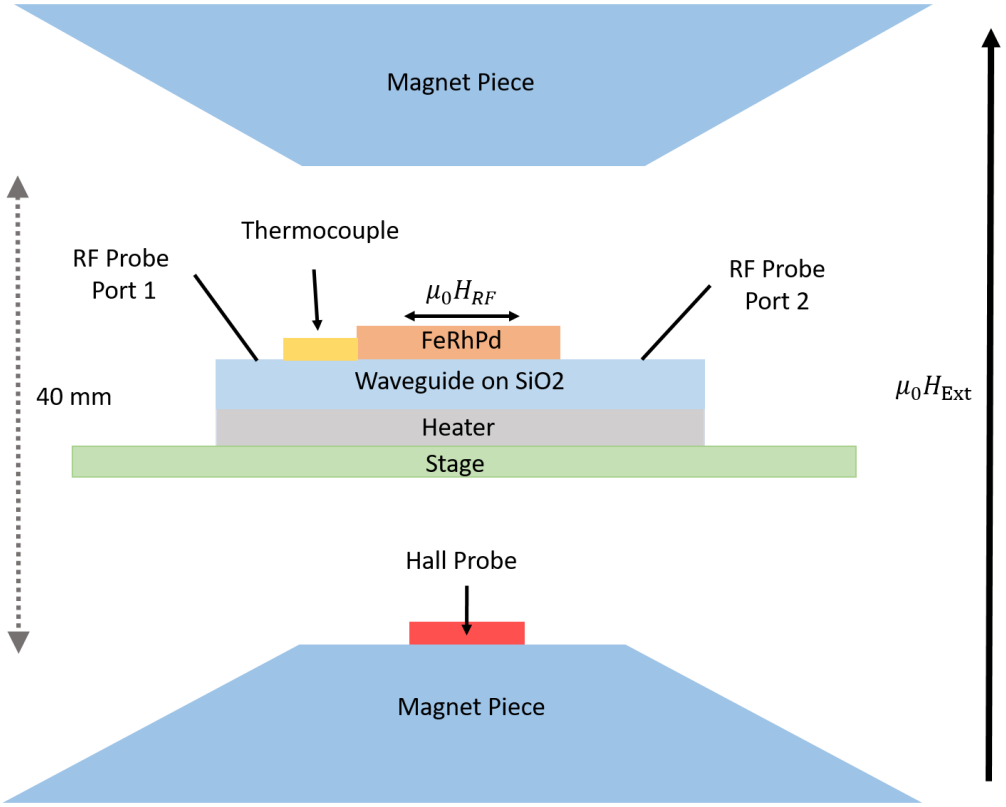

Figure 4.4: Schematic of the FMR/SWR apparatus. The externally applied magnetic field $\mu_0 H_{\mathrm{Ext}}$, is applied perpendicularly to the film surface with the RF field from the AC current, $\mu_0 H_{\mathrm{RF}}$, sitting within the film plane. A heater is used to control the temperature. A full description of the set up is included in section 4.3.4.

Once all of the apparatus has been properly configured, the GSG probes are lowered onto the ports either side of the sample so that the probes are in contact with the signal lines. The probes are attached to a vector network analyser (VNA) that is configured to pass an AC current at a defined frequency through the 35μm wide central stripline of the waveguide and measures the transmission of the signal through the sample, either from port 1 to port 2, S_{21} or *vice versa*, S_{12}. The VNA is set to sweep the frequency of the alternating current between 0.01 and 26 GHz at this stage with 0.01 GHz spacing between points. Once the sample is in position, the external magnet is moved into

position and the sample is heated to the desired temperature.

Once at the desired temperature, the temperature is left to equilibrate and the probe-waveguide arrangement is adjusted to ensure the correct alignment. A measurement of S is then taken across the frequency range with no external field applied. This measurement and each measurement henceforth is an average of 10 sweeps of the frequency at a given field, which is performed in order to improve the signal to noise ratio. The current amplitude used in these experiments is constant throughout each measurement and is 10 dBm. Then the field is changed to the desired field, which is orientated perpendicularly to the film surface as shown in Fig. 4.4, and another measurement is taken. The measurements were then processed to extract the magnitude of the difference between the background $S(\mu_0 H_{\text{Ext}} = 0T)$ and the measurement $S(\mu_0 H_{\text{Ext}})$ such that

$$I(\mu_0 H_{\text{Ext}}) = S(\mu_0 H_{\text{Ext}}) - S(\mu_0 H_{\text{Ext}} = 0T). \tag{4.19}$$

At a given temperature, measurements are taken at a series of field strengths betwen $\mu_0 H_{\text{Ext}} = 1.4 - 2$ T, with 50 mT between field values. These measurement sets are taken at a series of different temperatures on both the heating and cooling branch of the transition. The transition temperature in FeRh is sensitive to the application of external magnetic field [23]. Therefore, the field is held constant whilst the frequency is swept to identify the resonant frequency.

For the FMR measurements, the measurement sets are used to extract values of quantities that are associated with the temperature at which the measurements were taken. However, in the SWR experiments, each of the measurements taken at a given field and temperature corresponds to a separate point within the transition and each point is used separately.

4.4 Soft X-Ray Methods

All of the measurements presented in chapters 7 and 8 were taken at the I10 beamline of Diamond Light Source, a schematic of which is shown in Fig. 4.5. Here, there are two undulators that allow for the control of the helicity and polarization of the light. The operational energy range of this beamline is concentrated around 0.4 - 2 keV where the 3d and 4f transition metal edges are situated, which allows for maximum contrast for dichroism experiments involving transition metal magnets. The two undulators

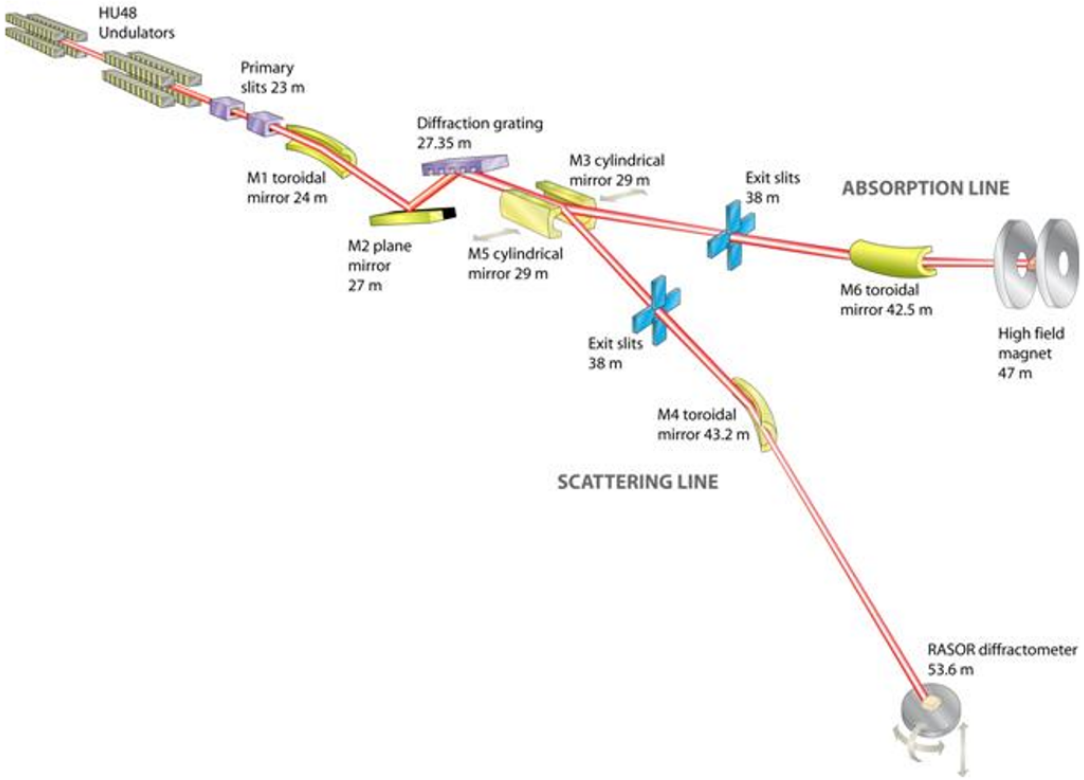

Figure 4.5: Optical configuration of the I10 Beamline at and Diamond Light Source. The RASOR diffractometer endstation is used for the experiments presented in this thesis. Image taken from Ref. [126].

give full control over the polarization of the light and can operate with right and left circularly or vertically and horizontally polarized light suitable for both XMCD and XMLD investigations. The undulator produces a polarized beam that travels through a series of slits that define the beam profile. The subsequent sequence of mirrors then refine the beam profile, focusing it in the horizontal direction and collimating in the vertical direction. The monochromator diffraction grating is used to select the beam energy.

The beam is then split by the two cylindrical mirrors into the two endstations present at the I10 beamline. The beamline used in this thesis is that of the Reflectivity and Advanced Scattering from Ordered Regimes (RASOR) diffractometer endstation. On this particular line, there is a set of exit slits that can define the profile of the beam to be 20×200 μm^2, which is then refocused by the second torodial mirror and

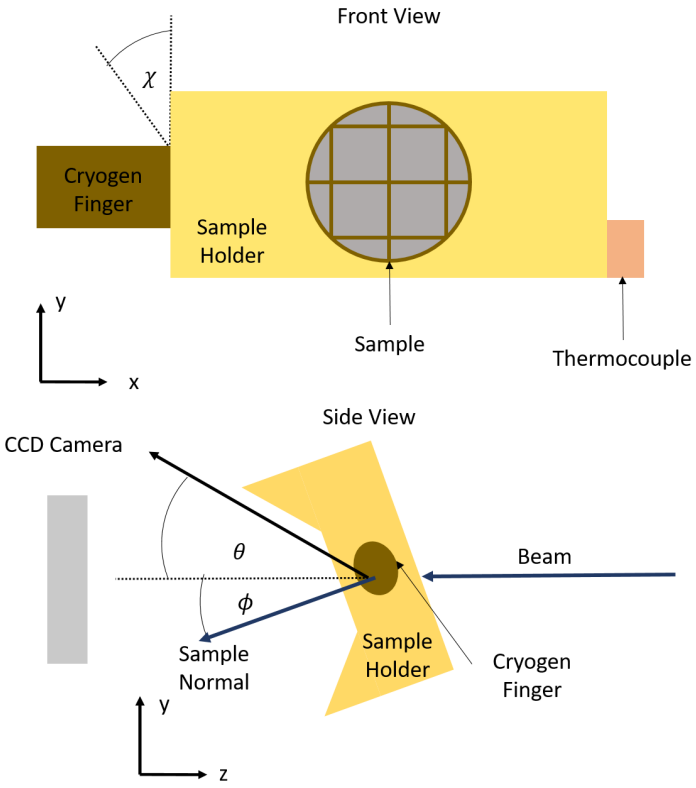

Figure 4.6: Configuration of the sample environment from the front and side view, a thorough description of the sample environment is included in the text.

reimaged at the sample position in the diffractometer.

A schematic of the sample environment from the front and the side of the sample holder is shown in Fig. 4.6. The sample is mounted upon a holder that sits on the end of an arm attached to a cryogenic cold finger that can achieve temperatures between 15 - 450 K. A thermocouple is attached to the sample holder to measure the temperature at the sample position. The position of the sample relative to the centre of the diffractometer is described by the coordinate system (x, y, z). It is also possible to rotate the sample holder through 2 different angles: χ which describes the angle between the surface of the cold finger and the attached surface of the sample holder and ϕ which describes the angle between the sample normal and the beam. The detector can be mounted either to a stage which allows for rotation through θ or to the end of the sample chamber at defined angles.

The detectors available here are a Si photodiode 'point' detector, which is used to align the beam, and a 2D charged coupled device (CCD) camera made up of 2048 × 2048 pixels, which is used for the imaging of the speckle pattern seen in chapters 7 and 8. The camera is mounted on the end of the RASOR chamber approximately 0.8 m from the sample at $\theta = 0$. As this is in the direct path of the beam, a beamstop is placed on the flange between the diffractometer chamber and the camera itself to prevent damage to the detector from the intense straight through beam

In these investigations images are taken at the Fe L_3 edge, which enhances the scattering intensity through resonant magnetic scattering as set out in section 3.2.3. The determination of the L_3 edge is included in chapter 7. For this particular system, the charge and magnetic scattering occur in different places in reciprocal space as they are determined by different length scales [74, 82], this is also confirmed by looking at the resonant and non-resonant scattering profiles in chapter 7. Magnetic domains in FeRh are believed to be between $200 - 1000$ nm in size [27, 31–35] which means the resultant scattering profiles are confined to a narrow Q range concentrated around the central region. In order to access this region the experiment must take place within the transmission regime with the beam passing straight through the sample.

In order to transfer the angular momentum of the incoming x-ray to the photo-excited electron required for the XMCD investigations, a component of the magnetization must lie within the photon momentum direction. So, as the magnetization points within the plane of the film and the angular momentum of the photon is perpendicular to it in this arrangement, the sample is tilted by 26° to project a component of the magnetization into the beam path for the XMCD measurements. This allows for the angular momentum transfer required for the RMSAXS. This angle is the largest available that allows the beam to pass through the sample holder unhindered. This is not the case for XMLD and the sample normal is held at 0° to the beam direction in these experiments.

The generation of a speckle pattern requires an x-ray beam that is coherent in both time and space in all dimensions probed here. The reader is invited to refer to the characterization of the coherence of this particular beamline which was performed by S. Morley [115]. For the purposes of this thesis, coherence is achieved by moving a pinhole 20 μm in diameter into the beam path. The presence of the coherence is evident in the emergence of the speckle pattern seen in the images in chapter 7 and 8.

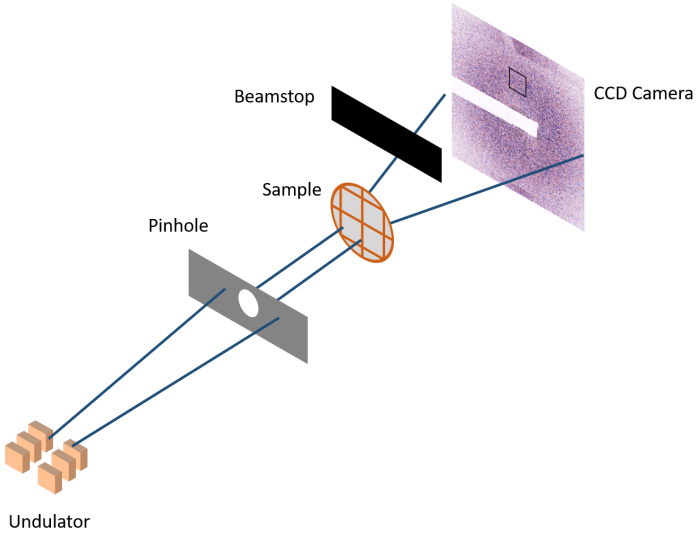

Figure 4.7: XPCS experimental configuration. Polarized light from the undulator is passed through a 20 μm pinhole close to the sample to ensure the light is coherent before reaching the sample. The CCD camera is then used to take an image of the resultant speckle pattern. A beamstop is placed between the sample and the CCD detector to prevent damage from the intense straight through beam. The black box on the image is used to demonstrate an example region of the image that is taken forward for correlation analysis.

4.4.1 X-Ray Photon Correlated Spectroscopy

Described here is the technique used to measure the dynamic behaviour through the transition presented in chapter 8. These measurements were taken as a series of images, each of which consisted of 200 single images. Consecutive images in these series were taken with opposing helicities or orientations. Each image uses an exposure time that is dependent on the strength of the signal and ranged from 0.5 to 2 s. The read out time of the CCD is then approximately 4 s, so each image takes about 6 s in total. In order to improve the signal-noise ratio of the images, the images series where it was possible to change helicities have consecutive images subtracted from each other using the method outlined by Fischer in equation 3.34 in post-processing to form a final image series with 100 images [73]. Moving the undulator means that the time difference between two images of the same helicity is around 54 s between images for XMCD measurements

and 68 s for XMLD. This time difference is taken as the spacing between images. This method is adopted for images taken using both linearly and circularly polarized light, to access XMLD and XMCD respectively and were taken at various temperatures through the transition. Between measurements at a given temperature, the sample is thermally cycled to reset the magnetic state. All measurements were taken in the absence of an external magnetic field.

It is also important to note here that some of the measurements included in the experiments presented in chapters 7 and 8 were performed after the undulator had failed and it was no longer possible to move the magnet arrays. This meant it was no longer possible to vary the helicity between images and only a single helicity is used. These image series consist of between 400-900 single images, with are separated by between 6 - 9 seconds. The information gained from these experiments is the same as that obtained using images of two helicities, but the signal is much smaller. Analysis of these measurements gives similar values to those performed on the images using both helicities and so are included here for completeness. Both give similar values for the parameters characterising the relaxation behaviour and so are included in the analysis.

The first image of each temporal correlation series was taken to calculate the length scales involved in the magnetic scattering, the results of which are presented in chapter 7. For this analysis the radial average of the image is taken to form an intensity curve, which is fitted to a log-normal profile to extract the length scales associated with the peak. In order to calculate the dynamic behaviour the whole image series is then auto-correlated against each other. This is a technique known as X-Ray Photon Correlation Spectroscopy (XPCS) and is a powerful tool for extracting the dynamics of systems [81]. XPCS tracks the temporal correlation of the speckle pattern, which, for magnetic systems is the Fourier transform of the domain structure that creates it [81, 82]. Therefore, any changes in the domain structure are reflected in the speckle pattern in real time.

In order to calculate the temporal correlation behaviour, it is necessary to crop the image due to memory limitations. Each image is cropped into a 200 $\times$ 200 box centered around the position of Q associated with the peak in the radial intensity profile, examples of which can be seen in Fig. 4.8. The correlation between two images is calculated using the g_2 function introduced in the previous chapter. However, before we proceed to the discussion regarding this calculation it is necessary to define the two

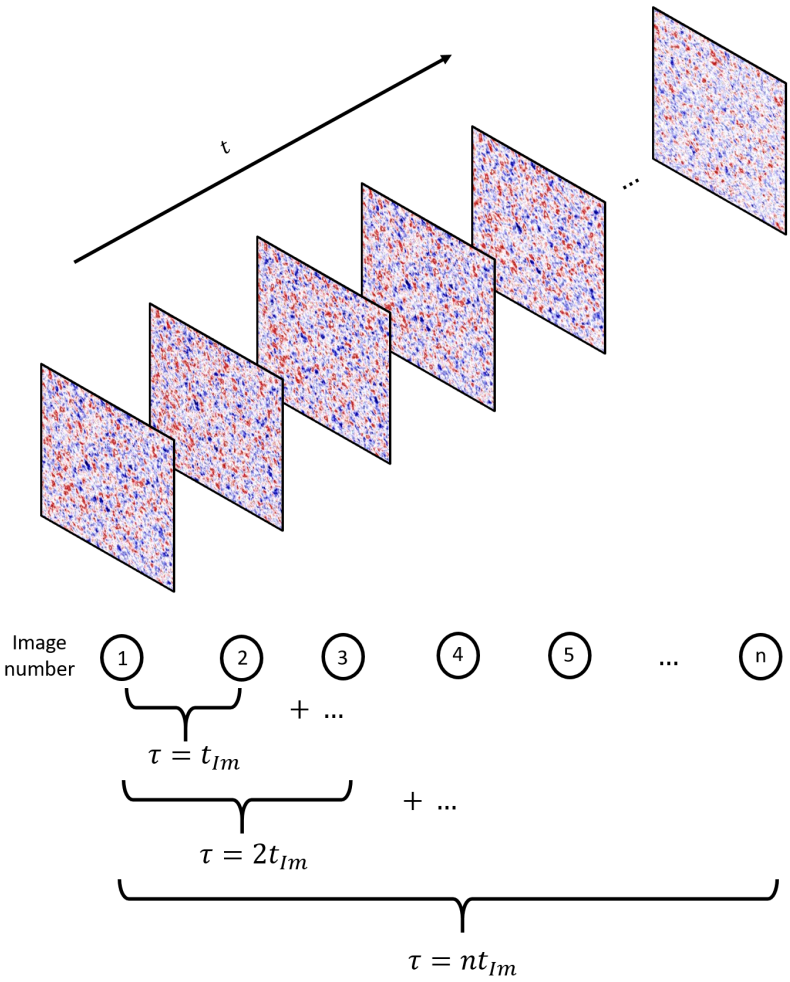

Figure 4.8: Correlation behaviour calculation schematic. An example image series that is used in the calculation of the correlation behaviour. The schematic of how the delay between images, τ, evolves through the measurement is shown beneath the image series. The measurement time t is seen at the top of the images and increases through the measurement time. After completing the calculation of the g_2 function for $\tau = t_{\mathrm{Im}}$ where t_{Im} is the time difference between images, τ is then increased by to $2t_{\mathrm{Im}}$ and the process is repeated. This continues until the correlation behaviour for images separated by $\tau = nt_{\mathrm{Im}}$, where n is the number of images is calculated.

times used in this experiment. These are the time since the measurement began, t and the time delay between images τ. The g_2 is defined in the previous chapter as,

$$g_2(\mathbf{Q},\tau) = \frac{\langle I(\mathbf{Q},t)I(\mathbf{Q},t+\tau)\rangle_t}{\langle I(\mathbf{Q},t)\rangle_t^2} \tag{4.20}$$

where $I(\mathbf{Q},t)$ is the intensity at position $\mathbf{Q}$ at time t and $\langle ...\rangle_t$ denotes a time average. The presence of $\mathbf{Q}$ here is used to separate g_2 functions for different pixels, i.e. different points in $\mathbf{Q}$ within the image, as these may differ. The g_2 functions are calculated for each pixel in the image, by multiplying the intensity for the each pixel of one image taken at time t with the corresponding pixel in the image taken at $t+\tau$. This process is repeated until this quantity is extracted for a given value of $\mathbf{Q}$ for all images that are separated by the time τ. The time average of this quantity is then taken and divided by the time average of square of the intensity for that given pixel and assigned as $g_2(\mathbf{Q},\tau)$. This calculation is repeated for images separated by all of the different values of τ in the experiment, which is taken to be integer values of the time between images t_{Im} in this experiment, such that $\tau = t_{\mathrm{Im}}, 2t_{\mathrm{Im}}, +... + nt_{\mathrm{Im}}$ where n is the total number of images. Once the g_2 function has been calculated for all values of $\mathbf{Q}$ within the image, the $\mathbf{Q}$ dependence is removed by averaging the g_2 functions over the entire image. Example images along with how t and τ evolve are seen in Fig. 4.8. Examples of the resultant g_2 functions are included in Fig. 8.2.

4.5 Computer Simulations of Atomistic Spin Dynamics

Chapter 6 presents the results of computer simulations of atomistic spin dynamics. These simulations are included to aid in the understanding of the results of the FMR and SWR experiments, which are presented in chapters 5 and 6 respectively. They provide a solid theoretical basis against which possible interpretations of the experimental data can be tested. For these simulations the candidate was involved in discussion regarding their scientific direction, however all of the simulations were performed by M. Strungaru of the University of York using the VAMPIRE software [127]. Analysis of the lengthscales presented in chapter 6 was performed by the candidate.

Previously, it has been shown that the competition between bilinear and four-spin exchange interactions present in FeRh can be used to explain the metamagnetic transition [128]. Bilinear exchange is used to model the nearest and next-nearest neighbour exchange interactions present between the Fe atoms. The presence of the Rh moment

complicates matters and makes the system difficult to model. In this particular case however, it is possible to model the set of intricate interactions brought on by the presence of the Rh moment using the interactions between quartets of Fe atoms, which is known as the four-spin interaction. This four-spin model is an extension of the biquadratic spin Hamiltonian that lifts the degeneracy of the biquadratic interpretation for the AF and FM regimes [128]. The four-spin interactions are responsible for the AF order at low temperature and break down with temperature quicker than the FM bilinear exchange. This shift in the dominant interaction with temperature is responsible for the metamagnetic transition [128].

The Hamiltonian used in these simulations includes the nearest and next-nearest neighbour interactions, the four-spin interactions, both the externally applied and oscillating RF field, as well as the uniaxial anisotropy, such that:

$$\begin{aligned}\mathcal{H} &= -\frac{1}{2}\sum_{i,j} J_{ij}\,(\mathbf{S}_i \cdot \mathbf{S}_j\,) \\ &\quad -\frac{1}{3}\sum_{i,j,k,l} D_{ijkl}\,(\mathbf{S}_i \cdot \mathbf{S}_j\,)(\mathbf{S}_k \cdot \mathbf{S}_l\,) \\ &\quad -\sum_i (\mu_0 \mu_{\mathrm{Fe}} \mathbf{S}_i \cdot [\mathbf{H}_{\mathrm{Ext}} + \mathbf{H}_{\mathrm{RF}}]) - K_{\mathrm{U}} \sum_i (\mathbf{S}_i \cdot \hat{\mathbf{e}})^2, \end{aligned} \tag{4.21}$$

where $\mathbf{S}_{\mathrm{i}}$ is the spin-vector at each site in the system, J_{ij} and D_{ijkl} represent the bilinear and four-spin exchange interactions between Fe atomic sites, K_{U} represents the uniaxial anisotropy constant, the value of which was taken from Ostler *et al.* [18], μ_{Fe} is the moment of the Fe spin and $\hat{\mathbf{e}}$ representing the easy axis direction.

To calculate the static and dynamic properties of the system for finite temperatures the LL equation with Langevin dynamics is solved for each individual spin as per reference [127, 128],

$$\frac{\partial \mathbf{S}_{\mathrm{i}}}{\partial t} = -\frac{\gamma}{1+\alpha^2}(\mathbf{S}_{\mathrm{i}} \times \mathbf{H}_{\mathrm{i}} + \alpha \mathbf{S}_{\mathrm{i}} \times (\mathbf{S}_{\mathrm{i}} \times \mathbf{H}_{\mathrm{i}})), \tag{4.22}$$

with the effective magnetic field on each lattice site being described by

$$\mathbf{H}_{\mathrm{i}} = -\frac{1}{\mu_{\mathrm{Fe}}}\frac{\partial \mathcal{H}}{\partial \mathbf{S}_{\mathrm{i}}} + \xi_{\mathrm{i}} \tag{4.23}$$

where ξ is a stochastic field-like term representing on-site thermal fluctuations [127, 128]. The effect of temperature is included in these micromagnetic simulations by including these thermal fluctuations, which can represented in the white noise limit by

[127, 128],

$$\xi_{\mathrm{i}} = \mathbf{\Gamma}(t)\sqrt{\frac{2\alpha k_{\mathrm{B}}T}{\gamma\mu_{\mathrm{Fe}}\Delta t}}, \tag{4.24}$$

where $\mathbf{\Gamma}$ represents the thermal fluctuations given by a Gaussian distribution in three dimensions with a mean of zero, k_{B} is the Boltzmann constant, T is the system temperature and Δt is the integration time step. The larger the temperature, the larger the width of the Gaussian white noise distribution increases which gives stronger thermal fluctuations [127, 128]. The parameters used in the simulations are presented in table 6.1.

Chapter 5

Ferromagnetic Resonance Investigations in the Mixed Magnetic Phase

5.1 Introduction

Measuring the exchange coupling between the two magnetic phases in FeRh remains a controversial subject [55, 56, 63]. The studies presented in the literature that create this controversy are based on ferromagnetic resonance (FMR) investigations when entering the mixed magnetic phase (MMP) [55, 56, 63]. These studies see a developing magnetocrystalline anisotropy (MCA) field as regions of antiferromagnetic (AF) material are introduced into the system when cooling from the fully ferromagnetic (FM) state [55, 56, 63]. The physical origin of this field has been attributed to exchange coupling [55], magnetoelastic (ME) effects [56] as well as general phase coexistence [63]. The study in which it is claimed that this anisotropy field is due to exchange coupling fail to provide a solid theoretical or experimental basis for this observation [55], whilst the study in which ME is claimed to be responsible provides an estimate of the field strength which fails to fully account for the size of the MCA field [56]. The origin of this MCA seen when entering the MMP remains unknown. What is clear is that there is a drastic change in the high frequency behaviour of the FeRh system when entering the MMP from the fully FM phase.

This chapter will present FMR investigations through a limited temperature range of the metamagnetic phase transition where phase coexistence occurs. The behaviour of the spectroscopic splitting factor, g, implies that a contribution from the AF layer is present, which indicates that a non-zero magnetic moment is present in this region. This moment is believed to be a consequence of an exchange coupling across the magnetic phase boundary (MPB). The MCA field is measured to be consistent within error bar through the measurement range and can be mostly accounted for by the ME effects at the substrate and at the MPB. The behaviour of both g and the Gilbert damping parameter, α, is consistent with a thickness dependent phase transition (TDPT) that takes place in the AF layer.

Work attributed to the author are the growth and characterization of the Pd-doped FeRh sample for its structural and magnetic properties, as well the FMR experiments for the Pd-doped FeRh, which were performed on secondment at RIKEN. K. Matsumoto assisted with the set-up of the apparatus and is responsible for the growth and FMR characterization of the Py sample, as well as the thickness analysis of the FeRh sample, the measurement of which was performed by T. Higo. All data analysis of the FMR experiments were performed by the candidate.

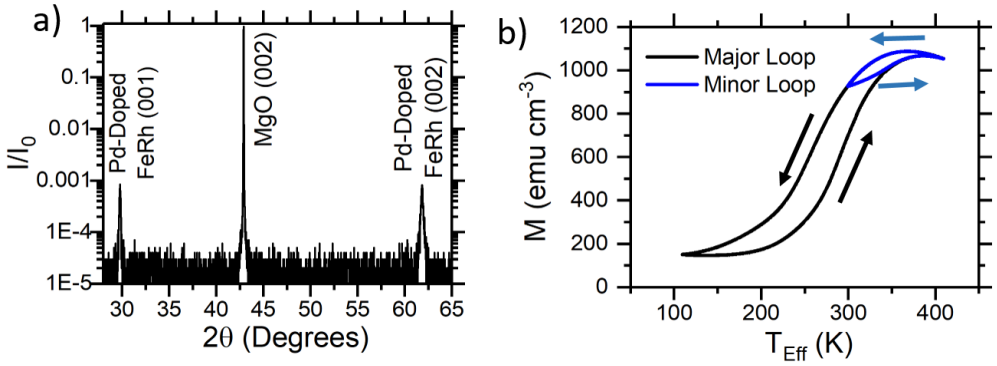

Figure 5.1: Sample characterization results. Panel (a) shows the XRD spectrum labelled with the corresponding peaks for Pd-doped FeRh. The presence of the two peaks demonstrates B2 order with an order parameter of $S = 0.76 \pm 0.02$. Panel (b) shows the temperature dependent magnetization behaviour measured using the SQUID-VSM, with a 1 T field applied in the film plane. The temperature here has been corrected for the use of the field using equation 5.1. The black curve shows a measurement over the temperature range where the transition finishes in both directions and is named the major loop. Whilst the blue curve shows the magnetization behaviour through the temperature range available in the experiment and is known as the minor loop. The arrows are used here to demonstrate the temperature sweep direction.

5.1.1 Sample Growth and Characterization

The sample used in this experiment is a Pd-doped FeRh epilayer grown using DC magnetron sputtering on a MgO substrate. The Pd doping was used here to move the transition temperature so that the transition straddled the available temperature range. The substrate was annealed overnight at 700°C with the Pd-doped FeRh layer deposited at 600°C from a $Fe_{0.47}Rh_{0.5}Pd_{0.03}$ target. The sample was then annealed *in situ* at 700°C for 1 hour. After removal from the sputtering chamber the sample was characterized for its thickness using X-Ray Reflectivity (XRR), its structural properties using X-Ray Diffraction (XRD), and its magnetic properties using the SQUID-VSM.

Characterization results for the sample used in this experiment are shown in Fig. 5.1. These include the XRD scan in Fig. 5.1(a) which clearly shows the presence of two peaks either side of the central substrate peak, including a peak for the (001) reflection,

which is forbidden for BCC structures of a single atomic species. This is indicative of an epitaxial growth with the presence of B2 order, with an order parameter, $S = 0.76 \pm 0.02$ and an average room temperature lattice constant across both peaks of $a = 2.998 \pm 0.001$ Å. The XRR scan that yields a thickness of $t = 134 \pm 4$ nm is included in Fig. 4.2.

The temperature dependent magnetization behaviour is presented in Fig. 5.1(b). The scan in which the transition is completed in both directions is included as the major loop shown by the black curve. As there was no active cooling apparatus available during the FMR experiment, it was not possible to cool below room temperature. Therefore, to get a more accurate description of the behaviour seen in the experiment a loop around the available temperature range (290 - 400 K) was also performed and is shown by the blue line. Both of the major and minor magnetic loops seen in Fig. 5.1(b) were performed in a 1 T field applied within the film plane and have been corrected for the influence of the diamagnetic MgO substrate. The saturation magnetization for this sample is $M_S = 1090 \pm 40$ emu cm^{-3}, which corresponds to $\mu_0 M_S = 1.37 \pm 0.05$ T.

In this experiment the effective temperature, T_{Eff}, is used as a proxy for the position within the transition. T_{Eff} is used to account for the change in the transition temperature due to the application of external field and gives the temperature where the same magnetization is expected in the absence of external magnetic field, as the measurement taken when field is applied. The formula used to calculate it is given by

$$T_{\mathrm{Eff}} = T_0 - \frac{dT_{\mathrm{T}}}{d(\mu_0 H_{\mathrm{Ext}})} \mu_0 H_{\mathrm{Ext}}, \tag{5.1}$$

where T_0 is the true sample temperature and T_{T} is the transition midpoint. For this sample, the value of $dT_{\mathrm{T}}/d(\mu_0 H_{\mathrm{Ext}}) = -9.6 \pm 0.9$ KT^{-1} when cooling and $dT_{\mathrm{T}}/d(\mu_0 H_{\mathrm{Ext}}) = -9.3 \pm 0.5$ KT^{-1} when heating. This was measured by fitting a Gaussian to dM/dT to identify the midpoint for a series of fields and then fitting to find the general trend [23]. The dM/dT measurements were performed with the field situated perpendicularly to the film surface to most accurately reflect the behaviour of the sample in the FMR geometry. The sample holder used for these measurements has a series of quartz beads either side of the sample. These beads contribute to the measured signal which means that the value of the moment measured using this sample holder is far higher than the value obtained for the holder where the external field is oriented in the sample plane. However, the increase in signal for the out-of-plane holder compared to the in-plane holder is temperature independent and so the behaviour of dM/dT is valid. As this spurious signal is not expected for measurements performed using the in-plane holder,

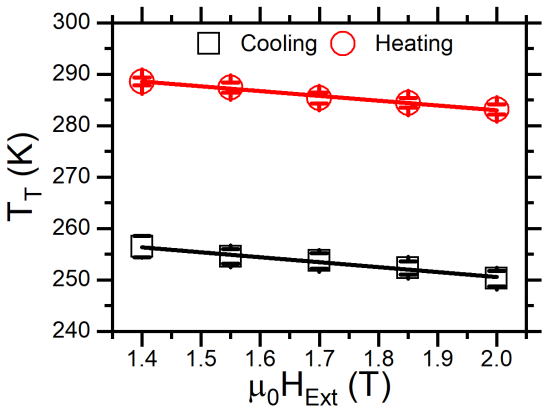

Figure 5.2: Measurements of $dT_{\mathrm{T}}/d(\mu_0 H_{\mathrm{Ext}})$. The position of the transition midpoint, T_{T}, which was extracted by fitting a Gaussian profile to the dM/dT, is shown here plotted against the external field in which the measurement was taken for measurements taken when heating (red) and cooling (black). These are fitted to a straight line to extract the value of $dT_{\mathrm{T}}/d(\mu_0 H_{\mathrm{Ext}}) = -9.6 \pm 0.9$ KT^{-1} when cooling and $dT_{\mathrm{T}}/d(\mu_0 H_{\mathrm{Ext}}) = -9.3 \pm 0.5$ KT^{-1} when heating.

the values of M used in this experiment are all taken from the in plane measurements. The position of the T_{T} extracted by fitting a Gaussian to the dM/dT profiles for various fields are shown in Fig. 5.2.

5.1.2 Experimental Set Up

The experimental set up is described in detail in section 4.3.4. FMR measurements were taken at a series of temperatures on both the heating and cooling branches of the transition. In these experiments, the Pd-doped FeRh layer is placed face down on a coplanar waveguide. An RF current is applied down the central line of the waveguide and the transmission of the current through the sample is measured using a Vector Network Analyser. This RF current produces a small magnetic field that oscillates at the frequency of the RF current, and which lies in the sample plane. For each measurement the static DC external magnetic field, $\mu_0 H_{\mathrm{Ext}}$, is applied perpendicularly to the film surface and the frequency of the RF current is swept between 0.01 - 26 GHz. When the frequency of the RF current is equal to the FMR frequency of the system, which is determined by $\mu_0 H_{\mathrm{Ext}}$, the signal will be absorbed which allows for the identification of

the resonant frequency. Frequency-swept FMR is used here as the inherent sensitivity of the transition temperature to the application of external field would make field-swept difficult to interpret [23]. This process is repeated for fields between $\mu_0 H_{\mathrm{Ext}} =$ 1.4 - 2 T in 50 mT steps at a given temperature. The temperature of the system is then changed and the process is repeated, giving a set of resonant frequencies for different external magnetic field strengths for each temperature. These sets of measurements are then fitted to equation 5.2 to extract the effective magnetization $\mu_0 M_{\mathrm{Eff}} = \mu_0(M_{\mathrm{S}} - H_{\mathrm{K}})$, where $\mu_0 H_{\mathrm{K}}$ is the MCA field, and the spectroscopic splitting factor, g, for a given measurement set.

Here, it is important to note that the touching down of the RF probes reduced the maximum possible effective temperature of the system to $\approx$ 360 K, as it is believed that the RF probes act as a heat sink. This corresponds to the largest measured temperature of $T_0 \approx$ 338 K. On heating, the temperature was varied with these probes on. These probes were then removed to reset the system by heating it into the fully FM state and replaced when cooling. The system was left to thermally equilibrate for around 10 minutes after the probes had been replaced before proceeding with the measurements.

5.2 FMR Measurements

This chapter will focus on the development of the spectroscopic splitting factor, g, the MCA field, $\mu_0 H_{\mathrm{K}}$, and the Gilbert Damping parameter, α, through the transition. The equation governing the resonant frequency, f, of the FMR and its dependence on g and $\mu_0 H_{\mathrm{K}}$ for FMR experiments with the external field applied perpendicularly to the film-plane in the low damping limit is given by [68],

$$f = \frac{g\mu_{\mathrm{B}}\mu_0}{h}\Big(H_{\mathrm{Ext}} - M_{\mathrm{Eff}}\Big), \tag{5.2}$$

where μ_{B} is the Bohr Magneton and h is Planck's constant.

5.2.1 Initial Characterization

An example measurement series taken at $T_0 = 312.6$ K on the heating branch is shown in Fig. 5.3(a). In this figure $I(\mu_0 H_{\mathrm{Ext}}) = S_{\mathrm{ij}}(\mu_0 H_{\mathrm{Ext}}) - S_{\mathrm{ij}}(\mu_0 H_{\mathrm{Ext}} = 0\ T)$, where ij are the ports on the VNA and S_{ij} is the magnitude of the signal which comprises of both real and imaginary parts. The spectra seen in Fig. 5.3(a) are noisy and there

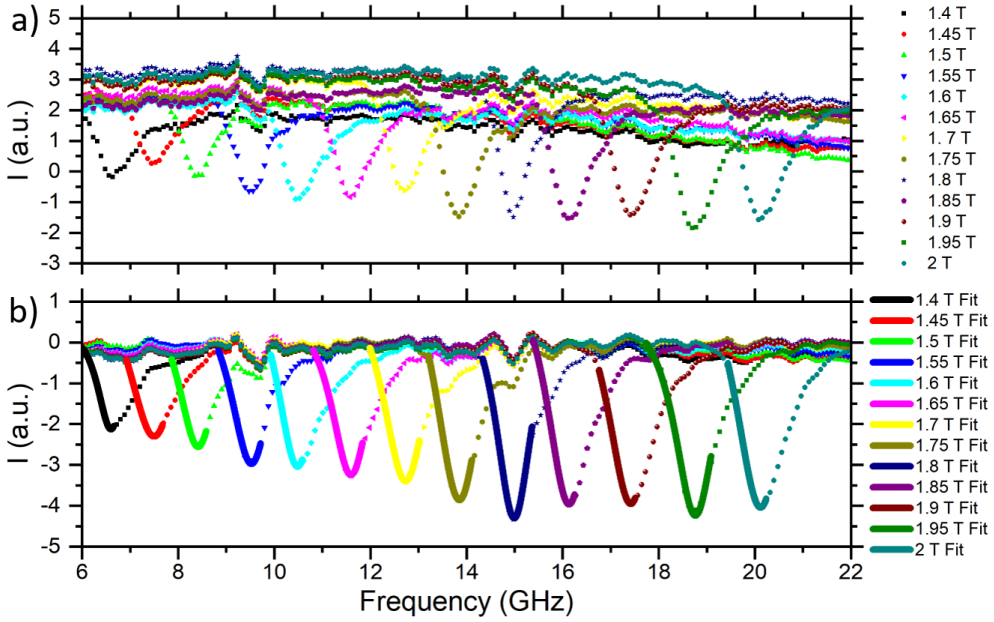

Figure 5.3: Example of a FMR measurement at $T_0 = 312.6$ K on the heating arm. Panel (a) shows the raw data taken for a range of different fields and clearly demonstrates the large peak associated with the excitation of FMR for each field. Panel (b) shows the same data set after having been smoothed and having had the background removed. The solid lines shown here show fits of Lorentzian profiles to the data to extract the resonant frequency for FMR, f, and the linewidth, Δf.

is a curved background present that varies with the field. The background is fitted for each spectra using the asymmetric least squares fitting algorithm in the Origin software after the data has been smoothed and is then subsequently removed from the spectra. Processing the data in this way produces a series of spectra such as those seen in Fig. 5.3(b), that clearly demonstrate the peaks that track along with the field as expected for FMR excitations.

Fig.5.3(b) also shows examples of Lorentzian fits to the data, which are used to extract f and Δf. It is clear from this figure that the fits only encompass the left hand side of each of the peaks. At this juncture it is important to note that excitations of perpendicular standing spin-waves (PSSWs) were also seen in these investigations, examples of which can be seen in Fig. 5.5 and Fig. 6.2. The study of these peaks will be

the focus of the next chapter. These PSSW peaks appear on the right hand side of the FMR peak [68]. These PSSW excitations may be hidden by the large resonance peak associated with the FMR mode excitation and would not be clearly visible within the spectra, however they may influence the width and position of the peak if included in the fit. To avoid the influence of these PSSW excitations the FMR modes are fitted to the left-hand side of the peak only, as this minimizes the influence of the PSSW excitations. Performing the analysis in this way still only leads to small errors associated with the quantities extracted from the fit. The candidate here also acknowledges that there may be other contributions to the damping that may result in an asymmetric peak profile, however these will be indistinguishable from the influence of the PSSW excitations and are not considered here.

Also, from Fig. 5.3(b) it is clear that there are features within the background that are retained after the initial removal, such as the peak like object seen at ≈ 15 GHz. These peaks are believed to originate from defects in the waveguide or an impedance mismatch between the waveguide and the RF probes due to the temperature gradient across it. It was found to be possible to remove these background peaks by averaging all the spectra taken at a given temperature, normalizing it to its minimum value, and removing this from each of the individual spectra, which was also normalized to its minimum value. However, removal of the background in this way leads to negative, and therefore unrealistic, values of α and it was not used in the analysis of the spectra presented in this chapter. However, this background removal did reveal peaks that were previously difficult to discern from the background for some measurements. Once identified, the region where these peaks are present is then fitted in the original spectra and are included in the analysis. These objects in the background are considered when choosing the region over which the Lorentzian fit is taken. It is important to stress that the FMR is a preliminary experiment for the SWR and is used to obtain values g through the temperature range, which are required by the SWR calculations.

The values of f extracted from the Lorentzian fits to the dataset shown in Fig. 5.3(b) are plotted against their corresponding value of $\mu_0 H_{\text{Ext}}$ in Fig. 5.4(a). The red line here is a fit to equation 5.2 which is used to extract g and $\mu_0 M_{\text{Eff}}$, the results of which for all measurements are shown in Fig. 5.4(b) and (c), respectively. As the value of the field changes the position within the transition for each measurement at a given temperature, the value of T_{Eff} also varies across the measurement range. Therefore, by collating

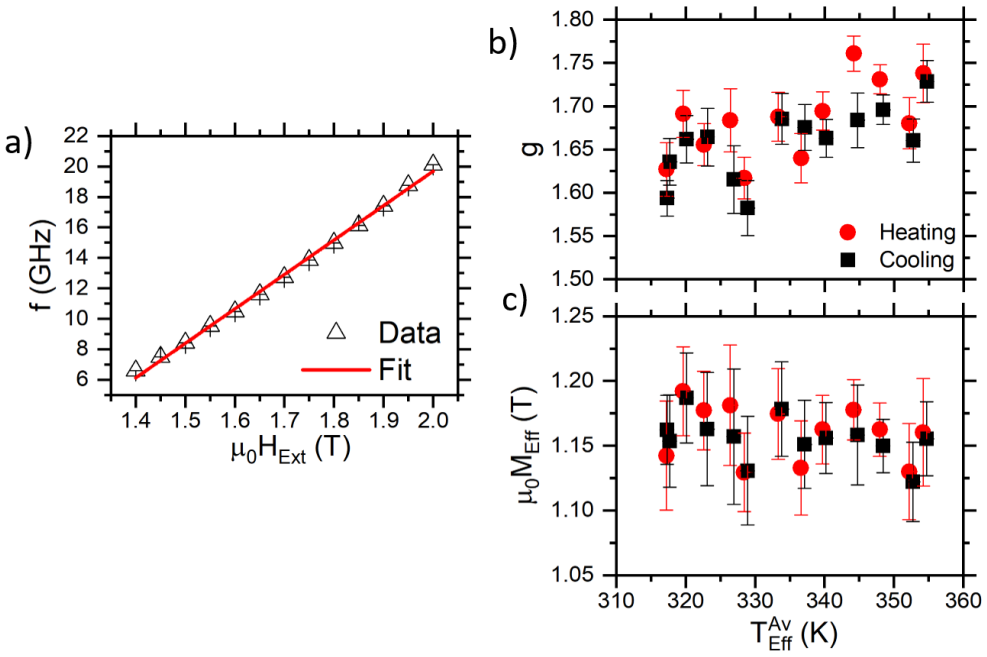

Figure 5.4: Initial FMR results against $T_{\text{Eff}}^{\text{Av}}$. Panel (a) shows the values of f obtained from the fitting to the spectra for all measurements included in Fig. 5.3(b), the red line here shows a fit of the data to equation 5.2. Panels (b) and (c) show the behaviour of both g and $\mu_0 M_{\text{Eff}}$ extracted from the fits to equation 5.2 for all measurement sets as a function of $T_{\text{Eff}}^{\text{Av}}$. Here, the measurements taken on the heating arm are shown by red circles, whilst the cooling arm measurements are shown by black squares. This convention is adopted throughout this chapter and should be assumed to be the case unless specified otherwise.

the average of these values it is possible to gather a more accurate representation of the temperature dependence compared to the use of the T_0 and as such fitting results are plotted against the average value of T_{Eff} for each of the measurement sets taken at different initial temperatures, $T_{\text{Eff}}^{\text{Av}}$. Fig. 5.4(b) shows that the value of g sits well below the free electron value of ≈ 2 and appears to decrease with decreasing temperature when cooling between ~ 1.75 and 1.6, the opposite behaviour is seen when heating. Panel (c) of the same figure shows that value of $\mu_0 M_{\text{Eff}}$ increases slightly with decreasing temperature when cooling, though it is difficult to pick out a definitive trend

here. The same behaviour is seen in reverse when heating. The measurement taken at $T_{\mathrm{Eff}}^{\mathrm{Av}} = 348.4 \pm 0.5$ K was repeated as it showed no signal for the spin-wave resonance excitations, the results of which are presented in the next chapter. The results for that experiment are shown here as an error weighted average of the two measurements.

The spectroscopic splitting factor, g, denotes the ability of a magnetic moment to couple to an externally applied magnetic field [68, 96]. When a magnetic moment is subject to a magnetic field, the available energy states of the system split depending on the orientation of the field relative to the moment [96]. For free electrons this splitting factor is $g \sim 2$ [96]. However, if spin-orbit coupling is present in the system, then the orientation favoured by this interaction can also influence the value of the spectroscopic splitting factor measured [97]. The spin-orbit splitting can favour either the direction parallel or anti-parallel to the applied field, meaning that the g factor can exist both above and below 2 [97]. Nibarger *et al.* describe the relationship between the g-factor and the ratio of the orbital, μ_{L}, and spin magnetic moment, μ_{S}, to be [97],

$$g = 2\left(1 \pm \frac{\mu_{\mathrm{L}}}{\mu_{\mathrm{S}}}\right). \tag{5.3}$$

The values of g extracted for FeRh here are by no means unrealistic, but it does differ significantly from the previously measured value for the fully FM regime measured by Mancini *et al.* where $g = 2.05 \pm 0.06$ [55], which suggests inconsistencies between the two set-ups.

One method of checking whether the value of g can be believed is to test it against a reference sample. Py is a material that is well tested in FMR studies and is known to have a g-factor of $g_{\mathrm{Py}} = 2.11$ [64, 129]. A 380 nm thick sample of Py was tested for its value of g in the same geometry as those performed for the FeRh to test the validity of the measurement set up. In the Py measurements the transmission through the waveguide was measured using a nanovoltmeter rather than a VNA. Example FMR traces for Py taken at $T_0 = 301$ K are shown in Fig. 5.5(a). The quantity I is still calculated using the method outlined in equation 4.19. These spectra were taken by sweeping the frequency between $4 - 20$ GHz at external magnetic field strengths of between $\mu_0 H_{\mathrm{Ext}} = 1.15 - 1.35$ T. Example spectra taken at different fields at $T = 301$ K are shown in Fig. 5.5(a). The extra peaks to the right-hand-side of the FMR peak are associated with the excitation of PSSWs and will be discussed in more detail in the next chapter. The results of the fitting for the different values of $\mu_0 H_{\mathrm{Ext}}$ used in this experiment is shown in panel (b) along with the fit to equation 5.2 (solid lines) used

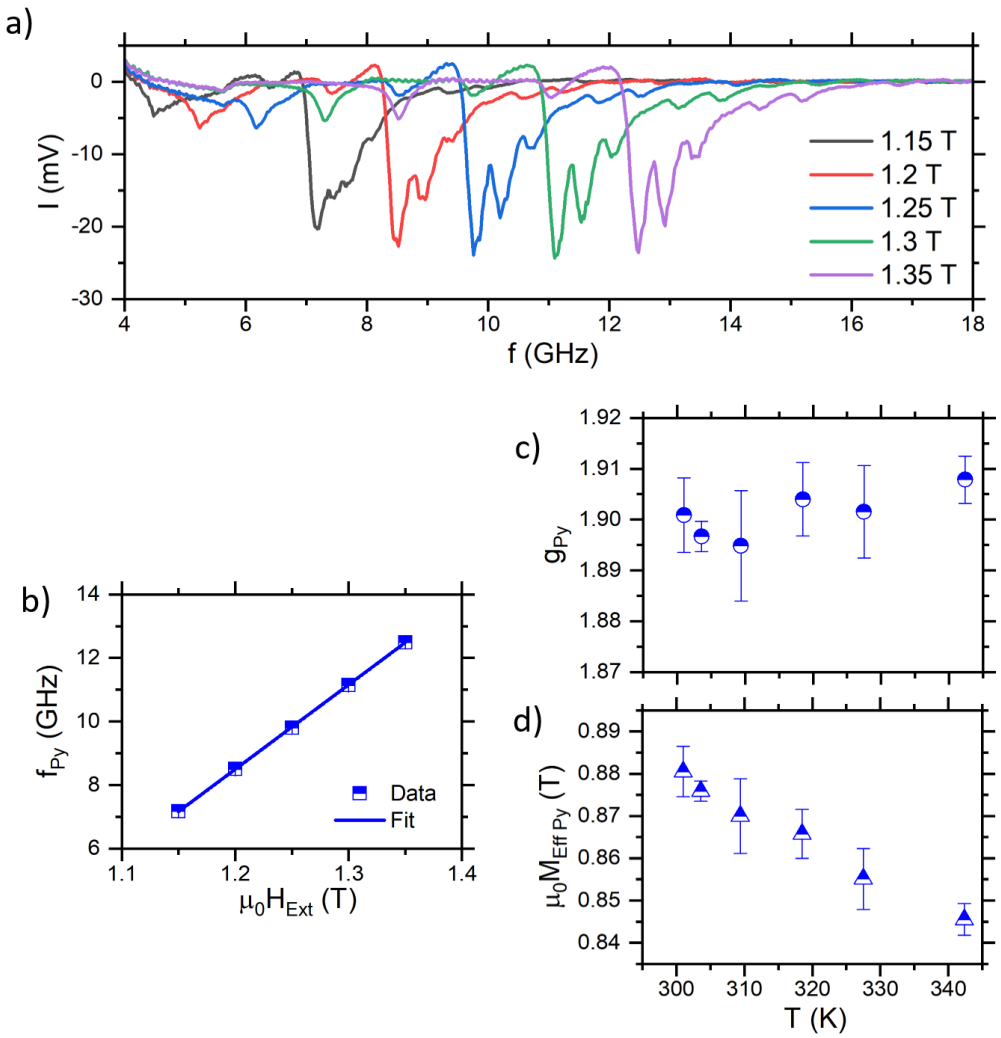

Figure 5.5: FMR analysis of a 380 nm Py film. Panels (a) shows the FMR spectra taken at different fields at $T = 301$ K, which clearly show the presence of PSSW excitations which will be discussed in more detail in the next chapter. Panel (b) shows the extracted resonant frequency, f_{Py}, against the field which is fitted (solid line) to equation 5.2 to extract the value of g_{Py} and $\mu_0 M_{\mathrm{Eff\ Py}}$. The extracted values of these quantities are shown against temperature in panels (c) and (d) respectively.

to extract the value g-factor for Py, g_{Py}, and Py's effective magnetization, $\mu_0 M_{\mathrm{Eff\ Py}}$. The values of these quantities extracted for a series of temperatures is shown in panels (c) and (d) of Fig. 5.5.

It is clear that the value of g_{Py} sits at around 1.9 which is well below the expected value of 2.11 for all measurements presented here. The value of $\mu_0 M_{\mathrm{Eff\ Py}}$ also sits below other previously reported values, it does however, exhibit the temperature dependence expected of a Py thin film [64, 97]. The asymmetry between the measured values from this experiment and the literature values implies that that the calibration for the applied magnetic field is not necessarily reflective of the field experienced by the sample. Indeed, it was later confirmed by the RIKEN group that the field was calibrated for the field at the top of the stage and not where the sample would sit after the heater had been introduced into the apparatus, as seen in Fig. 4.4. This may be the source of the low values of g seen in this work. This therefore means that the value of both g and $\mu_0 M_{\mathrm{Eff}}$ extracted from the experiments may not be the true value of the sample and this should be considered for the remainder of the discussion presented in this chapter.

Despite this, the value of g extracted from FeRh sits well below the value of g_{Py}, where the previously measured values for both materials are consistent within error bar [55, 64, 129] implying that the method of extracting g for FeRh is somewhat incomplete. Interestingly, the value extracted for both g and $\mu_0 M_{\mathrm{Eff}}$ appears to depend quite dramatically on the number of points used to fit it, evidence of which is seen in panels (a) and (b) of Fig. 5.7. This has been seen previously in literature and the method used to account for this dependence, here denoted the Shaw method after the author of the work, will now be discussed in more detail [129].

5.2.2 Application of the Shaw Method

The Shaw method was outlined in a work that demonstrates a dependence on the derived value of g on the number of fitting points used in the fitting [129]. Examples of such behaviour for the measurements taken in this experiment are shown in panels (a) and (b) of Fig. 5.7. In the Shaw work, they increase the upper bounds of the fitting frequency, f_{Up}, and observe a changing value of both g and $\mu_0 M_{\mathrm{Eff}}$ when fitting the data to the Kittel equation [129]. This behaviour is attributed to the fact that the functional form of the fitting equation changes with the range of fields used [129]. In the case of perpendicular FMR where the resonant frequency of the system is determined

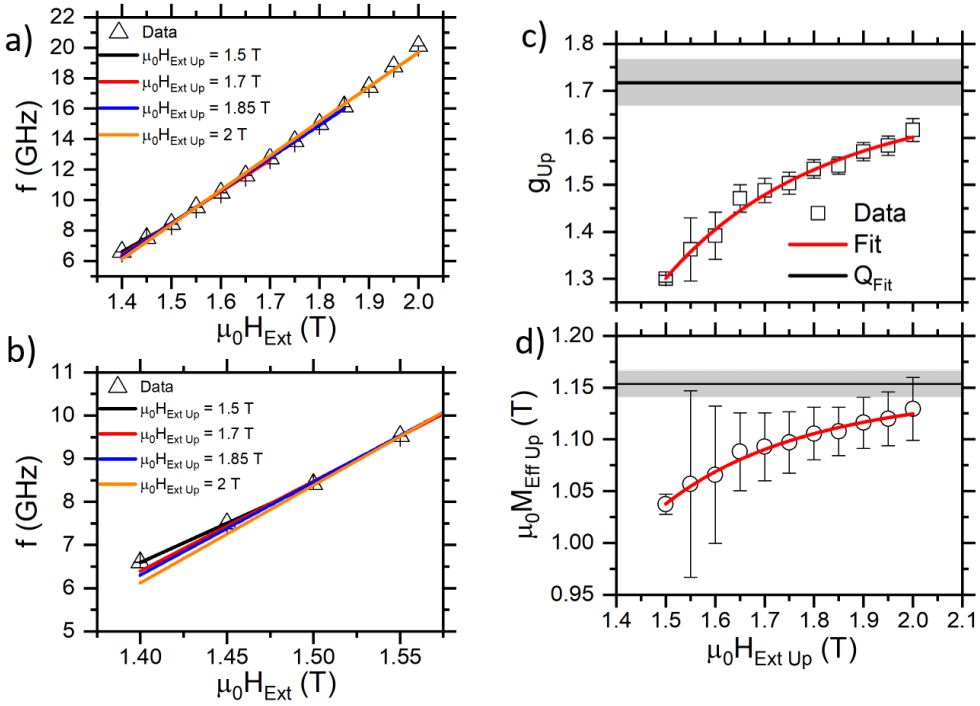

Figure 5.6: FMR analysis using the Shaw method [129]. Panel (a) shows examples of fits of equation 5.2 to the values of f extracted for fits to the data set taken at $T_0 = 312.6$ K when heating, seen in Fig. 5.3(b), for different values of the upper fitting field $\mu_0 H_{\text{Ext Up}}$. Panel (b) then shows a close up the same plot focussed around the lowest values of $\mu_0 H_{\text{Ext Up}}$, where the gradient of the line is seen to change with increasing $\mu_0 H_{\text{Up}}$. Panels (c) and (d) show the behaviour of the g-factor and $\mu_0 M_{\text{Eff}}$ extracted for a given value of $\mu_0 H_{\text{Ext Up}}$, denoted Q_{Up}, extracted from the analysis seen in panels (a) and (b). These panels also include fits of equation 5.5 to the data which is shown by the red lines and the value of the extracted value of Q_{Fit} shown by the black line, with the region encompassed by the error bar shown in grey. The behaviour of both quantities is indicative of an asymptotic dependence on $\mu_0 H_{\text{Ext Up}}$. The success of this fitting also shows that the analysis method suggested by Shaw for field-swept experiments also apply to frequency-swept measurements here.

by equation 5.2, which is valid so long as $H_{\mathrm{Ext}} > M_{\mathrm{S}}$. In this scenario, it is possible to fully separate g and $\mu_0 M_{\mathrm{Eff}}$, leading to accurate values. However, if $H_{\mathrm{Ext}} \approx M_{\mathrm{S}}$ then the frequency relation becomes,

$$f \approx \frac{g\mu_{\mathrm{B}}\mu_0}{h} H_{\mathrm{K}}, \tag{5.4}$$

where, as $M_{\mathrm{Eff}} = M_{\mathrm{S}} - H_{\mathrm{K}}$, it is no longer possible to separate out g and M_{Eff} leading to an error in their determination. In this case the functional form of the equation depends on whether the externally applied field is sufficient to overcome the demagnetizing field of the sample, which may lead to a non-uniform magnetization within the film [129]. As the field increases to beyond the scope of the demagnetizing field, g and $\mu_0 M_{\mathrm{Eff}}$ become increasingly separate and can then be extracted independently, reducing the error in the extracted value. Eventually, for sufficiently high fields the value of either quantity should tend to its true value and applies for FMR for any field orientation [129]. The Shaw method can then be used to bridge the gap between the two regimes, overcoming the influence of the non-uniform magnetic field and leads to accurate values of g [129].

The method proposed by Shaw says that the value for a quantity, Q_{Up}, extracted from fits to the Kittel equation at a given value of f_{Up} tends asymptotically towards the true value, Q_{Fit} with increasing f_{Up} according to the equation,

$$Q_{\mathrm{Up}} = Q_{\mathrm{Fit}} - A_{\mathrm{Q}} f_{\mathrm{Up}}^{n_{\mathrm{Q}}}, \tag{5.5}$$

where A_{Q} is a constant and n_{Q} is the exponent that governs the asymptotic approach [129]. Here, Q is used to denote quantities calculated from the fits to the Kittel equation and can be either g or $\mu_0 M_{\mathrm{Eff}}$. In the Shaw paper, the value of n_{Q} is found to be either -2 or -1.2 depending on whether the fit includes an MCA term and is the same for both measured quantities [129].

However, the values of g and $\mu_0 M_{\mathrm{Eff}}$ presented in the Shaw paper are extracted using field-swept FMR [129], which is the opposite case to the work presented here. Due to the reciprocity between field and frequency given by equation 5.2, it may be that the same asymptotic dependence on the number of fitting points would be expected within frequency swept experiments as well. As the demagnetizing field in this geometry ($\mu_0 H_{\mathrm{Demag}} = \mu_0 M_{\mathrm{S}} = 1.37 \pm 0.05$ T) is close to the lower end of the field range used in this experiment is $\mu_0 H_{\mathrm{Ext}} = 1.4$ T, and the complicated domain structure of FeRh

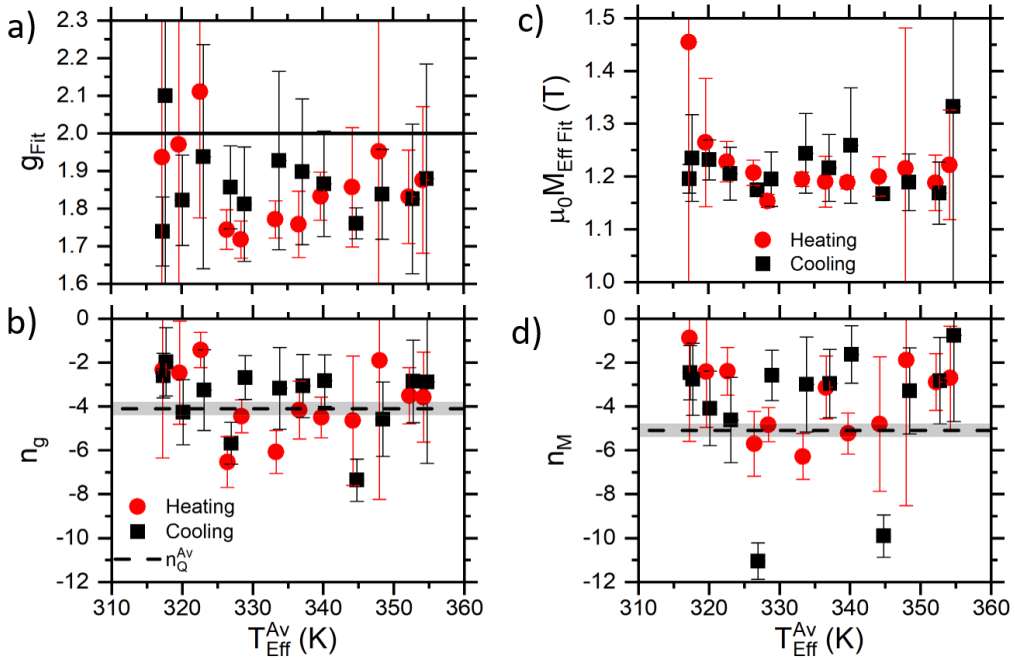

Figure 5.7: Results of the analysis of the FMR data using the Shaw method analysis. FMR analysis using the Shaw method [129]. Panels (a) and (b) show the results of fitting using the Shaw method to all data sets for the asymptotic value g_{Fit} and $\mu_0 M_{\mathrm{Eff\ Fit}}$ respectively. The solid black line in panel (a) is used to demonstrate the position of the free-electron value of the spectroscopic splitting factor where $g = 2$. Panels (c) and (d) show the results of the fittings for the exponent of the asymptotic approach n_{g} and n_{M} respectively. On these panels the black dashed line is used to indicate the position of the weighted average value of n for each quantity, with the region encompassed by the error bars shown in grey. All measurements presented in panels (c)-(f) are plotted as a function of $T_{\mathrm{Eff}}^{\mathrm{Av}}$.

which may lead to non-uniform magnetization through the sample, it would also be expected that the asymptotic dependence would be present in this work.

There is yet to be a demonstration of this relationship between the value of the extracted quantities and the number of points for frequency swept FMR in the literature and to verify whether it is applicable here the Shaw method is applied to the data set taken at $T_0 = 312.6$ K shown in Fig. 5.3(b). This involves fitting the data to equation

5.2 for a given upper bound on $\mu_0 H_{\text{Ext}}$, which here is denoted $\mu_0 H_{\text{Ext Up}}$. Examples of these fits of equation 5.2 to the data for various $\mu_0 H_{\text{Ext Up}}$ for the measurement set shown in Fig. 5.3(b) can be seen in Fig. 5.6(a). A close up of these fits are also seen in panel (b) of the same figure, and show that the fitted lines vary with the value of $\mu_0 H_{\text{Ext Up}}$. Performing the fits in this way produces values of Q for each value of $\mu_0 H_{\text{Ext Up}}$, which are then named Q_{Up} to differentiate between those and other previously obtained values of these quantities. This process is repeated for all available values of $\mu_0 H_{\text{Ext Up}}$ whilst the lower fitting boundary is always held at $\mu_0 H_{\text{Ext}} = 1.4$ T to maximise the number of points. The behaviour of Q_{Up} against $\mu_0 H_{\text{Ext Up}}$ data set seen in Fig. 5.3(b) can be seen in Fig. 5.6(c) and (d) for g_{Up} and $\mu_0 M_{\text{Eff Up}}$ respectively. The red lines in these figures represent the fits of equation 5.5 where the abscissa is now $\mu_0 H_{\text{Ext Up}}$ rather than f_{Up}. On both of these panels the value of the asymptote Q_{Fit} is shown by the black solid line with the region encompassed by the error bars is shown in grey. It is clear that this equation describes the behaviour well and the asymptotic relationship predicted by Shaw for field-swept FMR can also be used to describe the behaviour of frequency-swept FMR as expected.

Now that the asymptotic relationship between Q_{Up} and $\mu_0 H_{\text{Ext Up}}$ has been validated, this analysis is then performed on all measurement sets presented here. The results of the value of Q_{Fit} extracted from these fits is shown in panels (a) and (b) of Fig. 5.7. It is clear from these results that these extracted quantities have large error bars for most of the measurements here. Performing the analysis in this way allows the extracted value of g_{Fit} to recover towards the free electron value of $g \sim 2$, which is demonstrated by the solid black line in Fig. 5.7(a). The majority of the points here are now consistent with 2 to within the error bar. There is no discernible temperature dependence for the value of g_{Fit} here. The extracted values of $\mu_0 M_{\text{Eff Fit}}$ seen in panel (b) of the same figure show that there is no discernible temperature dependence and that the values are consistent within error bar across the temperature range.

The lack of a temperature dependence and significant error bars are also seen in the extracted values of n_{Q}, the results of which are shown in Fig. 5.7(c) and (d). There is also a large spread in the values of both n_{g} and n_{M}. The average exponent for all measurements weighted by the error bars for the extraction of g_{Fit} is $n_{\text{g}}^{\text{Av}} = -(4.1 \pm 0.3)$, and the same quantity calculated for the fits of $\mu_0 M_{\text{Eff Up}}$, $n_{\text{M}} = -(5.1 \pm 0.3)$. This point is marked on their respective figure panels by the black dotted line alongside the

region encompassed by the error bars which is shown in grey.

Despite the clear demonstration that the asymptotic behaviour predicted by Shaw describes the behaviour well, the values extracted from the fits are imprecise and the large error bars associated with the extracted quantities makes the data difficult to analyse in any meaningful way. Ideally, these measurements would have a larger point density, however, time and apparatus restrictions meant this was not possible. To reduce the error within the Shaw work they have assumed the value of n_{Q} [129]. Assuming the value of n_{Q} in this way explains all of the behaviour observed in that work and leads to more precise values of either quantity [129]. In order to try and reduce the error bar in this experiment, the value of n_{Q} is fixed and the fits are re-performed.

For consistency the same value of n_{Q} is assumed through the analysis. This value is taken to be the average of n_{g} and n_{M} at $n_{\mathrm{Q}}^{\mathrm{Av}}$ at -4.6. Example fits of the data shown in Fig. 5.7(a) and (b) are shown in Fig. 5.8(a) and (b) and show excellent agreement with the data. Despite the large spread in the extracted values of n_{Q} this assumed value is seen to fit well to all data sets seen in the experiment. Results of the values extracted using this method, which are designated Q_{Fix}, can be found plotted against $T_{\mathrm{Eff}}^{\mathrm{Av}}$ in Fig. 5.8(c) and (e).

Again, neither quantity shows any appreciable temperature dependence when analysed in this way through the temperature range probed here. The values of g_{Fix} are closer to the free electron value after using this method though most do still sit below 2. They are now more consistent with the value for Py extracted previously from this experiment, before the Shaw method was applied. This indicates that the Shaw method can be used here to compensate for the large demagnetizing field within the sample and the complications this causes with regards to the extraction of g and $\mu_0 M_{\mathrm{Eff}}$. FeRh's complicated magnetic domain structure may also contribute to the supressed value of g, which the Shaw method is also seen to correct for. The value of $\mu_0 M_{\mathrm{Eff\ Fix}}$ is seen to it below the value of $\mu_0 M_{\mathrm{S}}$ obtained using magnetometry techniques, which is shown by the black dashed line with the region encompassed by the error bars in grey. By fixing the value of n_{Q} to -4.6 the errors in the extracted quantities have been reduced as desired and shows that the method outlined by Shaw for extracting the asymptotic value of field-swept FMR can also be applied to frequency swept FMR.

It is also possible to use another metric to measure the progress of the transition, which is the FM volume fraction, $\phi(T_{\mathrm{Eff}}) = M(T_{\mathrm{Eff}})/M_{\mathrm{S}}$. As the position within the

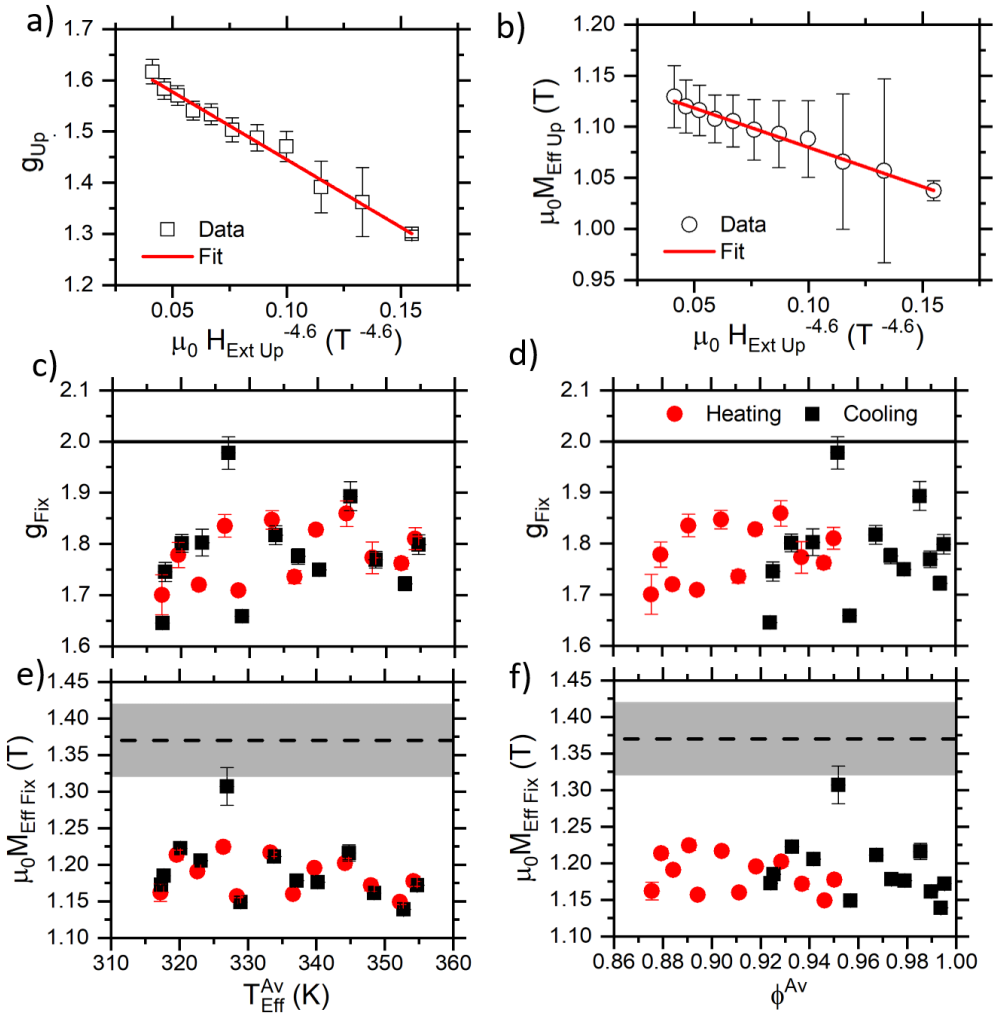

Figure 5.8: FMR characterization results using the Shaw method with n_Q fixed. Panels (a) and (b) show the fitting (solid lines) of the data for the $T_0 = 312.6$ K data shown in Fig. 5.7 to equation 5.5 where the value of n_Q is fixed at -4.6 and the abscicca is $\mu_0 H_{\text{Ext Up}}$. Panels (c) and (d) show the values of the g_{Fix} plotted against $T_{\text{Eff}}^{\text{Av}}$ and ϕ^{Av} for each measurement set, respectively. The solid black line in this figure shows the free electron value of $g = 2$. Whilst, panels (e) and (f) show the behaviour of $\mu_0 M_{\text{Eff Fix}}$ plotted against the same quantities. The value of $\mu_0 M_S$ is shown by the black dashed line with the region encompassed by the error bars shown in grey in panels (e) and (f).

transition changes with externally applied magnetic field throughout a measurement set, so does ϕ. Therefore, the value presented here is the average of ϕ for each measurement set at a given temperature, ϕ^{Av} which is calculated from the minor loop magnetometry trace. Fig. 5.8(c) and (d) show the behaviour of g_{Fix} and $\mu_0 M_{\mathrm{Eff\ Fix}}$ against ϕ^{Av}, respectively. Switching to the ϕ^{Av} metric for both quantities again demonstrates a lack of any appreciable dependence for either quantity.

It was not possible to measure the system in the fully FM phase in this experiment and all measurements here are believed to have AF material present. The value of g that has been measured previously for the FM phase of FeRh is found to be $g = 2.05 \pm 0.06$ [55] and it is clear here that even modest amounts of AF material have a profound effect on the high frequency properties of the system. The influence of the AF material on each of the quantities of interest will be discussed in more detail in the next section.

5.3 Influence of the Mixed Magnetic Phase

In order to quantitatively evaluate the influence of the introduction of AF material into the system, a model of the development of the magnetic phases relative to each other in the MMP is required. To this end the trilayer model, which is based on observations seen in the literature is defined and then applied to the results here.

5.3.1 Outline of Trilayer Model

The domain structure of B2-ordered FeRh and its development through the transition has been studied throughout its history [27, 31, 32, 34–36]. The evidence suggests that nucleation of the FM domains occurs around defects and centres of local symmetry breaking, as usual for first order phase transitions [23, 30]. However, there is only one study that has managed to image the transition through a vertical cross section of a thin film using electron holography [36]. This study maps the development of the magnetic domains as a function of thickness through the transition and demonstrates that FM domains nucleate at either surface and proceed into the bulk of the material as the transition progresses, with the opposite being true for the development of the AF domains when cooling [36]. Regions of FM material that persist well into the nominally fully AF state have been seen at the film/substrate interface using PNR [7, 37, 130].

XMCD-PEEM measurements on an uncapped 90 nm thick FeRh film have shown

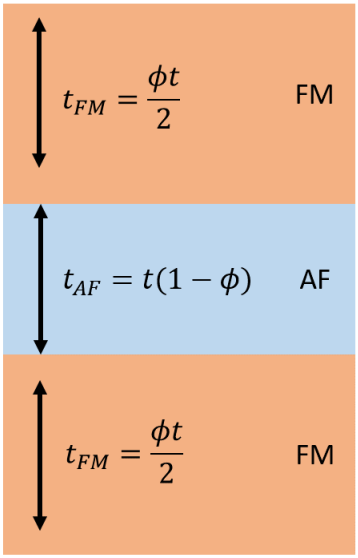

Figure 5.9: Trilayer model schematic including the thicknesses of each region.

that the development of these domains at the top surface of the material throughout the transition is not trivial as the coexistence of the two magnetic phases is seen at the surface [27, 32, 34]. However, these XMCD-PEEM studies also show that the magnetic domain profile encompasses the entire surface before the end of the transition as defined by the magnetization [27, 32]. This implies that the material at the surface has become FM whilst those within the bulk of the film are yet to transition, as consistent with the electron holography results. In practice, this gives regions of FM material at either surface, separated by a region of AF material in a FM/AF/FM trilayer configuration.

The PEEM data fails to pinpoint exactly where the surface domain structure begins to disintegrate. It does, however, show that the surface magnetism remains intact for $\phi \geq 0.75$ on the either transition branch [32]. This encompasses the range of measurements shown in this experiment and the trilayer geometry is assumed to apply for all measurements presented here and in the subsequent chapter.

A simple model is to separate the total thickness by phase volume fraction, which is itself determined by the magnetization. This would lead to the thickness of the AF layer of $t_{\mathrm{AF}} = t(1-\phi)$ and the thickness of the FM layers being $t_{\mathrm{FM}} = \phi t$ which is distributed between the two layers. The presence of the externally applied field in both the experiment and the magnetometry measurements ensures that the FM layers

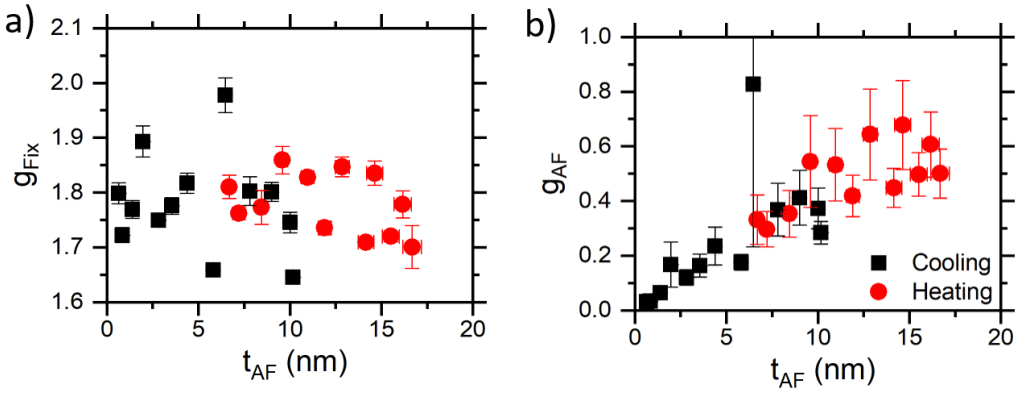

Figure 5.10: Influence of AF layer thickness on the spectroscopic splitting factor. Panel (a) shows the behaviour of g_{Fix} against t_{AF}. Panel (b) shows the behaviour of the g-factor of the AF layer g_{AF} calculated using equation 5.7 as a function of t_{AF}.

exhibit a uniform structure. A schematic of the trilayer model with equal sized FM layers are shown in Fig. 5.9.

5.3.2 Spectroscopic Splitting Factor

Now that the trilayer model has been outlined, it is possible to begin to investigate the influence of the introduction of the AF phase on the properties of the system. The spectroscopic splitting factor, g, describes the ability of a magnetic moment to couple to an externally applied magnetic field [68]. The g-factor extracted from the FMR experiments using the Shaw method with the exponent fixed, g_{Fix}, is plotted against t_{AF} as calculated using the trilayer model using ϕ^{Av} for each measurement set in Fig. 5.10(a). g_{Fix} appears to increase with increasing t_{AF} when cooling after $t_{\mathrm{AF}} \sim 2.5$ nm, being mostly consistent within error bar at around $g_{\mathrm{Fix}} \sim 1.75$ before this. This increase stops after around 5 nm after which there is no obvious thickness dependence. Measurements taken when heating show no appreciable dependence on t_{AF}. Interestingly however the values of g_{Fix} appear to consistent where the two transition branches overlap.

g has been shown to be sensitive to the presence of spin-orbit coupling or interfaces within the system [97, 107]. Within the interface between magnetic and non-magnetic layers the two layers mix which brings about uncompensated orbital angular momentum into the system which then affects the value of the g-factor [97]. It is believed that the

magnetism persists into the interfacial intermixed regions but their orbital angular momentum is dominated by the non-magnetic contributions and $g < 2$ [97]. The measured g-factor is then an average of the g-factor for each of the different contributing regions, i, weighted by their volume, V, and spin-density, ρ, such that [97],

$$g_{\mathrm{Fix}} = \frac{\sum_i \rho_{\mathrm{i}} V_{\mathrm{i}}}{\sum_i \frac{\rho_{\mathrm{i}} V_{\mathrm{i}}}{g_{\mathrm{i}}}}. \tag{5.6}$$

The intermixing of elements at the interface between the FM/AF layers is not applicable to the case presented here, as this experiment was performed on a single sheet film. However, it may be that the same analogy can be extended to an interface where intermixing of the magnetic phases are expected. This would lead to lattice mismatch strain and magnetic roughness which would give the uncompensated orbital angular momentum required to alter the g-factor in this interfacial region and equation 5.6 would still apply.

By evaluating this equation fully for the FM and AF regions in this experiment it is possible to rearrange this equation to direct evaluate g_{AF} via,

$$g_{\mathrm{AF}} = \frac{kt_{\mathrm{AF}}}{\frac{t_{\mathrm{FM}}+kt_{\mathrm{AF}}}{g_{\mathrm{Fix}}} - \frac{t_{\mathrm{FM}}}{g_{\mathrm{FM}}}} \tag{5.7}$$

where $k = \rho_{\mathrm{AF}}/\rho_{\mathrm{FM}}$. For the purposes of this calculation, as it was not possible to obtain a value of g_{Fit} for the fully FM phase, that is taken to be that that extracted by Mancini *et al.* at $g_{\mathrm{FM}} = 2.05 \pm 0.06$ [55]. This is assumed to be constant through the measurement range, as are both ρ_{FM} and ρ_{AF} are constant throughout the measurement range. At this current point ρ_{AF} is unknown, but it would be expected that, as it is an AF and would not couple to the field that $\rho_{\mathrm{AF}} = 0$. If this was true then g would be constant through the measurement range which is clearly not the case, implying that there is a non-zero spin density in the region defined by the magnetization as being AF. This approach also assumed that the deviation from the free electron value of g is real and that the Shaw method addresses the issue and is analytical in nature [97].

This observation implies that the two magnetic states intermix at the boundary and as the FM region is believed to be rigid in the trilayer model, this is taken as FM order premeating into the region defined by the magnetization as being AF. In this interpretation the non-zero moment seen in the AF region would be brought about by the exchange coupling across the MPB. This non-zero spin density in the AF layer then

causes the MPB to contribute to the measured g-factor value leading to the results seen here.

As it is not possible to evaluate ρ_{AF} at this time, it is necessary to assume a value of k. Naturally, as this is an AF material and is expected to have a small non-zero magnetic moment due to the influence of exchange coupling across the AF/FM interface it is fair to assume that the $\rho_{AF} < \rho_{FM}$. Here, it is assumed that there is a linear intermixing profile across the MPB and that the average $k = 0.5$. The values of g_{AF} extracted in this manner are shown in Fig. 5.10(b).

Here it is clear that at low t_{AF} when cooling there is a small contribution to g_{AF}, which is close to 0 and is consistent with the behaviour expected of an AF layer. At around $t_{AF} \sim 1$ nm, the value of g_{AF} begins to increase with increasing t_{AF}, with the increase in g_{AF} continuing across the measurement range here. Interestingly, the measurements of the two transition branches overlap well and have measurements consistent within error bar for similar values of t_{AF}. The strength of exchange coupling in AF/FM bilayer systems has been seen to follow a similar dependence on AF layer thickness to that seen here in g_{AF} [60, 102, 131, 132]. However in the literature, the exchange coupling strength is seen to saturate at a given AF layer thickness [60, 102, 131, 132]. The large spread in the data makes it difficult to say for certain if this saturation does indeed occur and further evidence for this is needed. However, the development of g_{AF} with t_{AF} suggests that the development of the exchange coupling as a function of AF layer thickness is responsible for the behaviour seen here. In the exchange coupled AF/FM bilayer systems previously studied, this dependence on the t_{AF} for the strength of the exchange coupling is attributed to a TDPT that takes place within the AF layer with increasing thickness [60, 131, 132].

In AF materials that are below a certain critical thickness, the anisotropy in the layer cannot stabilize regions of AF material and the system exhibits a paramagnetic (PM) state [60, 131, 132]. Increasing the thickness of the AF layer allows for the formation of areas of AF material within the PM system, as the anisotropy of the AF layer increases with thickness [60, 131]. If this AF layer is situated next to an FM layer, then it is at this stage that exchange coupling across the interface begins to actualize [60, 131]. Naturally, as the amount of AF material in the layer increases with thickness, so does the strength of the exchange coupling [60, 131]. When the AF layer is of a thickness where the anisotropy in the AF layer is completely developed and

the layer exists solely in an AF state, then the exchange coupling also plateaus having reached its peak value [60, 131].

However, evidence suggests that B2-ordered FeRh does not exhibit a PM state and exists only in either the AF or FM state [133]. This again means that it cannot be a TDPT from a PM to an AF in the AF layer that is taking place here. Also, the behaviour of g_{AF} suggests that a region where the two magnetic states of FeRh are intermixed exists at the boundary between the two, which may affect the stabilization of bulk AF domains. The development of the g_{AF}, and by extension the exchange coupling, in this experiment is consistent with the behaviour expected of a TDPT in the AF layer. Therefore, it may be that at the very low thicknesses the system is AF but has no global orientation of the spin-axis. As the thickness of the AF layer increases, it will reach a critical value where the anisotropy can stabilize regions of AF material that share a common spin-axis. The size of these AF regions with a common spin-axis will continue to increase with the thickness until the entire AF layer exists in a globally ordered state. This behaviour would give the exchange coupling a similar profile to the one expected for the PM-AF TDPT and would explain the behaviour of g_{AF} seen in this experiment, with the onset of the TDPT being $t_{\mathrm{AF}} \sim 1$ nm and the end coming between $t_{\mathrm{AF}} \sim$4-6 nm.

AF FeRh is known to orient its spin-axis perpendicularly to the applied field [6, 54]. As the out-of-plane anisotropy of the AF is large and that the FM has a negligible in-plane anisotropy [55] it is likely that when the field is applied perpendicularly to the film surface, that the AF will orient itself within the film plane to minimize energy. In the case of this experiment, this then means that there is an FM region, whose magnetization is pointed perpendiularly to the film surface, is in direct contact to an AF region whose spin-axis lies within the film plane. The large field applied means that the FM layer is rigid and that any exchange coupling across the MPB acts to pull the AF spins out of the film plane, inducing a non-zero moment in the AF layer and would account for the behaviour of g_{AF} seen here. Therefore, the behaviour of g_{AF} here implies that a TDPT occurs in the AF layer that brings with it an exchange coupling across the MPB that induces a non-zero magnetic moment in the AF layer which then contributes to the g-factor behaviour.

All of the above discussion is predicated on the fact that the behaviour of the g-factor is real. Doubts regarding the validity of this assumption arise from the consistently

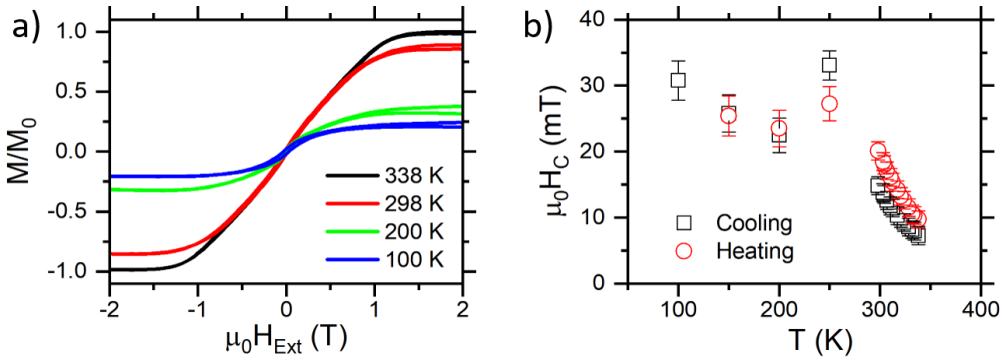

Figure 5.11: Behaviour of the coercive field, $\mu_0 H_C$, through the transition. Panel (a) shows hysteresis loops taken with the field oriented perpendicularly to the film surface at various temperatures on the cooling branch. Panel (b) shows the extracted $\mu_0 H_C$ against temperature for all measurements performed on both the heating and cooling branches.

low value of g extracted from this experiment when compared to literature for both Py and FeRh [55, 129]. Nevertheless, it is possible to get independent corroboration for the presence of exchange coupling between the FM and AF phases of FeRh through different means, one of which is the coercivity of the hysteresis loops. The coercive field, $\mu_0 H_C$, of a magnet is the field required to switch the orientation of the magnetization between two orientations. $\mu_0 H_C$ is related to the anisotropy of the magnet via,

$$\mu_0 H_C = \frac{2K}{M_S}, \tag{5.8}$$

where K is the anisotropy energy. Therefore, any changes in $\mu_0 H_C$ imply that either K or M_S has changed.

Hysteresis loops were performed at a series of temperatures on the sample investigated in this work, in which the field was oriented perpendicular to the field plane. Examples of these loops are shown in Fig. 5.11(a). These loops have been corrected for the diamagnetic background of the substrate and are normalized to the largest M for $T_0 = 338$ K measurement, M_0. The extracted $\mu_0 H_C$ for all measurements can be seen in Fig. 5.11(b). It is clear here that $\mu_0 H_C$ increases with decreasing temperature when cooling and saturates around 250 K. The system exhibits the opposite behaviour when

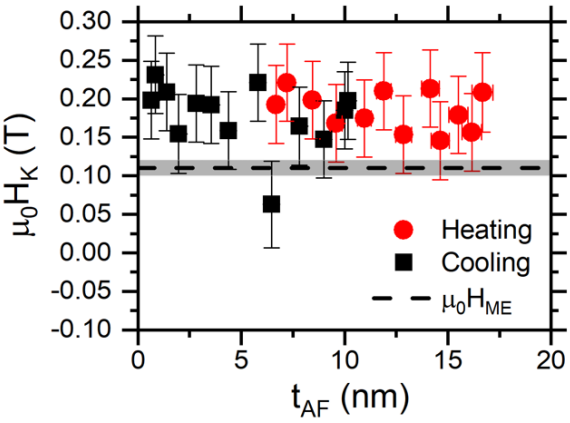

Figure 5.12: Dependence of $\mu_0 H_K$ as a function of t_{AF}. The dashed black line here shows the position of $\mu_0 H_{ME}$ derived from the Kumar *et al.* work and applied to this system assuming contributions from the substrate/film interface and both AF/FM interfaces, alongside the region encompassed by the error bars which is shown in grey. The value of $\mu_0 H_K$ predicted in this way gives reasonable agreement to the extracted values of $\mu_0 H_K$.

heating. As M_S is expected to increase with decreasing temperature, the increase in $\mu_0 H_C$ implies an increase in K occurs over the temperature range.

The only change over the temperature range in the system would be the introduction of AF material and the formation of AF domains. The increase in $\mu_0 H_C$ then implies that the anisotropy of the FM layer increases due to the introduction of AF material. This behaviour is indicative of an exchange coupling between the two magnetic phases and serves as evidence to support the claims made here. It is also clear that the coercivities are higher for the heating branch than they are the cooling branch in the 350 - 300 K temperature range, implying that the exchange coupling between the two phases is larger when heating.

5.3.3 Magnetocrystalline Anisotropy

The search for the strength of the exchange coupling in FeRh using FMR is a source of controversy as there are differing interpretations of the behaviour of $\mu_0 H_K$ when entering the MMP [55, 56, 63]. There are two possible explanations that currently exist for the observed behaviour of $\mu_0 H_K$ when entering the MMP which are i) the

presence of an interfacial exchange coupling [55] or ii) ME effects at the substrate and the MPB [56]. As we have seen evidence suggestive of an exchange coupling in the behaviour of the g-factor, a thorough investigation of the behaviour of $\mu_0 H_K$ may also help to elucidate which of these possible interpretations is correct.

The MCA measured here is an effective MCA made up of various contributions such that,

$$K_{Eff} = K_{Shape} + K_{ME} + K_{EC}, \tag{5.9}$$

where K_i corresponds to the MCA constant of each of the different contributions. The shape contribution is responsible for the M_S term present in equation 5.2 and is believed to be constant through the measurement range due to the retention of the shape of the FM layers through the experiment. All other contributions to the MCA energies are collected into the H_K term in the equation 5.2. The K_{ME} is the contribution due to magnetoelastic effects and K_{EC} is that due to exchange coupling. Both of these contributions will now be discussed in turn.

The values of $\mu_0 H_K$ calculated using $\mu_0 M_S$ from the magnetometry measurements and $\mu_0 M_{Eff\,Fix}$ in conjunction with the definition of $\mu_0 M_{Eff}$ are shown in Fig. 5.12 against t_{AF}. It is clear that all of the measurements of $\mu_0 H_K$ are consistent within error bar with each other, except for those measurements where $\mu_0 M_{Eff} > \mu_0 M_S$ which are believed to dubious due to the method of extraction. The lack of a dependence on t_{AF} suggests that the behaviour cannot be explained by exchange coupling as this is known to have an AF layer thickness dependence as seen in equation 2.30 [60, 61].

Recently, a similar study to the one presented here was performed by Kumar *et al.* which claims that the change in $\mu_0 H_K$ seen when entering the MMP can be accounted for by ME effects due to the lattice mismatch strain at the substrate [56]. This is believed to account for most of the anisotropy field that develops throughout the transition in this work [56]. In the Kumar et al. work it is claimed that the MCA field can be explained by ME effects at the interface [56]. The equation used to calculate the anisotropy field expected due to ME effects, $\mu_0 H_{ME}$, is given by,

$$\mu_0 H_{ME} = \frac{2K_{ME}}{M_S} = \frac{-3\lambda E \epsilon_x}{M_S}, \tag{5.10}$$

where K_{ME} is the anisotropy constant for ME effects, λ is the saturation magnetostriction, E is the Youngs modulus of the material, ϵ_x is the strain in the x-direction [56]. Kumar *et al.* use a value of $\lambda \approx 1 \times 10^{-5}$, which is an average value of those presented

in the literature, and obtain a value for $\mu_0 H_{\mathrm{ME}} = 0.072$ T for $\epsilon_x = -0.73$ % strain with the substrate with an $\mu_0 M_S = 1.16$ T.

At the interface between the FeRh film and the substrate, the substrate mismatch strain is known to cause tetragonal distortion of the FeRh lattice [56]. This is an in-plane distortion caused by the clamping of the in-plane lattice parameter by the substrate [56]. However, this sample is much thicker than the region said to be affected by the substrate, which is typically around 50 nm, and so the out-of-plane lattice parameter here will be dominated by contributions from the bulk of the material [56, 134]. It is also seen to agree well with the bulk value of the FM phase and is taken as the bulk value in all directions [11]. It is then possible to calculate the in-plane strain due to lattice mismatch at the substrate. This is calculated as the average of that seen for the two reflections in the XRD scan to be $\epsilon_x = -(0.64 \pm 0.04)$ %. Accounting for the change in M_S between our work and theirs the expected value of the strain due to lattice mismatch at the substrate is $\mu_0 H_{\mathrm{ME\ Sub}} = 0.054 \pm 0.007$ T, which clearly fails to account for the entirety of the MCA field seen in this experiment.

Another possible source of ME effects could be the strain between magnetic phases at the MPB, which could be as large as 0.4% in any direction, as the volume expansion in the transition is believed to be symmetric [13, 56]. When scaling $\mu_0 H_{\mathrm{ME}}$ to the strain expected at the interface between the two magnetic phases and the value of M_S for this sample, the size of the field due to ME effects at the MPB falls to $\mu_0 H_{\mathrm{ME\ Int}} = 0.033 \pm 0.004$ T according to equation 5.10. The trilayer model predicts that there are two MPBs in the system which leads to a total contribution due to the ME effects at the interface of $2\mu_0 H_{\mathrm{ME\ Int}} = 0.066 \pm 0.007$ T, which also fails to account for the size of the MCA field through the measurement range.

By adding together these contributions to give the total MCA field expected due to ME effects in the system the value of $\mu_0 H_{\mathrm{ME}} = 0.12 \pm 0.01$ T is obtained and is plotted in Fig. 5.12 as the black dashed line. Analysing the data in this way gives reasonable agreement with the value of the MCA field throughout the measurement range and suggests that the MCA field measured in this experiment can be fully accounted for by ME effects at both the substrate and the AF/FM boundary. The addition of these strain terms implies that the strain through the system is uniform, which may not be the case and further investigations are required to ascertain the validity of this approach. Measurements of the Youngs modulus and saturation magnetostriction for this sample

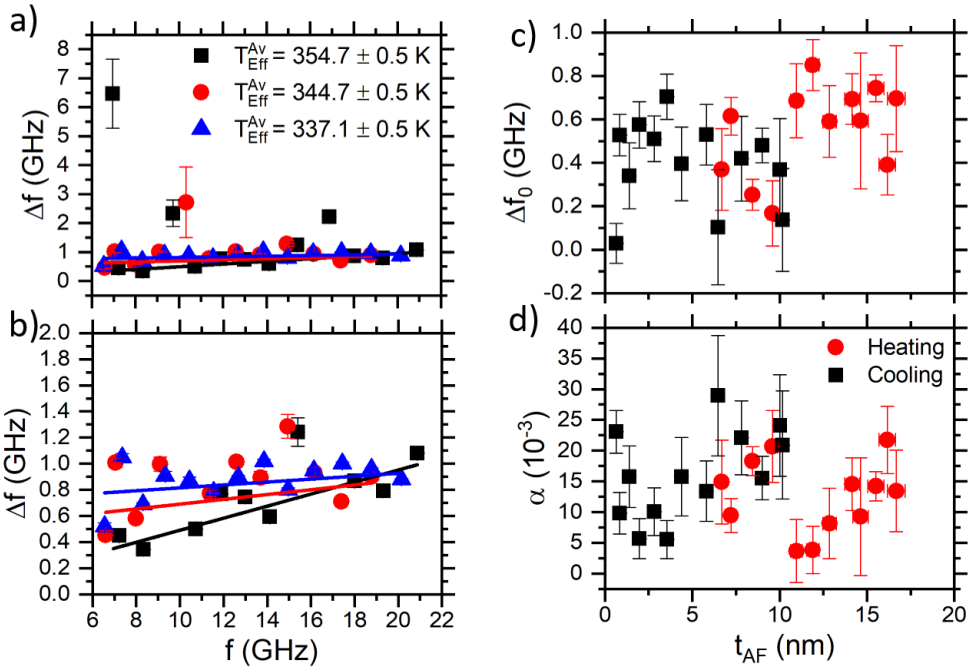

Figure 5.13: Gilbert damping results. Panel (a) shows the linewidth against frequency (symbols) for various temperature sets on the cooling branch. Both quantities were extracted using a fitting of the curve to a Lorentzian function. The straight lines in this figure are fits of the data to equation 5.12. Panel (b) shows the same figure but zoomed in to emphasize the changes in behaviour of the gradient from which α is extracted. Panels (c) and (d) then shows the results of the fitting for Δf_0 and α, respectively, plotted against t_{AF}.

are also required to say for certain that this is the case. It is clear here that there is no obvious dependence of $\mu_0 H_{\mathrm{K}}$ on t_{AF} as would be expected for the development of an exchange coupling between the two magnetic phases seen in equation 2.30. Being able to account for the size of $\mu_0 H_{\mathrm{K}}$ in this way, as well as the the lack of a thickness dependence, suggests that there is no evidence of exchange coupling present in the measured MCA field.

5.3.4 Gilbert Damping

The Gilbert damping parameter, α, is an important property of materials that are of interest for technological applications as it determines the operating speed of the devices [2, 125]. For fully FM FeRh α has been measured to be $\alpha = (1.3 \pm 0.8) \times 10^{-3}$ in the same geometry as that used in this experiment [55]. The Gilbert damping parameter has been seen to increase as the system moves into the MMP [55, 56]. Armed now with the trilayer model it is possible to add a new layer of understanding to these results in terms of the development of the AF layer with temperature. The results of such an investigation are presented here.

α is extracted from the linewidth of the FMR excitation. For field swept experiments, the equation governing the relationship between the frequency, the linewidth, ΔH, and the damping parameter is given by [70, 135],

$$\Delta H = \Delta H_0 + \frac{4\pi\alpha f}{\gamma}, \tag{5.11}$$

where ΔH_0 being the intrinsic contribution of the material to the linewidth. However, as this is a frequency swept experiment, we require the linewidth in frequency and not field. For the purposes of this calculation all linewidth quantities are taken to be the FWHM of the peak. In the small damping limit, $\alpha^2 \ll 1$, the differential of the resonant frequency with respect to H_{Ext} is constant and so Δf can be written as

$$\Delta f = \Delta f_0 + 2\alpha f, \tag{5.12}$$

with Δf_0 being the materials intrinsic contribution to the linewidth.

The values of Δf is plotted against f for various measurements on the cooling arm in Fig. 5.13(a) and a close up is shown in panel (b). The solid line in these figures show the fit of equation 5.12 to the data. The extracted values of Δf_0 and α extracted for all measurements shown against t_{AF} in panels (c) and (d) of Fig. 5.13 respectively. The value of α for the lowest value of t_{AF} when cooling, i.e. when the system is in its closest proximity to the fully FM phase, is seen to be 0.023 ± 0.003. This value is substantially higher than that which is measured for the fully FM state previously [55]. This suggests that even a slight amount of AF material can substantially increase the damping parameter of the system. Interestingly, after this point the damping appears to decrease with increasing t_{AF} reaching a minimum at around 2.5 nm, which persists up to thicknesses of 4 nm. After this point the values demonstrate a quasi-linear increase with increasing thickness.

Similar behaviour is seen in the heating branch measurements, with the dip in α centered around $t_{\mathrm{AF}} \sim 10$ nm and the quasi-linear increase coming for thicknesses in excess of this point. The dip seen in the heating branch measurements is not mirrored by any changes in the other measured quantities and also corresponds to measurements that are consistent with 0 and their valdity is questionable. Again, the measurements on heating are consistent with those on the cooling branch where the two overlap and are mostly consistent within error bar.

The behaviour of α is qualitatively comparable to the previous investigations on FeRh and shows a similar behaviour with decreasing temperature [55, 56]. The value of Δf_0 appears to peak as the damping dips when cooling, decreasing as the thickness of the AF layer increases. This implies that there is an increase in the intrinsic damping of the system with increasing t_{AF} in a manner similar to the change in α implies that the two have the same physical origin.

Interestingly, the point at which α dips when cooling is also the point at which the increase in g_{Fix} is seen at around $t_{\mathrm{AF}} \sim 2.5$ nm. The behaviour of g_{Fix} was attributed to an exchange coupling across the MPB which induces a non-zero magnetic moment in the AF layer, resulting in the behaviour of g_{AF} also seen previously. The value of g_{AF} may exhibit a saturation at thicknesses around $t_{\mathrm{AF}} \sim 5 - 7$ nm, which is the thickness where the quasi-linear increase in α is seen here.

The exchange coupling believed to be present in this system develops with thickness as the AF layer undergoes a TDPT from a disordered to ordered AF state. The point at which the exchange coupling is fully established is where the TDPT has finished and the AF layer now exhibits global AF order. Due to the geometry of the system, any changes in α are believed to be due to spin-pumping into the AF layer and the variations seen in α over the same length scale associated with the development of the exchange coupling implies that the AF layer undergoes a change in its properties over this thickness window. This observation is again consistent with the idea that the AF layer undergoes a TDPT in this region.

If we assume that equation 2.30 governs the behaviour of the exchange coupling in this system and that it applies to the case seen here, then the thickness at which point exchange coupling would begin to materialize would be $t_{\mathrm{AF}} = J_{\mathrm{EC}}/2K_{\mathrm{AF}}$. This means that the thickness where the TDPT occurs is dependent on the size of the exchange coupling across the interface, J_{EC}, and the anisotropy of the AF layer, K_{AF}. These

TDPTs typically take place at $t_{AF} < 2$ nm which is consistent with the length scales seen on the cooling branch, but is not consistent with those on the heating branch [60, 131]. This either implies that the TDPT is not the cause of the dip or that the properties of the AF layer are substantially different for this range of the transition depending on the temperature sweep direction. This would be consistent with the behaviour of the coercive field through the transition presented in Fig. 5.11(b). It may be that the dip seen when heating corresponds to a TDPT that takes place at a higher t_{AF} due to the different properties of the AF layer.

Previously, peaks seen in the damping when spin pumping into AF materials have been associated with increased spin fluctuations in the AF layer due to a phase transition in the spin-sink layer [132, 136]. The phase transition presented in these works is that of a second-order transition between an AF state to that of PM state at the Néel temperature of the AF [136]. An increase in damping across the TDPT in IrMn has also been seen when increasing the thickness of the AF layer between 0 and 4 nm [132]. Therefore, as the AF to PM transition would not be expected in this temperature regime for the metamagnetic transition in FeRh, it is likely that the TDPT used to explain the behaviour of g_{AF} seen in this experiment may also result in the increase in damping also seen in this work. The TDPT seen within the AF layer would be of second-order and would also be expected to present an increase in damping due to the change in magnetic susceptibility across the transition [132, 136]. The consistency between the behaviour expected from the TDPT and the dip in α seen in this experiment observed in the behaviour of g_{AF} and α seen here implies that it is responsible for the behaviour seen in this experiment.

After the dip in the α seen when cooling, the behaviour of the damping appears to take on a different trajectory and can be seen on both transition branches with the damping appearing to increase linearly and then is constant within error bar through the remainder of the measurement range. This linear increase is seen for t_{AF} between 5 and 10 nm when cooling. A linear increase in damping has been seen previously in the literature and is attributed to dephasing of the spins as they through move the AF layer [137]. The damping then saturates after the AF layer thickness exceeds that through which the spin current an travel coherently through the AF layer [137]. If the saturation seen here is to be believed, it takes place at around 10 nm in this system.

Exchange coupling at the AF/FM is known to result in magnon spin pumping into

the AF layer when the FM layer is driven at its FMR frequency [72, 138]. These have been seen to carry spin currents that decay exponentially across characteristic distances of around 10 nm for NiO, which is an AF insulator [138]. This is similar to the distances seen here and may account for the dephasing of the spin currents over large distances seen here, assuming that the trend can be believed given the size of the error bars and the extent to which the data scatters. Further investigations are required to ascertain the nature of the spin current passing through the AF layer and the characteristic lengths that two possible sources of spin pumping, electron and magnon spin-pumping, can carry excitations through the AF layer.

It is important to note here that performing the analysis in this way introduces an error in the value of I which was not considered for the data analysis presented in this chapter. The errors were considered and the analysis was reperformed for a single dataset and was found to give values consistent within error bar. Therefore, the consideration of the errors on I has no influence on the overall results of the experiment and its omission is justified.

Before concluding the chapter there are many issues that have been raised regarding the validity of the results that should be addressed. All of the analysis performed here is based on two assumptions: i) that the magnetic state is that which is described by the trilayer model and ii) that all of the values of the extracted quantities are real. The first assumption here is believed to be valid throughout the measurement range for the reasons outlined in section 5.3.1. All of the behaviour seen in this chapter can be explained using this assumption which adds to its validity, however independent experimental evidence for the presence of the trilayer configuration through the range probed here is necessary to say for certain whether this is the case. The validity of the second assumption is called into question due to the persistently low g-value extracted from both the Py and the FeRh systems, even after having been corrected using the Shaw method. All of this stems from the fact that the field experienced by the sample may not have been calibrated properly before the experiment was performed. In order to test the validity of the conclusions drawn from this experiment, it should be reperformed in a system in which the field is properly calibrated.

It is also seen that the behaviour of g_{Fix} and $\mu_0 M_{\mathrm{Eff\ Fix}}$ is consistent regardless of the fixed value of n_{Q} which is used to extract them. However, the values of g_{Fix} or $\mu_0 M_{\mathrm{Eff\ Fix}}$ do differ depending on the fixed value of n_{Q} used to extract them. This does

raise questions as to the validity of the Shaw method which require further investigation. This observation means that the behaviour is likely to be real, though the exact numbers may be treated with some scepticism. It is also seen that the fits of the g_{Up} and $\mu_0 M_{\mathrm{Eff\ Up}}$ as a function of $\mu_0 H_{\mathrm{Ext\ Up}}$, such as those seen in Fig. 5.6, are dependent on the initial conditions used when fitting. All of the fits in this work performed with the same initial conditions and are therefore beleived to be comparable. However it is seen that the values of the exchange stiffness extracted from the investigations into the behaviour of the PSSW mode behaviour are impervious to these two features of the data and the conclusions of the experiment do not change.

Before proceeding to the discussion regarding the damping behaviour extracted from the FeRh sample, it is again necessary to address the validity of the method employed in this experiment. Throughout this work, the analysis of the data is performed on the quantity I which is defined by equation 4.19 as the difference of the magnitude of the S_{ij} between the substrate and when the field is applied. However, the S_{ij} trace measured using a VNA contains contributions from both real and imaginary components and the influence of the damping is only seen in the imaginary component [139]. This means that it would be more accurate to investigate the damping behaviour by analysing the isolated imaginary component of the spectra, rather than the magnitude as seen in this experiment. Perfoming the analysis in the way seen in this experiment may lead to incorrect values of the damping component. To test its influence on the results of the experiment the damping analysis is reperformed on five right most points on the heating branch as seen in Fig. 5.13 and is presented in Fig. 5.14.

This figure compares the value of the damping extracted using the quantity, I, (red circles) and the method outlined earlier in the section, to that extracted by performing the same analysis on the imaginary component only, $\mathrm{Im}(\Delta S_{\mathrm{ij}})$ (blue triangles). It is important to note here that due to the quality of the data to extract any meaningful spectra from the imaginary components it is necessary to take the magnitude of each of the traces before performing the calculation. The spectra calculated using only the imaginary components is subject to the same smoothing and background removal processes as the remainder of the spectra presented in this chapter for consistency and comparability. The phase of the imaginary component was not considered in this analysis.

It is clear to see from Fig. 5.14 that the values extracted using the two methods

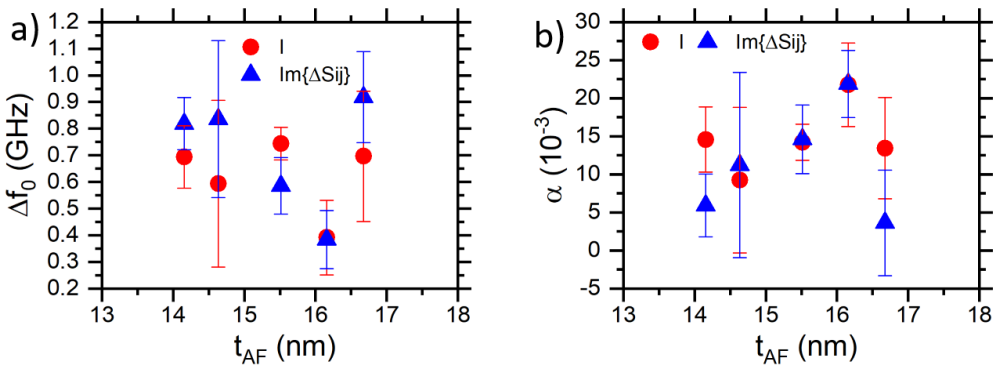

Figure 5.14: Comparison of the damping analysis performed on the quantity I (red circles) and the imaginary component only (blue circles) for a selection of points on the heating branch. Panel a) compares the value of Δf_0 for the two analysis methods extracted using equation 5.12. Panel b) shows the comparision of the value of α extracted for the two analysis types.

are largely consistent within error bar for both Δf_0 (panel (a))and α (panel (b)). The point at $t_{\mathrm{AF}} \sim 14$ nm is the only point where the α is not consistent within error bar between the two analysis methods. This figure suggests that the analysis methods are equivalent and the behaviour is damping extracted in this way is correct.

Again, a good test for the validity of the method is to check the Py, whose damping behaviour is well established [64]. This is also a good test here as the Py measurements were performed using a nanovoltmeter which only measures the magnitude. The behaviour of the Δf_{Py} against f_{Py} is shown in Fig. 5.15(a) for the measurement performed at 301 K, with the extracted values of α_{Py} for all measurements shown in panel (b) of the same figure. These extracted values of α_{Py} agree well with literature measurements that are performed on the imaginary part of S_{21} [64] The consistency between the two approaches implies that the method used here is valid for the extraction of the damping behaviour. Again however, the error bars associated with the extraction of α extracted for both materials are large which hinders the ability to discern any meaningful conclusions as to the temperature dependence. The fitting for the Py damping was performed such that it yielded a positive value of α, as some of the attempts lead to values of $\alpha < 0$ which is a non-physical result. The size of the error bars perhaps reflect the difficulties in fitting the data.

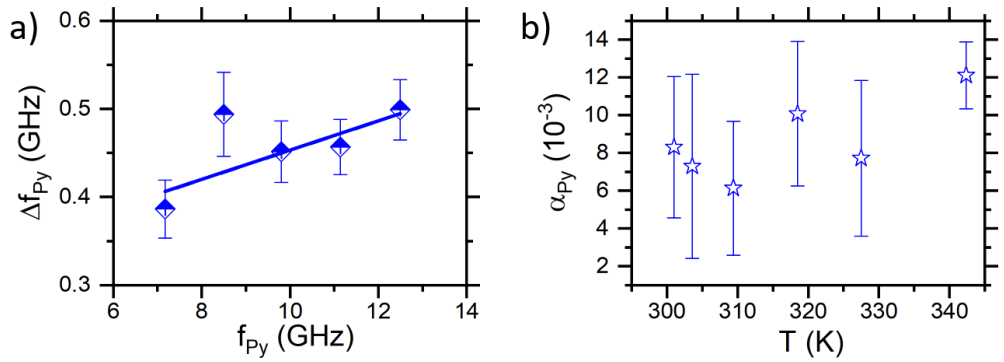

Figure 5.15: Gilbert damping results for Py. Panel (a) shows the linewidth against frequency (symbols) for the measurement performed at $T_0 = 301$ K shown in Fig. 5.5(a) (points) and the fit of equation 5.12 to the data (solid line). Panel (b) shows the extracted value of α for all measurements performed at different temperatures.

It is also important to note here that there is some ambiguity in whether the area used in the calculation of M_S is the correct one for the piece of the sample measured in the SQUID. This was retested approximately 18 months after the initial measurement and lead to $\mu_0 M_S = 1.23 \pm 0.08$ T and $\mu_0 M_S = 1.18 \pm 0.06$ T, from what is believed to be the initial sample split into two smaller pieces. These are lower than the initial measurement which suggest oxidation or damage to the sample is present. Regardless of this, the value of M_S has no influence on the outcomes of either this chapter or the next chapter and the value extracted from the initial measurement is used to more accurately reflect the behaviour of the sample at the time it was measured.

Upon reviewing the calculation of $\mu_0 M_S$ an error was found in the subtraction of the diamagnetic signal from the substrate, meaning that all values presented for M_S are higher than the correct values. The correct value obtained from the initial measurement is $\mu_0 M_S = 1.32 \pm 0.05$ T, whilst the values extracted for the subsequent measurements are $\mu_0 M_S = 1.16 \pm 0.07$ T and $\mu_0 M_S = 1.14 \pm 0.06$ T. These are all consistent within error bar with the previous values. The error in the calculation means that the values of quantities derived from M_S presented in this work may also be inaccurate. However, the error in the calculation has no influence on the conclusions of this or the SWR experiment and it was not deemed necessary to redo the analysis. The new value

extracted from the initial measurement is still believed to most accurately reflect the behaviour at the time the sample was measured and is taken as the correct value.

5.4 Conclusion

A systematic FMR study was performed through the high-temperature part of the MMP of FeRh's metamagnetic phase transition. Initial attempts to extract the spectroscopic splitting factor, g, reveal values well below the expected value of 2, whilst the $\mu_0 M_{\mathrm{Eff}}$ is seen to have a large spread in the data. Both g and $\mu_0 M$Eff were then seen to have an asymptotic dependence on the number of points used in the fitting to extract it. The model proposed by Shaw *et al.* [129], that describes the same behaviour seen in field swept FMR experiment, is then adapted for frequency-swept experiments and is also seen to be applicable to this method. To recude the error bars associated with the extraction of the asymptotic quantity, the exponent governing the asymptotic approach was fixed at $n_{\mathrm{Q}} = -4.6$.

Performing the analysis in this manner reveals that the spectroscopic splitting factor presents a substantial variation to that measured for the fully FM phase previously [55]. This is attributed to the influence of the MPB interface in this system. To gain a better understanding of this influence, the FM/AF/FM trilayer model is introduced and reveals that the effect that the AF phase has on the high frequency properties of the system varies systematically with the AF layer thickness. It also reveals that the AF layer contributes to the behaviour of the g-factor which means that it must have a non-zero magnetic moment, which is believed to be brought about by exchange coupling at the MPB. This influence may saturate at $t_{\mathrm{AF}} \sim 5 - 7$ nm and is consistent with the behaviour expected of the development of exchange coupling due to a TDPT in the AF layer, if the saturation is real. More evidence is required to say for certain if this is the case. Evidence for the presence of an exchange coupling is also provided by the behaviour of the coercive field measured through the transition.

The focus then changed to looking for evidence of exchange coupling in the MCA field which has been previously suggested to be the cause a changing MCA previously reported in literature [55]. However, it was found that the size of the MCA field can be explained entirely using predicted values of the ME at the substrate and the MPB in the system. Though again, the assumptions that lead to this conclusion require independent corroboration.

The Gilbert damping is seen to increase with increasing AF fraction and is attributed to spin-pumping into the AF layer. There appears to be a peak in the damping on the cooling at thicknesses consistent with those predicted by the TDPT used to explain the behaviour of the behaviour of the AF layer g-factor. A TDPT would bring about a change in the magnetic susceptibility across the phase transition and would account for this increase in damping seen over this thickness range. Consistency between the two observations implies that a TDPT takes place in the AF layer and is responsible for the behaviour seen here. It is seen that after the peak that the damping takes on a linear trajectory that is attributed to the dephasing of spins as they pass through the AF layer. This increase is seen up to thicknesses of the AF layer of 10 nm, which is rather large and so further work is required to identify the source of the spin-pumping in this system. Asymmetries in the t_{AF} for which these dips occur between the transition branches implies that the properties of the AF layer are different depending on the temperature sweep direction.

All of the conclusions drawn from this chapter are based on assumptions that may not be true for the sample for reasons outlined throughout the chapter. To ascertain the validity of these conclusions, independent validations of these results are required.

Nevertheless, as the investigations using FMR did not provide any clear cut answers to the nature of the exchange coupling between the two magnetic phases, we then instead moved the focus to the behaviour of the higher-order spin-wave modes in our spectra, the results of which are presented in the next chapter.

Chapter 6

Phase Boundary Exchange Coupling Probed Using Spin-Wave Resonance

6.1 Introduction

The previous chapter shows ferromagnetic resonance (FMR) investigations that suggest the possibility of an exchange coupling across the magnetic phase boundary (MPB) that induces a magnetic moment in the antiferromagnetic (AF) layer. However, doubts remain over the validity of the method used to extract these values and a more robust method is necessary to corroborate these findings. Spin-Wave Resonance (SWR) is an extension of FMR that uses the excitation of perpendicular standing spin-waves (PSSWs) to probe exchange stiffness behaviour [64, 67–71]. These PSSWs excitations appear as extra peaks in the FMR spectrum and the energy of these excitations is related to the exchange stiffness across the film thickness. The development of the effective exchange stiffness at various points through the mixed magnetic phase (MMP) is shown in this chapter, looking for evidence of any exchange coupling across the MPB.

The exchange stiffness is seen to decrease with temperature for both transition branches and demonstrates a reduced value for all measurements when compared to that expected for the fully ferromagnetic (FM) regime. As regions of AF material are expected throughout the measurement range this is believed to be due to the influence of the AF phase. It is found, with the help of computer simulations of atomistic spin dynamics, that the behaviour of the exchange stiffness can be accounted for by the intermixing of magnetic states at the interface and the introduction of magnon spin-pumping into the system at the completion of the thickness dependent phase transition (TDPT) in the AF layer seen in the previous chapter.

The work attributed to the author is the same as that of the previous chapter. In addition to those measurements, high temperature magnetization measurements on FeRh were also performed by K. Matsumoto using a Quantum Design Physical Properties Measurement System (PPMS). K. Matsumoto is also responsible for the growth and SWR measurements the Py thin film. The candidate is responsible for all the analysis of the SWR experiments. There are also computer simulations of atomistic spin dynamics presented in this chapter that were performed by M. Strungaru of the University of York. For these simulation results the candidate can only claim to have been involved in the discussions regarding their scientific direction as well as the interpretation of the results.

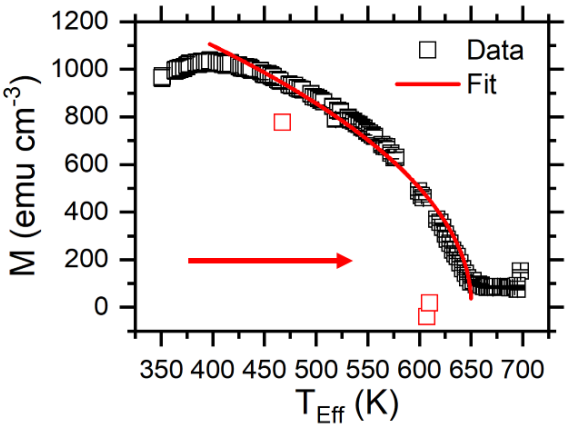

Figure 6.1: High temperature magnetometry used to extract the Curie temperature. The high temperature magnetization behaviour (hollow squares) which is fitted to equation 6.1 to extract the Curie Temperature (red line) measured in an in plane field of 0.1 T. The red squares here are not considered when fitting the data. The temperature has been corrected here for the application of external field. The arrow demonstrates the temperature sweep direction.

6.1.1 Sample Growth & Characterization

This experiment is a direct extension of the FMR experiment presented in the previous chapter and as such, the same sample and experimental method are used for both experiments. The reader is invited to refer to sections 5.1.1 and 5.1.2 in the previous chapter for the relevant information.

Further to the previous sample characterization, high temperature magnetization measurements were performed using the PPMS to identify the Curie temperature, T_C, of the system. These measurements were performed in a 0.1 T field applied in the film plane and are shown in against T_{Eff} in Fig. 6.1. To extract T_C, the data were fitted by

$$M = M_0\left(1 - \frac{T}{T_C}\right)^{\beta}, \tag{6.1}$$

where M is the magnetization, T is the temperature, M_0 is the magnetization at $T = 0$ K and β is the critical exponent. Points between 400 and 650 K excluding those shown in red were considered during the fitting, as the inclusion of these points means the fit fails to accurately reflect the behaviour of the data. The fitting gives $T_C = 650 \pm 1$ K and $\beta = 0.49 \pm 0.02$, which gives excellent agreement with the mean-field model [140].

It is then possible to extract a value for the exchange constant of the FM regime, J_{FM}, using the mean field model via [140, 141]

$$J_{\mathrm{FM}} = \frac{3k_{\mathrm{B}}T_{\mathrm{C}}g^2}{2Z\mu_{\mathrm{Fe}}^2} = (9.4 \pm 0.4) \times 10^{-22}\mathrm{J} \tag{6.2}$$

where k_{B} is Boltzmann's constant, μ_{Fe} is the magnetic moment per Fe atom in units of Bohr magnetons, μ_{B}, Z is the coordination number and g is the spectroscopic splitting factor [141].

In order to complete the calculation a number of assumptions are made regarding the system. Firstly, as it was not possible to obtain a value of g for the fully FM phase and doubts remain as to the validity of the values extracted from the previous chapter, the value of g is taken to be that measured by Mancini *et al.* for the fully FM phase $g = 2.05 \pm 0.06$ [55]. Secondly, as it is possible to recreate the transition seen in FeRh by ignoring the influence of the Rh moment and instead modeling its influence as a higher order exchange interaction due to the Fe atoms as outlined in section 4.5 [128], the magnetic structure is assumed to be simple cubic and the influence of the Rh moment is ignored. This means that the system exhibits a simple cubic lattice comprising of Fe atoms only and $Z = 6$ [128]. This assumption is adopted in this investigation to simplify the understanding of the experiment and for consistency with the simulations of atomistic spin dynamics presented in section 6.3.

For completeness, the calculation of μ_{Fe} from M_{S} is also included here. As M_{S} is a density of magnet moments in the system, it is assumed that this denisty is constant through the film and can be expressed in terms of the moment for a given unit cell, μ_{UC}, and its volume, V_{UC}, therefore

$$M_{\mathrm{S}} = \frac{\mu_{UC}}{V_{\mathrm{UC}}} = \frac{\mu_{\mathrm{UC}}}{a^3} = (1.09 \pm 0.04) \times 10^6 \mathrm{Am}^{-1}, \tag{6.3}$$

where the lattice constant, a, is taken to be the average of that measured for the two FeRh reflections seen in the XRD data which is $a = 2.998 \pm 0.001$ Å. Rearranging this then gives

$$\begin{aligned} \mu_{\mathrm{UC}} = M_{\mathrm{S}}a^3 &= (1.09 \pm 0.04) \times 10^6 \mathrm{Am}^{-1} \times ((2.998 \pm 0.001) \times 10^{-10}\mathrm{m})^3 \\ &= (2.9 \pm 0.1) \times 10^{-23}\mathrm{Am}^2 = (3.2 \pm 0.1)\ \mu_{\mathrm{B}}. \end{aligned} \tag{6.4}$$

As FeRh is taken to be a simple cubic structure here, there is a single Fe atom in the unit cell and $\mu_{\mathrm{Fe}} = \mu_{\mathrm{UC}}$. This value agrees well with measurements previously made using neutron diffraction [39].

For the purposes of this investigation however it is necessary to discuss the changes in the exchange behaviour in terms of the exchange stiffness, A, which can be calculated from the exchange constant using [142],

$$A_{\mathrm{FM}} = \frac{JS^2}{a} = (7.5 \pm 0.6)\ \mathrm{pJm}^{-1}, \tag{6.5}$$

where S^2 is the spin per unit atom squared and a is the lattice constant. This form of A is that for a simple cubic lattice [142]. Previously in literature, measurements of the exchange properties of material are often spoke of in terms of the spin-wave stiffness, D, which is related to the exchange stiffness via [143],

$$D = \frac{2g\mu_{\mathrm{B}}A}{M_{\mathrm{S}}}. \tag{6.6}$$

For the FeRh film measured in this sample in the fully FM phase, $D_{\mathrm{FM}} = (160 \pm 20)$ meV Å^2, which is smaller than that measured for BCC Fe using different techniques, $D_{\mathrm{Fe}} \sim 280 - 330$ meV Å^2 as expected for the smaller T_{C} [144]. In the calculation of A_{FM}, the value of S is calculated using the expression,

$$S = \frac{M_{\mathrm{S}}a^3}{g\mu_{\mathrm{B}}} = (1.55 \pm 0.07)\ \hbar. \tag{6.7}$$

6.2 Spin-Wave Resonance Measurements

6.2.1 Initial Characterization

Example SWR spectra taken at $T_0 = 338.4$ K on the heating arm are presented in Fig. 6.2(b) where each field measurement shows peaks at frequencies in excess of that expected for the large peak associated with FMR. The behaviour of the FMR mode throughout the transition range probed here was discussed in the previous chapter, whilst this chapter will focus on the behaviour of these extra peaks seen in the spectra. These extra peaks also appear to track along with $\mu_0 H_{\mathrm{Ext}}$. To emphasize this observation the spectra taken for $\mu_0 H_{\mathrm{Ext}} = 1.9$ T is isolated and shown in Fig. 6.2(b). The higher energy peaks associated with the excitation of PSSWs are clearly demonstrated here and are marked for their corresponding mode number, or number of antinodes across the film thickness, n. Each PSSW peak is fitted to a Lorentzian lineshape, examples of which are also shown in Fig. 6.2(b). The frequency of a given PSSW mode, f_n, can be written as [68, 143],

$$f_n = f_0 + \frac{2Ag\mu_{\mathrm{B}}}{M_{\mathrm{S}}h}\left(\frac{n\pi}{t}\right)^2, \tag{6.8}$$

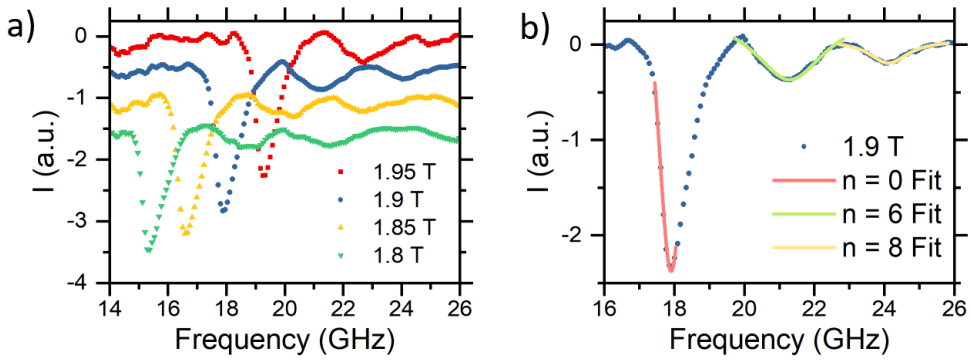

Figure 6.2: SWR spectra example taken at $T_0 = 338.4$ K on the heating branch. Panel (a) shows the spectra for a series of different external magnetic field strengths clearly showing peaks to the right hand side of the FMR peak that track along with the field that are attributed to the excitations of PSSWs. These have been artifically offset from each other in the ordinate direction to make the PSSW peaks easier to distinguish. Panel (b) shows a close up of the $\mu_0 H_{\mathrm{Ext}} = 1.9$ T measurement alongside the fits used to extract the position of the resonant frequency for the given PSSW mode, f_{n}. The assigned mode number is also labeled here.

where f_0 is the FMR mode frequency.

Before proceeding on to the results of this analysis, there are facets of SWR investigations that should be considered. Firstly, SWR comes about because there are pinning conditions at the surface that allow for the excitation of PSSW wave modes [67, 68, 123]. In uniformly magnetized films of a single magnetic species, the only place where the exchange field can differ and therefore boundary conditions can occur is at either end of the film thickness [123, 145]. In this scenario, the abrupt change in the magnetization across the interface exerts a torque, τ on the magnetization vector, $\mathbf{M}$, which is given by the Rado-Weertman equation [67, 123, 145],

$$\left(\frac{2A}{M}\right)\left[\mathbf{M} \times \partial_{\mathrm{z}}\mathbf{M}\right] + \tau = 0, \tag{6.9}$$

where ∂_{z} is the derivative in the direction normal to the interface. Solving this equation then leads to boundary conditions that are dependent on the pinning conditions at either interface [123]. In general these pinning conditions are taken to be symmetric in films with uniform magnetization [68, 123].

The mixed magnetic phase of B2-ordered FeRh cannot be described as a single layer of uniform magnetization however, and a reconsideration of the boundary conditions are required. The Rado-Weertman boundary conditions fail to account for the strength of any exchange coupling between the two layers [145], which is expected to be present at the boundary between the two magnetic phases in FeRh [18]. Consideration of the strength of the exchange interaction between these layers leads to the Hoffman boundary conditions [145]. For two magnetic layers, named A and B, each with their own magnetization that are situated a distance δ and $-\delta$ from the interface and are exchange coupled across the interface between them with interaction strength J_{Int}, the Hoffman boundary conditions are given by [123, 145]:

$$\left(\frac{J_{\mathrm{Int}}}{2}\right)\mathbf{M}_{\mathrm{A}}|_{\delta} \times \mathbf{M}_{\mathrm{B}}|_{-\delta} - \left[\mathbf{M}_{\mathrm{A}} \times \partial_{\mathrm{z}}\left(\frac{2A}{M_{\mathrm{A}}}\right)\mathbf{M}_{\mathrm{A}}\right]\Big|_{\delta} = 0, \tag{6.10}$$

where $k|_j$ means quantity k evaluated at point j. Again, solving these equations leads to boundary conditions where the allowed wavevectors are dependent on the coupling between the two layers [123]. In a bilayer system both layers have asymmetric pinning conditions at either interface if subject to these boundary conditions [123].

Previously in literature, in systems with uniform magnetization across the film thickness the symmetric boundary conditions have led to the wavevector of the PSSW modes being defined by odd numbers of half wavelengths in the system, as modes with even numbers no longer couple to the field [68]. However, in practice this is not the case, with both odd and even modes being observed in Py films [64, 65]. This is attributed to asymmetric pinning conditions at either end of the film thickness [64]. Odd and even numbered modes have also been seen in bilayer systems that are exchange coupled at the interface between them [71].

Due to the non-uniform nature of the magnetization in FeRh and the exchange coupling believed to be present at the AF/FM interface, it is taken that modes containing both even and odd numbers of half wavelengths are present in this system in the mixed magnetic phase. To limit the discussion to dealing with integer numbers of half wavelengths and for direct comparision with the literature, the pinning conditions at either end of the film thickness are also taken to be asymmetric [64, 71]. For direct comparison with literature, the large FMR peak is taken to be the 0th mode i.e. $n = 0$. Again, these are assumptions and the physical picture may differ from this in reality and comparison against literature should be performed where possible for validiation.

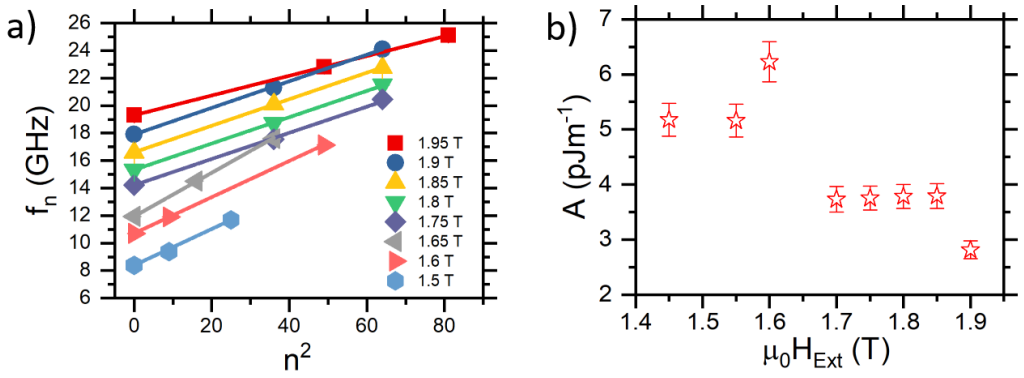

Figure 6.3: Extraction of the spin-wave stiffness, A. Panel (a) shows the excitation frequency, f_n, plotted against the square of the assigned mode number, n^2, for the measurement set taken at $T_0 = 338.4$ K on the heating branch, some of the corresponding spectra of which is shown in Fig. 6.2. The points are taken from fits of the PSSW excitations and the solid lines are linear fits to the data. The gradient of this line is used to extract A in accordance with equation 6.8 which are shown plotted against $\mu_0 H_{\text{Ext}}$ for these measurements in panel (b).

From equation 6.8, it follows that A can be extracted via the gradient of the graph of f_n against n^2. An example of this analysis performed for the measurement series shown in Fig. 6.2(a) is shown in Fig. 6.3. This equation also implies that for a given set of peaks with the mode numbers correctly assigned that $(f_n - f_0)/n^2$ is constant. This condition, as well as the ratio of the distances between adjacent peaks, is used to assign the mode numbers during the analysis to evaluate A. From this figure it can be seen that there are mode numbers that are missing across the range here. The reason for this could be two-fold: i) that the complicated pinning conditions born of the complex magnetic structure in FeRh means the excitation of certain modes is not possible and this changes with the magnetic configuration through the measurement range here, or that ii) the method used to assign the mode numbers and the underlying assumptions that lead to this method are incorrect. Both possibilities are feasible here and further investigations are required to ascertain the source of this behaviour.

In the previous chapter doubts were raised regarding the field validity of the field calibration and whether the field experienced by the sample is that measured by the

Hall probe. This could be the reason behind the supressed value of g measured in that experiment. For this experiment however, the PSSW modes and the value of A extracted from them use measurements of an individual field only. The extracted values of A for the measurement set presented in Fig. 6.3(a) are plotted against the field at which the measurements were taken in Fig. 6.3(b). It is not clear as to what the dependence of the extracted value of A should be with regards to the value of $\mu_0 H_{\mathrm{Ext}}$ used to extract it. These A values are seen to increase with decreasing applied field here, but in general the nature of the correlation across the field range changes with the temperature. Again, as the magnetic structure in FeRh is temperature dependent this implies that the magnetic state has an influence on the measured exchange stiffness behaviour. This may mean that the complicated magnetic structure of FeRh can lead to supression of certain mode numbers, though further investigation is required to say for sure.

It is also clear from Fig. 6.2(b) that not all of the measurements taken at the different field values have a measurement of A associated with them. This is because some measurements did not have a sufficient number of peaks in order to be able to fit a straight line to the data. Also in some cases, it was not possible to distinguish between the peaks in the background discussed in the previous chapter and the possible PSSW peaks. These are not included in the analysis as they are deemed to be invalid and may influence the behaviour of measurements where the presence of PSSW excitations are clear.

The extracted values of A for all measurements can be seen in panels (a) and (b) of Fig. 6.4 plotted against T_{Eff} and ϕ respectively. Both panels also show the value of A_{FM} by the black dashed line and the region encompassed by the error bars shown in grey. In this calculation the value of $\mu_0 M_{\mathrm{S}}$ identified from the magnetometry measurements is used as is the value of g_{Fix} for each individual measurement set presented in the previous chapter. The sample thickness used is $t = 134 \pm 4$ nm, which is extracted from the XRR measurements.

It is clear from Fig. 6.4(a) that the value of A has no clear temperature dependence and appears to vary significantly across the measurement range. There are some measurements that exceeds the value of A_{FM} across the measurement ranges, though there is no obvious trend to the data here. The observation of $A > A_{\mathrm{FM}}$ again implies that mode numbers have been mistakenly assigned. The bulk of the measurements however

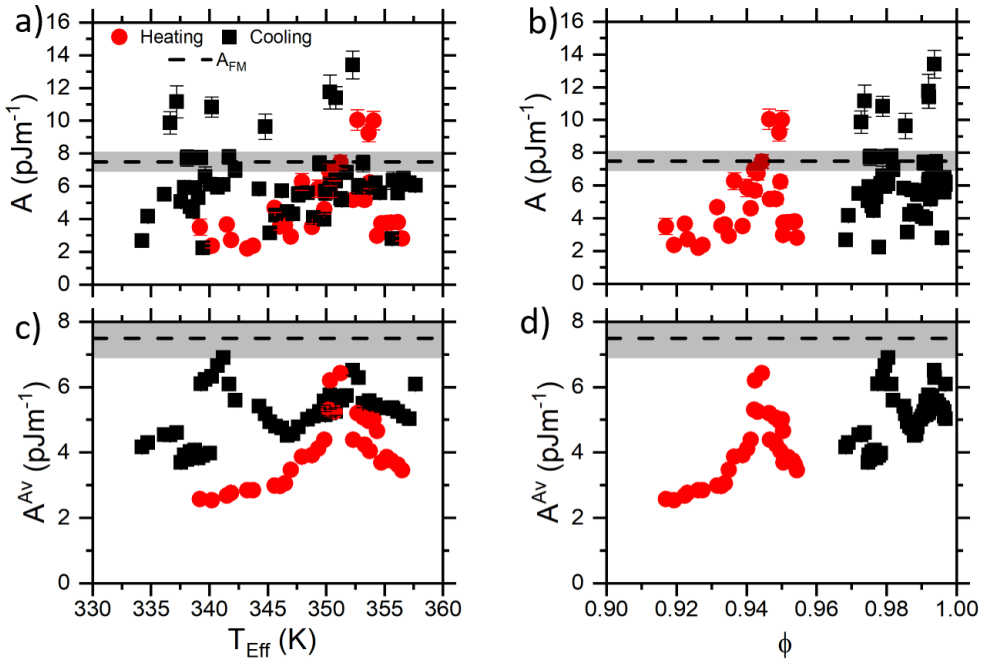

Figure 6.4: Extracted exchange stiffness behaviour. Panels (a) and (b) shows the behaviour A as a function of T_{Eff} and the FM volume fraction, ϕ, respectively. Panels (c) and (d) show the value of a nine-point adjacent weighted average of A, A^{Av} against t_{Eff} and ϕ respectively. Both panels have measurements from the cooling (black squares) and heating (red circles) branches, plotted alongside the value of A_{FM} (black dotted line) with the region encompassed by the error bars shown in grey.

show $A \leq A_{\mathrm{FM}}$, which adds credence to hypothesis of supressed mode numbers in the system. Switching to the ϕ metric as seen in panel (b) of the same figure, separates the heating and cooling measurements as expected. It is now possible to discern a peak in the behaviour of A in the heating branch measurements though there is again a large spread in the data seen here. A does appear to decrease across the measurement range for the cooling branch measurements when plotted against ϕ despite the large spread in the data. Errors on the extracted value of ϕ are not shown for clarity.

Evidently, it is difficult to deduce any meaningful conclusions from the data in its current form. In order to help improve this, a nine point rolling adjacent average which is symmetric about the original point, A^{Av}, is calculated for each point. This average

is weighted by the errors associated with each of the points. A^{Av} is plotted against T_{Eff} and ϕ in panels (c) and (d) of Fig. 6.4 respectively. It is seen that the inclusion of points in which $A \geq A_{\mathrm{FM}}$ has no effect on the results of A^{Av} and are included here for completeness.

Performing this analysis reveals that A^{Av} when cooling has an undulatory behaviour, showing what appear to be two peaks in the data, a large peak at around $T_{\mathrm{Eff}} \sim 340$ and a smaller peak at $T_{\mathrm{Eff}} \sim 350$ K, with an overall decrease across the temperature range. The heating branch measurements appear to have a peak at around $T_{\mathrm{Eff}} = 352$ K. The same behaviour is seen when converting to the ϕ^{Av} metric in panel (d). Interestingly, only a single measurement is consistent with A_{FM} within error bar and this occurs in the peak at ~ 340 K when cooling. As the deviation in the FM fraction is small, the corresponding change in A either implies that the AF phase contributes to the behaviour seen here or that the values of A extracted using this method are unreliable.

To test whether these numbers can be believed, SWR measurements were performed at a series of temperatures on a 380 nm Py film in order to compare this to literature values. All aspects of the measurements on Py are the same as those performed on FeRh, except now the transmission of the RF current through the sample is measured using a nanovoltmeter rather than a VNA. All aspects of this experiment are the same as those listed for the Py experiment in the previous chapter. Examples of the spectra taken at $T_0 = 301$ K at different fields can be seen in Fig. 5.5(a), with the $\mu_0 H_{\mathrm{Ext}} = 1.2$ T isolated with the peaks labelled for their assigned mode number in Fig, 6.5(a).

Here, it is again taken that odd and even PSSW modes can be excited due to asymmetric boundary conditions and that there is negligible out-of-plane anisotropy in this system which means that g and $\mu_0 M_{\mathrm{Eff}}$ extracted from the FMR measurements can be used directly in the calculation of the exchange stiffness of Py, A_{Py} [64]. A summary of the frequencies for a PSSW excitation of a given mode is plotted against the assigned mode number in panel (b) of Fig. 6.5, with the error weighted average value of A_{Py} for each temperature set shown in panel (c) of the same figure. This yields a value of $A_{\mathrm{Py}} = 10.6 \pm 0.1$ pJm^{-1} with gives excellent agreement with the value of $A_{\mathrm{Py}} = 10.7 \pm 0.2$ pJm^{-1} measured by Schoen *et al.* at room temperature, when taking the value of $g = 2.11 \pm 0.01$ measured by Shaw *et al.* [64, 129]. The decrease of A_{Py} with temperature is also expected [70].

The literature value quoted here was extracted by looking at the real and imaginary

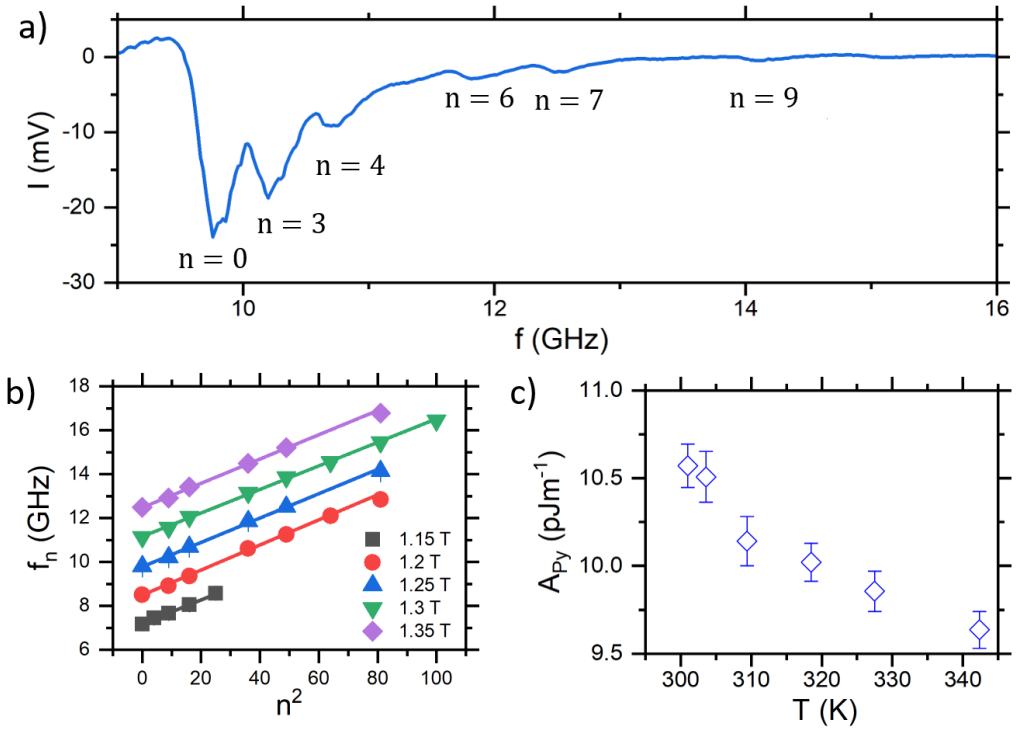

Figure 6.5: Spin-Wave Resonance in a 380 nm Py film. Panels (a) shows the SWR spectra taken at $\mu_0 H_{\mathrm{Ext}} = 1.2$ T at $T = 301$ K, already shown in Fig. 5.5(a), now with the labelled PSSW mode peaks. Panel (b) shows the frequencies of the mode number, f_n, plotted against the square of the mode number, n^2. This is used to extract the values of the exchange stiffness for Py, A_{Py}, seen in panel (c) using equation 6.8. These values of A_{Py} agree well with previously measured values using the same technique [64].

parts of the S_{21} trace [64]. The agreement between the value of A extracted using the two methods confirms their equivalence with regards to the extraction of A. For the Py analysis, the mode numbers are assigned using the same method used for the FeRh measurements. There are again mode numbers that are missing, which will be addressed in greater detail later. Despite this the value of A_{Py} is consistent with literature in which consecutive modes are assumed [64]. This adds credence to the method used here for the mode number assignment. The agreement between the value of A_{Py} extracted here and that presented in literature means that the method used to calculate the values

of A is reliable and therefore the behaviour seen when measured in A is measured for FeRh is real and is a consequence of the system behaviour.

All measurements presented here for FeRh are taken at points in the transition in which $\phi < 1$, which means that AF material will be present in the system. It is important here to acknowledge that these values are calculated using the size of the entire film thickness. If these objects were trapped in the FM region then the t used in the calculation of A would become t_{FM}, which would mean that the exchange stiffness of the system in this scenario would be equal to A/ϕ^2, assuming that the trilayer model applies and that the AF region doesnt contribute. In theory, if this was the case, then A_{FM} should be recovered across the measurement range. However, reperforming the calculation of A with this in mind, reveals the same behaviour as that seen for A^{Av}, with only a single point being within error bar with A_{FM}. This implies that the behaviour extracted using the assumption that the excitation passes through the entire thickness is real and its use is validated. In this case, it is clear then that even a modest amount of AF material is reponsible for deviations from the value of the fully FM phase for the measured value of A for this material. Therefore the AF phase clearly contributes to the behaviour seen here. However, it is unclear as to how the measured exchange constant corresponds to the exchange energies of the two magnetic phases at this stage. To try and quantitatively evaluate how the introduction of the AF layer affects the exchange energy within the entire system, the trilayer model is introduced here in a similar fashion to the FMR experiment.

6.2.2 Spin-Wave Resonance in the Trilayer Geometry

Firstly, it important to note that when applying the trilayer geometry to this scenario it may indeed be possible to see PSSW's that have been confined to the FM regions. If this was the case according to equation 6.8 as $t \geq t_{\mathrm{FM}}$ and $t_{\mathrm{FM}} \propto \phi$, PSSW's confined to the FM region would lead to a larger values of A with decreasing ϕ, which is clearly not the case. Therefore, the PSSW excitation is not confined to the FM region and must travel through the AF layer across the whole film thickness. In order to properly understand the behaviour of A measured here, the contribution of the AF layer must also be taken into account. To do that, we must now consider SWR in magnetic multilayers.

It has been previously established by van Stapele *et al.* that for a system of al-

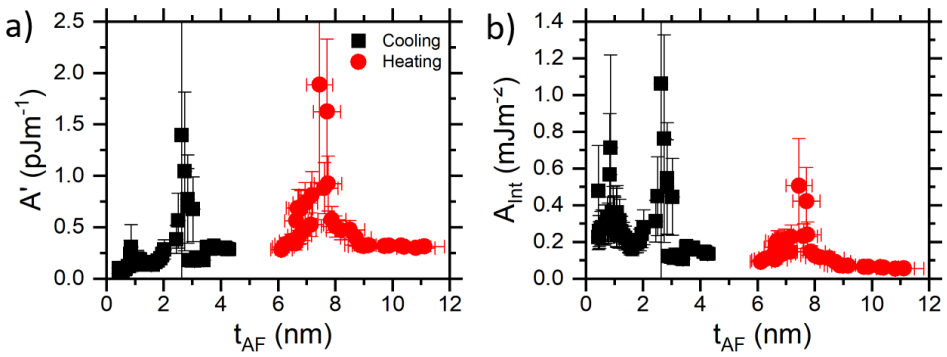

Figure 6.6: Behaviour of A' and A_{Int} against t_{AF} through the transition. Panel (a) shows the behaviour of A' against t_{AF}, whilst panel (b) shows the behaviour of A_{Int} against the same metric.

ternating magnetic layers that are exchange coupled across the interface, driven at the resonant frequency of one of the layers but not the other, that the exchange coupling across the interface will begin to contribute to the measured value of A [67]. The influence of the interfacial exchange coupling now means that the measured exchange stiffness becomes a volume weighted average of the exchange stiffness' of each of the different regions across the entire film thickness [67]. In practice, what is measured is an effective exchange stiffness across the film thickness, A_{Eff}, is which comprises contributions from each of the different regions within the system [67].

This model was derived originally for two FM layers in contact with each other and assumes that there will be a magnetic moment in both layers [67]. However, in order for this model to be applicable all that is required is an exchange stifness in each region and an exchange coupling between them [67]. Therefore, van Stapele's model is believed to apply to this material system in which the layer not driven at its resonant frequency is AF.

If we assume the trilayer geometry outlined in the previous chapter applies here, then we have two FM layers separated by the AF layer. Each of the FM layers is taken to have the exchange stiffness A_{FM} measured for the fully FM state in the T_{C} experiment. Contributions of the AF layer to the behaviour of A_{Eff} are denoted by A' which is the exchange stiffness in the AF layer. In the model proposed by van Stapele *et al.* the strength of the interfacial exchange coupling, A_{Int}, is determined by the

properties of the layer that is not held at its resonant frequency, the AF layer in this case, via [67],

$$A_{\text{Int}} = \frac{2A'}{t_{\text{AF}}}. \tag{6.11}$$

It is then possible to explicitly evaluate the measured effective exchange constant across the film thickness as [67],

$$A_{\text{Eff}} = \frac{t_{\text{AF}} + t_{\text{FM}}}{\frac{t_{\text{AF}}}{A'} + \frac{t_{\text{FM}}}{A_{\text{FM}}}}. \tag{6.12}$$

It is important to note here that this form of A_{Eff} assumes that the wavevector in the system is small and the spins at the interface are free and are coupled across the interface between the two magnetic phases via a strong exchange interaction [67]. This equation comes from a derivation in the van Stapele work where the spins experience a modulated magnetic anisotropy at the interface between the two layers, something which is believed to be the case in this system due to exchange coupling. In the van Stapele work, it is made clear that this form of the equation is an approximation [67]. However, it is tested against values that are calculated using numerical means and then tested against a couple of Py/Ni multilayer samples and good agreement is seen between that predicted by this model and that measured in the experiment [67]. Py has been seen to have pinned spins at the interface meaning that the assumptions that lead to this form of equation 6.12 are not strictly true, however this approximation gives good agreement with the values calculated numerically using the correct boundary conditions [64, 67]. The size of the wavevector in the van Stapele work is comparable to those seen in this work and so the assumptions that lead to this equation are believed to be satisfied so that it can be used in this work.

By using the explicit forms of t_{AF} and t_{FM} defined by the trilayer model, it is possible to rearrange equation 6.12 to directly evaluate A' such that

$$A' = \frac{A_{\text{Eff}} A_{\text{FM}} (1 - \phi)}{A_{\text{FM}} - \phi A_{\text{Eff}}}. \tag{6.13}$$

As it is again the influence of the AF region that is under investigation here, the values of A' calculated using this equation with the values of A^{Av} are shown against t_{AF} in Fig. 6.6(a). $A' \neq 0$ implies means there is an exchange stifness in the region defined by the magnetization as being AF and that a spin-wave is present in this region. On cooling, A' is seen to increase with increasing t_{AF} and appears to saturate at $t_{\text{AF}} \sim 1$ nm, which is a similar thickness to that associated with the start of the TDPT in the AF layer used to explain the behaviour of g_{AF} and α in the previous chapter. The

value of A' then increases in a peak like object at $t_{\mathrm{AF}} \sim 3$ nm, a thickness consistent with the dip in α seen in the previous chapter.

Interestingly, the heating branch measurements also show the same value for most of the points included in the measurement range. This is apart from the apparent peak like object that appears at around $t_{\mathrm{AF}} \sim 8$ nm. It is worth noting here that the end of the data sets here marks the point at which it was no longer possible to identify the SWR peaks against the noisy background and the signal is assumed to be lost.

In the previous chapter the peak in α and a possible saturation of g_{AF} were attributed to a TDPT that takes place in the AF layer with increasing thickness. These data show that this TDPT brings with it an exchange coupling across the MPB which may induce a non-zero magnetic moment in the region defined by the magnetization as being AF. The behaviour of A' here shows an increasing exchange energy that saturates over the same thickness range. This behaviour is consistent with that expected of the TDPT and the results of the previous chapter. This means that the source of the FM exchange energy seen within the AF is the weakened region of FM material at the MPB. Contributions to A' from this region at the interface would be expected on both transition branches.

It is now possible to compare the behaviour of A^{Av} in Fig. 6.4 to that of A' in Fig. 6.6(a)to try and ascertain the source of the undulation seen in A^{Av}. The first peak in A^{Av} to consider is that seen at $T_{\mathrm{Eff}} \sim 350$ K, which corresponds to $t_{\mathrm{AF}} \sim 1$ nm. No peak in A' is seen at this stage, instead this thickness agrees well with the initial increase in A'. This point also agrees well with the thickness at which the value of g_{AF} is seen to increase in Fig. 5.10(b) in the previous chapter. As the thickness dependent behaviour of g_{AF} seen in the previous chapter is attributed to the development of an exchange coupling across the MPB as a consequence of a TDPT in the AF layer, the increase in A^{Av} here is believed to correspond to the point in the transition in which the exchange coupling across the MPB begins to develop. The induced moment in the AF then contributes to the measured value of A causing the peak seen here.

The second peak in A^{Av} is seen at around $T_{\mathrm{Eff}} \sim 340$ K, which corresponds to $t_{\mathrm{AF}} \sim 3$ nm. This agrees well with the dip in α seen in Fig. 5.13(d) in the previous chapter, as well as the peak in A' also seen. The consistency in length scales between these three objects suggests that the decrease in α contributes to the behaviour of A' and ultimately A here. As there is no evidence for the confinement of the PSSWs

within a FM layer, it is taken that the PSSW excitation must pass through the AF layer. The change in A' at this stage suggests that a change in the properties of the AF layer increases the exchange energy in the layer at this point. Further investigations are required to ascertain why this is the case.

Upon heating, the peak in A is seen at temperatures that correspond to $t_{\mathrm{AF}} \sim 8$ nm. Again, this peak is reflected in the behaviour of A' and is not mirrored by any changes in α. The asymmetry in the position of the dip in α implies that the properties of the AF layer are dependent on the temperature sweep direction.

Using the values of A' calculated here it is also possible to directly evaluate the strength of the interfacial exchange coupling across the MPB A_{Int}, which is plotted as a function of t_{AF} in Fig. 6.6(b). A_{Int} clearly shows that an exchange energy is present in the AF region which decays across the thickness range probed here. Again, the peak in A' at $t_{\mathrm{AF}} \sim 3$ nm when cooling and $t_{\mathrm{AF}} \sim 8$ nm when heating are also seen here, and appear to be superimposed upon the decaying profile. No peak in A^{Int} is seen at $t_{\mathrm{AF}} \sim 1$ nm, which is consistent with the idea that it is a direct consequence of the exchange coupling across the MPB and not due to the damping. This measurement constitutes the first direct evaluation of the strength of the exchange coupling between the two phases in the FeRh system.

By using the theory behind exchange coupling outlined in section 2.6 it is then possible to estimate the maximum exchange coupling field to be $\mu_0 H_{\mathrm{EC}} = 7.4 \pm 0.7$ mT. This estimate is ~ 20 times smaller than the value predicted for the field expected due to ME effects and explains why the behaviour of $\mu_0 H_{\mathrm{K}}$ in the previous chapter shows no evidence of interfacial exchange coupling.

Combining the results of this chapter thus far and those of the previous chapter, we have seen evidence for a TDPT in the AF layer that brings about a non-zero magnetic moment in the AF layer through exchange coupling across the MPB. This change then has a profound affect on the behaviour of the exchange stiffness measured through SWR. The behaviour of A' suggests that there is a change in the behaviour of the AF layer at this stage, the origin of which is unclear at this stage. To try and ascertain what this change is in the AF layer, computer simulations of atomistic spin dynamics were performed.

Table 6.1: Parameters used for the atomistic simulations of the MMP regime of FeRh.

Quantity	Value
J_{nn}	0.4×10^{-21} J
J_{nnn}	2.75×10^{-21} J
$D_{q,1}$	0.16×10^{-21} J
$D_{q,2}$	0.23×10^{-21} J
K_{u}	1.404×10^{-23} J
μ_{Fe}	3.15 μ_{B}
$\lvert\mu_0 \mathbf{H}_{\mathrm{Ext}}\rvert$	2 T
$\lvert\mu_0 \mathbf{H}_{\mathrm{RF}}\rvert$	0.05 T
ν	varied GHz
z_{D}	0, 2, 4, 10 & 20
α	1

6.3 Computer Simulations of Atomistic Spin Dynamics

In order to investigate the nature of A' measured here, computer simulations of atomistic spin dynamics were performed in line with the method presented in section 4.5. All simulations presented here were performed by M. Strungaru at the University of York. For this section the candidate can only claim to have been involved in the discussions regarding the development of the simulation concept and the analysis of the subsequent results. These simulations are included here as they are an illuminating way to interpret the SWR data.

As the evaluation of the four-spin interaction is computationally expensive, it is not possible to simulate systems of comparable size to the one used in the experiment. Therefore, it is necessary to create a system of a manageable size that exhibits both magnetic phases in a similar geometry to that used in the experimental model. To achieve this, a region in the centre of the film z_{D} atomic planes thick was chosen to have the strength of its four-spin interaction enhanced ($D_{q,2}$) relative to its surroundings ($D_{q,1}$), such that, for a select range of temperatures, it presents in the AF state when the adjacent regions exhibit the FM state. This creates an FM/AF/FM trilayer consistent

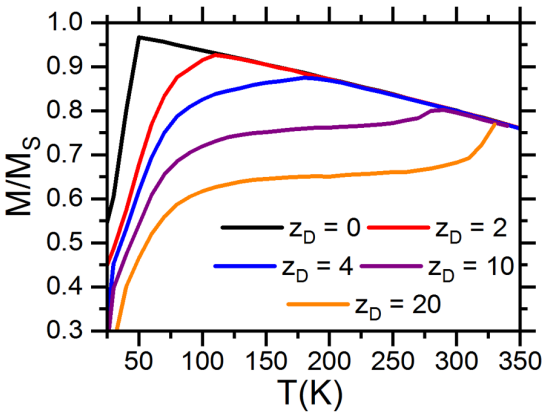

Figure 6.7: Temperature dependent magnetization profiles for a series of z_{D} values on the cooling branch of the transition.

with the model used to interpret the experimental results. Creating the system in this vein allows for direct control of ϕ by varying z_{D} and allows for the study of the effect of the exchange coupling across the interface. The quantities used in the computer simulations are listed in table 6.1.

Temperature dependent magnetization measurements on the cooling branch of the transition were performed for various z_{D} values and are shown in 6.7. Increasing z_{D} appears to elongate the transition and produces a profile qualitatively similar to that of the experimental sample seen in Fig. 5.1(b). The recovery of the magnetization profiles from the simulations is encouraging and the focus now moves to trying to replicate the exchange stiffness behaviour seen in the experiment, for which simulations of SWR were performed.

In the SWR simulations the experimental set up is replicated exactly, with a large external field $\mu_0 H_{\mathrm{Ext}}$ applied perpendicularly to the film plane, an oscillating RF field $\mu_0 H_{\mathrm{RF}}$ of frequency ν applied in the film plane. The time dependent behaviour of the in-plane magnetization component is studied in response to varying ν and the amplitude of the Fourier transform of this behaviour are used as the SWR spectra. A large surface anisotropy is induced at either edge of the film thickness that pins the spins and creates the boundary conditions necessary for PSSW excitations, This is used to replicate as best as possible the pinning situation in the experiment. These simulations were performed at a variety of temperatures for each value of z_{D}. The

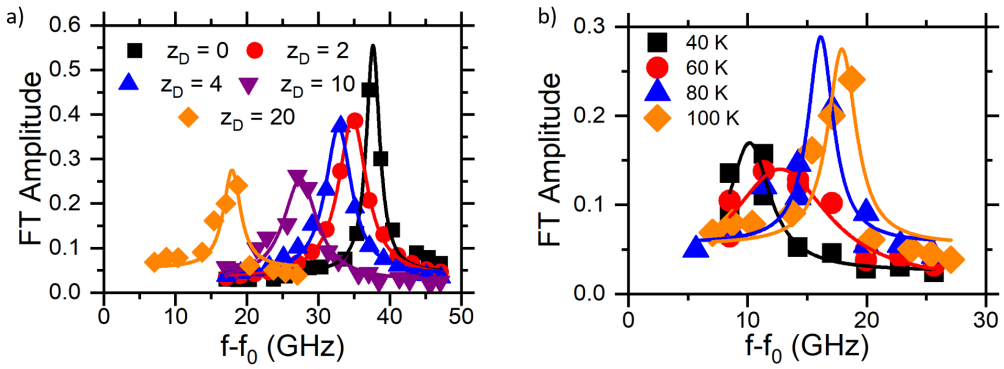

Figure 6.8: Behaviour of the $n = 1$ SW mode extracted from simulations. Panel (a) shows the amplitude of the $n = 1$ mode at 100 K for different values of z_{D}. The resonant frequency is seen to decrease with increasing z_{D}. Panel (b) shows the temperature dependence of the amplitude of the $n = 1$ mode for the $z_{\mathrm{D}} = 20$ system, where a decrease in the resonant frequency with decreasing temperature. Both changing z_{D} for a given temperature, and changing the temperature for a given z_{D} are equivalent to varying ϕ. Both figures here indicate that the exchange stiffness across the film thickness decreases with decreasing ϕ. Both the results of simulations (points) and Lorentzian fits to the data (solid lines) are shown.

results of this investigation are shown in Fig. 6.8.

Fig. 6.8(a) shows the behaviour of the $n = 1$ PSSW mode for the different z_{D} at 100 K. Keeping the temperature constant and varying the size of z_{D} in this way is analogous to varying ϕ and therefore t_{AF}. The lower values of z_{D} have a higher frequency for the position of the first PSSW mode when compared to the higher z_{D} values. These results mean that a smaller value of A_{Eff} is present for a larger value of t_{AF}. Fig. 6.8(b) shows the temperature dependence of the SW mode for the $z_{\mathrm{D}} = 20$ system and shows that the frequency of the first PSSW mode increases with increasing temperature. The behaviour seen within the simulations is consistent with the general increase in A^{Av} across the temperature range seen in the experiment. The differences between the size of the resonant frequency in the experiment and the simulations is attributed to the differences in thickness, whilst the difference in temperature is due to the much smaller system size for the simulations compared to the experiment.

The simulations of SWR have been able to replicate the behaviour of A_{Eff} across the

film thickness seen in the experiment. So now the focus moves to trying to demonstrate the intermixing of magnetic phases at the boundary between them.

6.3.1 Nature of the Interfacial Region

Using this simulation engine it is possible to visualize the magnetization at every point in the system. Doing this will allow for visualization of the spin structure at the MPB and if there is a region of weakened FM in the AF region. To achieve the visualization of the spin structure, field cooled simulations were performed in which the system is cooled in a $\mu_0 H_{\mathrm{Ext}} = 2$ T from 750 K to either 100, 120 or 140 K. The cooling took place within 1 ns and the system was left to evolve for the same time again, by which time the system had reached equilibrium. The damping parameter used here is $\alpha = 1$ to help minimize the simulation time. An example output of the equilibrium spin configuration is shown in Fig. 6.9 for the $z_{\mathrm{D}} = 10$ system at 100 K.

The component of the magnetization in the x, y, z directions is shown for each point in the simulation system in Fig. 6.9. The colour at each point represents the strength and direction of the magnetization at that point in the system, with the corresponding scale shown on the right hand side of the figure. The region defined by z_{D} (between green lines) clearly demonstrates AF order with its spin-axis lying within the film plane, with regions of FM material whose magnetization points along the z-direction perpendicular to the AF spin axis present at either end of the system. This is in line with the prediction made in the previous chapter as to the arrangement and orientation of the magnetic phases that is responsible for the exchange coupling seen in that chapter. The region in between the two magnetic phases however demonstrates a disordered spin-structure in which both magnetic phases are present to some extent. This is suggestive of intermixing of the two magnetic phases within the MPB as consistent with the behaviour of g_{AF} seen in the previous chapter. This intermixing is thought to be brought about by an exchange coupling between the two magnetic phases that blurs the boundary between them.

Throughout the analysis of the FMR and SWR experiments using the trilayer model, all of the properties of the FM layer have been assumed to be constant throughout the measurement range and that all changes in the system are due to changes in the AF layer. According to Fig. 6.7 the $z_{\mathrm{D}} = 10$ system should exhibit $\phi \approx 0.7$ at $T = 100$ K. The simulation shown in Fig. 6.9 has 58 points in the z-direction, t_{AF}

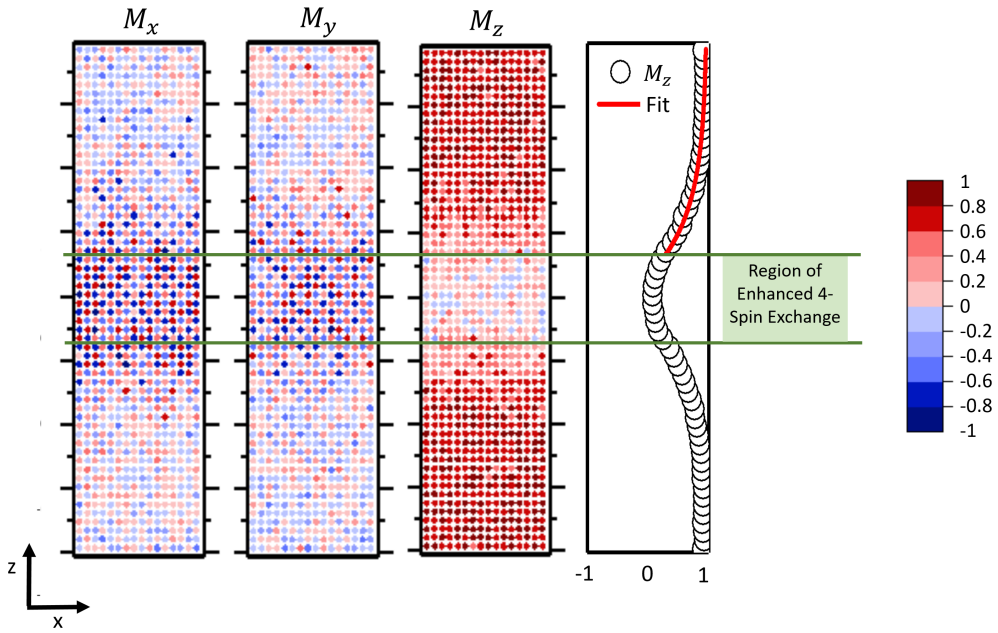

Figure 6.9: Example simulation output for $z_D = 10$ system in an equilibrium state after field cooling from 750 to 100 K. Each of the magnetization components are presented and labeled here alongside M_Z (hollow circles) which has been fitted for penetration of FM order into the AF regions (red line). Each point here represents the strength and direction of the magnetization at that given point in the system. The scale used to colour these points is shown by the colour bar on the right hand side of the figure. The region of enhanced four-spin exchange is marked in green. This system is $16 \times 16 \times 58$ spins.

should be 18 layers at this stage. This includes the 10 layers described by z_D and leaves 8 layers left over, 4 either side of the region encompassed by z_D. It is clear from Fig. 6.9 that it is these 4 layers either side of the z_D region that exhibit this disordered spin structure rather than as an AF as predicted by the magnetization. Therefore, the exchange coupling across the MPB favours the stablization of the FM phase within the region defined by the magnetization as being AF, so that it presents as a region with intermixed magnetic phases. This finding is consistent with the behaviour presented in the previous chapter in which the exchange coupling is believed to induce a magnetic

moment in the AF layer.

It may be then that this region of intermixed magnetic phases in the AF accounts for the behaviour of A' seen in the experiment. This region of intermixed magnetic phases at the boundary was used to explain the behaviour of the spectroscpoic splitting factor seen in the previous chapter. However, the values of g_{AF} may saturate at a given t_{AF}, which implies that the intermixed region has a finite size and for thicknesses greater than the maximum size of this region that bulk AF material is present. This behaviour is also implied by the saturation of A' at around $t_{\mathrm{AF}} \sim 1$ nm. In order to quantify the length scales of the intermixing of magnetic phases across the interface the depth dependent M_{Z} profile is fitted to the equation

$$M_{\mathrm{Z}}(z) = M - \Delta e^{-\frac{z}{z_{\mathrm{P}}}}, \tag{6.14}$$

where z is the atomic layer index, M is the order parameter of the magnetization in the FM layer, Δ is the amplitude of the penetration in terms of the magnetization and z_{P} is the characteristic penetration depth of the magnetic moment into the AF layer. As all of the values of the magnetization are normalized to the value of S for each atom, M and Δ have no units and are themselves normalized in the same fashion. These fittings go from the region defined by z_{D}, which is taken to be bulk AF where no intermixing is expected, and track the magnetization out in to the FM phase. The results of this fitting averaged over 20 time-steps are shown in Fig. 6.10. An example of one of these fits (red line) to the magnetization profile (hollow circles) is also shown in Fig. 6.9.

From Fig. 6.10(a), M is constant for all of the values of z_{D} for each temperature and decreases with increasing temperature. Δ is shown in Fig. 6.10(b) to increase with the size of z_{D} and appears to have saturated by $z_{\mathrm{D}} = 10$. The same can also be said of z_{P}, which shows that between 2 and 5 atomic layers outside of the region encompassed by z_{D} present in as a region of intermixed magnetic phases due to the exchange coupling across the interface. For both of these quantities the decreasing value with temperature signifies the increasing proximity to the completion of the transition and the reduced strength of $D_{i,j,k,l}$ with temperature.

The maximum value of $z_{\mathrm{P}} = 4.2 \pm 0.4$ atomic layers agrees well with the value predicted just by counting the number of AF layers performed previously and the rigid behaviour of the FM phase is again believed to be valid here. Where rigid here means that all of the changes come in the AF layer and the FM layer is impervious to perturbations of its properties. As this is only for a single boundary and there are

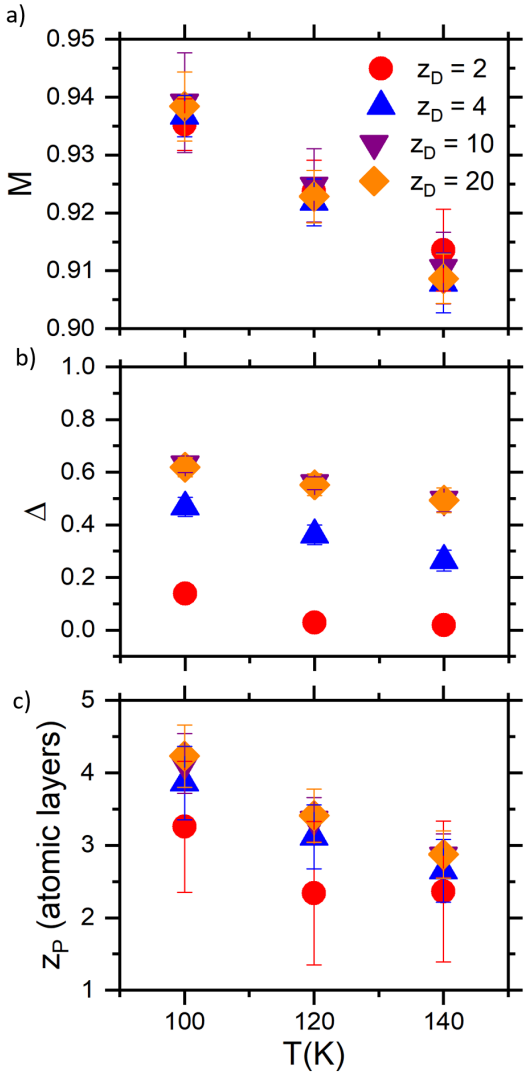

Figure 6.10: Penetration fitting results. (a), (b) and (c) show the results of the fitting for the length scale of the FM exchange outside of the region encompassed by z_{D} for the magnetization order parameter in the FM regime, M, the amplitude of the penetration, Δ, and the penetration distance, z_P, respectively.

two present in the trilayer model, the maximum size of the AF layer that can exhibit this intermixed magnetic states is believed to be twice that for a single boundary and yields a real space distance of $t_{\mathrm{Int}} = 2.6 \pm 0.2$ nm, when calculated using the value of

a extracted from the XRD. For AF thickness in excess of this value bulk AF material is expected to be present.

The behaviour of α seen in Fig. 5.13(d) in the previous chapter suggests that a TDPT occurs within the AF layer, which brings with it an exchange coupling across the MPB. This is then thought to induce a magnetic moment in the AF layer that then contributes to the measured value of g in that experiment. These simulations demonstrate that the AF layer can be described by an intermixing of magnetic states due to the exchange coupling across the MPB as predicted by the behaviour of g_{AF} in the previous chapter. The qualitative agreement between the behaviour seen in the experiment and that seen in the simulations presents a strong case for the development of an exchange coupling across the MPB due to a TDPT in the AF layer causing an intermixing of magnetic states being the origin of the behaviour seen thus far. This statement is made under the assumption that the magnetic configuration can be described using the trilayer model.

However, the origin of the peak in A' is unknown and to try and identify this behaviour, the focus is moved to how the PSSW excitations pass through the AF layer.

6.3.2 Spin Transfer Through The Antiferromagnetic Layer

In the simulations, all materials are considered to be insulators. The non-zero value of A', which is the exchange stiffness seen in the AF region, implies that a spin-wave is present in the AF layer that carries the PSSW through it. This has been seen previously in literature and is attributed to the excitation of evanescent spin-waves (ESWs) in the AF layer due to coupling across the interface [72, 138, 146, 147].

Previously in experiments performed on AF/FM bilayers have seen the AF insulator materials transmit spin-currents through distances of up to ≈ 10 nm, when the system is held at the resonant frequency of the FM layer [72, 138, 146, 147]. It has been theorized that the resonant excitation of the spins in the FM layer and the exchange coupling at the interface cause excitations of the Neél vector in the AF [72]. The Neél vector $\mathbf{L}$ is defined as [72, 147],

$$\mathbf{L} = \frac{\mathbf{m}_1 - \mathbf{m}_2}{M_{\mathrm{S}}}, \tag{6.15}$$

where $\mathbf{m}_{\mathrm{i}}$ denotes the magnetization of the various sublattices. The frequencies associated with the excitation of antiferromagnetic resonance (AFMR), f_{AF}, which corres-

pond to the resonant frequency for coherent excitations of **L** is given by [68]

$$f_{\mathrm{AF}} = \frac{\mu_0 \mu_{\mathrm{B}} g}{h} \sqrt{H_{\mathrm{K}}(H_{\mathrm{K}} + 2H_{\mathrm{Ex}})}, \tag{6.16}$$

where $\mu_0 H_{\mathrm{Ex}}$ is the size of the exchange field that one sublattice exerts on the other and $\mu_0 H_{\mathrm{K}}$ is the anistropy field [68]. These fields can be as large as 100 T in AF materials and so these frequencies are far larger than those associated with FMR [68]. As such, the excitations of the Neél vector are evanescent and travel a finite distance, λ, through the AF layer which is given by [72]

$$\lambda_{\mathrm{ESW}} = \frac{c}{\sqrt{f_{\mathrm{AF}}^2 - f_n^2}}, \tag{6.17}$$

where c is the speed of the spin-wave in the AF layer. Due to their short-lived nature, these excitations of the Neél vector are known as evanescent spin-waves (ESW) [72].

In order to test whether ESWs are seen in the simulations and if they carry the PSSW excitation through the AF region, the Fourier transform of both **L** and the magnetization $\mathbf{M} = (\mathbf{m}_1 + \mathbf{m}_2)/M_{\mathrm{S}}$ is calculated as a function of z through thickness of the $z_{\mathrm{D}} = 20$ system at $T = 120$ K. Each component of these quantities is shown as a function of z in Fig. 6.11. The region defined by z_{D} is again shown in green and there is a clear non-zero value of the amplitude of the Fourier transform for each component of **L** in this region. Also, the amplitude of the Fourier transform for the in-plane magnetization components are non-zero through the entireity of the region defined by z_{D}. In this figure the symmetry is broken between x and y directions for **L** but not **M**, implying that there is an in-plane anisotropy in the AF layer that is not present in the FM layer, though further investigations are required to say for certain. As no intermixing is seen in the z_{D} region previously in the simulations, this observation of the non-zero components of **M** within this region, combined with the observation of a non-zero **L** in this region, indicates that ESWs are present in the AF regions and act to pass the PSSW excitation through the AF layer.

The observation of ESWs in the simulations is strongly suggestive of an exchange coupling between the AF/FM layers in this system. The observation of PSSW excitations in the simulations, suggests that the ESW are responsible for the carrying of the PSSW excitation through the AF layer, as all materials are considered as insulators here. Evanescent excitations are known to follow an exponential decay in the region into which they are injected. So, by fitting the decay of M_{x} seen within the

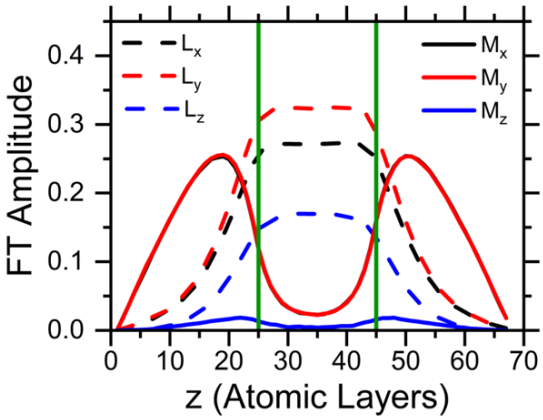

Figure 6.11: Investigations into spin-transfer through the AF layer using ESWs. The Fourier transform of each directional component of **L** , dashed lines, and **M**, solid lines, as a function of z through the $z_{\mathrm{D}} = 20$ at $T = 120$ K. The region defined by z_{D} is situated within the green lines. The system here is a $16 \times 16 \times 68$ spin system. The non-zero component of **L** and **M** with z_{D} suggests that ESWs are present there that help to carry the PSSW excitation through the AF layer.

region of enhanced z_{D} for the ESW seen in Fig. 6.11 gives a characteristic real space distance of $\lambda = 1.1 \pm 0.1$ nm. This is much smaller than the characteristic length scales seen of the decay of the spin-currents carried through NiO via the same mechanism [72, 138, 146, 147]. For the $z_{\mathrm{D}} = 20$ system in which this measurement is performed, the bulk AF layer is around 5 times that of λ and PSSWs are still observed. Therefore, the ESWs in this simulation can carry PSSW excitations through AF layers that are large compared to their decay length.

For the experiment, we know that there is angular momentum transfer through the AF layer as a non-zero value of A' is measured. Both magnetic phases of FeRh are metallic and so both electron and magnon spin-pumping would also be expected to contribute to any angular momentum transfer through the AF layer here.

ESWs require the presence of an **L** vector and an exchange couping across the interface in order to be actualised [72]. Therefore, it is fair to assume that these would only appear in the system after the TDPT has completed and bulk AF material is present. This point is determined by the behaviour of α and g_{AF} and is believed to lie between $t_{\mathrm{AF}} \sim 2$ and 5 nm. This thickness regime corresponds to a peak in A'

seen. The introduction of ESWs would increase the spin-current in the AF layer and increase the exchange energy in this region, which would explain the peak in A' seen when cooling here.

The signal in the SWR experiment for measurements on the cooling branch becomes indistinguishable from the background for thicknesses greater than $t_{\mathrm{AF}} \sim 4$ nm. If this is the point at which the signal drops out in Fig. 6.6(a) and is not a consequence of the artefacts within the data concealing the real behaviour, then this would give a length scale for the travelling of these ESWs through the AF layer that is qualitatively comparable to that predicted by the experiment. The linear increase in α seen out to 10 nm when cooling in Fig. 5.13(d) suggests that a spin-current is present up to these AF layer thicknesses. This would imply that, at least in theory, the spin-current could carry the PSSW excitations through the AF layer up to these thicknesses. It is not possible to say for certain at this stage why the PSW signal is lost when cooling.

The PSSW excitations when heating are seen out to $t_{\mathrm{AF}} \sim 12$ nm in Fig. 6.6(a), which is well in excess of the 4 nm where the signal is lost on the cooling branch. In the previous chapter it was postulated that the dip in α seen on the heating branch could correspond to a TDPT if the properties of the AF layer are different depending on the temperature sweep direction. The dip in α seen on heating in Fig. 5.13(d) appears at $t_{\mathrm{AF}} \sim 10$ nm, which does not align exactly with the peak in A' seen in Fig. 6.6(a) which is seen at $t_{\mathrm{AF}} \sim 8$ nm. However, the PSSW signal is also lost not long after the dip in a similar manner to that seen on the cooling branch. As the loss of the PSSW signal when cooling is attributed to the inability of the PSSW to pass through bulk AF material, the consistency between the behaviour on the two transition branches implies that the same happens on the heating branch. This implies that the AF layer undergoes a TDPT when heating at a different thickness to that seen for the cooling arm, which is consistent with the hypothesis of the previous chapter in that the AF layer has different properties depending on the temperature sweep direction. Further investigations are required to say for sure if this is the case.

Before concluding the chapter there are several points raised in this work that require further discussion. The first of which is the apparent supression of PSSW modes, which appears in both the analysis of the FeRh and the Py seen in this experiment. Our discussion on this point will begin with Py as this is the simpler system. Previously, in literature analysis of the PSSW modes in Py has been assumed to contain modes

where the wavevector can be described by an integer number of half wavelengths, where consecutive exctiations have consective mode numbers assigned to them [64]. The pinning conditions in SWR experiments are complicated and the half wavelength modes are a good way of removing these complications. However, as the approach in which consecutive modes are assumed and the method used in this work, where this is not the case, yield values consistent within error bar for the desired quantities, it is not clear which approach is more appropriate. It is possible that the pinning conditions for the two Py films are not the same meaning modes are supressed in the film measured in this work that arent in the Schoen *et al.* work [64], though this is unclear and further investigations are required.

In FeRh, the pinning picture is much more complicated due to the non-uniform magnetization profile and the presence of the AF material. It may be that these considerations changes the landscape of the available PSSWs and causes a suppression. As the magnetic structure changes the transition, this would also explain why the mode number assignment may also change with it. Again, this is unclear and further work is required to ascertain the validity of this approach.

In the previous chapter, there was concern regarding the value of g extracted and the calibration of the field experienced by the sample. As the Py sample gives values of A consistent with literature, this issue appears not to affect the extracted value of A, meaning the behaviour here is believable.

As is the case with the previous chapter, the conclusions drawn here are all predicated on the assumption that the magnetic state can be described using the trilayer model. Again, all of the behaviour seen here can be explained using this interpretation, and is consistent with the behaviour expected in similar systems. The trilayer model is an idealised interpretation of the phyiscal picture presented by literature investigations and may not be the case in reality. Though other models such as patches of AF material spattered throughout the layer would also see columns of FM material across the whole stack, which again would show values consistent with the fully FM phase, which is not seen here. The simulations here are designed to exhibit a trilayer model consistent with the model used to interpret the experimental results and present similar behaviour, which adds to the credibility of the trilayer model here. However, these simulations also show that the interface between the two magnetic phases is blurred and the validity of the rigid boundary is compromised. It may be more appropriate

to consider the boundary between the two magnetic phases as a layer in its own right that is separate from the FM and AF layers if the analysis was to be reperformed.

The blurring of the boundary makes it difficult to ascertain which of the two layers has its properties changed. In consistency with the previous chapter, all changes in behaviour are assumed to come from changes to the AF layer, which may not be the case in reality. It is likely that the exchange coupling affects both layers, which should be considered going forward. Despite this, assuming the behaviour occurs within the AF phase gives reasonable agreement with the crude method of counting the affected layers employed earlier in the chapter.

Recently, vertical exchange bias and coercivity enhancements have been seen in FeRh using the anomolous Nernst effect [148]. These findings are consistent with the presence of the exchange coupling measured in this experiment and corroborate the results here.

It is also necessary to state here that the assumption that $\phi \neq 1$ at any point is made by neglecting the error on the calculated quantity of ϕ. The error on the calculated value of ϕ is around 5%, most of which comes from the volume in the calculation of M_{S}. This is beleived to artifically induce large error in the calculated value and so is not considered when making the statement regarding the state of the system.

6.4 Conclusions

SWR measurements were used to measure the behaviour of the exchange stiffness A for a Pd-doped FeRh epilayer through the metamagnetic transition. A is seen to be lower than the independently measured mean-field value for this system throughout the measured temperature range, which is believed to be due to the influence of the AF phase. There is also no clear temperature dependence observed for the behaviour of A. The same lack of a temperature dependence is also seen when the behaviour of A is plotted against ϕ. By averaging the behaviour of A across the measurement range it is possible to then show that A has an oscillatory behaviour superimposed on a decrease across the temperature range on both transition branches.

It is then shown that this behaviour can be explained by applying the FM/AF/FM trilayer model in conjunction with models of SWR in magnetic multilayers. No evidence is seen for excitations confined to the FM regions and so the excitation must pass through the AF layer. To do this an effective exchange constant, A_{Eff} is introduced

as a weighted average across the film thickness. This allows for the extraction of the exchange constant of the AF region, A', which shows a non-zero value which increases over length scales consistent with the onset of the TDPT and culminates in a peak at AF layer thicknesses consistent with the dip in α seen in the previous chapter when cooling. A similar peak is seen when heating which does not correspond to any other feature in the experiment thus far.

It was also seen to be possible to directly evaluate the strength of the interfacial exchange coupling across the MPB A_{Int} in this experiment and is the first direct measurement of this quantity within this material system. This also shows peaks consistent with those seen in the behaviour of A' superimposed on a decaying background. This also allowed for the estimation of the strength of the field due to exchange coupling at the interface which is predicted to be $\mu_0 H_{\mathrm{EC}} = 7.4 \pm 0.7$ mT. Such a low value also explains why it was not seen in the behaviour of $\mu_0 H_{\mathrm{K}}$ in the previous chapter.

In order to try and ascertain the source of the A' behaviour, computer simulations of atomistic spin dynamics were performed. It is possible to replicate the change in A_{Eff} seen with decreasing temperature across the film thickness by adopting a FM/AF/FM trilayer geometry in the simulations. Field cooled measurements reveal that there the MPB is blurred due to an exchange coupling between the two magnetic phases. For comparison with the previous chapter, this is taken to be a region of weakened FM exchange within the region defined by the magnetization as being AF, which is consistent with the results of the previous chapter. This weakened FM exchange appears for between 2 and 5 atomic layers away from the area defined by z_{D}. It is seen to saturate at a certain value of z_{D}. This penetration depth corresponds to decays over characteristic distances of 2.6 ± 0.2 nm which agrees well with the length scale set out by the TDPT and the associated behaviours of the AF layer seen in this and the previous chapters.

These simulations also reveal that the PSSW excitation is carried through the AF layer by ESWs in the simulation due to the exchange coupling at the interface. In the experiment, contributions from both the electron and magnon spin-pumping would be expected and the peak in A' when cooling can be explained using the introduction of ESWs after the TDPT in the AF layer is complete. The origin of the peak in A' when heating is unclear and requires further investigation.

The conclusions of this work are predicated on the assumption that the trilayer

model accurately describes the magnetic state of the sample through the temperature range probed. The hypothesis is supported by the use of the simulations where the trilayer model is artificially induced and the same behaviour is seen with regards to the change in the exchange stiffness with temperature. However, independent corroboration of the magnetic state is required to say for certain.

Chapter 7

Resonant Magnetic Small Angle X-Ray Scattering Through the Transition

7.1 Introduction

Small Angle X-Ray Scattering (SAXS) is a technique used to characterise objects on the nm length scale [78]. Previously, it has been used to analyse particles in solution, proteins and even the domain size in magnetic thin films [73–75, 78]. By combining SAXS with Resonant Magnetic X-Ray Scattering (RXMS) it has been seen that the signal from magnetic thin films can be enhanced by using X-Ray Magnetic Circular Dichroism (XMCD) in a technique known as Resonant Magnetic Small Angle X-Ray Scattering (RMSAXS) [73]. Thus far this technique has only been utilized with XMCD to measure ferromagnetic (FM) domains [73–75]. However, it is entirely possible that the same experiment can be performed using X-Ray Magnetic Linear Dichroism (XMLD) to investigate the magnetic structure of antiferromagnetic (AF) materials, which is yet to be demonstrated in the literature.

The well established coexistence of the two magnetic phases in FeRh [7, 12, 27, 30–32, 34, 35] makes it the ideal candidate to test whether RMSAXS can be used to measure both magnetic phases and their development through the transition. This chapter will demonstrate that RMSAXS can be used with both XMCD and XMLD to measure the length scales associated with a peak in the radial scattering profile for both the FM and AF phases through the transition. The length scale of this peak changes through the measurement range in a manner consistent with the change in the nature of the scatterer.

Work attributed to the author in this section is the growth and characterization of the sample, all experimental work including those taken at x-ray facilities, as well as the analysis of the data. R. P. Campion is accredited with the growth of the GaAs/AlAs/GaAs substrate, whilst N. A. Peters performed the HF etch of the sheet film to produce the x-ray transparent membranes. The data from the x-ray facilities was taken with the help of R. C. Temple, R. Fan, R. Lamb, T. P. Almeida, D. McGrouther, P. Steadman and C. H. Marrows.

7.1.1 Sample Growth & Characterization

The sample investigated here is a 100 nm NiAl/100 nm FeRh bilayer grown on a GaAs/AlAs/GaAs heterostructure using DC magnetron sputtering. The substrate was annealed overnight at 400°C and the NiAl layer was deposited at this temperature. The stack was then heated to 600 °C where the FeRh layer was deposited, after which,

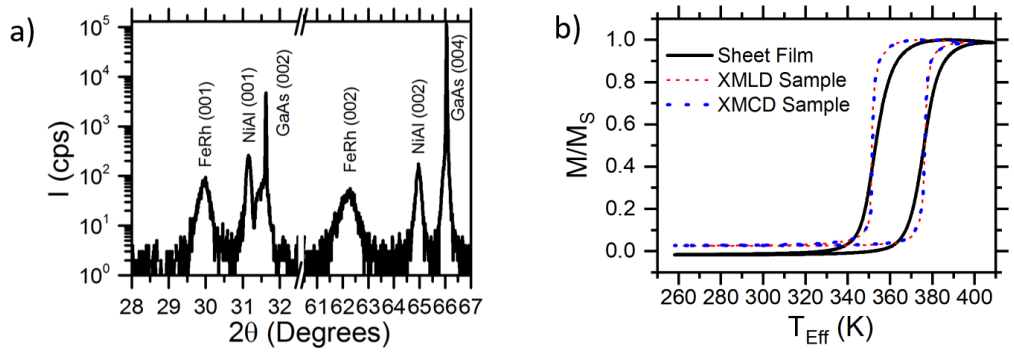

Figure 7.1: Sample characterization results. Panel (a) shows the XRD scan, taken before the sample is made into a membrane, demonstrating both (001) and (002) peaks for NiAl and FeRh implying B2 order is present in both materials. Panel (b) shows the normalized temperature dependent magnetization behaviour both before (black line) and after (red and blue lines) being made into a membrane. These measurements are taken in 1 T field applied within the film plane and are shown against T_{Eff}. The red and blue lines here are used to distinquish between the two samples used in different beamtimes.

the sample was annealed *in situ* at 700°C for 1 hour. NiAl is a B2-ordered material that is used here to alleviate the lattice mismatch strain between GaAs and FeRh and promote ordered epitaxial growth of the FeRh [149].

After growth, the sample was removed from the sputtering chamber and characterized for its structural and magnetic properties, the results of which can be seen in Fig. 7.1. The XRD scan, seen in Fig. 7.1(a), demonstrates the presence of both the (001) and (002) reflections for FeRh and NiAl confirming an epitaxial growth with the presence of B2 order with $S = 0.86 \pm 0.02$ for the FeRh. The magnetometry scan for the as-grown sample, as measured in a 1 T in plane applied field is shown against T_{Eff} by the black line in Fig. 7.1(b).

The μm size magnetic domains in FeRh correspond to scattering angles of $\theta \approx 0.05°$ at the Fe L_3 edge, which are not accessible in the reflection regime [27, 34, 35]. Therefore, in order to access the scattering from these domains, the experiment must take place in the transmission geometry and an x-ray transparent sample is required.

To this end, the samples underwent an etching process, in which hydrofluoric acid

(HF) is used to remove the substrate via the method outlined in section 4.1.2. The substrate here is chosen because the HF will favourably etch the AlAs layer, leaving the GaAs intact [119]. By using methods outlined in Ref. [119] it is possible to remove the substrate and isolate a GaAs/NiAl/FeRh layer. After the AlAs is removed, this layer then floats to the top of the acid, where it is collected between two Cu TEM grids. This creates x-ray transparent membranes of B2-ordered FeRh as required.

After etching, the samples were characterized again for their magnetic properties which are shown by the coloured lines in Fig. 7.1(b). Two membrane samples were used in these experiments, one for the XMCD (red dashed line) with the other for the XMLD (blue dashed line), as the sample used for the XMCD measurements was destroyed between beamtimes. However, both samples are taken from the same parent film and are indistinguishable in terms of the their magnetic properties, as can be seen from Fig. 7.1(b). As the membrane is very fragile, it was not possible to characterize the structural properties of the sample after the etching process.

The survival of the magnetic transition in the membrane samples is clear in Fig. 7.1(b) and confirms that the etching process was successful in manufacturing x-ray transparent (001)-orientated B2-ordered FeRh membranes. The transition of the membrane samples is noticeably sharper than that of the the sheet film which can be attributed to the removal of substrate tension during the etching process.

In Fig. 7.1(b) all of the magnetometry traces are performed in a 1 T field applied within the film plane and are plotted against T_{Eff}. T_{Eff} is calculated using the equation 5.1 using $dT_{\mathrm{T}}/d(\mu_0 H_{\mathrm{Ext}}) = -(8 \pm 0.1)$ KT^{-1} when heating and $-(8.8 \pm 0.1)$ KT^{-1} when cooling, which is measured for this sample. As the measurements in this chapter all take place in the absence of an externally applied field, T_{Eff} is used in Fig. 7.1(b) as the correct temperature reference set.

7.1.2 Experimental Set Up

The measurements presented in this chapter were taken using the RASOR endstation of the I10 beamline of Diamond Light Source. The images were taken using a 2D CCD camera situated 0.8 m downstream of the sample, with a beamstop between the two to prevent the beam from damaging the detector.

To identify the position of the Fe L_3 edge, X-Ray Absorption (XAS) spectra were taken by sweeping the beam energy from 690 eV to 740 eV for both polarization types at

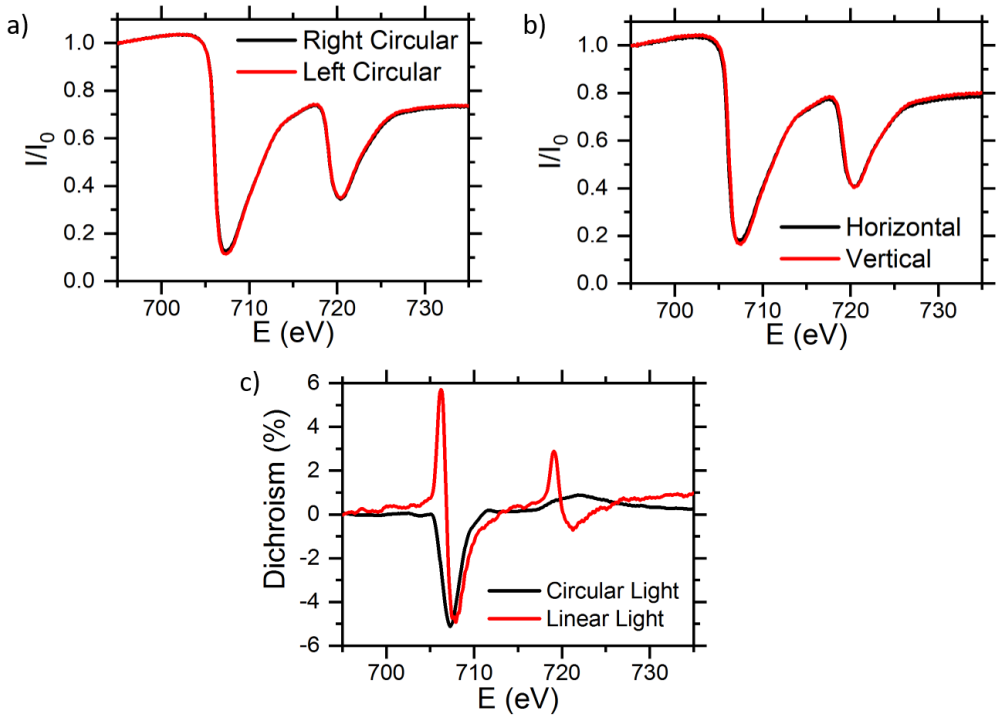

Figure 7.2: Dichroism characteristics in the fully FM phase at 400 K on the heating branch. Panels (a) and (b) show the XAS scans taken using circular and linear light respectively. The two colours demonstrate the absorption spectra for the two orientations of either polarization type. Panel (c) shows the resultant dichroism behaviour for both linear (red) and circular (black) light. These were calculated with the method outlined in section 3.2 using equation 3.18.

400 K, the results of which are shown in Fig. 7.2(a) and (b) for circular and linear light respectively. Each of these panels shows the XAS scans in different orientations used to calculate the energy dependent dichroism profile for each polarization type, which is shown in Fig. 7.2(c). The dichroism, which is calculated using equation 3.18, shows a signal strength of around 6% for both polarization types. The energies corresponding to maximum signal strength are found to be $E_{\mathrm{XMCD}} = 707.4 \pm 0.01$ eV and $E_{\mathrm{XMLD}} = 706.2 \pm 0.03$ eV by the fitting of Lorentzian profiles to the data. For the first beamtime where measurements are performed using XMCD, the beam energy was $E_{\mathrm{XMCD}} = 707$ eV. This is close to the resonance peak and is therefore taken to be comparable to the data taken at $E_{\mathrm{XMCD}} = 707.4$ eV.

The position of the Fe L_3 edge when calculated using XMCD should stay the same through the transition, as the properties of the Fe atom within the FM phase are invariant through the transition [133]. However, given that the FM domain structure of FeRh changes through the transition from domains in the fully FM phase to flux closed structures at the beginning of the transition, it may be that the orbital projection of the orbital in a given direction may change through the transition [27, 31]. This means there may be a temperature dependence of the position of maximum signal for measurements taken using XMLD. However, due to time constraints the energy of the maximum signal for linear dichroism was identified at 400 K and used as the energy throughout the temperature range for XMLD measurements.

After identifying the energy of the Fe L_3 edge, it is possible to move on to demonstrating the presence of RMXS, which is achieved by comparing images taken on and off the Fe L_3 resonance edge for each polarization type. Here, a 20 μm diameter pinhole is moved into the path of the beam and provides the spatial coherence required to observe the speckle pattern. Example images taken with the beam energy both off (690 eV) and on the Fe L_3 edge ($E = E_{\mathrm{XMCD}}$) for circular dichroism are shown in panels (a) and (b) of Fig. 7.3, whilst the corresponding images taken using linear light are shown in panels (d) and (e) of the same figure.

There is a stark difference between the images taken at the different beam energies, with a speckle pattern visible for the images taken at the Fe L_3 energy and no appreciable scattering of any kind seen in the images taken with the beam energy away from the L_3 resonance edge. The difference between the two is confirmed by the radial intensity profiles shown in panels (c) and (f) of Fig. 7.3, for circular and linear light respectively. These demonstrate a much larger intensity for images taken on the Fe L_3 resonance edge compared to those taken off it for both dichroism types. The presence of the speckle pattern in the image taken on the Fe L_3 resonance edge for both polarization types implies that the objects responsible for the scattering are disordered and are sensitive to resonant enhancement of their scattering at the Fe L_3 edge. This is consistent with the scattering from the magnetic domain pattern expected for this stage in the transition [27, 31] and as there is no appreciable scattering seen away from the Fe L_3 resonance edge, the scattering is taken to originate from the magnetic domain structure.

The peak seen at $Q \approx 10-12\times10^{-3}$ Å^{-1} in the radial intensity profiles corresponds

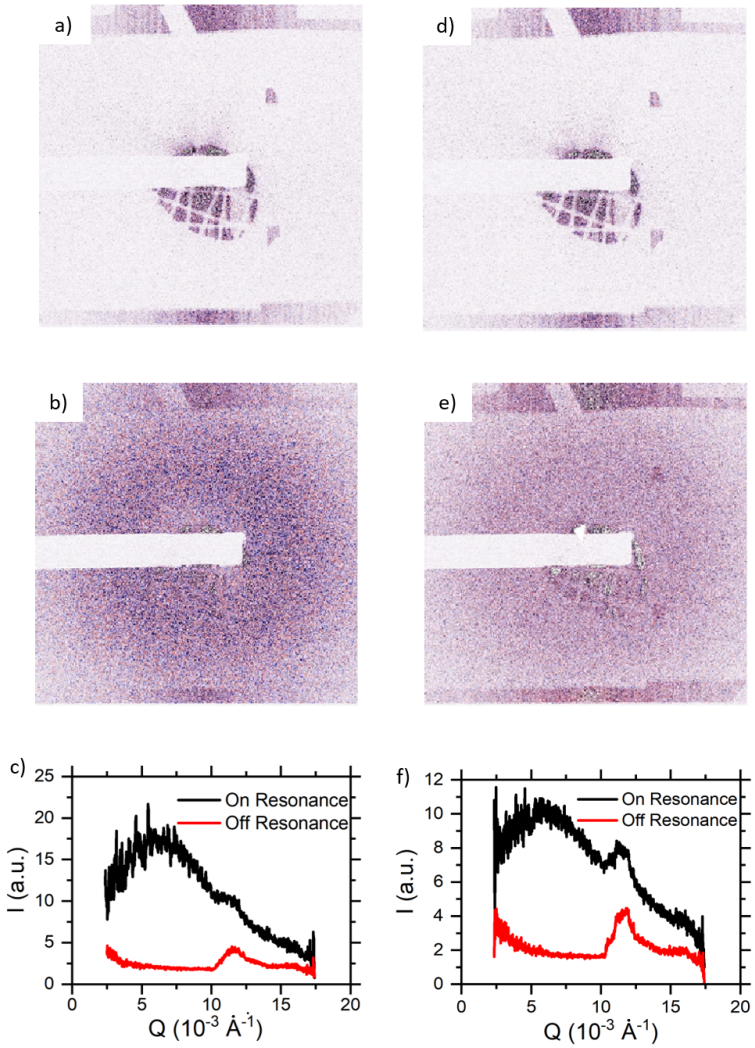

Figure 7.3: Evidence of magnetically sensitive x-ray scattering at 400 K on the heating branch. Panels (a) and (b) show the off and on Fe L_3 resonance images for circularly polarized light, with panel (c) showing the radial intensity profiles, calculated using the method outlined in section 7.2, for both images shown in panel (c). Panels (d) - (f) show the same for the images taken using linearly polarized light. The appearance of a speckle pattern when moving onto the Fe L_3 resonance edge confirms the presence of magnetically sensitive x-ray scattering, evidence of which is also seen in the radial intensity profiles.

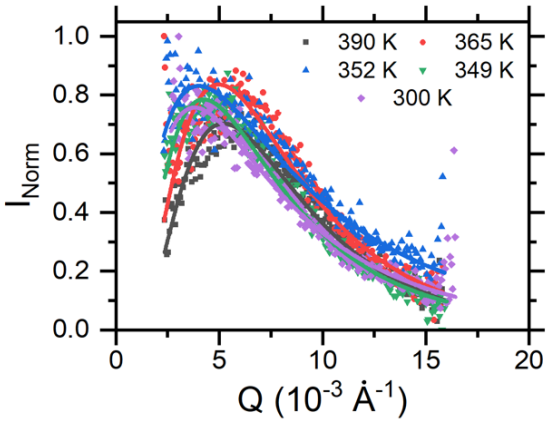

Figure 7.4: Examples of radial analysis curves (points) for various points on the cooling branch when using linear light. These are fitted to a log-normal function to extract the peak position (solid line), the distribution width and the area of the peak.

to spatial length scales of between 30-50 nm. This may be consistent with As rich deposits left on the sample after the etching process, however, the irregular shape of the peak suggests that it is likely to be due to an artefact within the image. This is peak is seen to come from the region of the image where the sample holder no longer covers the camera and can be removed by blocking out that region of the image as can be seen in Fig. 7.4.

7.2 Scatterer Characterization Using Magnetic Small Angle X-ray Scattering

For each of the images used in this experiment, images that use both helicities for circularly polarized light or orientations for linearly polarized light are taken one after the other. Then, as per the method outlined by Fischer *et al.* [73], the images corresponding to the two different light orientations for either polarization type are taken away from the other leaving the dichroic image. Processing the images in this manner should increase the magnetic signal.

The images used in this analysis are the first in the image series used in the calculation of the temporal correlation, the results of which are presented in the next chapter. Each of these images, which are taken at different temperatures, then have their struc-

tural properties analyzed for that point in the transition. In between images series, the temperature is thermally cycled so that the system enters either the fully AF or fully FM phase depending on the transition branch being investigated. This resets the state and protects against changes in the structure due to any possible relaxation behaviour [58]. After resetting the state, the temperature is then changed to the desired temperature for the next measurement. A full and comprehensive description of the method used to take these images is included in section 4.4.1.

The scattering profiles seen in Fig. 7.3 show a diffuse ring like structure, implying an isotropic size distribution of the domain pattern [75]. For systems that exhibit this SAXS pattern, it is possible to take the radial average in Fourier space to reduce the dimensions to that of the magnitude of Q only [75].

These dichroic images are then converted to a radial intensity profile and fitted to an appropriate distribution function to ascertain the stuctural properties. For the purposes of the radial intensity calculation, all possible sources of artefacts within the image are removed before processing. These include the region where the sample holder no longer covers the camera, the projection of the grid in the centre of the image, the beamstop as well as any holes in the sample holder. For the measurements in which a single helicity is used and for images taken using XMCD on one of the two beamtimes, the final 50 pixels have very little signal and are seen to introduce large offsets into the normalized intensity and so are removed from the calculation. It was also necessary to perform this on the measurments taken when cooling in the first XMCD experiment. Performing the analysis in this way leads to intensity profiles such as those seen in Fig. 7.4.

For the radial average calculation $Q = 0$ was taken to be the centre of mass of the image with Q from this point being calculated using equation 3.8. The centre of mass was calculated after the artefacts are removed from the image. Here, it is possible to directly evaluate Q as a function of the number of pixels, n_{P}, by approximating $\sin\theta \approx n_{\mathrm{p}} d_{\mathrm{p}}/x$ with d_p being the size of the individual pixel and x being the sample-camera distance, which leads to,

$$Q = \frac{4\pi}{\lambda}\frac{n_{\mathrm{p}} d_{\mathrm{p}}}{x} = 1.2 \times 10^{-5} n_{\mathrm{P}} \text{ Å}^{-1}, \tag{7.1}$$

where λ is the light of the incoming wavelength. The values used in this calculation are listed in table 7.1.

Table 7.1: Quantities used in the calculation of the scattering vector Q.

Quantity	Symbol	Value
Wavelength	λ	17.6 Å
Pixel dimension	d_{p}	13.5 μm
Sample-Camera Distance	x	0.8 m

All intensity curves have all been normalized using,

$$I_{\mathrm{Norm}}(Q) = \frac{I(Q) - I_{\mathrm{Min}}}{I_{\mathrm{Max}} - I_{\mathrm{Min}}}. \tag{7.2}$$

Normalizing the curves to themselves in this manner removes all dependence on the polarization and the state of the beam and all measurements are then directly comparable with each other. Points that have an error that is larger than 100% of the extracted value are excluded from this analysis as they are deemed to be unreliable and introduce large error into the rest of the measurements. As each of the fits is weighted by their error bars, these points would have little influence on the outcome of the fits and are deemed dispensible. Examples of the radial intensity profiles taken at various points on the cooling branch using linear light are shown in Fig. 7.4 and reveal a peak in the radial intensity, at $Q \approx 6 \times 10^{-3}$ Å^{-1}, with a large width in Q. According to equation 3.29, this is consistent with a peak in the structure factor, with the large width of the peak in Q corresponding to large variations in the size of the domains [75, 112].

Previously in literature, peaks in the structure factor for SAXS experiments have been fitted to log-normal distributions [73] and this distribution is also used to fit the intensity curves in this chapter and uses the form,

$$I_{\mathrm{Norm}}(Q) = c + \frac{1}{\sqrt{2\pi\omega Q^2}} e^{-\frac{(\ln(Q/Q_0))^2}{2\omega^2}}, \tag{7.3}$$

where c is the offset, ω is the log of the FWHM and Q_0 is the centre of the distribution. All fits were performed with the offset fixed at 0 as dictated by the normalization procedure. The log-normal distribution is chosen for the fittings here as the intensity goes to 0 at $Q = 0$. The position of the maximum intensity, Q_{Peak} is found to sit at $Q_{\mathrm{Peak}} = Q_0 e^{-\omega^2}$ and can be converted to the corresponding length scale in real space via $d = 2\pi/Q_{\mathrm{Peak}}$ [73]. Examples of these fits can be seen in Fig. 7.4 and the results for all experiments are shown in Fig. 7.5. Any temperatures where measurements were

repeated are presented as an error weighted average. The errors associated with the calculation of I_{Norm} are included in the fitting but are not shown in Fig. 7.4 for clarity. It is also important to note here that some images were taken using a single helicity due to issues with the undulator during the experiment. These are seen to give radial intensity profiles that are similar to those calculated from dichroic images and are included in this analysis. Upon reviewing the calculation of the errors, it was deemed that these were calculated incorrectly. However, testing the fits without the inclusion of the error bars lead to no change in the behaviour of the system measured, with slight changes in the size of the lengthscale extracted. As this has no influence on the conclusions of the chapter it was deemed unnecessary to reperform the calculations.

7.3 Characterization of Ferromagnetic Domains Through the Transition Using Circular Dichroism

Investigations using circular dichroism have been shown to provide insight into FM structures using RMSAXS [73–75] and are used here as a control experiment to demonstrate that the principles of the experiment are sound as well as providing context for the investigations into the dynamic behaviour presented in the next chapter. Panels (a)-(c) of Fig. 7.5 shows the results for the fitting of a log-normal profile to the radial intensity curves for all measurements taken using XMCD. For the purposes of this investigation all measurements that gave a value of Q_{Peak} outside the available Q range are not considered to be valid and are excluded from the analysis. These are likely due to a lack of signal for the measurements in question. In total there are 9 of these measurements out of a possible 115, most of which are measurements that have been repeated at a given temperature and are therefore deemed to not affect the conclusions drawn from the experiment.

Fig. 7.5(a) shows the results for the real space length scale associated with the peak in the structure factor, d, for measurements taken using XMCD. Between 390 and 360 K on the cooling branch d appears to be constant at $\approx$ 150 nm. When cooling past 360 K, d increases to $\sim$ 300 nm at around 351 K. On heating, the length scale associated with the peak position increases initially peaking again at around 300 nm at 376 K. After this point d decreases continuously to around 150 nm at 400 K. The dotted lines in this figure show the transition midpoint as measured using the SQUID-VSM, and both

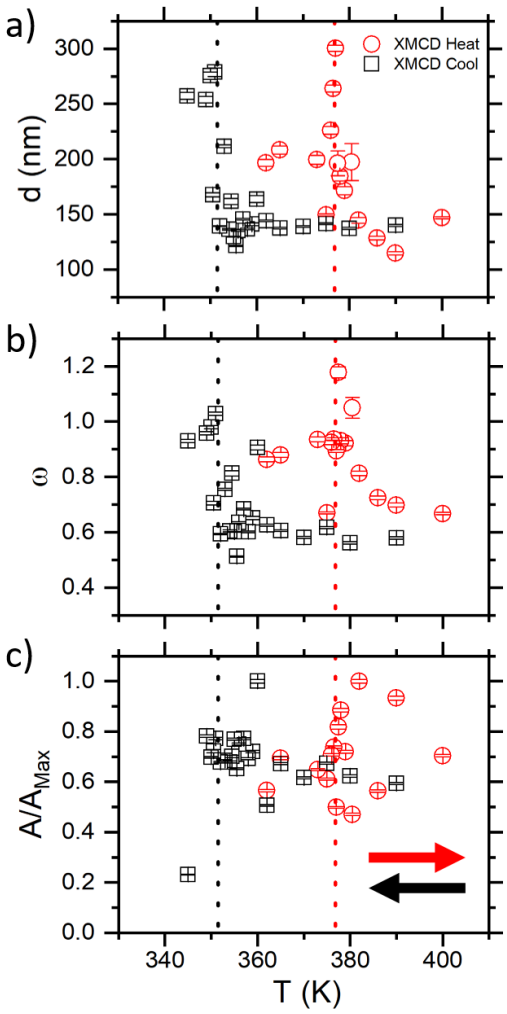

Figure 7.5: Results of fitting log-normal distributions to the radial intensity profiles for the measurements performed using XMCD. Panels (a) - (c) show the values extracted for the real-space lengthscale extracted from the peak in the radial intensity profile, d, the logarithmic width of the log-normal distribution, ω and the normalized peak area, A/A_{Max}, for measurements taken on the heating (red circles) and cooling (black squares) branches of the transition for measurements taken using XMCD. The dotted lines are used to mark the position of the transition midpoint on either transition branch in all panels. The coloured arrows depict the temperature sweep direction. The value of d appears to peak around the transition midpoint.

transition branches appear to have peaks in d that coincide well with this point. The values of d seen at temperatures below the transition midpoint is consistent with the size of domains at this stage in the transition, whilst those at the higher temperatures are far smaller than the expected FM domain size [27, 31]. This suggests that the nature of the scatterer measured at temperatures in excess of the transition midpoint are not domains and their nature is unclear at this stage.

The logarithmic width of the distribution, ω, for the XMCD measurements is shown in Fig. 7.5(b). The behaviour of ω on both transition branches follows the behaviour of d. The increase in ω around the transition midpoint suggests that the distribution of scatterer sizes increases when passing through this temperature on either transition branch. This could be due to changes in the domain state or changes in the nature of the scatterer at this point.

The peak area, A, normalized to the maximum value for that particular transition branch, A_{Max}, is shown in Fig.7.5(c). There is no obvious temperature correlation seen here for either temperature sweep direction. The scattering intensity for a system where there are two magnetic phases, an AF phase with phase volume $(1-\phi)$ and form factor f_{AF} and the ferromagnet with phase volume ϕ and form factor f_{FM}, follows [73]:

$$\frac{d\sigma}{d\Omega} \propto |\phi f_{\mathrm{FM}} - (1-\phi) f_{\mathrm{AF}}|^2. \tag{7.4}$$

The AF phase would not contribute to the XMCD behaviour and therefore $f_{\mathrm{AF}} = 0$. By considering the magnetic enhancements at the Fe L_3 resonance edge of the f_{FM} for the two light polarizations, as per the method outlined in 3.3.1, the total XMCD scattering cross-section becomes that which is described in equation 3.34 multiplied by ϕ^2. Therefore, the area of the peak for the entire scattering cross section would be expected to follow ϕ^2, which is clearly not the case here. Further investigations into why this is the case are required. In order to identify why this may be the case an in-depth analysis of the scattering objects expected and their development through the transition is required.

7.3.1 Determining the Nature of the Scatterer

The development of the magnetic structure through the transition in B2-ordered FeRh is anything but trivial. An example image series taken using XMCD-PEEM is shown in Fig. 7.6 demonstrates how the domain structure changes through the transition and

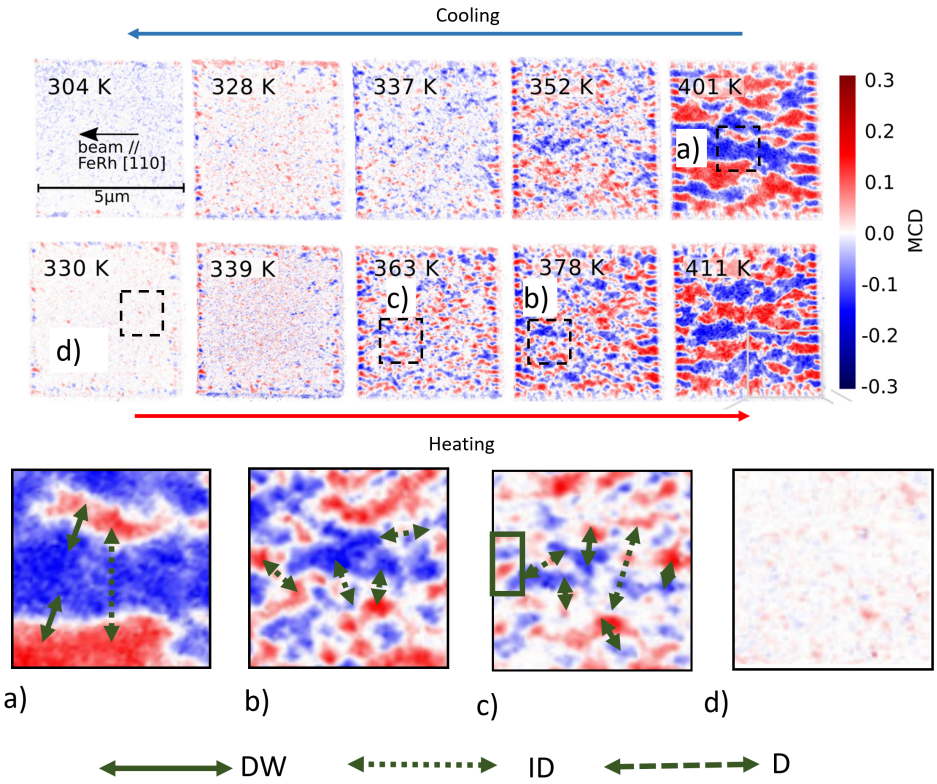

Figure 7.6: XMCD-PEEM images of the magnetic domain structure through the transition. This is an adaptation of a figure in Temple *et al.*'s work that demonstrates the development of the magnetic domain size through the transition [27]. The original figure is shown on the left hand side of the work with permission, where the colour in each image represents the component of the magnetization parallel to the beam direction, for which the colour bar is shown. Some of the panels have dotted boxes within them that are labelled (a)-(d). These areas are magnified and are shown next to the corresponding label on the right hand side of the figure. In these boxes the different types of arrow are used to demonstrate different possible sources of the scattering responsible correlations in the structure factor, with scattering from domain walls (DW) shown by the solid arrows, scattering between two FM domains across an AF domain (ID) shown by the dotted arrows and scattering from domains themselves (D) shown by the dashed arrows. The green box in panel (c) is used to highlight flux-closed structures.

is included here to aid the discussion. This figure is an adaptation of the one presented in Temple *et al.*'s work for which the candidate is a coauthor [27]. This figure presents a series of images at different temperatures on the two transition branches taken using XMCD-PEEM at the I06 beamline at Diamond Light Source. Each square corresponds to a 5×5 μm^2 area of patterned FeRh and the colour included in each square represents the orientation of the magnetic domains at that temperature. The colour corresponds to the component of the magnetization found parallel to the direction of the beam as per equation 3.17. The colour scale used in these images is shown by the scale bar in the right hand side of the figure. The red regions have their magnetization point parallel to the beam, whilst the blue regions are directed anti-parallel, the white regions have either no magnetic contrast or have their magnetization directed perpendicularly to the beam direction.

In the high temperature regime, such as the 401 K image when cooling, a close up of which is seen in panel (a) of Fig. 7.6, and the 411 K when heating, the domain structure takes a striped orientation, where the stripes have μm dimensions [27, 31]. Direct scattering from objects of this size is likely to have been lost within the beamstop. Therefore, the peak in the correlations corresponding to nm length scales for the high temperature measurements is likely to be due to the distance between two scattering sites and not the domains themselves. A close up section of the 401 K image on cooling, defined by the dashed box, is shown in Fig. 7.6(a). Included on this image are arrows which show the possible sources of correlations for the structure factor. The solid arrows here show scattering across a magnetic domain wall (labelled DW in the diagram) and the dashed lines demonstrate scattering within the domain (labelled D in the diagram).

There are several other close-up images presented in this figure that show how the domain structure and the various possible sources of scattering progress through the transition. Fig. 7.6(b) is taken for the 378 K image when heating and shows the system for $\phi \approx 0.7$ [27]. It can be seen here that scattering between adjacent domains, i.e. across domain walls, would be expected but there is also scattering between domains that are not adjacent and are separated by regions of non-magnetic material, which is known as interdomain (labelled ID in the diagram) scattering and is shown by the dotted arrows. The figure here may be misleading as it is of course possible that the region between domains here could be FM oriented perpendicularly to the beam, but is taken to be AF here and is used here to demonstrate the concept of ID scattering.

The length scale associated with ID scattering would be expected to increase as more AF material is introduced into the system on cooling and *vice versa* when heating.

There will be a point at which the distance between scattering sites for interdomain scattering becomes too large to be measured using this technique. Such a point is shown in panel (c) of Fig. 7.6 which takes is a close up of a section of the 363 K image when heating. At this point, it is possible to see that there are regions of material that form flux closed structures, such as that highlighted by the green box in panel (c). This is a phenomena seen elsewhere for FeRh in the literature also [31]. The domain sizes have been seen to decrease with decreasing temperature with the smallest diameter being ≈ 150 nm [27, 31], which would be visible in the Q range probed in this experiment.

To summarize, there are three different possible sources of correlation seen in the structure factor here that may be have length scales on the dimensions seen here: i) scattering across a magnetic domain wall, ii) interdomain scattering between domains separated by AF material or iii) scattering between opposite sides of the domains themselves. The length scale associated with each of the different possible scattering types is expected to change throughout the transition, which may lead to changes in the length scale accessible using this technique as the transition progresses. It would be expected that the scattering would be dominated by scattering from domains, then as these coalesce as the transition progresses towards the fully FM state [27, 31]. The available Q range in this experiment limits the size of the observable structures to around $d \sim 300$ nm and as the domains sizes seen using other magnetic imaging techniques reaches μm dimensions [27, 30–35], they would become too large to be seen in this experiment. At this point the scattering between domains across regions of AF material would be expected. When the system reaches the fully FM state the length scale will be determined by the behaviour of the magnetic domain walls. With this expected behaviour in mind, the behaviour of d will now be discussed for each of the two transition branches.

Firstly, when cooling from the fully FM phase whose magnetic domain structure is shown in Fig. 7.6(a), as the domains are too large to be seen using this technique, the only available source of scattering would be across the FM domain wall. The magnetic domain wall width between two oppositely magnetized FM domains, δ, is known to be dependent on the exchange constant of the FM, J, and the anisotropy energy K, via $\delta \propto \sqrt{J/K}$ [150]. Within this region of the transition J would be expected to increase slightly when cooling through the temperature range here due to a reduction in the

influence of thermal fluctuations. From the FMR measurements presented in chapter 5, the anisotropy is expected to be flat through the temperature range. This means then that when entering the MMP that the size of the domain wall would be expected to be flat, a behaviour which is seen between 390 and 360 K for the cooling branch measurements despite the large scatter in the data seen in Fig. 7.5(a).

However, when cooling past 350 K an increase d is seen. This is in direct contrast to the behaviour expected of scattering across a FM domain wall. The expected domain configuration at this stage in the transition is shown in Fig. 7.6(b) and (c). It is clear from this figure that both inter- and intra-domain scattering is possible as AF material is now present. The values in this region of the transition are too small to be associated with scattering from magnetic domains and also have the wrong temperature dependence [27, 31]. Interdomain scattering would see an increase with decreasing temperature as regions of AF material are introduced into the system and separate the FM scattering sites, which is consistent with the behaviour seen when cooling in this transition region and is taken as the source of scattering here. When cooling past the transition midpoint, the length scale appears to decrease. These length scales are consistent with scattering from domains within the system at this point in the transition and so it is believed that this is the source of the scattering in this temperature region [27, 31]. More points are needed at temperatures below the transition midpoint when cooling as there are only 3 points and is not possible to say for sure whether this is the case.

The same increase towards the transition midpoint is seen on the heating branch however. The values at the lower temperatures when heating are again consistent with literature for the size of the magnetic domains for similar points in the transition [27, 31]. After the transition midpoint, d is seen to decrease again in a similar manner to the points attributed to inter-domain scattering on the cooling branch. The behaviour here is again inconsistent with that expected of scattering from an FM domain wall and interdomain scattering is the most likely candidate for the behaviour seen here. As the system approaches the fully FM phase with increasing temperature, the AF material is removed from the system and the scattering would then correspond to domain wall scattering. The value of d for the highest temperature point on the heating arm agrees well with the points attributed to FM domain wall scattering from the cooling branch.

To summarize here, there are believed to be three different scatterer types whose

scattering dominates proceedings at different points within the temperature range probed here. These are i) for temperatures less than the transition midpoint, the scattering is dominated by scattering from objects consistent with the size of magnetic domains [27, 31], ii) for temperatures in excess of the transition midpoint scattering across AF regions dominates and iii) for temperatures where the tranistion has completed, scattering across FM domain walls is seen. This behaviour is seen on both transition branches and would be consistent with that expected from the development of the FM domains previously seen in literature [27, 31].

It is also possible to address the inconsistencies between what is expected of the behaviour of the area with the actual results here. The ϕ^2 dependence for this scattering stands for the entire scattering cross-section and encompasses scattering from all of the sources mentioned in this work. As the scatterer type changes through the measurement range, we see the scattering only from that object and not the entire scattering cross-section. Therefore, the behaviour is not expected to follow that as predicted by equation 3.34, as only a portion of the total scattering cross-section is being measured at any one point in the temperature range.

7.4 Investigations Using Linear Dichroism

Now that the investigations using circular dichroism have been presented, and it is possible to extract meaningful data about the magnetic structure of the fully FM phase consistent with the behaviour expected from literature, the focus now falls to trying to demonstrate that it is possible to use the same technique and analysis to investigate the magnetic structure of AF materials. The study of AF materials using this technique would be the first of its kind.

By switching to XMLD these experiments are now sensitive to both FM and AF materials. As such, the three possible sources of scattering listed in the previous section are now also present for the AF material. In addition to this we are also now sensitive to scattering across the AF/FM boundary. Not much is known about the behaviour of the AF/FM boundary, however, the simulations presented in the previous chapter reveal that it is made up of both magnetic phase intermixed over a distance of ≈ 2.6 nm in the out-of-plane direction. There are no models that describe the development of such a boundary wall in the literature and so it is not clear how it would develop in the film plane. As the anisotropy is much smaller for both magnetic phases in the film

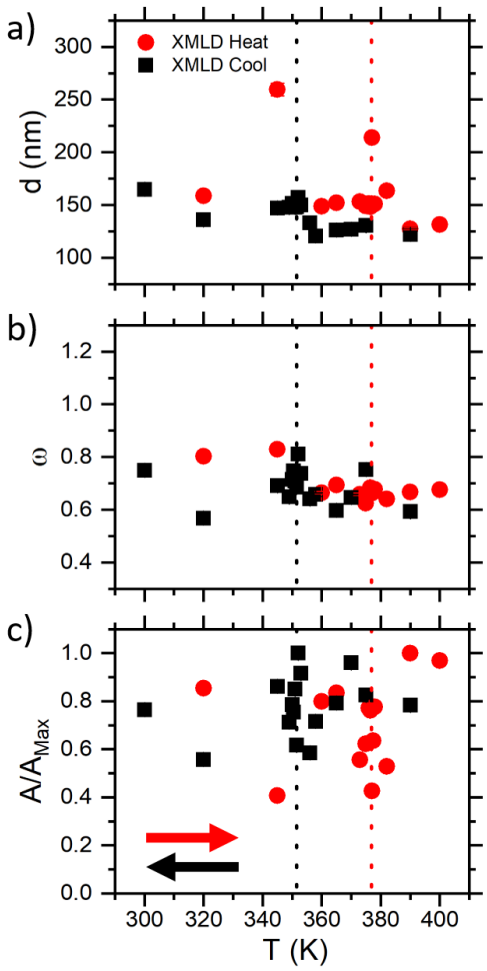

Figure 7.7: Results of fitting log-normal distributions to the radial intensity profiles for the measurements performed using XMLD. Panels (a) - (c) show the values extracted for the real-space lengthscale extracted from the peak in the radial intensity profile, d, the logarithmic width of the log-normal distribution, ω and the normalized peak area, A/A_{Max}, for measurements taken on the heating (red circles) and cooling (black squares) branches of the transition for measurements taken using XMLD. The dotted lines are used to mark the position of the transition midpoint on either transition branch in all panels. The coloured arrows depict the temperature sweep direction. These measurements show a temperature invariant lengthscale at temperatures below the transition midpoint.

plane than out-of-plane the size of the MPB may be larger.

Fig. 7.7(a) shows the length scale associated with the peak in Q for the measurements taken using XMLD, which is consistent with that of the XMCD measurements for measurements taken above the transition midpoint on both transition branches. As such, the same scatterer is believed to be responsible for the behaviour seen in this region. It is believed that the domain wall between FM domains is again being measured here, because no AF material is present in this area of the transition. For temperatures below the transition midpoint however, the behaviour of the data sets taken with the two different dichorism types diverges and the length scale associated with the peak in the XMLD measurements appears to be largely temperature invariant down to 300 K, with the length scale being around 150 nm.

The behaviour of ω for both transition branches, shown in Fig. 7.7(b), is again reflective of the behaviour of d and shows consistency with the XMCD measurements above the transition midpoint and not below. The normalized area profiles, which are again normalized to the maximum value of their respective measurement set, are shown in Fig. 7.5(f). These also show a lack of a temperature dependence as is the case with the XMCD measurements which is attributed to the same underlying cause.

By comparing the behaviour of d between Fig. 7.5 and Fig. 7.7 it can be seen that data is obtained using XMLD measurements at temperatures below the point where the XMCD signal drops out. The lowest temperature measurement, which is taken at 300 K on the cooling arm, corresponds to a $\phi = 0.04$ and as the signal from the FM domains has been lost at this point, the signal is believed to originate solely from scattering from the AF material present at this stage. It is possible to provide a theoretical basis for this observation by extending the model proposed by Fischer for the enhancement of the signal from a FM system when probed using XMCD using RMSAXS [73], to encompass contributions from both the FM and AF phases when probed using linear light.

The scattering cross-section for a two phase system would follow the form outlined in equation 7.4, except for XMLD investigations, both the AF and FM phase would contribute and both must be considered. By assumed that the FM and AF phases have different form factors and each phase has individual magnetic enhancements of the form factors as per the method outlined in 3.3.1. By considering the two different phases and their respective magnetic enhancements at the Fe L_3 resonance edge in the same

manner as that for the XMCD measurements the difference in cross section between the two polarizations is then given by:

$$\begin{aligned}\left(\frac{d\sigma}{d\Omega}\right)^{+} - \left(\frac{d\sigma}{d\Omega}\right)^{-} \approx\ & 4\phi^2\Big((f_0 + f'_{\mathrm{FM}})f'_{\mathrm{FM,mag}} + f''_{\mathrm{FM}}f''_{\mathrm{FM,mag}}\Big) \\ & +4(1-\phi)^2\Big((f_0 + f'_{\mathrm{AF}})f'_{\mathrm{AF,mag}} + f''_{\mathrm{AF}}f''_{\mathrm{AF,mag}}\Big) \\ & -4\phi(1-\phi)\Big[f_0(f'_{\mathrm{AF,mag}} + f'_{\mathrm{FM,mag}}) \\ & +(f'_{\mathrm{AF,mag}}f'_{\mathrm{FM}} + f'_{\mathrm{AF}}f'_{\mathrm{FM,mag}} + f'_{\mathrm{AF,mag}}f'_{\mathrm{FM,mag}}) \\ & +(f''_{\mathrm{AF,mag}}f''_{\mathrm{FM}} + f''_{\mathrm{AF}}f''_{\mathrm{FM,mag}} + f''_{\mathrm{AF,mag}}f''_{\mathrm{FM,mag}})\Big]. \quad (7.5)\end{aligned}$$

This equation predicts that for large ϕ the scattering intensity is dominated by the FM contributions and the equation tends to that seen in equation 3.34, which is later multiplied by ϕ^2 to explain the XMCD behaviour. The magnetic domain configuration in this phase is expected to be similar to the one shown by the 401 K on cooling panel in Fig. 7.6. The same can also be said for that of the AF phase for low ϕ, whose scattering has the same form as that of the solely FM phase. It also predicted that there will be a dip in the intensity between the two extremes, which is not inconsistent with the behaviour seen in the normalized area profiles here. Nevertheless, it is not possible to say for sure whether this is the case due to the large scatter in the data and the inability to access all the entire scattering cross-section here.

This equation is included to demonstrate that the scattering that is seen in this experiment at temperatures where the XMCD signal, which has a ϕ^2 dependence, has dropped out can be attributed directly to scattering from the AF regions. This then adds credence to the idea that the combination of RMSAXS and XMLD can be used to investigate the structural properties of AF materials. Qualitatively, the profile of the normalized area is somewhat consistent with the behaviour predicted by the equation, though further work is required to ascertain its validity. This RMSAXS from a system in which the entire scattering cross-section can be accessed should be performed to test the validity of this equation.

The largely temperature independent behaviour of the length scale after the XMCD signal has dropped out is also consistent with the only previous study of the size of AF FeRh through the transition which is performed by Baldasseroni *et al.* [35]. This study was performed using XMLD-PEEM and shows a largely temperature independent

behaviour of the domain size of AF FeRh, with the length scale being 300 nm in that case [35]. It also states in that study that the AF domain growth would be governed by the defect density [35], which may explain the difference in length scales between the two studies. As this has a similar behaviour to AF domains seen previously, it is believed that this 150 nm length scale corresponds to the size of the AF domain in this system.

It is important to note here that the drop out of the XMCD signal is assumed at this stage and no measurements were taken at temperatures lower than that presented here due to the low signal seen in the measurements at the low temperatures. It would be assumed from equation 7.4 that it would the XMCD signal would drop out around where the final measurement is taken but measurements at lower temperaures should be performed to say for sure.

7.5 Conclusion

RMSAXS was employed in conjunction with both XMCD and XMLD to investigate the development of the two magnetic phases through the transition. Both dichroism types demonstrate SAXS rings, which disappear when the beam energy is away from the magnetic resonance edge. This implies that the signal is magnetic in origin for both dichroism types. These images are then transformed into a radial intensity profiles from which the length scale corresponding to the peaks seen in the intensity profiles is extracted.

The XMCD measurements reveal that the length scales corresponding to the peak in the intensity profile sits around 150 nm when cooling from 390 to 360 K, at which point a gradual increase is seen in the extracted length scale. This increase continues when cooling through to the tranistion midpoint after which the length scale appears to decrease again. A similar behaviour is also seen for measurements taken when heating. The behaviour is attributed to a cross over in the nature of the scatterer from domains themselves to being between domains across AF material, then finally between domains across FM domain walls in the fully FM regime.

The length scales extracted using XMLD measurements are consistent with those extracted using XMCD for temperatures in excess of the transition midpoint, suggesting that the scattering object is the same between the two dichroism types. However, at temperatures lower than this the behaviour of the system deviates when probed using

the two different types of magnetic dichroism, which implies that object responsible for the scattering differs between the two at these temperatures. The length scale associated with the peak in the XMLD measurements after the transition midpoint is largely temperature invariant at 150 nm. As scattering is seen at temperatures below that where the XMCD signal drops out this behaviour is attributed to scattering from the AF phase, a hypothesis which is backed up by extending the theory of the expected scattering cross-section for RMSAXS using XMCD to a two phase system using XMLD. The behaviour of the AF phase is consistent with the only previous study of AF FeRh [35], and the AF domains here are believed to be 150 nm in size.

This work demonstrates for the first time that it is possible to measure the structural properties of AF materials by combining RMSAXS and XMLD. This may provide a useful avenue for exploration of AF materials in the future.

Chapter 8

Reciprocal Space Characterization of Magnetic Relaxation in the Mixed Magnetic Phase

8.1 Introduction

The results of the previous chapter revealed that it was possible to measure the properties of the magnetic structure for both magnetic phases through the transition using Resonant Magnetic X-Ray Scattering (RMSAXS) and the different types of magnetic dichroism. As the speckle pattern created by the RMSAXS is a Fourier transform of the domain pattern that creates it, any changes in the magnetic structure are reflected in the speckle pattern in real time. In the mixed magnetic phase (MMP) of B2 ordered FeRh these changes in the magnetic structure are expected to come from the presence of magnetic frustration at the magnetic phase boundary (MPB) [18, 57] and the growth and nucleation of FM domains due to thermal fluctuations [46, 47, 58]. X-Ray Photon Correlation Spectroscopy (XPCS) has been used to evaluate the temporal development of a number of different systems and provide insights into the nature of each systems dynamic behaviour [80–87, 90, 113].

This chapter presents XPCS investigations into the dynamic behaviour of B2 ordered FeRh at various temperatures through the metamagnetic phase transition, using both XMCD and XMLD in conjunction with RMSAXS as per the method outlined in the previous chapter. The resultant correlation behaviour is fitted to a stretched exponential model of relaxation and reveal a complicated dynamic behaviour which comprises contributions from long range interactions as well as the nucleation and development of FM domains when heating as predicted from the literature [58]. The dynamic behaviour of the system is found to be different depending on the type of dichroism used to probe it. It is seen to be possible to measure dynamic behaviour of the AF phase using XMLD and these investigations add a greater insight into the behaviour of the system.

As the work presented in this chapter is an extension of that presented in the previous chapter, the distribution of the work is the same as that listed there. Special thanks must also go to R. C. Temple for the analysis code for the XPCS data series.

8.1.1 Experimental Set Up

The work presented in this chapter is an extension of that of the previous chapter and so the samples used are the same. The reader is invited to refer back to section 7.1.1 for all the relevant details and Fig. 7.1 for the sample properties, should they be required. For the same reasons, all of the beam energies and other characterization of the beam seen in section 7.1.2 are carried forward and applies here.

For this experiment, the temporal correlation behaviour is identified by taking 200 images using the CCD camera placed on the end of the RASOR endstation of the I10 beamline at Diamond Light Source. The helicity of the incoming x-ray beam is changed between consecutive images and sets of 2 images are subtracted from each other in post processing to enhance the image signal via the method outlined in Fischer et al [73]. This leaves 100 images, each of which is then correlated against each of the subsequent images in the series to find the g_2 function via the method outlined in section 4.4.1, and uses the equation,

$$g_2(\tau) = \left\langle \frac{\langle I(\mathbf{Q},t)I(\mathbf{Q},t+\tau)\rangle_t}{\langle I(\mathbf{Q},t)\rangle_t^2} \right\rangle_{\mathbf{Q}} \tag{8.1}$$

where $I(\mathbf{Q},t)$ is the intensity at position $\mathbf{Q}$ at time t, $\langle ... \rangle_{t,\mathbf{Q}}$ denotes a average over time or over $\mathbf{Q}$ and τ is the time delay. In this equation, the g_2 function for an individual pixel or $\mathbf{Q}$ is calculated and averaged over the entire area to give the final g_2 function. The time delay is taken to be integer values of the time between images, which is $\approx$ 54 s for images taken using XMCD and $\approx$ 68 s between images taken using XMLD. As such the time taken for 200 individual images ranged between 90-120 minutes. These images series are performed at a series of different temperatures and are used to calculate the dynamic behaviour through the transition. As mentioned in the previous chapter, there are some measurements taken as a single helicity due to issues with the undulator. These measurements are performed over the same timescale and consist of between 400 - 900 images. The time between images is now reduced to between 6 - 9 s, however, the volume of images means it is now necessary to consider only every tenth image for these sequences and so the actual time between processed images becomes either 60 or 90s. These are seen to give results that are comparable to the measurements that use both helicities and so are included in the analysis here. Between measurements the magnetic state is reset by thermally cycling the sample so it enters either the fully FM or AF state depending on the transition branch being measured. The images are taken using the method outlined in section 4.4.1.

For the calculation of the correlation however, it is not possible to use an entire image as there is simply too much data to process. Therefore, each image is cropped into 200 $\times$ 200 pixel box that is centered around the value of Q_{Peak} measured in the previous chapter for all measurements. Performing the analysis in this way allows for the correlation of the dynamic behaviour with the nature of the scatterer.

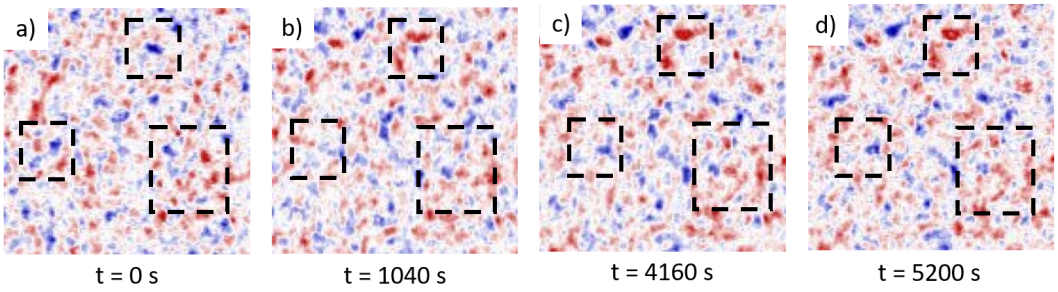

Figure 8.1: Examples of speckle patterns for 380 K on the cooling branch measured using linear light at various times through a measurement, the time of which is noted underneath the image. The dashed boxes are used to highlight examples of regions where the speckle pattern changes with time.

8.2 X-Ray Photon Correlation Spectroscopy Investigations

In order to demonstrate that dynamic behaviour is present in this system, a representative example of a small region of these images for the series taken using linear light at 380 K on the cooling arm is shown in Fig. 8.1. In this figure, the intensity of the signal received at each pixel is shown by the colour. All images are normalized to their own mean before processing to guard against fluctuations in the intensity during the course of the measurement. It is clear from this image series that some of the features of the speckle pattern, such as those highlighted in the dashed boxes in Fig. 8.1, are seen to vary across the measurement time. The colour used in these images is used to demonstrate the intensity of each pixel. As this is a difference image, the pixels that show a red colour have a larger signal coming from one polarization of the light, whilst the blue points have a larger signal coming from the other light polarization. This temporal variation in the speckle pattern is indicative of dynamic behaviour of the magnetic domain structure. The switching of some of the pixels in the boxes from red to blue or *vice versa* implies a reorientation of the magnetization direction here.

For a more thorough assessment of the dynamic behaviour of the system, the temporal correlation behaviour was calculated for each temperature using the g_2 function. Examples of these g_2 functions calculated for measurements on the cooling arm taken using circularly polarized light are seen in Fig. 8.2.

In order to extract the dynamic behaviour of the system, the g_2 functions can be

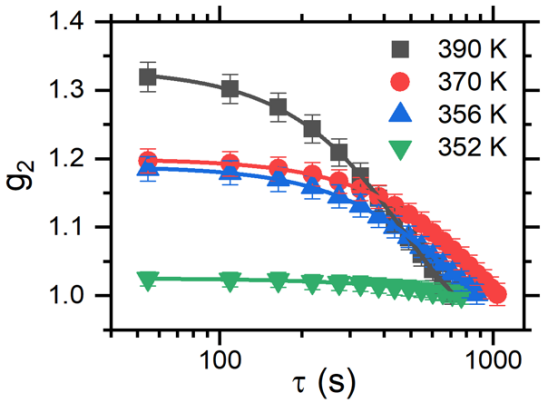

Figure 8.2: Examples of g_2 behaviour calculated for measurements on the cooling arm using images taken with circularly polarized light. The solid lines here are fits to equation 8.2 with $\omega \neq 0$. It is clear here that the correlation behaviour varies across the temperature range probed in this experiment.

fitted to stretched exponential models [81–83, 85–87, 113],

$$g_2(\tau) = 1 + A\cos(\omega\tau)\, e^{-\left(\frac{\tau}{\lambda}\right)^{\beta}}, \tag{8.2}$$

where A is the speckle intensity or correlation amplitude, ω is the heterodyne mixing frequency between the signal and the static reference signal, β is the stretching exponent and λ is the relaxation time.

8.2.1 Comparison of the Hetero- and Homo-dyne Models of the Dynamic Behaviour

The form of equation 8.2 assumes there is a static reference signal that mixes with the scattering from the sample and is known as the heterodyne model [81, 82, 113]. The model in which no static reference signal is expected, where $\omega = 0$, is known as the homodyne model [113]. In this model, the form of the stretched exponential that governs the relaxation takes the form $e^{-2(t/\tau)^{\beta}}$ [81, 83, 85–87, 117].

To decide which model is appropriate for use in this experiment, the results of fitting to the two models are compared and are shown in Fig. 8.3. Panel (a) shows examples of fitting for both the heterodyne (solid line) and homodyne models (dashed line) to the 390 K curve of the example g_2 functions shown in Fig. 8.2. Before analysis all g_2

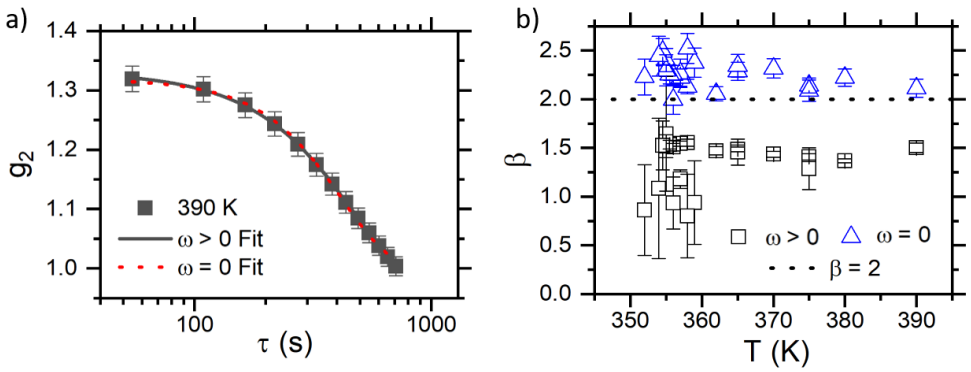

Figure 8.3: Comparison of the results for the hetero- and homo-dyne models. Panel (a) shows example fits using both the heterodyne (grey line) and the homodyne model (red dashed line) to the g_2 behaviour of the 390 K curve seen in Fig. 8.2(b). Panel (b) shows the results of the fitting for β for the homodyne (black squares) and heterodyne (blue triangle) models alongside the theoretical limit of β taken from [151].

functions are clipped only to include points where $g_2 > 1$ as the functional form of equation 8.2 implies this must be the case for the homodyne model. It is also seen to be give good fits to the data for the heterodyne model whereas fitting the whole g_2 over the whole measurement range does not.

It is clear from Fig. 8.3(a) that the two models are indistinguishable for their fit to the data. Panel (b) shows the results of fit for β using the heterodyne model ($\omega > 0$), shown by the black squares, whilst the results of the fitting of the homodyne model ($\omega = 0$) are shown by the blue triangles. This figure provides evidence that the heterodyne model is the appropriate one to use in this experiment, as according to Hansen *et al.* the upper limit for β is 2, which is shown by the black dashed line [151]. Evidently, the values extracted using the homodyne model exceed this physical limit, whereas the results extracted from the heterodyne model do not. As such, the heterodyne model is used in the rest of the analysis of the auto-correlation behaviour. It is not clear as to the source of the static reference signal in this experiment and it may come from leakage of light from the beampipe, the beam that passes through the sample without interacting with it or a static signal that comes from the sample itself. Further work is required to ascertain the source of this reference signal. Results of the fittings of the heterodyne model to all measurements are shown in Fig. 8.4.

During the course of this experiment, measurements at some temperatures were repeated. The values for each temperature are collected in a weighted average and presented as a single object. There are measurements performed at 400 K when heating taken using both XMCD and XMLD that begin some time after the temperature sweep has begun which are not included as they are not longer consistent with the measurements that begin as soon as the temperature sweep has completed. Measurements in which the fits yielded values that had an error bar of larger than 100 % were not included as it was not possible to identify any meaningful results from these measurements. These measurements are excluded from the analysis as they are not believed to accurately reflect the behaviour. All in all there are two points that satisfy this criteria, one point on each of the transition branches when the system is measured using XMCD. The removal of these points does not affect the conclusions drawn from the chapter and is therefore deemed to be approproate. The measurements that use a single helicity do still provide measurable g_2 behaviour with values of λ and β that are consistent with those collected from measurements in which two helicities are used, and are included in the weighted averages. Their signal strength however is much lower and their contribution to A is ignored. It is also important to note here that after the functions have been clipped some do not have sufficient signal to be fitted. These are generally in the measurements where there were issues with the undulator or at low temperature measurements for the XMCD measurements, implying that the drop out of the signal is real as no dynamic behaviour is observed.

8.2.2 Initial Characterization of the Dynamic Behaviour

The results of the fitting for the dynamic behaviour to the measurements that utilize circularly polarized light are shown in panels (a)-(d) of Fig. 8.4. The transition midpoint as extracted from the magnetometry data is also shown here as the dotted line. The speckle intensity, A, shown in panel (a) of the same figure, appears to have a profile similar to that of the behaviour of the magnetization for both transition branches seen here. The results of ω, shown in Fig. 8.4(b), are expressed in terms of the time associated with the extracted frequency, $2\pi/\omega$, and appear to be consistent with the measurement time for all measurements as expected [82]. The extracted values of β, shown in Fig. 8.4(c), appears to be constant at $\beta \approx 1.5$, for all measurements in excess of the transition midpoint on both transition branches. For temperatures below this

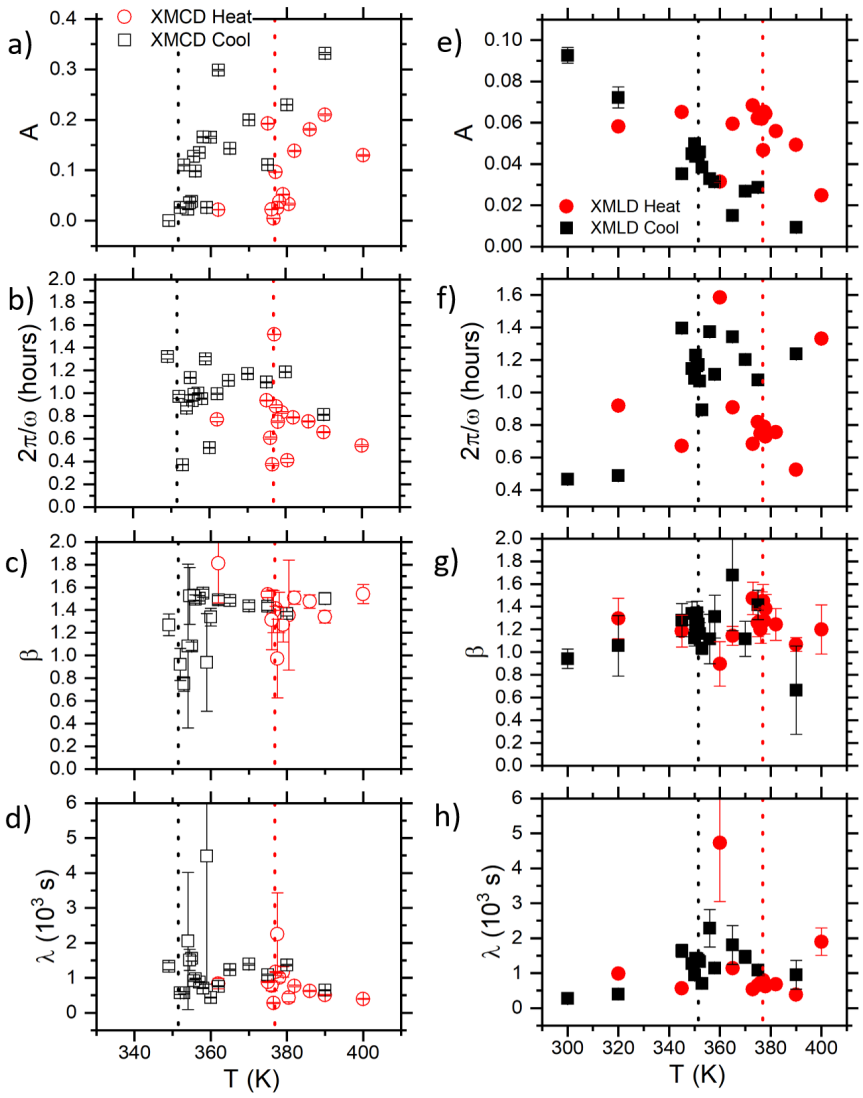

Figure 8.4: Results of fitting heterodyne model to the g_2 behaviour. Panels (a) - (d) show the fitting results for A, $2\pi/\omega$, β and λ for measurements taken using circularly polarized light. Panels (e) - (h) show the same quantities but extracted from the measurements taken using linearly polarized light. Both sets of measurements have the cooling (black) and heating (red) measurements included and show the transition midpoint for each transition branch by the dotted line.

point the values of β are seen to decrease towards 1 for both transition branches, before recovering towards $\beta \sim 1.5$. The relaxation time, λ, which is seen in Fig. 8.4(d), also appears to have no discernible temperature dependence across the measured range here.

The speckle intensity extracted from measurements using XMLD is seen in Fig. 8.4(e) and appears to decrease with increasing temperature on both transition branches. A appears to peak on both transition branches at temperatures close to the transition midpoint for each temperature sweep direction as measured using the SQUID-VSM, which is shown on these panels using the dotted lines. $2\pi/\omega$ extracted for XMLD measurements is also consistent with the overall measurement time for all measurements. The behaviour of β is different to those extracted from the XMCD measurements, as can be seen in Fig. 8.4(g). When heating, the stretching exponent is consistent within error at around 1.3 up to the transition midpoint, after which a decrease from $\beta \approx 1.5$ to $\beta \approx 1$ is seen. A similar behaviour is seen on the cooling branch. The value of β for the XMLD lies mostly below 1.5 but does approach this value when the temperature moves towards the transition midpoint on both transition branches. The behaviour of λ, shown in Fig. 8.4(h), also shows no discernible temperature dependence for either transition branch across the measurement range.

The dynamic behaviour of the system is characterized here using β and λ as these are the quantities sensitive to the behaviour of the system [81, 82, 151, 152]. The fact they these quantities appear to be different between the two dichroism types used in this experiment implies that the dynamic processes to which they are sensitive are different. In order to ascertain whether this is the case and what the difference between the two might be, a better understanding of these parameters is required.

8.3 Interpretation of Dynamic Behaviour

The interpretation of the dynamic behaviour lies within the behaviour of β and λ, which are extracted by fitting a exponential to the g_2 function, such as that seen in equation 8.2. In this fitting the argument of the exponential is raised to a power, β, the value of which has a significant effect on the behaviour measured [151, 152]. The β parameter is used to describe systems which have more than one characteristic relaxation [151, 152]. If $0 < \beta \leq 1$, then the inclusion of the β parameter elongates the behaviour of the system relative to the $\beta = 1$ case and this is known as a stretched exponential function [152]. Conversely, if $1 < \beta \leq 2$, then the behaviour is shortened compared to the $\beta = 1$

case and this is known as a compressed exponential function [151]. Each of these two cases is said to have different dynamic properties which will be discussed in more detail [151, 152].

Stretched exponential relaxation (SER) is used to describe systems where the probability of a relaxation event occurring is governed by an exponential probability distribution [152]. In this case, β takes values of $\beta \leq 1$ [152]. For $\beta = 1$, the relaxation in the system can be described by a simple exponential distribution with a single relaxation time. Compressed exponential relaxation (CER) describes situations in which $1 < \beta \leq 2$. The stretching exponent and the relaxation time obey exactly the same principles as they would in stretched exponential relaxation, except now the relaxation events follow a Gaussian probability distribution rather than exponential ones [151]. Systems described by $\beta = 2$ can be modeled using a Gaussian probability distribution with a single characteristic relaxation time. Systems in which β exhibits values between these extremes, the system can be described by more than 1 characteristic relaxation time [151, 152]. The value of β itself is related to the logarithmic width of the probability distribution as a function of relaxation times [152]. The smaller the value of β, the larger the width of the probability distribution that governs the relaxation [151, 152].

It is important to note here that this ability to describe the system using a given probability distribution depending on its value of β is the reason given for the limit of $\beta = 2$ suggested in the previous section. Though it is entirely possible for a probability distribution to be governed by value of $\beta \geq 2$, it is not clear what the physical interpretation such a behaviour would be. It is also necessary to state here that values of the stretching exponent collected from literature have values of $\beta \leq 2$ [80–87, 90, 113]. Though this is in no way a definitive answer, it does provide some argument for the case used in the previous section to justify the use of the heterodyne model. Further investigations are required to say for certain whether this is the case in reality.

The exact influence of the introduction of different relaxation times due to these different processes is unclear. However, SER is typically associated with dynamics of individual particles whereas CER is typically associated with collective dynamics in which the relaxation behaviour of the system depends on the orientation of the system as a whole [83, 85, 87]. Systems that exhibit relaxation consistent with CER, are often based on the fluctuations of domain walls in antiferromagnetic (AF) materials and talk of jammed dynamics, which carries a characteristic value of $\beta = 1.5$ [83, 87]. Jammed

dynamics are used to describe system where the state is both rigid and disordered [153]. In magnetic systems, this jammed behaviour is attrributed to the inability of the system to resolve interactions in the domain wall due to correlated fluctuations due to the presence of long range Ruderman-Kittel-Kasuya-Yoshida (RKKY) interaction which results in $\beta = 1.5$ [87]. For domain walls in ferromagnetic (FM) materials, the influence of dipolar interactions may also lead to lead to long range collective interactions and yield the same result.

8.3.1 Stretching Exponent Behaviour

The results of the previous chapter demonstrate that the peak seen in the radial intensity profile corresponds to scattering from different objects depending on the position within the transition. To help aid the discussion, the behaviour of d and β is reshown in Fig. 8.5. For the measurements taken using XMCD on both transition branches it is believed that the scattering corresponds to the size of the FM domains at the lowest temperatures, then as the temperature increases it corresponds to the distance between FM domains separated by AF material and then the length scale associated with FM domain walls at the highest available temperatures. The behaviour of d extracted for the XMCD measurements is reshown in Fig. 8.5(a). Measurements at temperatures below the transition midpoint when heating, where the scattering is believed to originate from the magnetic domains, show $\beta \sim 1.5$. This behaviour is also seen at measurements in excess of the transition midpoint, where the peak in the length scale seen in the previous chapter is attributed to scattering between domains separated by regions of AF material. Values of $\beta \sim 1.5$ are associated with systems in which the dynamic behaviour is jammed, where relaxation is determined by long range interactions such as the RKKY or dipolar interactions [87, 89]. Interestingly, when heating towards the transition midpoint, the value of β appears to decrease towards 1 before recovering at the higher temperatures, as can be seen in Fig. 8.5(b). This move away from jammed dynamics is indicative of a change in the dynamic behaviour of the system approaching the transition midpoint. The change in β in this manner implies that the distribution of relaxation times widens approaching the transition midpoint, only to narrow again at temperatures in excess of this value.

A similar behaviour is also seen when cooling using XMCD, as at the higher temperatures $\beta \sim 1.5$, but this quickly decays towards 1 when approaching the trans-

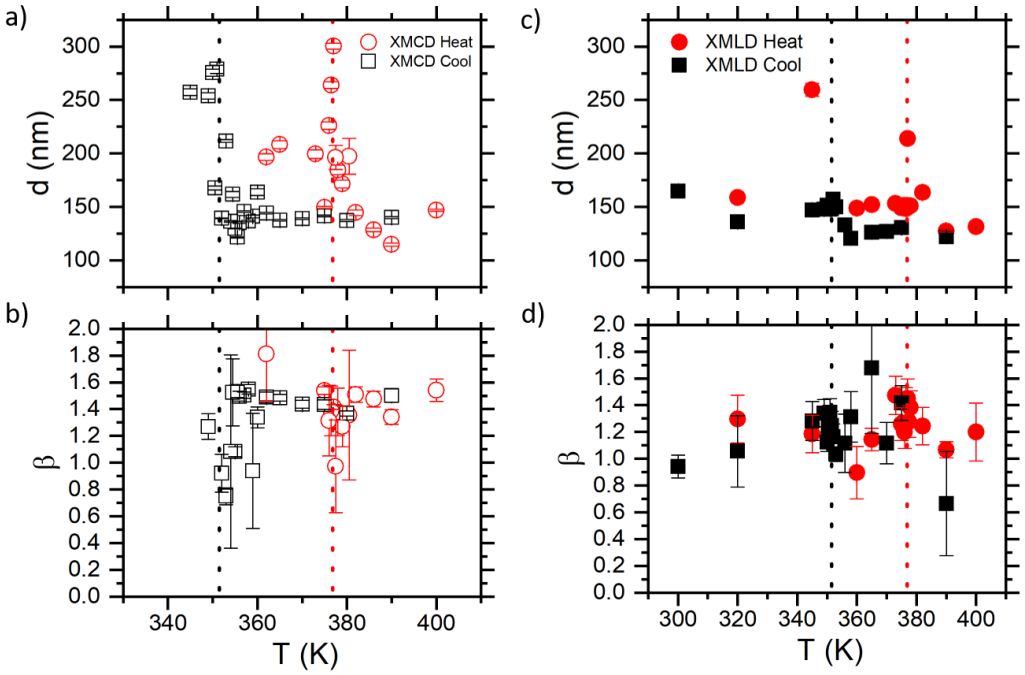

Figure 8.5: Comparison of the length scale and stretching exponent behaviours. Panels (a) shows the behaviour of length scale, d, extracted from the structural analysis presented in the previous chapter for the measurements performed using XMCD. Panel (b) shows the behaviour of the stretching exponent, β, extracted from the temporal correlation behaviour for the XMCD measurements. Panels (c) and (d) show the same quantities but for the measurements performed using XMLD. The transition midpoint for each transition branch is shown by the dotted line. The behaviour of d and β appear to vary at the same temperatures through the measurement range.

ition midpoint. When cooling, the analysis of the magnetic structure again showed a change between scattering across magnetic domain walls to domains centered around the transition midpoint. The observation of the recovery of β towards 1.5 at the lower tempeartures is not clear as it is on the heating branch due to the lack of points. However, what is clear is that the dynamic behaviour of the system changes approaching the transition midpoint. This change in β indicates that the dynamic behaviour of the system again changes in the temperature region surrounding the transition midpoint and the long range interactions are no longer present within the system. This region

of the transition corresponds to the point where maximum coexistence is expected for the system. The reason for this change in β is unclear at this stage however.

Interestingly, for the measurements taken using XMLD, the high temperature measurements are expected to correspond to scattering from the same objects as those in the XMCD measurements. However, the value of β is not consistent between the measurements taken with the different types of magnetic dichroism for measurements taken in excess of the transition midpoint on the either transition branch, as can be seen by comparing either Fig. 8.4(c) and (g) or Fig. 8.5(b) and (d). When heating β is seen to decrease for the XMLD measurements from $\beta \approx 1.3 \rightarrow 1$ at the highest temperature measurements, implying a transition from collective to individual dynamics on heating. At the highest temperatures the relaxation behaviour can be fully described using a single relaxation time. The same transition is seen on the cooling branch measurements taken using XMLD, with measurements at temperatures lower than 400 K showing results consistent with collective dynamics. As XMLD is sensitive only to the orientation of the spin-axis, the presence of dynamic behaviour seen here implies that this is subject to fluctuations during the course of the measurement here.

It is also important to remember that the results of the previous chapter show that the XMLD measurements see a change in the dominant scatterer, between AF and FM material, with temperature, with the behaviour of d extracted for XMLD measurements in the previous chapter also reshown in Fig. 8.5(c). This transition is believed to take place at the transition midpoint. However, there is no obvious difference in the relaxation behaviour being probed either side of the transition midpoint. This result is particularly pertinent as it shows that the dynamic behaviour of AF materials can be measured directly using XMLD. This is the first such direct demonstration that XMLD measurements can be used to measure the dynamic behaviour of AF materials, with the other previous studies using either resonant magneic scattering using a single linear polarization [87, 90], non-resonant scattering [86] or an artifical AF system [83].

Measurements using both types of magnetic dichroism see fluctuations of the magnetic structure. The two types of dichroism will measure different properties of the system. XMLD is sensitive to the orientation of the orbital projection and can therefore only see changes in the direction of this quantity, whilst XMCD is sensitive to the projection of the moment in the beam direction. For measurements taken using XMCD it is not possible to discern between changes in the magnetic structure due to a rotation

of the magnetic moment or a change in the moment itself. For the XMLD we know that the orientation of the moment is changing through the measurement time. There is, however, an asymmetry between the behaviours probed using the different types of magnetic dichroism. In particular, the nature of the change in β when approaching the transition midpoint is inverted between the dichroism types, the reason for which is unclear. From previous experiments on FeRh a spin-glass state has been theorized to be present in the MPB and nucleation of FM domains has also been seen to cause magnetic relaxation [27, 57, 58, 88], each of which may contribute to the behaviour seen here. To see if there is any evidence of these phenomena in the behaviour seen here, a more quantitative analysis of the behaviour of the relaxation time is performed.

8.3.2 Investigations into the Relaxation Time Behaviour

The first model that is tested here is that of the Arrhenius model [58]. This model was previously used to explain the magnetic relaxation behaviour seen by Loving, which is attributed to the thermally driven nucleation and development of FM domains when the sample is held at a given temperature [58]. This model states that in order for a processes to occur it first must overcome the activation energy, E_{A}, to transition between the energy states. The rate, λ^{-1}, at which this process occurs then follows the temperature dependent probability of the event such that,

$$\lambda^{-1} = Ae^{\frac{-E_{\mathrm{A}}}{k_{\mathrm{B}}T}}, \tag{8.3}$$

where A is a constant and k_{B} is the Boltzmann constant. Rearranging this equation leads to,

$$\ln(\lambda^{-1}) = \ln(A) - \frac{E_{\mathrm{A}}}{k_{\mathrm{B}}T}, \tag{8.4}$$

from which E_{A} can be extracted as from the gradient of $\ln(\lambda^{-1})$ against T^{-1}. Such an analysis is shown for both dichroism types in Fig. 8.6(a) and (b), along with the results for E_{A} in panel (c).

Firstly, this analysis is seen to be valid for the measurements taken on the heating branch using XMCD and yields an activation energy of $E_{\mathrm{A}}/k_{\mathrm{B}} = 6000 \pm 1000$ K. The XMCD measurements on the cooling arm can be made to fit an Arrhenius type behaviour but the value of the activation energy is negative, which is a non-physical result. The same is true for the measurements taken using XMLD when cooling, whilst

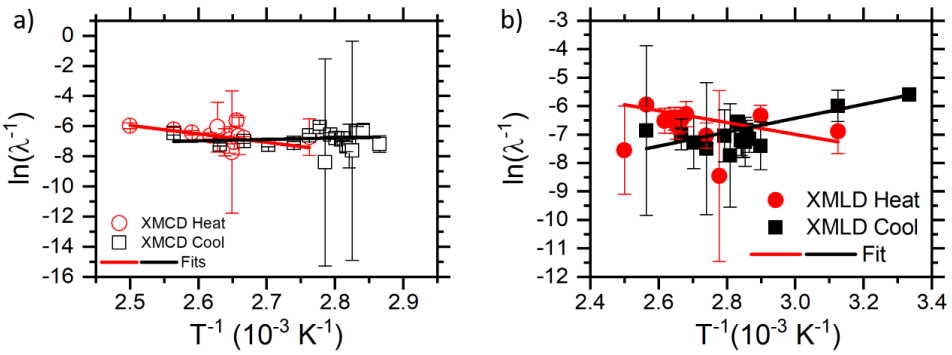

Figure 8.6: Arrhenius analysis for both dichroism types. Panel (a) shows the results for the measurements taken using XMCD. Panel (b) shows the results of the fitting for the XMLD measurements. Both panels here shows the fitting to equation 8.4 as the solid lines.

the fits to the heating branch yield $E_A/k_B = 2100 \pm 800$ K. The asymmetry between the dichroism types again implies that the behaviour measured is different between them.

Previously, a study similar to the one presented here into the relaxation behaviour in the MMP of B2-ordered FeRh was performed using magnetometry techniques by Loving [58]. This study reveals that the behaviour can be explained well using an Arrhenius model, which yields activation energies of $E_A/k_B = 13000 \pm 4000$ K for FeRh grown on MgO or $E_A/k_B = 4200 \pm 1000$ K for FeRh grown on Al_2O_3, for measurements on the heating branch [58]. As the magnetometry technique is only sensitive to the behaviour of the FM domains, the relaxation behaviour in that study was attributed to the random growth and nucleation of FM domains [58]. The activation energy for the relaxation process identified using magnetometry is present only for the heating branch and the sample with the lower activation energy is consistent with the value extracted from this experiment using XMCD when heating and suggests that the same process is occurring here. However, the activation energy is seen to be highly dependent on the substrate used and an independent corroboration of activation energy for this sample is required to say for certain if this is the case.

There is a discrepancy between the value measured for relaxation process measured using magnetometry and that extracted from the fitting to the XMLD measurement here. As the nucleation of FM domains would be expected throughout the transition

when heating, the asymmetry between the activation energies for the two dichroism types suggests that the XMLD measurements are not as sensitive to the influence of this relaxation process as their XMCD counterparts. Given that the total relaxation time is a combination of all of the various relaxation processes in the experiment and the difference in the property of the material which is measured using the different dichroism types, it is not surprising that the value of E_A extracted for the two dichroism types do not agree [151, 152]. This analysis implies that there are a series of different relaxation processes taking place in this system, each of which have different contributions to the total relaxation time depending on the type of magnetic dichroism used to probe the behaviour.

The fits of the Arrhenius law to the measurements performed when cooling lead to negative activations energies, which is an unphysical results. The inability to obtain physical data from the fits of the Arrhenius model to the cooling branch suggests that the nucleation of FM domains is not present on this transition branch. On this transition branch the nucleation and agglomeration of domains would take place within the AF phase. As the FM phase is metastable and is subject to supercooling on this transition branch [12], it is possible that the relaxation time associated with this process exceeds the timescales probed in this experiment. Further work is required to ascertain whether this is the case.

Another model that was tested for its ability to describe the behaviour of the relaxation time is that of critical slowing down. This model is used to describe the dependence of the relaxation behaviour in terms of its proximity to temperatures associated with phase transitions [82, 106]. It predicts that the time associated with fluctuations in a system scales critically with the proximity of the system to its critical temperature T_C [106]. The critical slowing down model predicts that the relaxation time depends on T_C according to [82, 106],

$$\lambda = \lambda_0 \left(\frac{T}{T_C} - 1 \right)^{-zv}, \tag{8.5}$$

where λ_0 is the relaxation time expected as $T \to \infty$ and zv is the critical exponent. For the critical exponent here, z is the exponent that describes the relationship between the correlation length and the proximity to the transition temperature and v then describes the dependence of the relaxation time on the correlation length [106]. The fitting of this equation to the data taken using XMCD and XMLD are shown in Fig. 8.7(a) and (b), respectively.

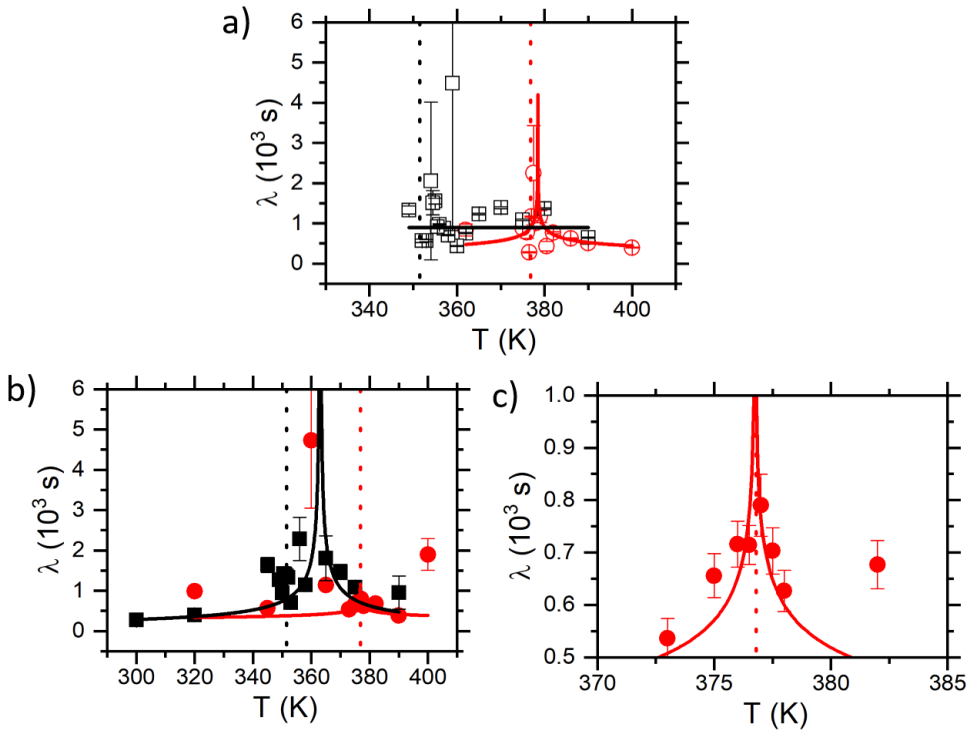

Figure 8.7: Application of the critical slowing down model to the relaxation time behaviour. Panel (a) shows the fitting of equation 8.5 to the data taken using XMCD. Panel (b) shows the fitting of the same equation to the data taken using XMLD, with a close up of the XMLD heating data set concentrated around the transition midpoint shown in panel (c). It was found not to be possible to accurate describe the measurements taken using XMCD when cooling using this model.

This equation appears to fit reasonably well to the relaxation behaviour of the heating branch measurements investigated using XMCD despite the large spread in the data. The extracted value of this critical temperature, $T_C = 378 \pm 2$ K, agrees reasonably well with the position of the transition midpoint, $T_T = 376.8 \pm 0.02$ K, extracted from the magnetometry measurements. The extracted value of $zv = 0.3 \pm 0.1$. This model fails to describe the behaviour of the relaxation time for measurements taken using XMCD when cooling. The model of critical slowing down is found to only really describe the behaviour well for the XMLD measurements taken when heating, in a

region surrounding the transition midpoint, as can seen by panel (c) of Fig. 8.7. Again, a good agreement between the extracted value of $T_C = 377 \pm 2$ K and the transition midpoint is seen in these measurements. The results of this critical temperature are consistent between the measurements performed using the two types of magnetic dichroism, implying that they observe the same process. The value of $zv = 0.15 \pm 0.08$ extracted for the XMLD measurements supports this hypothesis as the two values are consistent within error bar.

When looking at the fitting of the critical slowing down model to the behaviour of the cooling branch measurements performed using XMLD, the position of the critical temperature $T_C = 363 \pm 1$ K does not agree well with the position of the transition midpoint extracted using magnetometry $T_T = 351.5 \pm 0.02$ K. The extracted value of $zv = 0.6 \pm 0.1$ is much higher than that extracted for the heating branch measurements. Despite the ability of the critical slowing down equation to fit the data seen here, it is not clear whether this model accurately reflects the behaviour. Its validity is cast into further doubt as the critical temperature here does not correspond to a physical change in the system and appears to be a consequence of the spread in the data. Further investigations are required to ascertain the validity of this model to describe the behaviour seen here. However, the success of the fits for the measurements performed on the heating branch for both dichroism types suggests that critical slowing down is observed in the relaxation time here.

This model has been used previously to describe the behaviour of Ising spin-glasses and yields values of $zv \approx 5-10$ [82, 106] which is much larger than the values seen here. This implies that the relaxation process being measured here is not that of an Ising spin-glass. It also implies that the dependence of the dynamic behaviour on the proximity to this critical temperature is weak. The critical slowing down model is reliant on the divergence of the correlation length approaching the critical temperature associated with the phase transition [106]. This is a characteristic behaviour of a second-order phase transition and its applicability to first-order phase transitions is unclear [104].

As the behaviour of the stretching exponent is seen to follow the nature of the scattering object in this experiment, the relaxation time may also do the same. It can be seen from Fig. 8.4 that the behaviour in λ does agree well with the decrease in β for all data sets. Therefore, it is not possible to rule out that a change in the scatterer type and therefore the dynamic behaviour being measured is responsible for the observation

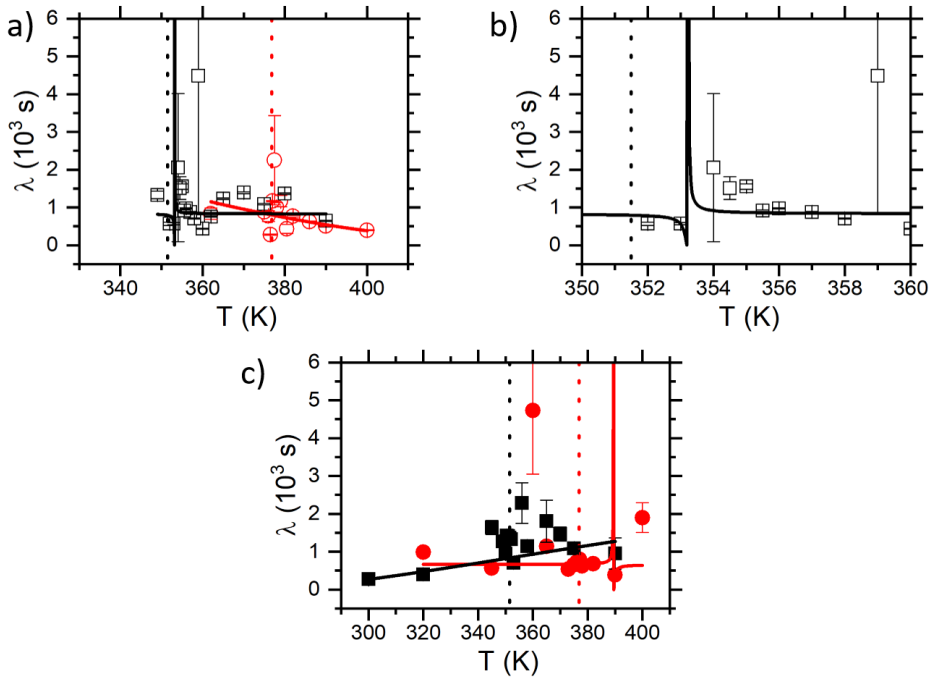

Figure 8.8: Application of the Vogel-Fulcher-Tammann model to the relaxation time behaviour. Panel (a) shows the fitting of equation 8.6 to the data taken using XMCD. Panel (b) shows a close up of the behaviour of the cooling branch when taken using XMCD focused around the transition midpoint. Panel (c) shows the results of fitting the Vogel-Fulcher-Tammann law to the measurements performed using XMLD. This law is believed not to describe the behaviour of any of the data sets here.

of this slowing down behaviour seen here and further investigations are required to ascertain if this is the case.

Another model that was tested was that of the Vogel-Fulcher-Tammann law [82, 83, 87, 154]. This model is similar to the Arrhenius model except there is now a temperature dependent activation energy present within the system [82, 83, 87, 154]. This type of relaxation is typically associated with freezing kinetics of glassy systems [82, 83, 87, 154]. Below the freezing temperature, T_0, the thermal excitations are no longer sufficient to overcome the energy barrier associated with the fluctuation and the relaxation time diverges. These relaxation processes have a temperature above which they can occur, which is known as the activation temperature T_A. The form of this

equation is given by,

$$\lambda = \lambda_{SA} e^{\frac{T_A}{T-T_0}}, \tag{8.6}$$

where λ_{SA} is the relaxation time for $T \to \infty$. The fits of this equation to the data for the measurements performed using XMCD is shown in Fig. 8.8(a). The fitting for the measurements taken when heating has clearly failed to accurately depict the behaviour here. Interestingly, when cooling there is a discontinuity in the fitted data implying that the freezing temperature occurs before the transition midpoint. However, upon closer inspection, such as that seen in panel (b) of Fig. 8.8, it can be seen that the function does not accurately describe the behaviour here and instead fits only the drop in λ at the same point as the discontinuity. The value of $T_0 = 353.2 \pm 0.2$ K, does not agree well with the transition midpoint and the reason for a freezing transition at this stage is unclear. This inflection in the fitted function is believed to be due to the drop in the values of λ seen in the data and the success of the fit is purely a consequence of this sudden change in λ, the reason for which is unclear at this stage. It is believed that this model does not accurately reflect the behaviour of the data here. The fitting of this function to the data taken using XMLD is shown in Fig. 8.8(c). Again, this fails to accurately reflect the behaviour of the data. All measurements yield values of T_A that are consistent with 0 with significant error bars. The inability of this model to effectively describe the behaviour means and the consistency with zero for the value of the activation temperature imply that this model cannot be used to describe the behaviour seen here. We take this to be a lack of evidence for the presence of glassy relaxation measured in this experiment.

The lack of a definitive conclusion regarding the relaxation time behaviour seen on the cooling branch measurements implies that a single model is not sufficient to describe the relaxation behaviour taking place in this system. Throughout the FeRh transition it may be expected that contributions arise from a series of different magnetic relaxation mechanisms. These include the nucleation of FM domains due to thermal fluctuations [58], possible relaxation of a spin-glass state in the domain wall [57] and relaxation due to magnetic frustration within the domain wall [18]. In theory, each of these possible relaxation pathways could exist at the same temperature, and would be subject to their own temperature dependence making the overall picture difficult to understand and further investigations are required to ascertain the underlying physical picture of what is being measured.

From the stretching exponent behaviour there is evidence of jammed dynamics within the region of the transition probed. These behaviours are often attributed to long range interactions such as RKKY and the dipolar interaction. This interpretation would make sense for the measurements performed using XMCD above the transition midpoint, where the magnetic domains would be in close proximity. In this scenario, the domains would be closely packed enough to affect each other through the RKKY and dipolar interactions. This, in turn, would lead to a system in which it is not posisble to totally resolve all of the competing interactions, leading to magnetic frustration within the region between FM domains and across the system as a whole, creating a rigid, diordered state as required. These interactions could lead to rotations of the magnetic structure as the system attempts to reach the lowest energy state configuration, which would then explain the observation of dynamic behaviour when measured by XMLD.

For the region of the transition below the tranistion midpoint however, where jammed dynamics are also seen, the applicability of the long range interactions is somewhat unclear. In this region of the transition, the FM domains are separated by lengthscales in excess of 300 nm, so the influence of FM domains on each other due to these long range interactions would be small. Therefore, the rigid behaviour is likely to come from another source. From the investigations into the behaviour of the relaxation time seen here, it is believed that the spontaneous nucleation of FM domains is present on the heating branch. The activation energy suggests that the rate at which these events occur would be slow and so for the lower temperatures it may be that the system appears to be rigid as it cannot relax quickly. Further investigations are required to say for sure if this is the case.

The observation of dynamics in which $\beta \sim 1$ when the system is probed using XMLD implies that the orientation of the spin-axis is not subject to the long range interactions at high temperatures when the system would be close to being fully FM. The contrast between the XMCD and XMLD measurements in the value of β in this region of the transition proves that the two are measuring fundamentally different behaviour in the system, as the value of β, and therefore the width of the relaxation time distribution, is different. As XMLD is senstive only to the rotation of the spin-axis and as the FM domains have a larger common spin-axis than the domain wall would do, the signal from these domains would be expected to dominate for XMLD. This may explain the large distribution of relaxation times measured in XMLD, as each of the different domains

will see a different environment and therefore have a different probability of having its spin-axis rotated due to thermal fluctuations. For XMCD measurements however, the magnetization of the individual domains is likely to change on a much longer timescale than fluctuations in the domain wall, and so this is likely the source of the dynamic behaviour measured using XMCD. The relaxation behaviour of the domains may be the source of the static reference signal seen in this experiment.

When moving towards the transition midpoint from the higher temperatures, the dynamic behaviour becomes increasingly jammed when measured by the XMLD. The behaviour in this region exhibits jammed dynamics when measured using XMCD, which implies that either the domain wall fluctuations start to influence the behaviour of the XMLD or that the domains begin to influence each others behaviour through long range interactions. Given that regions of AF material would also be introduced into the system at these temperatures, it is also not possible to rule out their influence in proceedings here.

At temperatures in immeadiate proximity to the transition midpoint when measured using XMCD, this jammed behaviour is seen to give way to behaviour that can be described by $\beta \sim 1$. This point coincides with the change in the nature of the scatterer seen in the previous chapter. The transition away from jammed dynamics suggests that the rigidity of the system is broken when approaching the the transition midpoint and that the distribution of the relaxation times again changes. The reason for this is unclear but it implies that the long range interaction do not influence the relaxtion behaviour.

At temperatures below the transition midpoint when measured using XMLD, the scattering is expected to be dominated by contributions from the AF phase as shown in the previous chapter. It is seen here that the dynamics exhibits $\beta \sim 1.3$ implying a narrower relaxation time distribution compared to the higher temperature measurements. This may be due to relaxation of both the AF and FM phases or contributions of the domain walls between the two phases. This behaviour is seen to be present through to the lowest temperature measurement on the heating branch, though the cooling branch can be described using a single relaxation time for the lowest temperature measurement. This behaviour suggests that more than one relaxation time is present at 320 K when heating but are not present at 300 K when cooling. This again may be due to the nucleation of FM domains being present on the heating branch but not on the

cooling branch or a behaviour related to the AF phase, though further investigations are required to ascertain if this is the case.

From this work it is clear that the dynamic behaviour in the FeRh material system is difficult to understand fully. We see evidence of dynamics due to long range interactions, as well as due to nucleation of FM domains due to thermal fluctuations. The behaviour of the relaxation time is difficult to interpret as is contains contributions from each of the different relaxation processes, each of which will have their own temperature dependence. What is clear from this experiment however is that investigations using XMLD can be used alongside XMCD measurements to add a greater depth to the understanding of synchrotron experiments as well as being able to measure the dynamic and structural behaviour of AF materials directly.

8.4 Conclusion

X-Ray Photon Correlation Spectroscopy investigations were used to ascertain the development of the dynamic behaviour of the system through the transition. To this end, the temporal correlation of images within a series were taken for a range of temperatures on both the heating and cooling branches using both types of magnetic dichroism.

The dynamic behaviour associated with this temporal correlation is calculated using the g_2 functions which are fitted to stretched exponential distributions for quantitative measures of the development of the dynamic behaviour through the transition. The development of the stretching exponent is seen to vary between $\beta \sim 1 - 1.5$ in a systematic manner when approaching the transition midpoint. This change is seen to go in opposite directions depending on the nature of the dichroism used to probe the system. The behaviour of the system is seen to be different depending on the dichroism type used to measure it. This is attributed to the differences in the fundamental properties of the system measured using each dichroism type.

It is seen that the behaviour of the measurements taken when heating can be fitted to an Arrhenius model. This implies that the relaxation behaviour here is subject to a temperature independent activation energy. The value of the activation energy extracted from the measurements taken when heating is consistent with literature that claims the magnetic relaxation seen in that experiment is due to the nucleation of FM domains due to thermal fluctuations [58]. The value extracted for measurements taken using XMLD is not consistent with the literature value or the XMCD measurements implying

that the relaxation measurements performed using XMLD have a different sensitivity to the FM nucleation than the measurements performed using XMCD, consistent with the behaviour of the stretching exponent.

It is also seen to be possible to fit the behaviour of some of the datasets to a model of critical slowing down. These fits give good agreement with each other and the success of these fittings imply that a second-order phase transition takes place within the domain wall between two FM domains at temperatures consistent with the transition midpoint. It is seen however, that the behaviour of the relaxation time can also be attributed to a change in the scatterer type and further investigations are required to ascertain the origin of this observed critical slowing down behaviour. It was also seen to be possible to fit this model to the behaviour of the cooling branch measurements performe using XMLD, though this is taken to be dubious as it does not accurately reflect the data and further investigations are required to ascertain if this observation can be believed.

It was found that fitting the behaviour of the relaxation time for the measurements taken when cooling to the Arrhenius model yield a negative activation energy, a non-physical results, which we take as a lack of evidence for the observation of the nucleation of FM domains due to thermal fluctuations when cooling. It is also found that the Vogel-Fulcher-Tammann law fails to accurately describe the behaviour of any of the data sets here which implies that the relaxation of a glassy like state within the domain wall is not observed here. This behaviour is in keeping with the complicated nature of the dynamic behaviour probed here and further investigations are required to ascertain what the behaviour of the relaxation time on the cooling branch corresponds too.

In this experiment it was seen to be possible to obtain measurable data from temperatures where the scattering was shown to be dominated by AF domains in the previous chapter when the system is probed using XMLD. These investigations can add depth of understanding to those performed using XMCD. The success of this experiment demonstrates that by combining XPCS with XMLD it is possible to directly measure the dynamic behaviour of AF materials.

Chapter 9

Conclusions and Outlook

9.1 Summary and Conclusions

The aim of the work included in this thesis was to investigate the mixed magnetic phase (MMP) of B2 ordered FeRh and to try and address shortcomings in our understanding so that, if applicable, it may be considered for use in spintronic devices. The main focuses of the work were to conclusively demonstrate an interphase exchange coupling in the MMP, to track the domain development of the two magnetic phase through the transition and to test the system for its dynamic behaviour over long time scales. To this end, thin films of B2 ordered FeRh were grown using DC magnetron sputtering and characterized for their high frequency properties using different magnetic resonance techniques and their long term magnetization dynamics using X-Ray Photon Correlation Spectroscopy (XPCS).

The Ferromagnetic Resonance (FMR) experiments firstly, show a value of g that is well below the free electron value. It is found to be possible to rectify this by adapting the method outlined by Shaw *et al.* for frequency-swept FMR [129]. In this model, the field is not sufficient to overcome the anisotropy fields in that orientation, which is believed to be the case here as the demagnetizing field is close to the minimum value of $\mu_0 H_{\mathrm{Ext}}$ used in the experiment [129]. Performing the analysis in this way also leads to values of g that are below the free electron value and below the value extracted by Mancini *et al.* for the fully FM phase of FeRh [55]. The behaviour of g is known to be subject to the influence of any boundaries present in the system [97]. By using the trilayer model and a model used to describe the intermixing of magnetic and non-magnetic objects at the boundary between them, it is shown that the g-factor in the AF layer has a non-zero contribution to the measured value of g. This implies that the AF layer has a non-zero magnetic moment present due to the intermixing of states at the boundary. The development of the g-factor for the AF region, and therefore the magnetic moment in the AF layer, is consistent with an exchange coupling as a result of a thickness dependent phase transition (TDPT) taking place in the AF layer. The magnetocrystalline anisotropy field shows no apparent dependence on the AF layer thickness and the value agrees well with predictions made for the size of the anisotropy field due to magnetoelastic effects [56]. The Gilbert damping parameter extracted from this experiment shows a decrease in damping for increasing AF layer thickness when cooling. This decrease occurs over length scales comparable with that of the changes in the AF g-factor and is also believed to correspond to a TDPT in the AF layer.

After these thicknesses, the damping parameter appears to increase quasi-linearly with increase AF layer thickness up to AF layer thickness of 10 nm when cooling and 17 nm when heating. This behaviour is consistent with the dephasing of a spin-current as it passes through the AF layer [137]. All of the results of this experiment are built on the assumption that the magnetic state can be described by the trilayer model and all the behaviour seen is real. There are doubts as to the validity of these assumptions and further work is required to say for sure whether this is the case.

As the FMR only provides indirect evidence for the presence of an exchange coupling between the two magnetic phases, spin-wave resonance (SWR) measurements were performed to try and demonstrate its presence conclusively. It was seen that measured exchange stiffness across the film thickness exhibits peaks in the extracted value with temperature superimposed upon a decreasing value across the range of the transition probed in this experiment. All of the measurements here are taken where AF material is present and so this behaviour is believed to be due to the influence of the AF layer. Using the trilayer model it is possible to show that this change is due to the presence of a weak exchange energy in the region defined by the magnetization as being AF. The behaviour of the exchange stiffness within the AF layer is consistent with the development of the exchange coupling as a function of AF thickness but also demonstrates a peak in the extracted value at AF layer thicknesses consistent with the dip in the damping seen in the FMR experiment. To try and ascertain the origin the exchange stiffness in the AF region, computer simulations of atomistic spin dynamics were performed. These simulations demonstrate the presence of an intermixing of magnetic states at the interface between them believed to be due to exchange coupling across the magnetic phase boundary. These simulations also show that evanescent spin-waves (ESWs) carry the PSSW excitation through the AF layer and are brought about by the exchange coupling at the MPB. The introduction of these ESWs at the end of the TDPT in the AF layer are then thought to be responsible for the increase in the exchange stiffness of the AF layer when cooling. These TDPTs are used to explain the peaks seen for both transition branches, which implies an asymmetry in the properties of the AF layer depending on the temperature sweep direction. Again, these results are built on the assumption that the magnetic state can be described by the trilayer model. Independent corroboration of this assumption is required to say for sure.

The focus then moved to trying to measure the development of the two magnetic

phases through the transition using Resonant Magnetic Small Angle X-Ray Scattering (RMSAXS) performed at the Diamond Light Source synchrotron facility. Firstly, these experiments were performed using X-Ray Magnetic Circular Dichroism (XMCD) to measure the development of the FM domains. These investigations show scattering from objects whose size and behaviour is consistent with the scattering between two FM domains across a region of AF material for measurements taken when heating. A transition between scattering from adjacent FM domains to scattering from the magnetic domains themselves is seen for measurements taken when cooling. A similar study was then performed using X-Ray Magnetic Linear Dichroism (XMLD) to see if it was possible to measure the domain development of the AF phase through the transition. These measurements show scattering from objects consistent with those taken using XMCD for temperatures above the transition midpoint for both temperature sweep directions. However, a clear deviation between the measurements taken using the two types of magnetic dichroism are seen at the transition midpoint and continues for all temperatures lower than this. It is taken at this point that this change corresponds to the point at which the scattering from the system starts to be dominated by scattering from the AF phase. Below the transition midpoint, the scattering from the AF domains is seen to have a consistent length scale of around 150 nm. These measurements are believed to constitute the first direct measurements of AF materials for their magnetic structure using XMLD combined with RMSAXS.

The dynamic measurements of the MMP were also taken using the two types of magnetic dichroism and XPCS. By fitting the g_2 function that results from these investigations to models of stretched exponential behaviour it is seen that the behaviour of the stretching exponent varies for all measurement sets when approaching the transition midpoint. For the measurements taken using XMCD the dynamic behaviour is seen to vary from jammed dynamics, dominated by long range interactions, to a less rigid system when approaching transition midpoint. The opposite behaviour is seen for measurements performed using XMLD suggesting that the two types of magnetic dichroism have different sensitivities to the different relaxation processes probed. It is seen to be possible to fit the behaviour of the relaxation time taken when heating to an Arrhenius model for measurements taken using both XMLD and XMCD, that reveal asymmetric activation energies. This observation supports the idea that the two dichroism types have different sensitivities to different relaxation behaviours. It was

also possible to fit the relaxation behaviour for the heating branch measurements to a model of critical slowing down, which indicates the presence of a second-order phase transition taking place within the domain wall at temperatures approaching the transition midpoint. It is unclear at this stage as to whether this is real or corresponds to a change in the nature of the scatterer at the same temperature. Conclusive fits to these models were not possible for measurements taken when cooling. It was also seen that the Vogel-Fulcher-Tammann model fails to accurately reflect the behaviour of any of the data sets here, implying that no glassy state is present in the domain wall in this system. Due to the complicated nature of FeRh and its phase transition dynamics, it was not possible to build a comprehensive picture of the physical processes responsible for the behaviour of the relaxation time. This experiment does show however that RMSAXS can be combined with XMLD to directly measure the dynamic behaviour of AF materials. As well as in conjunctoin with XMCD on FM materials to add a greater insight into the behaviour taking place.

9.2 Outlook and Plans For Further Work

The aims of this thesis included work that would investigate the suitability of the MMP of B2 ordered FeRh for use in spintronic devices designed to operate at GHz frequencies. In the results of the magnetic resonance experiments, evidence for the presence of an interphase exchange coupling in the MMP is presented. The presence of the AF phase clearly affects the properties of the MMP of FeRh within the range of the transition measured here and its presence should be considered for FeRh based spintronic devices intended to operate at GHz frequencies. Further testing on potential device architectures using the MMP should now be performed in order to demonstrate the validity of such devices. It may also be useful to perform an experiment similar to the one presented in this work in which the magnetic field is aligned within the film plane to test if the same results would be seen in that experiment geometry.

The interphase exchange coupling could also influence the behaviour of devices intended to operate in the nominally AF phase, as regions of residual FM material are expected at the surface. A similar study to that presented by Moriyama *et al.* should be performed in the MMP to test if this is the case [6]. Another study that could help elucidate the properties and development of the AF phase, would be to perform a study similar to that presented here by using antiferromagnetic resonance.

Also, the magnetic resonance experiments presented in chapters 5 and 6 were only performed through a small range of the transition. Ideally, it would be possible to track the same high frequency behaviour through the transition in its entirety. This includes taking data that would fill in the gaps on the heating arm close to the fully FM phase and give a finer point density in the cooling branch to try and conclusively demonstrate a linear increase with t_{AF} there. It would also be beneficial to see how the behaviour changes, if it does so, when the trilayer model breaks down as the domains begin to disintegrate. Such a study is of paramount importance for understanding the applications of the MMP for high frequency spintronic devices. To test the validity of the results of this experiment, it may be beneficial to re-perform the experiment on another sample.

The behaviour of the magnetic resonance experiments would benefit from being re-performed in a system designed for high temperature magnetic resonance experiments. In theory, this will remove the artefacts seen in the experiment presented here and allow for the conclusion of the SWR investigations on both transition branches. It would also benefit from an independent corroboration as to the nature of the magnetic state through the range probed here to validate the use of the trilayer model.

The attempts to measure the domain development of both magnetic phases through the transition were successful to some degree, as it was seen that a transition between scattering from each magnetic phase is seen at the transition midpoint using RMSAXS and XMLD. However, it was not possible to measure the behaviour of the AF phase extensively through the entirety of the transition. Perhaps a more appropriate way of performing this experiment would be to use both XMCD- and XMLD-PEEM as per the Baldasseroni *et al.* study over the entire transition range [35].

The measurements of the dynamic behaviour of the system reveal that the nature of the magnetic relaxation in FeRh is a complicated one. There are likely to be several contributing relaxation processes each with their own temperature dependence which are difficult to deconvolute in this experiment. A thorough study of the behaviour of the different relaxation processes should be performed in order to try and fully understand the behaviour seen here. This would be of benefit to the understanding of the suitability of the AF phase for use in spintronic devices. Such a study should also be performed on the AF phase of FeRh for the same reasons.

The dynamic behaviour of the magnetic domain walls in B2-ordered FeRh will

affect the magnetic state of B2-ordered FeRh in the MMP. Further to this, previous measurements on sheet films that look at the relaxation of the system appear to show a changing magnetic state with time due to the nucleation of FM domains [58]. In this work a behaviour similar to this is observed though it is difficult to ascertain for sure whether this behaviour is seen here due to the difficulty in interpreting the results of the investigations into the dynamic behaviour. In order to ascertain whether this behaviour is appropriate to adopt here, a study similar to the one performed by Loving, in which the Avrami model is applied to relaxation behaviour measured using magnetometry techniques should also be performed on the sample used here in the XPCS experiments.

The nucleation of FM domains with time also suggests that the MMP of sheet films is not suitable for use in long term storage. However, it is unclear at this stage as to whether reducing the system size to dimensions in which the switching of individual regions can be seen would affect the relaxation of these types of devices. A comprehensive study focusing on relaxation in these system where the geometry is confined should be performed in order to be able to fully state the suitability of FeRh for use in these long term magnetic storage elements.

The RMSAXS experiments did show that XMLD is a viable tool for directly measuring the structural and dynamic properties of the AF state of FeRh and should be used to measure these properties in other AF materials. The combination of XPCS with XMLD provides a promising avenue for the study of dynamic behaviour in AF materials in the future. The frame rate of images in the experiment presented here is particularly slow at ≈ 1 Hz, however, recent advancements in technology has seen this increase to ≈ 50 Hz at other beamlines [83]. If these high frequency dynamics can be accessed it is possible that the high frequency dynamics of AF materials can be accessed using the XMLD in conjunction with XPCS.

References

[1] S.D. Bader and S.S.P. Parkin. Spintronics. *Annual Review of Condensed Matter Physics*, 1:71, 2010.

[2] A. Hirohata and K.Takanashi. Future perspectives for spintronic devices. *Journal of Physics D: Applied Physics*, 47:193001, 2014.

[3] J. U. Thiele, S. Maat, and E. E. Fullerton. FeRh/FePt exchange spring films for thermally assisted magnetic recording media. *Applied Physics Letters*, 82:2859, 2003.

[4] R. O. Cherifi, V. Ivanovskaya, L. C. Phillips, A. Zobelli, I. C. Infante, E. Jacquet, V. Garcia, S. Fusil, P. R. Briddon, N. Guiblin, A. Mougin, A. A. Unal, F. Kronast, S. Valencia, B. Dkhil, A. Barthélémy, and M. Bibes. Electric-field control of magnetic order above room temperature. *Nature Materials*, 13:345, 2014.

[5] Y. Lee, Z. Q. Liu, J. T. Heron, J. D. Clarkson, J. Hong, C. Ko, M. D. Biegalski, U. Aschauer, S. L. Hsu, M. E. Nowakowski, J. Wu, H. M. Christen, S. Salahuddin, J. B. Bokor, N. A. Spaldin, D. G. Schlom, and R. Ramesh. Large resistivity modulation in mixed-phase metallic systems. *Nature Communications*, 6:5959, 2015.

[6] T. Moriyama, N. Matsuzaki, K. J. Kim, I. Suzuki, T. Taniyama, and T. Ono. Sequential write-read operations in FeRh antiferromagnetic memory. *Applied Physics Letters*, 107:122403, 2015.

[7] C. Le Graet, T. R. Charlton, M. McLaren, M. Loving, S. A. Morley, C. J. Kinane, R. M.D. Brydson, L. H. Lewis, S. Langridge, and C. H. Marrows. Temperature

controlled motion of an antiferromagnet- ferromagnet interface within a dopant-graded FeRh epilayer. *APL Materials*, 3:041802, 2015.

[8] M. Fallot and R Hocart. On the appearance of ferromagnetism upon elevation of the temperature of iron and rhodium. *Revue Scientifique*, 8:498, 1939.

[9] J. S. Kouvel and C. C. Hartelius. Anomalous magnetic moments and transformations in the ordered alloy FeRh. *Journal of Applied Physics*, 33:1343, 1962.

[10] F. De Bergevin and L Muldawer. Crystallographic study of certain FeRh alloys. *Weekly Records of the Academy of Science Sessions*, 252:1347, 1961.

[11] A. I. Zakharov, A.M. Kadomtseva, R.Z. Levitin, and E.G. Ponyatovskii. Magnetic and magnetoelastic properties of a metamagnetic iron–rhodium alloy. *Soviet Physics JETP*, 19:1348, 1964.

[12] M. A. de Vries, M. Loving, M. McLaren, R. M. D. Brydson, X. Liu, S. Langridge, L. H. Lewis, and C. H. Marrows. Asymmetric "melting" and "freezing" kinetics of the magnetostructural phase transition in B2-ordered FeRh epilayers. *Applied Physics Letters*, 104:232407, 2014.

[13] M. A. de Vries, M. Loving, A. P. Mihai, L. H. Lewis, D. Heiman, and C. H. Marrows. Hall-effect characterization of the metamagnetic transition in FeRh. *New Journal of Physics*, 15:013008, 2013.

[14] J. S. Kouvel. Unusual nature of the abrupt magnetic transition in FeRh and its pseudobinary variants. *Journal of Applied Physics*, 37:1257, 1966.

[15] R. Barua, F. Jiménez-Villacorta, and L. H. Lewis. Predicting magnetostructural trends in FeRh-based ternary systems. *Applied Physics Letters*, 103:102407, 2013.

[16] R. C. Wayne. Pressure dependence of the magnetic transitions in Fe-Rh alloys. *Physical Review*, 170:523, 1968.

[17] A. J. Heeger. Pressure dependence of the FeRh first-order phase transition. *Journal of Applied Physics*, 41:4751, 1970.

[18] T. A. Ostler, C. Barton, T. Thomson, and G. Hrkac. Modeling the thickness dependence of the magnetic phase transition temperature in thin FeRh films. *Physical Review B*, 95:064415, 2017.

[19] C. W. Barton, T. A. Ostler, D. Huskisson, C. J. Kinane, S. J. Haigh, G. Hrkac, and T. Thomson. Substrate induced strain field in FeRh epilayers grown on single crystal MgO (001) substrates. *Scientific Reports*, 7:44397, 2017.

[20] L.J. Swartzendruber. The Fe-Rh (iron-rhodium) system. *Journal of Phase Equilibria*, 5:456, 1984.

[21] J. B. Staunton, R. Banerjee, M. Dos Santos Dias, A. Deak, and L. Szunyogh. Fluctuating local moments, itinerant electrons, and the magnetocaloric effect: Compositional hypersensitivity of FeRh. *Physical Review B*, 89:054427, 2014.

[22] M. Jiang, X.Z. Chen, X.J. Zhou, Y.Y. Wang, F. Pan, and C. Song. Influence of film composition on the transition temperature of FeRh films. *Journal of Crystal Growth*, 438:19, 2016.

[23] S. Maat, J. U. Thiele, and E. E. Fullerton. Temperature and field hysteresis of the antiferromagnetic-to-ferromagnetic phase transition in epitaxial FeRh films. *Physical Review B*, 72:214432, 2005.

[24] M. Loving, F. Jiménez-Villacorta, B. Kaeswurm, D. A. Arena, C. H. Marrows, and L. H. Lewis. Structural evidence for stabilized ferromagnetism in epitaxial ferh nanoislands. *Journal of Physics D: Applied Physics*, 46:162002, 2013.

[25] V Uhlíř, J. A. Arregi, and E. E. Fullerton. Colossal magnetic phase transition asymmetry in mesoscale FeRh stripes. *Nature Communications*, 7:13113, 2016.

[26] K. Matsumoto, M. Kimata, K. Kondou, R.C. Temple, C.H. Marrows, and Y. Otani. Magnetothermodynamic properties and anomalous magnetic phase transition in FeRh nanowires. *IEEE Transactions on Magnetics*, 54:2300904, 2018.

[27] R. C. Temple, T. P. Almeida, J. R. Massey, K. Fallon, R. Lamb, S. A. Morley, F. Maccherozzi, S. S. Dhesi, D. McGrouther, S. McVitie, T. A. Moore, and C. H. Marrows. Antiferromagnetic-ferromagnetic phase domain development in nanopatterned FeRh islands. *Physical Review Materials*, 2:104406, 2018.

[28] T. Naito, I. Suzuki, M. Itoh, and T. Taniyama. Effect of spin polarized current on magnetic phase transition of ordered FeRh wires. *Journal of Applied Physics*, 109:07C911, 2011.

[29] I. Suzuki, T. Naito, M. Itoh, and T. Taniyama. Barkhausen-like antiferromagnetic to ferromagnetic phase transition driven by spin polarized current. *Applied Physics Letters*, 107:082408, 2015.

[30] D. J. Keavney, Y. Choi, M. V. Holt, V. Uhlír, D. Arena, E. E. Fullerton, P. J. Ryan, and J.-W. Kim. Phase coexistence and kinetic arrest in the magnetostructural transition of the ordered alloy FeRh. *Scientific Reports*, 8:1778, 2018.

[31] T. P. Almeida, R. Temple, J. Massey, K. Fallon, D. McGrouther, T. Moore, C. H. Marrows, and S. McVitie. Quantitative TEM imaging of the magnetostructural and phase transitions in FeRh thin film systems. *Scientific Reports*, 7:17835, 2017.

[32] C. Baldasseroni, C. Bordel, A. X. Gray, A. M. Kaiser, F. Kronast, J. Herrero-Albillos, C. M. Schneider, C. S. Fadley, and F. Hellman. Temperature-driven nucleation of ferromagnetic domains in FeRh thin films. *Applied Physics Letters*, 100:262401, 2012.

[33] S. O. Mariager, L. Le Guyader, M. Buzzi, G. Ingold, and C. Quitmann. Imaging the antiferromagnetic to ferromagnetic first order phase transition of FeRh. *arXiv e-prints*, page arXiv:1301.4164, 2013.

[34] C. J. Kinane, M. Loving, M. A. de Vries, R. Fan, T. R. Charlton, J. S. Claydon, D. A. Arena, F. Maccherozzi, S. S. Dhesi, D. Heiman, C. H. Marrows, L. H. Lewis, and S. Langridge. Observation of a temperature dependent asymmetry in the domain structure of a Pd-doped FeRh epilayer. *New Journal of Physics*, 16: 113073, 2014.

[35] C. Baldasseroni, C. Bordel, C. Antonakos, A. Scholl, K. H. Stone, J. B. Kortright, and F. Hellman. Temperature-driven growth of antiferromagnetic domains in thin-film FeRh. *Journal of Physics: Condensed Matter*, 27:256001, 2015.

[36] C. Gatel, B. Warot-Fonrose, N. Biziere, L. A. Rodríguez, D. Reyes, R. Cours, M. Castiella, and M. J. Casanove. Inhomogeneous spatial distribution of the magnetic transition in an iron-rhodium thin film. *Nature Communications*, 8: 15703, 2017.

[37] R. Fan, C. J. Kinane, T. R. Charlton, R. Dorner, M. Ali, M. A. de Vries, R. M. D. Brydson, C. H. Marrows, B. J. Hickey, D. A. Arena, B. K. Tanner, G. Nisbet, and S. Langridge. Ferromagnetism at the interfaces of antiferromagnetic FeRh epilayers. *Physical Review B*, 82:184418, 2010.

[38] E. F. Bertaut, A. Delapalme, F. Forrat, G. Roult, F. De Bergevin, and R. Pauthenet. Magnetic structure work at the nuclear center of Grenoble. *Journal of Applied Physics*, 33:1123, 1962.

[39] G. Shirane, C.W. Chen, P.A. Flinn, and R. Nathans. Hyperfine fields and magnetic moments in the Fe-Rh system. *Journal of Applied Physics*, 34:1044, 1963.

[40] M. P. Annaorazov, S. A. Nikitin, A. L. Tyurin, K. A. Asatryan, and A. Kh Dovletov. Anomalously high entropy change in FeRh alloy. *Journal of Applied Physics*, 79:1689, 1996.

[41] S.A. Nikitin, G. Myalikgulyev, A.M. Tishin, M.P. Annaorazov, K.A. Asatryan, and A.L. Tyurin. The magnetocaloric effect in $Fe_{49}Rh_{51}$ compound. *Physics Letters A*, 148:363, 1990.

[42] Y. Liu, L. C. Phillips, R. Mattana, M. Bibes, A. Barthélémy, and B. Dkhil. Large reversible caloric effect in FeRh thin films via a dual-stimulus multicaloric cycle. *Nature communications*, 7:11614, 2016.

[43] E. Stern-Taulats, T. Castán, A. Planes, L. H. Lewis, R. Barua, S. Pramanick, S. Majumdar, and L. Manosa. Giant multicaloric response of bulk $Fe_{49}Rh_{51}$. *Physical Review B*, 95:104424, 2017.

[44] N. W. Ashcroft and N. D. Mermin. *Solid State Physics*, chapter 25, page 490. Harcourt College Publishers, 1976.

[45] J. A. Ricodeau and D. Melville. Model of the antiferromagnetic-ferromagnetic transition in FeRh alloys. *Journal of Physics F: Metal Physics*, 2:337, 1972.

[46] V. L. Moruzzi and P. M. Marcus. Antiferromagnetic-ferromagnetic transition in FeRh. *Physical Review B*, 46:2864, 1992.

[47] R. Y. Gu and V. P. Antropov. Dominance of the spin-wave contribution to the magnetic phase transition in FeRh. *Physical Review B*, 72:012403, 2005.

[48] L. M Sandratskii and P. Mavropoulos. Magnetic excitations and femtomagnetism of FeRh: A first-principles study. *Physical Review B*, 83:174408, 2011.

[49] C. Kittel. Model of exchange-inversion magnetization. *Physical Review*, 120:335, 1960.

[50] P. Tu, A.J. Heeger, J.S. Kouvel, and J.B. Comly. Mechanism for the first-order magnetic transition in the FeRh system. *Journal of Applied Physics*, 40:1368, 1969.

[51] J.-U. Thiele, M. Buess, and C. H. Back. Spin dynamics of the antiferromagnetic-to-ferromagnetic phase transition in FeRh on a sub-picosecond time scale. *Applied Physics Letters*, 85:2857, 2004.

[52] G. Ju, J. Hohlfeld, B. Bergman, R. J. M. van de Veerdonk, O. N. Mryasov, J.-Y. Kim, X. Wu, D. Weller, and B. Koopmans. Ultrafast generation of ferromagnetic order via a laser-induced phase transformation in FeRh thin films. *Physical Review Letters*, 93:197403, 2004.

[53] I. Radu, C. Stamm, N. Pontius, T. Kachel, P. Ramm, J.-U. Thiele, H.A. Dürr, and C.H. Back. Laser-induced generation and quenching of magnetization on FeRh studied with time-resolved x-ray magnetic circular dichroism. *Physical Review B*, 81:104415, 2010.

[54] X. Marti, I. Fina, C. Frontera, Jian Liu, P. Wadley, Q. He, R. J. Paull, J. D. Clarkson, J. Kudrnovský, I. Turek, J. Kuneš, D. Yi, J. H. Chu, C. T. Nelson, L. You, E. Arenholz, S. Salahuddin, J. Fontcuberta, T. Jungwirth, and R. Ramesh. Room-temperature antiferromagnetic memory resistor. *Nature Materials*, 13:367, 2014.

[55] E. Mancini, F. Pressacco, M. Haertinger, E. E. Fullerton, T. Suzuki, G. Woltersdorf, and C. H. Back. Magnetic phase transition in iron rhodium thin films probed by ferromagnetic resonance. *Journal of Physics D: Applied Physics*, 46:245302, 2013.

[56] H. Kumar, D. R. Cornejo, S. L. Morelhao, S. Kycia, I. M. Montellano, N. R. Alvarez, G. Alejandro, and A. Butera. Strain effects on the magnetic order of epitaxial FeRh thin films. *Journal of Applied Physics*, 124:085306, 2018.

[57] A. Hernando, E. Navarro, M. Multigner, A. R. Yavari, D. Fiorani, M. Rosenberg, G. Filoti, and R. Caciuffo. Boundary spin disorder in nanocrystalline FeRh alloys. *Physical Review B*, 58:5181, 1998.

[58] M. Loving. *Understanding the Magnetostructural Transformation in FeRh thin films*. PhD thesis, The Department of Chemical Engineering, Northeastern University, 2013.

[59] W. H. Meiklejohn and C. P. Bean. New magnetic anisotropy. *Physical Review*, 105:904, 1957.

[60] M. Ali, C. H. Marrows, and B. J. Hickey. Onset of exchange bias in ultrathin antiferromagnetic layers. *Physical Review B*, 67:172405, 2003.

[61] F. Radu. *Fundamental Aspects of Exchange Bias Effect in AF/F Bilayers and Multilayers*. PhD thesis, Ruhr-Universit at Bochum, 2005.

[62] M. Ali, P. Adie, C. H. Marrows, D. Greig, B. J. Hickey, and R. L. Stamps. Exchange bias using a spin glass. *Nature Materials*, 6:70, 2006.

[63] A. Heidarian, S. Stienen, A. Semisalova, Y. Yuan, E. Josten, R. Hübner, S. Salamon, H. Wende, R. A. Gallardo, J. Grenzer, K. Potzger, R. Bali, S. Facsko, and J. Lindner. Ferromagnetic resonance of MBE-grown FeRh thin films through the metamagnetic phase transition. *Physica Status Solidi B*, 254:1700145, 2017.

[64] M. A. W. Schoen, J. M. Shaw, H. T. Nembach, M. Weiler, and T. J. Silva. Radiative damping in waveguide-based ferromagnetic resonance measured via analysis of perpendicular standing spin waves in sputtered permalloy films. *Physical Review B*, 92:184417, 2015.

[65] M. H. Seavey and P. E. Tannenwald. Direct observation of spin-wave resonance. *Physical Review Letters*, 1:168, 1958.

[66] C. Kittel. Excitation of spin waves in an ferromagnet by a uniform RF field. *Physical Review*, 110:1295, 1959.

[67] R. P. van Stapele, F. J. A. M. Greidanus, and J. W. Smits. The spin-wave spectrum of layered magnetic thin films. *Journal of Applied Physics*, 57:1282, 1985.

[68] J. M. D. Coey. *Magnetism and Magnetic Materials*, chapter 9, page 315. Cambridge University Press, 3 edition, 2012.

[69] S. T. B. Goennenwein, T. Graf, T. Wassner, M. S. Brandt, M. Stutzmann, J. B. Philipp, R. Gross, M. Krieger, K. Zürn, P. Ziemann, A. Koeder, S. Frank, W. Schoch, and A. Waag. Spin wave resonance in $Ga_{1-x}Mn_xAs$. *Applied Physics Letters*, 82:730, 2003.

[70] Y. Yin, M. Ahlberg, P. Dürrenfeld, Y. Zhai, R. K. Dumas, and J. Åkerman. Ferromagnetic and spin-wave resonance on heavy-metal-doped permalloy films: Temperature effects. *IEEE Magnetics Letters*, 8:3502604, 2017.

[71] H. Qin, S. J. Hämäläinen, and S. van Dijken. Exchange-torque-induced excitations of perpendicular standing spin waves in nanometer-thick YIG films. *Scientific Reports*, 8:5755, 2018.

[72] R. Khymyn, I. Lisenkov, V. S. Tiberkevich, A. N. Slavin, and B. A. Ivanov. Transformation of spin current by antiferromagnetic insulators. *Physical Review B*, 93:224421, 2016.

[73] P. Fischer, R. Zeller, G. Schütz, G. Georigk, and H.G. Haubold. Magnetic small angle x-ray scattering. *Journal de Physique IV*, 7:753, 1997.

[74] J. B. Kortright, S.-K. Kim, G. P. Denbeaux, G. Zeltzer, K. Takano, and E. E. Fullerton. Soft-x-ray small-angle scattering as a sensitive probe of magnetic and charge heterogeneity. *Physical Review B*, 64:092401, 2001.

[75] K. Bagschik, R. Frömter, J. Bach, B. Beyersdorff, L. Müller, S. Schleitzer, M. H. Berntsen, C. Weier, R. Adam, J. Viefhaus, C. M. Schneider, G. Grübel, and H. P. Oepen. Employing soft x-ray resonant magnetic scattering to study domain sizes and anisotropy in Co/Pd multilayers. *Physical Review B*, 94:134413, 2016.

[76] J. Stohr and H. C. Siegmann. *Magnetism: From Fundamentals to Nanoscale Dynamics*, chapter 9. Springer Series in Solid State Physics, 2006.

[77] J. Stohr. X-ray magnetic circular dichroism spectroscopy of transition metal. *Journal of Electron Spectroscopy and Related Phenomena*, 75:253, 1995.

[78] O. Glatter and O. Kratky. *Small Angle X-ray Scattering*, chapter 2. Academic Press, 1982.

[79] C. Gutt, S. Streit-Nierobisch, L.-M. Stadler, B. Pfau, C. M. Günther, R. Könnecke, R. Frömter, A. Kobs, D. Stickler, H. P. Oepen, R. R. Fäustlin, R. Treusch, J. Feldhaus, E. Weckert, I. A. Vartanyants, M. Grunze, A. Rosenhahn, T. Wilhein, S. Eisebitt, and G. Grübel. Single-pulse resonant magnetic scattering using a soft x-ray free-electron laser. *Physical Review B*, 81:100401, 2010.

[80] O. G. Shpyrko. X-ray photon correlation spectroscopy. *Journal of synchrotron radiation*, 21:1057, 2014.

[81] S. K. Sinha, Z. Jiang, and L. B. Lurio. X-ray photon correlated spectroscopy studies of surfaces and thin films. *Advanced Materials*, 26:7764, 2014.

[82] S. A. Morley, D. Alba Venero, J. M. Porro, S. T. Riley, A. Stein, P. Steadman, R. L. Stamps, S. Langridge, and C. H. Marrows. Vogel-Fulcher-Tammann freezing of a thermally fluctuating artificial spin ice probed by x-ray photon correlation spectroscopy. *Physical Review B*, 95:104422, 2017.

[83] X. M. Chen, B. Farmer, J. S. Woods, S. Dhuey, W. Hu, C. Mazzoli, S.B. Wilkins, I. K. Robinson, L. E. De Long, S. Roy, and J.T. Hastings. Spontaneous magnetic superdomain wall fluctuations in an artificial antiferromagnet. *arXiv e-prints*, page 1809.05656, 2018.

[84] B. Ruta, Y. Chushkin, G. Monaco, L. Cipelletti, E. Pineda, P. Bruna, V.M. Giordano, and M. Gonzalez-Silveira. Atomic-scale relaxation dynamics and aging in a metallic glass probed by x-ray photon correlation spectroscopy. *Physical Review Letters*, 109:165701, 2012.

[85] Z. Evenson, B. Ruta, S. Hechler, M. Stolpe, E. Pineda, I. Gallino, and R. Busch. X-ray photon correlation spectroscopy reveals intermittent aging dynamics in a metallic glass. *Physical Review Letters*, 115:175701, 2015.

[86] O. G. Shpyrko, E. D. Isaacs, J. M. Logan, Y. Feng, G. Aeppli, R. Jaramillo, H. C. Kim, T. F. Rosenbaum, P. Zschack, M. Sprung, S. Narayanan, and A. R. Sandy.

Direct measurement of antiferromagnetic domain fluctuations. *Nature*, 447:68, 2007.

[87] S.-W. Chen, H. Guo, K. A. Seu, K. Dumesnil, S. Roy, and S. K. Sinha. Jamming behavior of domains in a spiral antiferromagnetic system. *Physical Review Letters*, 110:217201, 2013.

[88] S. P. Bennett, A. Herklotz, C. D. Cress, A. Ievlev, C. M. Rouleau, I. I. Mazin, and V. Lauter. Magnetic order multilayering in FeRh thin films by He-Ion irradiation. *Materials Research Letters*, 6:106, 2018.

[89] J. Chen, Y. Gao, L. Wu, J. Ma, and C.-W. Nan. A magnetic glass state over the first-order ferromagnetic-to-antiferromagnetic transition in FeRh film. *Materials Research Letters*, 5:329, 2017.

[90] S. Konings, C. Schüßler-Langeheine, H. Ott, E. Weschke, E. Schierle, H. Zabel, and J. B. Goedkoop. Magnetic domain fluctuations in an antiferromagnetic film observed with coherent resonant soft x-ray scattering. *Physical Review Letters*, 106:077402, 2011.

[91] N. W. Ashcroft and N. D. Mermin. *Solid State Physics*, chapter 2. Harcourt College Publishers, 1976.

[92] J. M. D. Coey. *Magnetism and Magnetic Materials*, chapter 3, page 242. Cambridge University Press, 3 edition, 2012.

[93] J. M. D. Coey. *Magnetism and Magnetic Materials*, chapter 5, page 242. Cambridge University Press, 3 edition, 2012.

[94] S. Blundell. *Magnetism In Condensed Matter*, chapter 7, page 146. Oxford University Press, 2001.

[95] S. Blundell. *Magnetism In Condensed Matter*, chapter Appendix C, page 210. Oxford University Press, 2001.

[96] A. H. Morrish. *The Physical Principles of Magnetism*, chapter 2. John Wiley and Sons, 1965.

[97] J. P. Nibarger, R. Lopusnik, Z. Celinski, and T. J. Silva. Variation of magnetization and the landé g factor with thickness in NiFe films. *Applied Physics Letters*, 83:93, 2003.

[98] J. Stohr and H. C. Siegmann. *Magnetism: From Fundamentals to Nanoscale Dynamics*, chapter 2. Springer Series in Solid State Physics, 2006.

[99] S. Blundell. *Magnetism In Condensed Matter*, chapter Appendix D, page 214. Oxford University Press, 2001.

[100] S. Blundell. *Magnetism In Condensed Matter*, chapter 6, page 128. Oxford University Press, 2001.

[101] C. Mitsumata and A. Sakuma. Generalized model of antiferromagnetic domain wall. *IEEE Transactions on Magnetics*, 47:3501, 2011.

[102] H. Béa, M. Bibes, F. Ott, B. Dupé, X.-H. Zhu, S. Petit, S. Fusil, C. Deranlot, K. Bouzehouane, and A. Barthélémy. Mechanisms of exchange bias with multiferroic $BiFeO_3$ epitaxial thin films. *Physical Review Letters*, 100:017204, 2008.

[103] S. Blundell. *Magnetism In Condensed Matter*, chapter 8, page 166. Oxford University Press, 2001.

[104] K. Binder. Theory of first-order phase transitions. *Reports on Progress in Physics*, 50:783, 1987.

[105] D. A. Porter and K. E. Easterling. *Phase Transformations in Metals and Alloys*, chapter 5. Van Nostrand Reinhold Publishing, 1981.

[106] C. Djurberg, P. Svedlindh, P. Nordblad, M. F. Hansen, F. Bødker, and S. Mørup. Dynamics of an interacting particle system: Evidence of critical slowing down. *Physical Review Letters*, 79:5154, 1997.

[107] C. Kittel. *Introduction to Solid State Physics*. John Wiley and Sons, 2005.

[108] N. W. Ashcroft and N. D. Mermin. *Solid State Physics*, chapter 6. Harcourt College Publishers, 1976.

[109] B. E. Warren. *X-Ray Diffraction*, chapter 12. Addison-Wesley Publishing Company, 1969.

[110] W. H. Bragg and W. L. Bragg. The reflection of x-rays by crystals. *Proceedings of the Royal Society of London. Series A*, 88:428, 1913.

[111] S. Czekaj, F. Nolting, L. J. Heyderman, P. R. Willmott, and G. van der Laan. Sign dependence of the x-ray magnetic linear dichroism on the antiferromagnetic spin axis in $LaFeO_3$ thin films. *Physical Review B*, 73:020401, 2006.

[112] D. S. Sivia. *Elementary Scattering Theory For X-Ray and Neutron Users*, chapter 5. Oxford University Press, 2011.

[113] F. Livet, F. Bley, F. Ehrburger-Dolle, I. Morfin, E. Geissler, and M. Sutton. X-ray intensity fluctuation spectroscopy by heterodyne detection. *Journal of Synchrotron Radiation*, 13:453, 2006.

[114] M. Sutton, S. G. J. Mochrie, T. Greytak, S. E. Nagler, L. E. Berman, G. A. Held, and G. B. Stephenson. Observation of speckle by diffraction with coherent x-rays. *Nature*, 352:608, 1991.

[115] S. A. Morley. *The Dynamics of Artificial Spin Ice in Real and Reciprocal Space*. PhD thesis, School of Physics and Astronomy, University of Leeds, 2015.

[116] M. Sutton, K. Laaziri, F. Livet, and F Bley. Using coherence to measure two-time correlation functions. *Optics Express*, 11:2268, 2003.

[117] W. H. de Jeu, A. Madsen, I. Sikharulidze, and S. Sprunt. Heterodyne and homodyne detection in fluctuating smectic membranes by photon correlation spectroscopy at x-ray and visible wavelengths. *Physica B: Condensed Matter*, 357:39, 2005.

[118] C. Le Graët, M. A. de Vries, M. McLaren, R. M. D. Brydson, M. Loving, D. Heiman, L. H. Lewis, and C. H. Marrows. Sputter growth and characterization of metamagnetic B2-ordered FeRh epilayers. *Journal of Visualized Experiments*, 80: 50603, 2013.

[119] C. Russell, C. D. Wood, A. D. Burnett, L. Li, E. H. Linfield, A. G. Davies, and J. E. Cunningham. Spectroscopy of polycrystalline materials using thinned-substrate planar goubau line at cryogenic temperatures. *Lab on a Chip*, 13:4065, 2013.

[120] H. Kiessig. Interferenz von röontgenstrahlen an düunnen schichten. *Annalen der Physik*, 10:769, 1931.

[121] M. Birkholz. *Thin film analysis by x-ray scattering*, chapter 4, page 168. Wiley, 2006.

[122] Quantum Design. *MPMS squid-vsm reference manual, Technical report*, 2010.

[123] D. S. Schmool and J. M. Barandiaran. Ferromagnetic resonance and spin wave resonance in multiphase materials: theoretical considerations. *Journal of Physics: Condensed Matter*, 10:10679, 1998.

[124] T. L. Gilbert. A phenomenological theory of damping in ferromagnetic materials. *IEEE Transactions on Magnetics*, 40:3443, 2004.

[125] Y. Tserkovnyak, A. Brataas, and G. E. W. Bauer. Enhanced gilbert damping in thin ferromagnetic films. *Physical Review Letters*, 88:117601, 2002.

[126] *Diamond Light Source I10 Website*, 2018. URL https://www.diamond.ac.uk/Instruments/Magnetic-Materials/I10/layout.html.

[127] R. F. L. Evans, W. J. Fan, P. Chureemart, T. A. Ostler, M. O. A. Ellis, and R. W. Chantrell. Atomistic spin model simulations of magnetic nanomaterials. *Journal of Physics Condensed Matter*, 26:103202, 2014.

[128] J. Barker and R. W. Chantrell. Higher-order exchange interactions leading to metamagnetism in FeRh. *Physical Review B*, 92:094402, 2015.

[129] J. M. Shaw, H. T. Nembach, T. J. Silva, and C. T. Boone. Precise determination of the spectroscopic g-factor by use of broadband ferromagnetic resonance spectroscopy. *Journal of Applied Physics*, 114:243906, 2013.

[130] Y. Ding, D. A. Arena, J. Dvorak, M. Ali, C. J. Kinane, C. H. Marrows, B. J. Hickey, and L. H. Lewis. Bulk and near-surface magnetic properties of FeRh thin films. *Journal of Applied Physics*, 103:07B515, 2008.

[131] R. A. Khan, H. T. Nembach, M. Ali, J. M. Shaw, C. H. Marrows, and T. A. Moore. Magnetic domain texture and the Dzyaloshinskii-Moriya interaction in Pt/Co/IrMn and Pt/Co/FeMn thin films with perpendicular exchange bias. *Physical Review B*, 98:064413, 2018.

[132] J. McCord, R. Mattheis, and D. Elefant. Dynamic magnetic anisotropy at the onset of exchange bias: The Ni Fe/ Ir Mn ferromagnet/antiferromagnet system. *Physical Review B*, 70:094420, 2004.

[133] C. Stamm, J.-U. Thiele, T. Kachel, I. Radu, P. Ramm, M. Kosuth, J. Minár, H. Ebert, H. A. Dürr, W. Eberhardt, and C. H. Back. Antiferromagnetic-ferromagnetic phase transition in FeRh probed by x-ray magnetic circular dichroism. *Physical Review B*, 77:184401, 2008.

[134] M. G. Loving, R. Barua, C. Le Graët, C. J. Kinane, D. Heiman, S. Langridge, C. H. Marrows, and L. H. Lewis. Strain-tuning of the magnetocaloric transition temperature in model FeRh films. *Journal of Physics D: Applied Physics*, 51: 024003, 2017.

[135] H. T. Nembach, T. J. Silva, J. M. Shaw, M. L. Schneider, M. J. Carey, S. Maat, and J. R. Childress. Perpendicular ferromagnetic resonance measurements of damping and Landé g-factor in sputtered $(Co_2Mn)_{1-x}Ge_x$ thin films. *Physical Review B*, 84:054424, 2011.

[136] L. Frangou, S. Oyarzún, S. Auffret, L. Vila, S. Gambarelli, and V. Baltz. Enhanced spin pumping efficiency in antiferromagnetic IrMn thin films around the magnetic phase transition. *Physical Review Letters*, 116:077203, 2016.

[137] P. Merodio, A. Ghosh, C. Lemonias, E. Gautier, U. Ebels, M. Chshiev, H. Béa, V. Baltz, and W. E. Bailey. Penetration depth and absorption mechanisms of spin currents in $Ir_{20}Mn_{80}$ and $Fe_{50}Mn_{50}$ polycrystalline films by ferromagnetic resonance and spin pumping. *Applied Physics Letters*, 104:032406, 2014.

[138] H. Wang, C. Du, P. C. Hammel, and F. Yang. Antiferromagnonic spin transport from $Y_3Fe_5O_{12}$ into NiO. *Physical Review Lett.*, 113:097202, 2014.

[139] D. D. Stancil and A. Prabhakar. *Spin Waves: Theory and Applications*, chapter 3, page 100. Springer, 2010.

[140] S. Blundell. *Magnetism in Condensed Matter*, chapter 6. Oxford University Press, 2001.

[141] J. Stohr and H. C. Siegmann. *Magnetism: From Fundamentals to Nanoscale Dynamics*, chapter 11. Springer Series in Solid State Physics, 2006.

[142] J. M. D. Coey. *Magnetism and Magnetic Materials*, chapter 7, page 235. Cambridge University Press, 3 edition, 2012.

[143] O. Ŝipr, S. Mankovsky, and H. Ebert. Spin wave stiffness and exchange stiffness of doped permalloy via ab-initio calculations. *arXiv e-prints*, page 1903.05506, 2019.

[144] M. Pajda, J. Kudrnovský, I. Turek, V. Drchal, and P. Bruno. Ab initio calculations of exchange interactions, spin-wave stiffness constants, and curie temperatures of Fe, Co, and Ni. *Physical Review B*, 64:174402, 2001.

[145] V. V. Kruglyak, O. Y. Gorobets, Y. I. Gorobets, and A. N. Kuchko. Magnetization boundary conditions at a ferromagnetic interface of finite thickness. *Journal of Physics: Condensed Matter*, 26:406001, 2014.

[146] C. Hahn, G. de Loubens, V. V. Naletov, J. Ben Youssef, O. Klein, and M. Viret. Conduction of spin currents through insulating antiferromagnetic oxides. *Europhysics Letters*, 108:57005, 2014.

[147] S. Takei, T. Moriyama, T. Ono, and Y. Tserkovnyak. Antiferromagnet-mediated spin transfer between a metal and a ferromagnet. *Physical Review B*, 92:020409, 2015.

[148] I. Gray, G. M. Stiehl, J. T. Heron, A. B. Mei, D. G. Schlom, R. Ramesh, D. C. Ralph, and G. D. Fuchs. Imaging uncompensated moments and exchange-biased emergent ferromagnetism in FeRh thin films. *arXiv e-prints*, page arXiv:1906.07243, 2019.

[149] D.N. Kande, S. Pisana, D. Weller, D. E. Laughlin, and J. G. Zhu. Enhanced B2 ordering of FeRh thin films using B2 NiAl underlayers. *IEEE Transactions on Magnetics*, 47:3296, 2011.

[150] J. M. D. Coey. *Magnetism and Magnetic Materials*, chapter 7, page 242. Cambridge University Press, 3 edition, 2012.

[151] E. W. Hansen, X. Gong, and Q. Chen. Compressed exponential response function arising from a continuous distribution of gaussian decays - distribution characteristics. *Macromolecular Chemistry and Physics*, 214:844, 2013.

[152] D. C. Johnston. Stretched exponential relaxation arising from a continuous sum of exponential decays. *Physical Review B*, 74:184430, 2006.

[153] E. J. Banigan, M. K. Illich, D. J. Stace-Naughton, and D. A. Egolf. The chaotic dynamics of jamming. *Nature Physics*, 9:288, 2013.

[154] C. Lui, E. Pineda, and D. Crespo. Mechanical relaxation of metallic glasses: An overview of experimental data and theoretical models. *Metals*, 5:1073, 2015.